Towards deterministic preparation of single Rydberg atoms and applications to quantum information processing

Carla Hermann Hermann Avigliano

Département de Physique
de L'École Normale Supérieure
Laboratoire Kastler Brossel

Departamento de Física
Centro de Óptica y Fotónica
Universidad de Concepción

THÈSE DE DOCTORAT DE L'UNIVERSITÉ PARIS VI
TESIS DE DOCTORADO DE LA UNIVERSIDA DE CONCEPCION

Spécialité/Especialidad : **Physique Quantique/Física Cuántica**

présentée par/presentada por

Carla HERMANN AVIGLIANO

pour obtenir le grade de/para obtener el grado de

Docteur de l'Université Paris VI
Doctor de la Universidad de Concepción

Sujet/Sujeto:

Towards deterministic preparation of single Rydberg atoms and applications to quantum information processing.

Soutenue le/Defendida el 25/11/2014 devant le jury composé de /delante del jurado compuesto por:

Dr.	Tatjana Wilk	Rapporteur/ Reportador
Pr.	Jean-Michel Raimond	Directeur de thèse/ Director de tesis
Pr.	Carlos Saavedra Rubilar	Directeur de thèse/ Director de tesis
Pr.	Catherine Schwob	Examinateur/ Examinador
Pr.	Pierre Pillet	Rapporteur/ Reportador

Mariza, Reinaldo, Lorena, Moma, Nonno, Lucy y Carlos.

Acknowledgements

This research has been supported by the EU Marie Curie Action CCQED, Project Number 264666, Call: FP7-People-2010-ITN; by the EU ICT Project SIQS Number 600645; and by the DECLIC ERC project.
For the first two years of Phd in Chile (2009-2010), I was supported by CONICYT.

Remerciements

Ce travail de recherche a été financé par l'Action Marie Curie (UE) CCQED, Projet numéro 264666, Appel: FP7-People-2010-ITN; par le projet ICT (UE) SIQS Numéro 600645; et par le projet ERC DECLIC.
Pour les deux premières années de thèse au Chili (2009-2010), j'ai été financée par CONICYT.

Agradecimientos

Esta investigación ha sido financiada por *UE Marie Curie Action* CCQED, Número del Proyecto 264666, llamado: FP7-People-2010-ITN; por el EU ICT Proyecto SIQS Número 600.645; y por el proyecto ERC DECLIC.
Durante los dos primeros años de doctorado en Chile (2009-2010), recibí el apoyo de CONICYT.

Contents

Introduction in English

My thesis, and hence this manuscript, is divided into two parts. One is devoted to an experiment with Rydberg atoms on a superconducting atom-chip, whose aim is to study the dipole blockade mechanism. This work has been done in Paris, under the supervision of professor Jean-Michel Raimond. The other part is a theoretical work, in which we propose a novel scheme for the generation of mesoscopic field state superpositions (MFSS) in the context of cavity quantum electrodynamics (CQED) experiments. This work was carried out in a co-supervision between professors Jean-Michel Raimond and Carlos Saavedra Rubilar (Concepción, Chile). Both topics deal with fundamental physics research about the manipulation of individual quantum systems.

The principles of quantum mechanics entail many counterintuitive consequences for a "classical" mind, and the fathers of the theory quickly became aware of this weirdness. Many thought experiments were proposed in order to achieve a better understanding of the emerging theory when applied to isolated atoms, photons, or electrons.

Important differences emerge between quantum and classical physics when it comes to the description of a measurement. In both the classical and quantum pictures, a measurement process is defined as an extraction of information from the system. Classically, we are able to measure some characteristics like velocity, position, etc., without ambiguity. We just need the appropriate apparatus to perform the measurement. The state of the system under study is not modified due to the measurement process.

Quantum mechanics tells us a different story. A measurement is associated with a projection: after an *ideal* measurement (projective, or von Neumann measurement), the state vector of the system is projected onto one of the eigenstates $|o\rangle$ of the associated observable O. The only possible results of the measurement are the eigenvalues of O. For a given initial state $|\psi\rangle$, the probability to obtain a given eigenvalue is defined by the decomposition of the state in the basis of the eigenvectors of O, $|o_i\rangle$. Thus, a measurement may modify the state of a system in the quantum realm. But even after a measurement has been performed and a value has been obtained, nothing guarantees that the same result would be obtained in a later measurement, due to the system evolution. The repeatability of the measurement is ensured for *quantum non demolition measurements* (QND) [1], for which the observable O is a constant of motion.

Entanglement is another weird quantum concept, which has no classical counterpart and is very deeply connected to the measurement problem. Let us just mention here one of the most famous examples: the thought experiment devised by Schrödinger in 1935 about

a cat that is *dead and alive*. In this scenario, a cat is trapped inside a box equipped with a *diabolical* system based on a radioactive particle and a Geiger counter. The particle may decay in one hour or may not, with equal probabilities. Therefore after one hour, the expression for the state of the system is:

$$|\psi\rangle = (|\psi_{alive}\rangle \otimes |1\rangle + |\psi_{dead}\rangle \otimes |2\rangle) \tag{1}$$

where $|1\rangle$ (resp. $|2\rangle$) denotes the state of the particle when it has not decayed (resp. it has decayed) and $|\psi_{alive}\rangle$ (resp. $|\psi_{dead}\rangle$) the alive (dead) state of the cat. In this situation, a microscopic quantum system is entangled to a macroscopic system. The particle governs the evolution of the state according to the Schrödinger evolution. If a measurement is performed on the microscopic system (using the Geiger counter to check for the radioactive decay), then a projection takes place both on the microscopic and the macroscopic systems that are mutually entangled. With this very simple thought experiment Schrödinger was pointing out the "ridiculous consequences" of the quantum weirdness when extrapolated to the macroscopic world.

These "ridiculous consequences" are of course never observed on large objects, such as a cat. A large quantum system always interacts strongly with its environment. The coupling to this utterly complex bath results in a fast leakage of information from the system into the environment and hence in a rapid destruction of mesoscopic state superpositions, transformed into mundane statistical mixtures. This is the decoherence process, which confines the quantum weirdness to the microscopic scale.

For the study of fundamental quantum process and quantum superpositions to be possible, the state *decoherence* must be avoided as far as possible. The coupling to the environment is inevitable for any system. Hence decreasing its effect to a minimum is undoubtedly one of the greatest challenges for experimental quantum physics. CQED experiments in the microwave regime [2] are quite well suited for the realization of quantum manipulations at the atom-photon level, with state superpositions preserved long enough to be observed [3]. These experiments combine a superconducting cavity and Rydberg atoms in circular states crossing it.

The Rydberg states are atomic states with remarkable, and even surprising properties, quite exaggerated when compared to those of ordinary atomic levels. Their properties include very large sizes (reaching up to the micrometer range), very strong dipole-dipole interactions, huge Stark polarizabilities scaling as n^{*7} with n^* being the (effective) principal quantum number, etc.

Most of all, *circular* Rydberg states have a very long lifetime, of the order of tens of milliseconds. These atoms and superconducting cavities (where photons may have very long lifetime due to the high-reflecting mirrors) are remarkable tools for the exploration of basic quantum phenomena and for quantum information processing experiments [2].

The principle of these experiments is very simple, with a single atom interacting with a single field mode stored in a cavity. This is the simplest matter-field system, described theoretically for the first time by Jaynes and Cummings in 1963 [4]. Its experimental realization nevertheless represents a big experimental challenge, since the system must be very well isolated from all sources of perturbation, including the blackbody radiation.

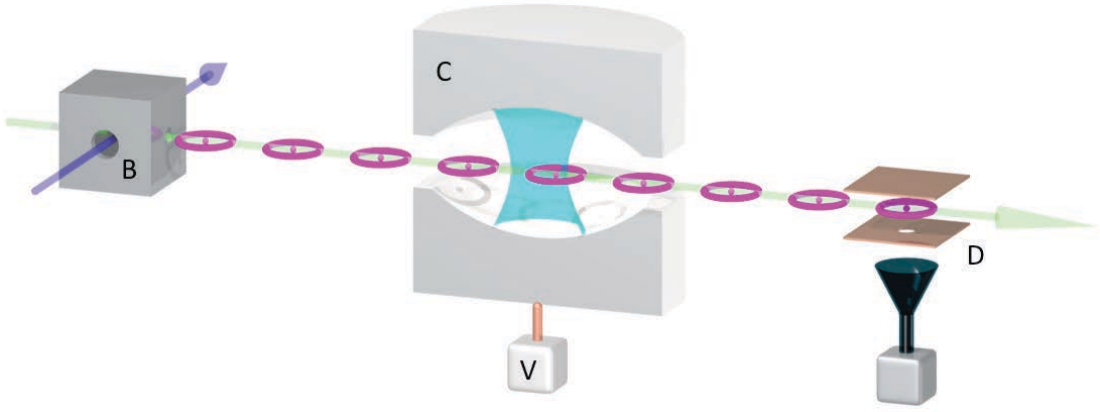

Figure 1: CQED experimental setup. B denotes the circular state preparation box. The atomic beam effuses from an oven (not shown). C is a high finesse microwave cavity made up of two superconducting mirrors between which the photons of the mode under study are trapped. The atomic state is finally measured by field-ionization in the detector D.

A very simplified version of the experimental setup is shown in figure 1. It uses the weak laser excitation of an atomic beam to produce Rydberg atoms at thermal velocities. All the parameters of the atomic samples are under control (velocity, preparation time, etc.), but the number of atoms in each sample is random and obeys a Poisson statistics. The average number of atoms per sample is set to a low value in order to have at most one single atom interacting with the cavity field at a time.

This initial laser excitation takes place in the box B (figure 1), where the atoms are also transferred into the circular states. They interact along their way through the apparatus with the superconducting cavity C, which may contain for instance a coherent field. The amplitude of this field can easily be varied from the classical range (many photons) to the quantum range (about a photon on average). The atomic state is finally detected in the detector D.

This experiment is particularly well suited for the generation and observation of mesoscopic field states superpositions (MFSS). The MFSS can be produced by the dispersive interaction of a single atom with a small coherent field stored in the cavity, a situation quite reminiscent of the Schrödinger cat [3].

MFSS can also be generated through the resonant interaction of a single atom with a coherent field. This MFSS generation procedure was theoretically proposed by Gea-Banacloche in the nineties [5, 6], and independently, by Buzek and Knight [7]. It was implemented for the first time in our group [8, 9] in CQED experiments.

In the theoretical part of this manuscript, we explore the resonant interaction of $N = 2$ two-level atoms with a coherent cavity field, within the context of these CQED experiments. We show that this interaction generates efficienly large MFSS once the atomic system has been detected in the appropriate state. This conditional process might lead to the practical generation of "cats" involving hundreds of photons, much larger than those reachable with a single atom interaction. We also discuss the extension of this scheme to more than two

atoms by making use of the "factorization approximation" [10, 11].

Chapter V is devoted to the presentation of the basic theoretical ingredients for the description of the light-matter interaction. We start first by describing the field, giving an overview of field quantization and of phase-space representations of the field quantum state. We then describe the atomic state. We recall in particular the Bloch sphere representation and the processes of manipulation of the internal states. This chapter also includes a description of the interaction in the resonant and the dispersive regimes, and a last part describing the decoherence process for the field.

In chapter VI, we present the main theoretical results of this work. We start with a brief reminder of the Dicke model and we introduce the factorization approximation. We then present a simple analytical approach for two two-level atoms interacting with a coherent cavity field. We show that interesting non-classical states are generated in the cavity once the atomic system is detected in the appropriate state. We then conclude and open some interesting perspectives for further work.

In order to realize such experiments, a source of Rydberg atoms providing controlled number of atoms on demand would be ideal. The Poisson distribution of the atom number in the CQED experiments discussed above is indeed a serious problem. The average number of atoms per sample is kept low, making the data acquisition time an exponential function of the required number of interacting atoms. This is a severe limitation for quantum information experiments, in which a precise number of qubits must be prepared deterministically.

The goal of the experimental part of my thesis was thus to develop a **deterministic source of Rydberg atoms for quantum information processing experiments** working on a superconducting atom-chip and making use of the so called *dipole blockade* effect [12].

Neutral atoms are always interacting with each other via the dipole-dipole van der Waals interaction. This interaction is most of the time negligible for ground state atoms at low densities, due to their small dipole moment. It can on the contrary be extremely large between Rydberg atoms. They have notably large dipoles, scaling as n^2 (with n of the order of 60 in our experiments). The dipole blockade effect stems from these interactions.

To explain the principle of dipole blockade, let us consider two ground state atoms at a distance r (frame (a) in figure 2). When r is large, the dipole-dipole interaction between these atoms is negligible and they can be excited independently into the Rydberg state $|e\rangle$ by the same laser frequency. When the atoms are closer, the dipole-dipole interaction strongly shifts the Rydberg levels of the pair. As soon as this energy shift is larger than the linewidth of the excitation laser and larger than the level linewidth, the probability to excite two Rydberg atoms at the same time with a laser tuned to the single atom excitation frequency is considerably reduced. The dipole blockade mechanism only allows the excitation of one atom in the pair.

This principle can be extended to a larger sample of ground state atoms. Once an atom is excited, the dipole-dipole interaction shifts all other Rydberg transitions in the close vicinity out of laser resonance. The distance at which the dipole-dipole shift overwhelms

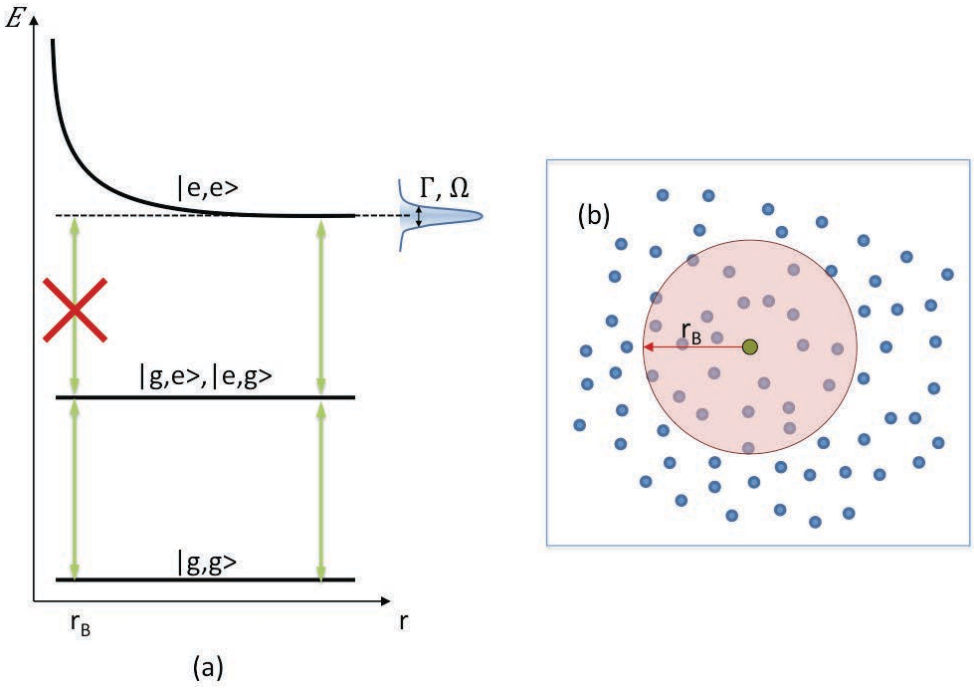

Figure 2: **(a)** Pictorial representation of the dipole-dipole interaction for two atoms. When they are far apart, the atoms are excited as if no interaction occurs. When they get closer, the energy of the pair Rydberg excitation $|e,e\rangle$ is shifted. If this shift is larger that the effective width of the transition (defined by Ω and Γ) the excitation of the second atom is out of resonance. **(b)** the same principle can be extrapolated to a sample with N atoms. Once an atom is excited, no other one can be excited inside a sphere defined by the blockade radius r_b.

the laser and atomic linewidths defines the blockade radius, in which no further atom can be excited. This blockade radius r_b is of the order of a few micrometers for the $60S$ state and a 600 kHz linewidth. This situation is pictorially represented in frame (b) of figure 2. In order to deterministically prepare a single atom out of an atomic cloud, the maximal distance between all atoms inside the excitation volume must be smaller than the blockade radius.

We have set up an experiment to investigate Rydberg-Rydberg interactions in a dense and small sample of ground-state atoms, containing a few hundred atoms within a size in the micrometer range. Such densities are obtained for instance in magnetic traps produced by atom chips, close to the Bose-Einstein condensation [13]. A few hundred atoms can indeed be trapped in a Ioffe-Pritchard trap, with transverse dimensions below 1 μm and a length of a few μm. Since Rydberg atoms are quite sensitive to thermal fields, the experiment is performed in a cryogenic environment, to which a superconducting chip is perfectly adapted.

The trap dimensions are compatible with the expected blockade volume for our target state (60S), of the order of a few $(\mu m)^3$. This holds as long as the Rydberg excitation

line is not broadened by laser instabilities or electric field inhomogeneities. The last point constitutes a severe bottleneck for these experiments, since Rydberg atoms are highly sensitive to electric fields.

Their huge Stark polarizability has a positive and a negative side. For the positive one, it allows us to tune the atomic transition with moderate electric fields. This feature is regularly used in CQED experiments. The high sensitivity to electric fields also lead to the selective field-ionization method (chapter I).

On the negative side, Rydberg atoms are extraordinarily sensitive to stray electric fields, which must therefore be controlled as carefully as possible. Uncontrolled electric fields are particularly harmful in the atom-chip context, since the atomic sample must reside very near to a cold metallic surface. Any isolating impurity on the surface can accumulate a large charge. Even if dust is avoided, the patch effects due to the contact between different metals or even the same metal with different crystalline orientations can create sizable fields a few tens of micrometers away from the surface.

In particular, the patch field created by the Rubidium atoms unavoidably deposited onto the chip surface have been found to be a problem [14, 15]. This uncontrolled deposition leads to the creation of intense field gradients near the chip, jeopardizing any possibility of achieving coherent state manipulations, not to mention the blockade effect. Most of the experimental work presented in this manuscript has in fact been devoted to the elimination of these stray electric fields, since it is the very first limitation to overcome in order to eventually reach the dipole blockade regime in this context.

In order to measure the electric field near the chip surface and to probe the coherence of our atoms by Ramsey and Spin-echo sequences, it is possible to make use of millimeter-wave field transition between neighbors Rydberg states. Similar sequences have been performed in reference [16], where coherent manipulations of the levels $49S$ and $48S$ were realized near an atom-chip surface, with coherence times of the microsecond range only.

Chapter I describes the basic theoretical elements necessary for the understanding of the experimental part of our work. We briefly recall the main properties of Rydberg atoms, including some aspects of the circular states, and we discuss in particular their response to electric and to magnetic fields. We then turn to the dipole blockade mechanism itself. We describe its principle, the dipole-dipole interactions involved, and we discuss the situation for the target state 60S. The chapter ends with simulations performed with realistic parameters.

In chapter II, we present the experimental setup, including all steps necessary for the optical cooling and trapping of the atoms. The core of the experiment is the superconducting atom chip, which is placed inside a cryogenic environment. We use the chip to create a magnetic trap, which is the final stage for the atomic confinement and the starting point for the Rydberg excitation experiments.

Chapter III is devoted to the first studies of the electric field in the excitation region. First, we describe the laser system stabilization. We then present the detection setup for the ions produced from the Rydberg atoms, which is installed inside the cryogenic environment. We finally present our first atomic spectra and the electric field measurements performed

using the optical two-photon transition $5S \rightarrow 60S$. We discuss the instabilities of the electric field in front of the superconducting surface and we end the chapter with the solution we finally found to get rid of the stray fields.

Finally chapter IV presents the main experimental results of the thesis. The stray field cancellation allows us to perform microwave spectroscopy of the Rydberg levels. We first use it to measure the electric field at different distances from the chip surface in order to characterize the excitation zone. After that, for two different distances from the chip, 150 μm and 450 μm, we perform Ramsey and Spin-echo sequences, revealing extremely long coherence lifetimes in the millisecond range. We finish the experimental part of the manuscript with a few pages devoted to conclusion and perspectives.

Introduction en français

Mon travail de doctorat est divisé, comme ce manuscrit, en deux parties. La première est consacrée à une expérience manipulant des atomes de Rydberg sur une puce à atomes supraconductrice, dont le but est d'étudier le mécanisme de blocage dipolaire. Ce travail a été effectué à Paris, sous la direction du Professeur Jean-Michel Raimond. La seconde est un travail théorique, dans lequel nous proposons un protocole original pour la création de superpositions mésoscopique d'états d'un champ (*mesoscopic field state superposition*, ou MFSS) dans le contexte d'expériences d'électrodynamique quantique en cavité (*cavity quantum electrodynamics*, ou CQED). Cette recherche a été menée sous la cotutelle des professeurs Jean-Michel Raimond et Carlos Saavedra Rubilar (Concepción, Chili). Ces deux sujets de recherche se rattachent au problème fondamental de la manipulation de systèmes quantiques individuels.

Les principes de la mécanique quantique entraînent de nombreuses conséquences contre-intuitives pour un esprit «classique», et les pères de la théorieont rapidement pris conscience de cette étrangeté. De nombreuses expériences de pensée ont été imaginées afin de mieux comprendre la théorie naissante lorsqu'elle s'applique à des atomes, des photons, ou des électrons individuels.

Des différences importantes apparaissent entre la physique classique et la physique quantique en ce qui concerne la description d'une mesure. Dans les deux cas, une mesure est définie comme l'extraction d'information du système étudié. Dans le cas classique, il est possible de mesurer certaines caractéristiques sur le système sans ambiguité. Il est juste nécessaire d'avoir l'appareil de mesure approprié. L'état du système étudié n'est pas non plus modifié par le processus de mesure.

L'histoire n'est pas la même en mécanique quantique. Une mesure est associée à une projection : après une mesure *idéale* (mesure projective, ou de von Neumann), le vecteur d'état du système est projeté sur l'un des états propres $|o\rangle$ de l'observable associée O. Les seuls résultats possibles de la mesure sont les valeurs propres de O. Pour un état initial $|\psi\rangle$, la probabilité d'obtenir une valeur propre donnée est définie par la décomposition de l'état sur la base des vecteurs propres de O, $|o_i\rangle$. Ainsi dans le monde quantique, l'état d'un système peut être modifié par une mesure. Mais même après qu'une mesure a été réalisée et une valeur obtenue, rien ne garantit que le même résultat soit obtenu lors d'une mesure ultérieure, du fait de l'évolution du système. Dans le cas d'une mesure quantique non-destructive (QND) [1], la répétabilité de la mesure est assurée par le fait que O est une constante du mouvement.

L'*intrication* est un autre concept étrange de la physique quantique, qui n'a pas d'équivalent classique et est très profondément lié au problème de la mesure. Mentionnons simplement ici l'un des exemples les plus connus: l'expérience de pensée, conçue par Schrödinger en 1935, mettant en scène un chat *mort et vivant*. Dans ce scénario, un chat est placé dans un boîte équipée d'un système diabolique constitué d'une particule radioactive et d'un compteur Geiger. Après une heure, la particule peut s'être désintégrée, ou non, avec des probabilités égales. Par conséquent, après une heure, l'état du système s'écrit:

$$|\psi\rangle = (|\psi_{alive}\rangle \otimes |1\rangle + |\psi_{dead}\rangle \otimes |2\rangle) \tag{2}$$

où $|1(2)\rangle$ dénote l'état de la particule lorsqu'elle ne s'est pas désintégrée (resp. s'est désintégrée) et $|\psi_{alive(dead)}\rangle$ l'état vivant (resp. mort) du chat. Dans cette situation, un système quantique est intriqué avec un système macroscopique. L'évolution de l'état est gouvernée par celle de la particule, qui obéit à l'équation de Schrödinger. Si l'on effectue une mesure sur le système microscopique (en utilisant le compteur Geiger pour vérifier si la désintégration radioactive a eu lieu), on projette l'état des deux systèmes, microscopique et macroscopique, qui sont mutuellement intriqués. Avec cette simple expérience de pensée, Schrödinger mettait en évidence les «conséquences ridicules» de l'étrangeté quantique, quand elle est étendue au monde macroscopique.

Ces «conséquences ridicules» ne sont bien entendu jamais observées pour de grands systèmes, comme un chat. Un grand système quantique interagit toujours fortement avec son environnement. Le couplage à ce bain extrêmement complexe induit une fuite d'information du système dans son environnement, et par conséquent une destruction rapide des superpositions macroscopiques d'états, transformées en de banals mélanges statistiques. C'est la *décohérence*, qui confine l'étrangeté quantique à l'échelle microscopique.

Si l'on veut étudier les processus quantiques et les superpositions d'états, la *décohérence* du système doit être évitée à tout prix. Le couplage à l'environnement est inévitable quel que soit le système. Réduire ses effets au minimum est donc sans aucun doute l'un des grands enjeux de la physique quantique expérimentale. Les expériences de CQED dans le domaine micro-onde [2] sont bien adaptées à la réalisation de manipulations quantiques à l'échelle de l'atome et du photon uniques, produisant des superpositions d'états de temps de vie assez long pour permettre leur observation [3]. Ces expériences combinent une cavité micro-onde supraconductrice et des atomes dans des états circulaires de Rydberg la traversant.

Les états de Rydberg sont des états atomiques aux propriétés remarquables, et même surprenantes, dépassant de beaucoup celles des niveaux atomiques ordinaires. Ils ont en particuler une extension très grande (atteignant des dimensions micrométriques), de très fortes interactions dipôle-dipôle et une polarisabilité Stark considérable, évoluant en n^{*7} où n^* est le nombre quantique principal (effectif).

Par-dessus tout, les états *circulaires* de Rydberg ont un temps de vie très grand, de l'ordre de la dizaine de millisecondes. De tels atomes et des cavités supraconductrices (où les photons micro-ondes piégés entre deux miroirs extrêmement réfléchissants peuvent avoir un temps de vie très long) constituent des outils remarquables pour l'exploration des phénomènes quantiques élémentaires et des expériences d'information quantique [2].

Ces expériences sont très simples en principe, faisant interagir un seul atome avec un seul mode du champ piégé dans une cavité. C'est le système matière-lumière le plus simple, décrit théoriquement pour la première fois par Jaynes et Cummings en 1963 [4]. Sa réalisation constitue cependant un vrai défi expérimental, le système devant être parfaitement isolé de toute perturbation, y compris du rayonnement du corps noir.

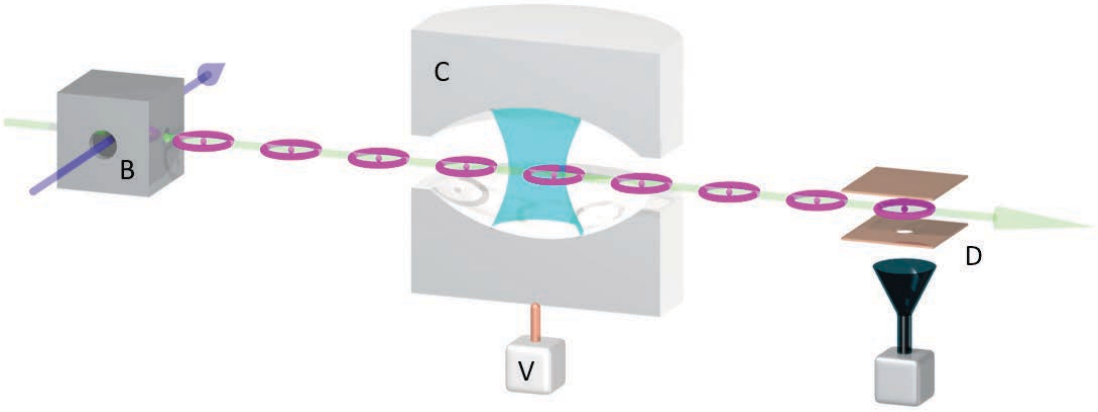

Figure 3: Dispositif expérimental de CQED. B dénote la boîte où sont préparés les états circulaires. Le jet atomique est issu d'un four (non montré). C est un cavité micro-onde de grande finesse constituée de deux miroirs supraconducteurs entre lesquels sont piégés les photons du mode étudié. L'état des atomes est finalement mesuré par ionisation par champ électrique dans le détecteur D.

Un schéma très simplifié du dispositif expérimental est montré sur la figure 3. Une faible excitation laser pulsée crée des atomes de Rydberg dans un jet atomique à des vitesses thermiques. Tous les paramètres dynamiques de l'échantillon excité sont contrôlés (vitesse, instant de préparation, etc.), mais le nombre d'atomes de Rydberg dans l'échantillon est aléatoire et distribué selon un loi de Poisson. Le nombre moyen d'atomes est choisi suffisamment faible pour n'avoir qu'au plus un atome à la fois interagissant avec la cavité.

L'excitation laser initiale a lieu dans la boîte B (figure 3), où les atomes sont aussi transférés dans les états circulaires. Leur de trajet à travers le dispositif, ils interagissent avec la cavité supraconductrice C, qui peut contenir par exemple un champ cohérent. L'amplitude de ce champ peut facilement être variée du régime classique (de nombreux photons) au régime quantique (nombre de photons moyen de l'ordre de l'unité). L'état des atomes est finalement mesuré dans le détecteur D.

Cette expérience est particulièrement adaptée à la création et l'observation de superpositions mésoscopiques de l'état du champ (MFSS). Les MFSS peuvent être produites par l'interaction dispersive d'un atome unique avec un petit champ cohérent piégé dans la cavité, une situation qui rappelle celle du chat de Schrödinger [3].

Des MFSS peuvent aussi être engendrées par interaction résonante entre un atome unique et un champ cohérent. Cette procédure a été proposée théoriquement par Gea-

Banacloche dans les années quatre-vingt-dix [5, 6] et indépendemment par Buzek et Knight [7]. Elle a été réalisée pour la première fois dans des expériences de CQED dans notre groupe [8, 9].

Dans la partie théorique de ce manuscrit, nous étudions le cas de l'interaction résonante de $N = 2$ atomes à deux niveaux avec un champ cohérent en cavité, dans le contexte de ces expériences de CQED. Nous montrons qu'une telle interaction produit efficacement des MFSS de grande taille, lorsque le système atomique est détecté dans un état bien précis. Cette production conditionnelle peut mener à la création de «chats» comprenant des centaines de photons, bien plus que ce qui est atteignable par interaction avec un seul atome. Nous discutons aussi de l'extension de ce procédé à plus de deux atomes, en utilisant «l'approximation de factorisation» [10, 11].

Le chapitre V est dédié à la présentation des outils théoriques de base pour la description de l'interaction lumière-matière. Nous commençons par décrire le champ, en donnant une vue d'ensemble de la quantification du champ et des représentations de l'état du champ dans l'espace des phases. Nous décrivons ensuite l'état de l'atome. Nous rappelons en particulier la représentation sur la sphère de Bloch, et les procédés de manipulation de l'état interne. Ce chapitre comprend également une description de l'interaction atome-champ dans les régimes résonant et dispersif, et une section finale décrivant le processus de décohérence du champ.

Dans le chapitre VI, nous présentons les principaux résultats théoriques de ce travail. Nous commençons par rappeler brièvement le modèle de Dicke, et introduisons l'approcimation de factorisation. Nous présentons ensuite une approche analytique simple du problème de deux atomes à deux niveaux interagissant avec un champ cohérent en cavité. Nous montrons que des états non-classiques sont produits dans la cavité lorsque le système atomique est détecté dans l'état idoine. Nous concluons et proposons quelques pistes intéressantes pour prolonger ce travail.

Pour réaliser de telles expériences, il serait idéal de disposer d'une source d'atomes de Rydberg fournissant un nombre d'atomes fixé à la demande. La distribution de Poisson du nombre d'atomes dans les expériences de CQED présentées ci-dessus est en effet un sérieux problème. Le nombre moyen d'atomes par échantillon doit être choisi faible, ce qui conduit à des temps d'acquisition de données variant exponentiellement avec le nombre d'atomes requis. Ceci est une limitation sévère pour des expériences d'information quantique, dans lesquelles un nombre précis de qbits doit être préparé de façon déterministe.

Le but de la partie expérimentale de ma thèse est donc de développer une **source déterministe d'atomes de Rydberg pour des expériences d'information quantique**, en travaillant sur une puce à atomes supraconductrice, et en exploitant l'effet de «blocage dipolaire» [12].

Des atomes neutres interagissent toujours entre eux par interactions dipôle-dipôle de Van der Waals. Cette interaction est la plupart du temps négligeable pour des atomes dans leur état fondamental et pour de faibles densités, étant donné leur faible moment dipôlaire. Elle peut au contraire être très forte entre atomes de Rydberg. Ils possèdent un dipôle particulièrement grand, qui varie comme n^2 (n est de l'ordre de 60 dans nos expériences).

L'effet de blocage dipolaire a pour origine ces fortes interactions.

Afin d'expliquer le principe du blocage dipolaire, considérons deux atomes dans l'état fondamental à une distance r (cadre (a) de la figure 4). Quand r est grand, l'interaction dipôle-dipôle entre ces atomes est négligeable et ils peuvent être indépendamment excités dans l'état de Rydberg $|e\rangle$ par la même fréquence laser. Quand les atomes sont plus proches, l'interaction dipôle-dipôle déplace fortement l'énergie des niveaux de Rydberg de la paire d'atomes. Dès que ce déplacement est plus grand que la largeur spectrale du laser d'excitation et que la largeur intrinsèque du niveau excité, la probabilité d'exciter deux atomes de Rydberg à la fois à l'aide d'un laser accordé à la fréquence d'excitation d'un atome individuel est considérablement réduite. Le *blocage dipolaire* ne permet l'excitation que d'un atome de la paire.

Ce principe peut être étendu à un échantillon plus grand d'atomes dans l'état fondamental. Une fois un atome excité, l'interaction dipôle-dipôle décale la transition de Rydberg hors de résonance avec le laser d'excitation pour tous les atomes dans son voisinage proche. La distance à laquelle le décalage dipôle-dipôle dépasse les largeurs spectrales du laser et de l'état excité définit le rayon de blocage dans lequel on ne peut plus exciter d'atome supplémentaire. Ce rayon de blocage, r_b, est de l'ordre de quelques micromètres pour l'état $60S$ et une largeur spectrale laser de 600 kHz. La situation est schématiquement représentée dans le cadre (b) de la figure 4. Afin de préparer un atome unique à partir d'un nuage atomique, la distance maximale entre atomes à l'intérieur du volume d'excitation doit être plus petite que le rayon de blocage.

Nous avons mis en place une expérience pour étudier les interactions Rydberg-Rydberg dans un petit échantillon dense d'atomes dans l'état fondamental, une centaine d'atomes dans un volume micrométrique. De telles densités peuvent être obtenues par exemple dans des pièges magnétiques créés par des puces à atomes, près de la condensation de Bose-Einstein [13]. On peut en effet piéger une centaine d'atomes dans un piège de Ioffe-Pritchard, de dimensions inférieures à 1 μm transversalement et de longueur quelques micromètres. Les atomes de Rydberg étant sensibles au champ thermique, l'expérience est menée en environnement cryogénique, auquel la puce supraconductrice est parfaitement adaptée.

Les dimensions du piège sont compatibles avec le volume de blocage attendu pour notre état-cible (60S), de l'ordre de quelques $(\mu m)^3$. Ceci est vrai tant que la raie d'excitation Rydberg n'est pas élargie par des instabilités laser ou des inhomogénéités de champ électriques. Ce dernier point constitue une contrainte forte pour ces expériences, les états de Rydberg étant extrêmement sensibles aux champs électriques.

Leur polarisabilité Stark considérable est à la fois un avantage et un inconvénient. Du côté positif, elle permet d'accorder facilement la transition atomique à l'aide de faibles champs électriques. Cette propriété est utilisée régulièrement dans les expériences de CQED. La grande sensibilité aux champs électriques rend également possible la détection de l'état atomique par ionisation (chapter I).

C'est aussi un inconvénient, car les atomes de Rydberg sont extraordinairement sensibles à des champs électriques parasites, qui doivent donc être contrôlés aussi précisément que possible. Des champs électriques mal contrôlés sont particulièrement néfastes dans le

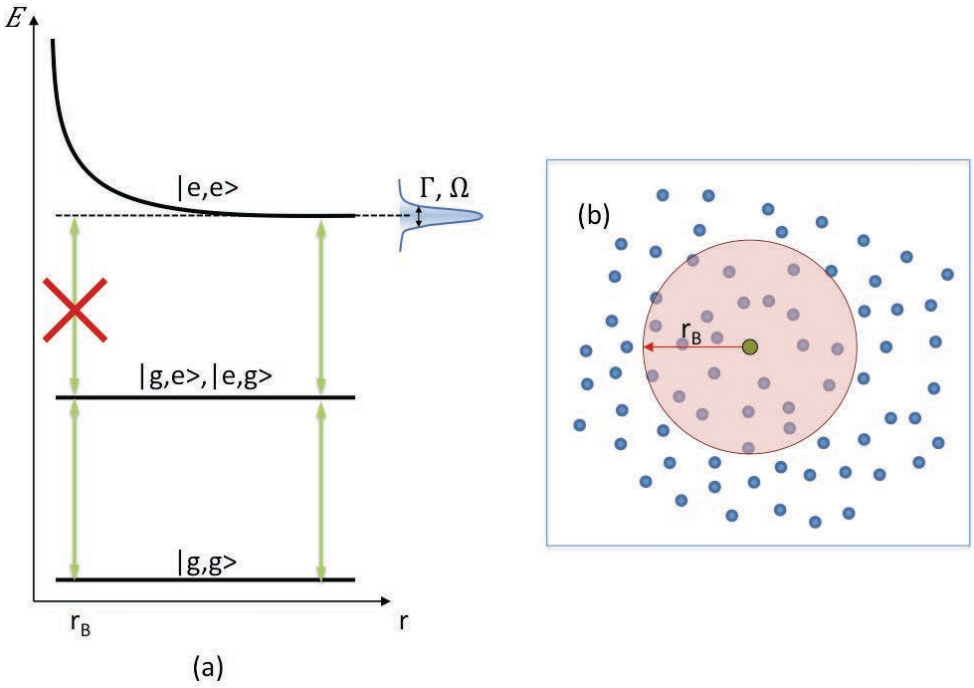

Figure 4: **(a)** Représentation schématique de l'interaction dipôle-dipôle entre deux atomes. Quand ils sont éloignés l'un de l'autre, les atomes sont excités comme s'il n'y avait pas d'interaction. Quand ils sont rapprochés, l'énergie d'excitation de la paire d'atomes de Rydberg $|e,e\rangle$ est décalée. Si ce décalage est plus grand que la largeur effective de la transition (définie par Ω et Γ), l'excitation du second atome est hors de résonance. **(b)** le même principe peut être extrapolé à un échantillon contenant N atomes dans lequel, une fois un premier atome excité, aucun autre atome ne peut l'être à l'intérieur d'un volume sphérique défini par le rayon de blocage r_b.

cas d'une puce à atomes, puisque le nuage atomique est maintenu très près d'une surface métallique froide. Toute impureté isolante sur cette surface peut accumuler une grande charge électrique. Même si toute poussière est évitée, les effets de contact ou de domaines (*patch effects*) dûs au contact entre deux métaux, ou même entre grains d'un même métal d'orientations cristallines différentes peuvent créer des champs électriques de taille conséquente à seulement quelques micromètres de la surface de la puce.

En particulier, le champ de contact créé par les atomes de rubidium qui se déposent inévitablement à la surface de la puce s'est révélé être un vrai problème [14, 15]. Ce dépôt incontrôlé engendre la création de forts gradients de champ au voisinage de la puce compromettant la possibilité de réaliser des manipulations cohérentes de l'état atomique, et, plus encore, le blocage dipolaire. La majeure partie du travail expérimental présenté dans ce manuscrit a donc été consacrée à l'élimination de ces champs électriques parasites, puisqu'il s'agit là de la toute première limitation à dépasser pour atteindre le régime de blocage dipolaire dans ce contexte.

Pour mesurer le champ électrique au voisinage de la puce, et pour tester la cohérence

de nos atomes à l'aide de séquences de Ramsey et d'écho de spin, il est possible d'utiliser les transitions millimétriques entre états de Rydberg voisins. Des séquences semblables ont été utilisées dans la référence [16], où des manipulations cohérentes des niveaux $49S$ et $48S$ ont été réalisées près de la surface d'une puce à atomes, et des temps de cohérence de l'ordre de la microseconde seulement ont été obtenus.

Le chapitre I décrit les outils théoriques de base nécessaires à la compréhension de la partie expérimentale de notre travail. Nous rappelons brièvement les principales propriétés des atomes de Rydberg, y compris certaines caractéristiques des états circulaires, et nous discutons en particulier de leur réponse à des champs électriques et magnétiques. Nous passons ensuite au mécanisme de blocage dipolaire. Nous en décrivons le principe, les interactions dipôle-dipôle mises en jeu, et étudions la situation pour l'état-cible 60S. Le chapitre se conclut par des simulations effectuées avec des paramètres réalistes.

Dans le chapitre II, nous présentons le dispositif expérimental, comprenant toutes les étapes nécessaires au refroidissement et au piégeage optique des atomes. Le coeur de l'expérience est constitué par la puce à atomes, placée en milieu cryogénique. Nous l'utilisons pour créer un piège magnétique, dernière étape du piégeage atomique, et point de départ pour les expériences d'excitation de Rydberg.

Le chapitre III est consacré aux premières études du champ électrique dans la zone d'excitation. Nous décrivons d'abord la stabilisation du système laser. Nous présentons ensuite le dispositif de détection des ions issus des atomes de Rydberg, qui est installé dans l'environnement cryogénique. Nous présentons finalement les premiers spectres atomiques et les mesures de champ électrique réalisées à l'aide de la transition optique à deux photons $5S \rightarrow 60S$. Nous discutons les instabilités du champ électrique au voisinage de la surface supraconductrice et concluons ce chapitre par la solution finalement trouvée pour se débarasser des champs électriques parasites.

Le chapitre IV présente finalement les principaux résulats expérimentaux de cette thèse. La suppression des champs électriques parasites nous permet d'effectuer la spectroscopie micro-onde des états de Rydberg. Nous l'utilisons d'abord pour mesurer le champ électrique à différentes distances de la puce, pour caractériser la zone d'excitation. Après cela, pour deux distances (150 μm et 450 μm) de la puce, nous réalisons des séquences de Ramsey et d'écho de spin, qui mettent en évidence des temps de cohérence très longs, de l'ordre de la milliseconde. Nous terminons la partie expérimentale de ce manuscrit par quelques pages consacrées à la conclusion et aux perspectives.

Introducción en español

Mi tesis, y por lo tanto este manuscrito, esta dividido en dos partes. La primera consagrada a la parte experimental con átomos de Rydberg en un chip atómico superconductor, que tiene como principal objetivo el estudio del mecanismo del efecto de bloqueo dipolar. Este trabajo fue realizado en Paris bajo la supervisión del profesor Jean-Michel Raimond. La otra parte consiste en un trabajo teórico, en el cual proponemos un nuevo esquema para generar estados de superposiciones mesoscópicas (*mesoscopic field state superposition*, o MFSS) en el contexto de la electrodinámica cuántica de cavidades (*cavity quantum electrodynamics*, o CQED). Este trabajo fue realizado bajo la co-supervisión de los profesores Jean-Michel Raimond y Carlos Saavedra Rubilar (Concepción, Chile). Ambos tópicos tratan la investigación a nivel de física fundamental, sobre la manipulación de sistemas cuánticos individuales.

Los principios de la mecánica cuántica conllevan muchas consecuencias contra-intuitivas para una mente "clásica"; los padres de la teoría rápidamente se dieron cuenta de esa rareza. Muchos experimentos pensados fueron propuestos con el objetivo de comprender mejor la teoría emergente cuando se aplica a átomos, fotones o electrones aislados.

Importantes diferencias surgen entre la física cuántica y la clásica a la hora de la descripción de una medida. En ambas, el proceso de medición es definido como la extracción de información de un sistema dado. Clásicamente, características como la velocidad, la posición, etc., pueden ser medidas sin ambigüedad. Solo es necesario un dispositivo apropiado para realizar la medida deseada. El estado del sistema bajo estudio no es modificado por el proceso de medida que se lleva a cabo.

La mecánica cuántica nos cuenta una historia diferente. Una medida es asociada a una proyección: luego de una medición *ideal* (o proyectiva, o de von Neumann), el estado (vector) del sistema es proyectado a uno de los estados propios $|o\rangle$ del observable asociado O. Los únicos posibles resultados de la medida son los autovalores de O. Para un estado arbitrario $|\psi\rangle$, la probabilidad de obtener un autovalor está definida a través de la descomposición de éste en la base de los estados propios de O, $|o_i\rangle$. Por lo tanto, una medida puede modificar el estado de un sistema en el reino cuántico. Pero aun más, incluso luego que una medida ha sido realizada y un valor ha sido obtenido, nada garantiza que el mismo resultado sea obtenido nuevamente, esto debido a la evolución del sistema. La repetibilidad de una medida es asegurada para *mediciones cuánticas no-destructivas* (*quantum non demolition measurements*, o QND) [1], para las cuales el observable O es una constante de movimiento.

El *entrelazamiento* es otro concepto cuántico extraño, que no tiene una contraparte clásica y que está profundamente relacionado con el problema de la medida. Consideramos aquí uno de los más famosos ejemplos: el experimento pensado ideado por Schrödinger en 1935 sobre el gato *vivo y muerto*. El escenario consiste en un gato encerrado dentro de una caja equipada con un sistema *diabólico* basado en una partícula radioactiva y un contador de Geiger. La partícula puede decaer en una hora o no, con igual probabilidad. Por consiguiente, luego de una hora, la expresión para el estado del sistema viene dado por:

$$|\psi\rangle = (|\psi_{alive}\rangle \otimes |1\rangle + |\psi_{dead}\rangle \otimes |2\rangle) \tag{3}$$

donde $|1\rangle$ ($|2\rangle$) denota el estado de la partícula cuando no ha decaído (cuando ya ha decaído) y $|\psi_{alive}\rangle$ ($|\psi_{dead}\rangle$) el estado del gato, vivo (muerto). En esta situación entonces, un sistema microscópico está entrelazado a un sistema macroscópico. La partícula gobierna la evolución del estado de acuerdo a la evolución de Schrödinger . Si una medida es realizada en el sistema microscópico (usando el contador de Geiger para ver si la partícula decayó o no), una proyección tiene a lugar en ambos sistemas, micro y macroscópico, debido al entrelazamiento. Con este simple experimento pensado, Schrödinger ejemplificaba las "ridículas consecuencias" de los contra-intuitivos conceptos cuánticos cuando se extrapolan al mundo macroscópico.

Por supuesto, estas "ridículas consecuencias" nunca son observadas en sistemas a gran escala, como los gatos. Los sistemas cuánticos grandes siempre interactúan fuertemente con el ambiente. El acoplamiento con este complejo baño resulta en una rápida perdida de información desde el sistema bajo estudio a éste, lo que conlleva a una rápida destrucción de estados de superposiciones mesoscópicas que son transformados en meras mezclas estadísticas. Esto se conoce como el proceso de decoherencia, que confina la rareza de la mecánica cuántica a la escala microscópica.

Para que sea posible estudiar procesos cuánticos fundamentales y superposiciones cuanticas, la decoherencia de un estado debe ser evitada en su máxima medida. El acoplamiento es inevitable para cualquier sistema, por lo que decrecer su efecto al mínimo es, sin lugar a dudas, uno de los más grandes retos experimentales en física cuántica. Los experimentos de CQED en el régimen de la radiación de microondas [2] son bastante adecuados para la realización de manipulaciones cuánticas al nivel de un simple átomo y fotón, en donde los estados de superposiciones son lo suficientemente preservadas, en términos temporales, para ser observadas [3]. Estos experimentos en particular combinan una cavidad superconductora y átomos de Rydberg en estados circulares que cruzan a través de ella.

Los estados de Rydberg son estados atómicos con características notables, incluso sorprendentes, bastante exageradas comparadas con niveles atómicos normales. Estas propiedades incluyen grandes tamaños (alcanzando el rango de micrómetros), fortísimas interacciones dipolares, polarizabilidades Starks gigantescas que escalan con n^{*7}, siendo n^* el numero cuántico principal (efectivo), etc.

Especiales son los estados de Rydberg *circulares* que presentan además largos tiempos de vida media, alcanzado las decenas de milisegundos. Estos átomos en conjunto con

cavidades superconductoras (donde los fotones pueden alcanzar a su vez tiempos de vida muy largos, debido a los espejos altamente reflectantes) son herramientas notables para la exploración de fenómenos cuánticos básicos ,y a su vez, para experimentos de procesos de información cuántica [2].

El principio de estos experimentos es bastante sencillo. Consisten en un simple átomo que interactúa con un único modo de campo almacenado en la cavidad. Este es el sistema mas sencillo de interacción radiación-materia, descrito teóricamente por primera vez por Jaynes & Cummings en 1963 [4]. Su realización experimental por el contrario, representa un reto experimental bastante grande, debido a que el sistema debe estar bien aislado de cualquier fuente de perturbación, incluida la radiación de cuerpo negro.

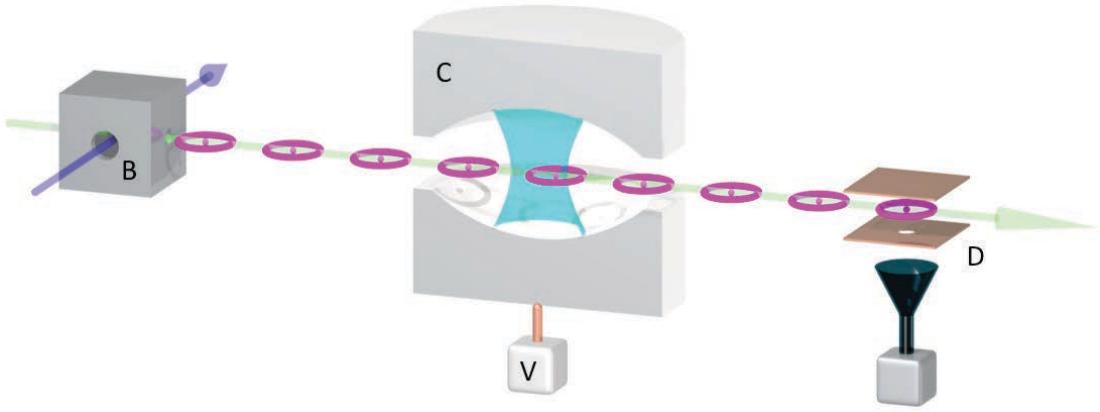

Figure 5: Típico setup experimental de experimentos de CQED. B representa la caja en donde los estados circulares son preparados. El haz atómico es emitido desde un horno (no aparece en la figura). C es la cavidad de microondas ultra-fina hecha de dos espejos superconductores entre los cuales los fotones del modo bajo estudio son atrapados. El estado de los átomos es medido finalmente por ionización en el detector D.

Una version simplificada del setup experimental se muestra en la figura 5. Una débil excitación laser crea átomos de Rydberg de un haz atómico a velocidades térmicas. Todos los parámetros del ensamble atómico están bajo control (velocidad, tiempo de preparación, etc.), menos el numero de átomos por muestra que obedece a una estadística de Poisson. El numero de promedio de átomos por muestra es ajustado a un valor bajo con el objetivo de tener a lo más un átomo interactuando con la cavidad por intervalo de tiempo.

Esta excitación de laser inicial tiene a lugar en la caja B (figura 5), en donde los átomos son también transferidos a los niveles de Rydberg circulares. A lo largo de su camino, mientras atraviesan el setup completo, interactúan con la cavidad superconductora C que puede contener, por ejemplo, un estado coherente. La amplitud de este estado puede ser variada fácilmente desde el limite clásico (muchos fotones) al limite cuántico (algunos fotones en promedio). El estado atómico es finalmente detectado en el detector D.

Este experimento es particularmente ideal para la generación y observación de superposiciones de estados mesoscópicos (MFSS). Los MFSS pueden producirse a través de la

interacción dispersiva de un átomo con un campo coherente pequeño dentro de una cavidad, una situación bastante evocadora para los gatos de Schrödinger [3].

Además los MFSS pueden ser generados a través de interacciones resonantes átomo-campo coherente. Este procedimiento para obtener MFSS fue propuesta en los noventa en forma teórica por Gea-Banacloche [5, 6], e independientemente por Buzek & Knight [7]. Su generación experimental fue implementada por primera vez en nuestro grupo [8, 9] en el contexto de los experimentos de CQED.

En la parte teórica de este manuscrito, exploramos la interacción de $N = 2$ átomos de dos niveles de energía con un campo coherente en la cavidad, en el contexto de los experimentos de CQED. Mostramos que esta interacción genera eficientemente largas MFSS una vez que el sistema atómico ha sido detectado en el estado apropiado. Este proceso condicional puede conllevar a una generación práctica de "gatos" involucrando cientos de fotones, mucho más largos que los alcanzados a través de la interacción de un solo átomo. También discutimos la extensión de este esquema de generación a la interacción de más átomos haciendo uno de la "aproximación de factorización" [10, 11].

El capítulo V esta dedicado a la presentación de los ingredientes teóricos básicos para la descripción de la interacción radiación-materia. Primeramente describimos el campo, dando una visión general de la cuantificación del campo electromagnético y de la representación de éste en el espacio de fase. Luego describimos el átomo. Recordamos en particular la representación de un estado atómico en la esfera de Bloch y los procesos de manipulación de sus estados internos. Este capitulo además incluye la descripción de la interacción resonante y dispersiva del átomo-campo. Se finaliza describiendo el proceso de decoherencia para el campo.

En el capítulo VI, presentamos los resultados teóricos de esta tesis. Empezamos con un pequeño recordatorio del modelo de Dicke e introducimos a su vez la aproximación de factorización. Presentamos luego una aproximación analítica simple para dos átomos de dos niveles interactuando con el campo coherente de la cavidad. Mostramos que interesantes estados no-clásicos son generados en la cavidad una vez que el sistema atómico es detectado en el estado apropiado. Terminamos esta parte con una conclusión y con perspectivas para trabajos futuros.

Para poder realizar este tipo de experimentos, una fuente de átomos de Rydberg que proporcione un número controlado de átomos a demanda sería ideal. Que el numero de átomos en los experimentos de CQED obedezca una distribución de Poisson como hemos discutido anteriormente es sin lugar a dudas un problema a considerar. El número promedio de átomos por muestra es mantenido bajo, lo que hace que el tiempo de adquisición de datos crezca exponencialmente en función del número de átomos que se requieran. Esta es una severa limitación para experimentos de información cuántica, en donde el numero de qubits debe ser preparado en forma determinada.

El objetivo de la parte experimental de mi tesis es entonces el desarrollo de **una fuente determinista de átomos de Rydberg para experimentos de procesos de información cuántica** en un chip superconductor haciendo uso del llamado efecto de *bloqueo dipolar* [12].

Los átomos neutros interactúan siempre entre ellos vía interacciones del tipo van del Waals dipolo-dipolo. Esta interacción es la mayor parte del tiempo despreciable para átomos en su estado basal a bajas densidades, debido a sus pequeños momentos dipolares. Por el contrario, la interacción puede ser extremadamente fuerte entre átomos de Rydberg. Estos presentan grandes dipolos, que crecen con n^2 (siendo n del orden de 60 para nuestros experimentos). El efecto de bloqueo dipolar deriva justamente de estas interacciones.

Para explicar el principio del bloqueo dipolar, consideremos dos átomos en su estado fundamental a una distancia r el uno del otro (panel (a) de la figura 6). Cuando r es grande, la interacción dipolo-dipolo entre el par de átomos es despreciable y ambos pueden ser independientemente excitados al nivel de Rydberg $|e\rangle$ a la misma frecuencia del laser. Cuando se empiezan a acercar, la interacción dipolar desplaza fuertemente los niveles de Rydberg del par de átomos. Apenas este corrimiento en energía es mayor que el ancho de línea del láser de excitación y más grande que la anchura de línea de nivel, la probabilidad para excitar dos átomos de Rydberg al mismo tiempo con el láser sintonizado a la frecuencia de excitación de un solo átomo se reduce considerablemente. El mecanismo de bloqueo dipolar sólo permite entonces la excitación de un átomo en el par.

Este principio puede extenderse a un conjunto de átomos en su estado fundamental. Una vez que uno de ellos es excitado, la interacción dipolo-dipolo cambia todas las demás transiciones de Rydberg en las inmediaciones de resonancia del láser. La distancia a la cual la interacción dipolar compensa las anchuras de línea del laser y atómicas define el radio de bloqueo, al interior del cual no más átomos pueden ser excitados. Este radio de bloqueo r_b es usualmente de unos pocos micrómetros para el nivel $60S$ para un ancho de línea de transición de 600 kHz. Esta situación está representada pictóricamente en el panel (b) de la figura 6. Con el objetivo de preparar de forma determinista un único átomo fuera de la nube atómica, la máxima distancia entre todos los átomos adentro del volumen de excitación debe ser mas pequeña que el radio de bloqueo.

Hemos desarrollado un experimento para investigar las interacciones del tipo Rydberg-Rydberg en una muestra densa y pequeña de átomos en su nivel fundamental, que contiene alrededor de unos cientos de átomos en unos cuantos micrómetros de rango. Este tipo de densidades se pueden obtener por ejemplo en trampas magnéticas producidas en chips atómicos, cerca de la condensación de Bose-Einstein [13]. Ciertamente unos pocos cientos de átomos pueden ser atrapados en una trampa del tipo Ioffe-Pritchard, cuyas dimensiones transversales son mas pequeñas que 1 μm y de largo unos cuantos μm. Como los átomos de Rydberg son bastante sensibles a la radiación térmica, el experimento es realizado en condiciones criogénicas, para las cuales un chip superconductor es lo ideal.

Las dimensiones de la trampa son compatibles con el volumen de bloqueo esperado para el nivel objetivo (60S), del orden de los $(\mu m)^3$. Esto es válido siempre y cuando la transición no esté ensanchada por inestabilidades del sistema laser o por inhomogeneidades de origen eléctrico. Este ultimo punto constituye un gran obstáculo para este tipo de experimentos, puesto que los átomos de Rydberg son justamente muy sensibles a campos eléctricos.

Las grandes polarizabilidades que estos átomos tienen presentan términos positivos y negativos. Por el lado positivo, una gran polarizabilidad nos permite sintonizar la transición atómica a través de campos eléctricos moderados. Esta característica es regularmente usada

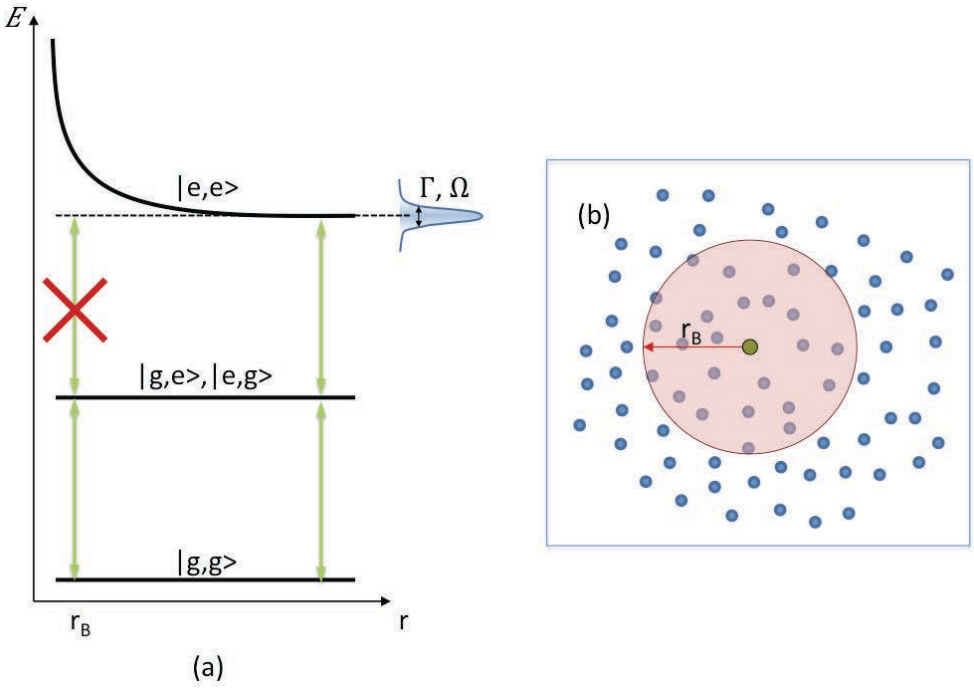

Figure 6: **(a)** Representación pictórica de la interacción dipolo-dipolo para dos átomos. Cuando estos están lejos, son excitados como si ninguna interacción tuviera a lugar. Cuando se acercan, la energía del estado par $|e, e\rangle$ es desplazada. Si este corrimiento de energía es mas grande que el ancho efectivo de la transición (definido por Ω el ancho del nivel y Γ el ancho del laser) entonces la excitación del segundo átomo queda fuera de resonancia. **(b)** El principio puede ser extrapolado a una muestra de N átomos donde, una vez que uno es excitado, ningún otro puede estarlo dentro de una esfera definida por el radio de bloqueo r_b.

en experimentos de CQED. La alta sensibilidad a los campos eléctricos además permite métodos de detección por ionización (capitulo I).

Por otro lado, con respecto a lo negativo, los átomos de Rydberg son extraordinariamente sensitivos a campos eléctricos parásitos, los cuales debemos mantener bajo control con el máximo de cuidado. Los campos eléctricos fuera de control son particularmente dañinos en el contexto de chips atómicos dado que la muestra atómica reside muy cerca de la helada superficie metálica. Cualquier impureza aislada en la superficie puede acumular una gran carga eléctrica. Pero incluso si las impurezas son evitadas cuidadosamente, los efectos por "zonas de contacto" (*patch effects*) entre los diferentes metales o incluso el mismo metal con diferentes orientaciones cristalinas pueden crear campos considerables a sólo unas pocas decenas de micrómetros de la superficie.

En particular, el potencial de contacto creado por los átomos de rubidio que inevitablemente se depositan en la superficie del chip durante las secuencias experimentales ha resultado ser un problema[14, 15]. Este depósito incontrolado lleva a la creación de intensos gradientes de campo cerca del chip, poniendo en peligro cualquier posibilidad de llevar a

cabo una manipulación coherente de átomos de Rydberg, ni mencionar el efecto del bloqueo dipolar. La mayoría del trabajo presentado en este manuscrito estuvo de hecho consagrado a la eliminación de estos campos eléctricos parásitos, puesto que es la primera limitación a superar para eventualmente observar el régimen de bloqueo en este contexto.

Para medir el campo eléctrico cerca de la superficie del chip y para probar luego la coherencia de los átomos a través de secuencias de Ramsey y de spin-eco, es posible usar transiciones de microondas entre los estados de Rydberg vecinos. Secuencias similares han sido realizadas en la referencia [16], en donde la manipulación coherente de los niveles $49S$ y $48S$ fueron llevadas a cabo cerca de la superficie de un chip atomico obteniendo tiempos de decoherencia del rango de los microsegundos.

El capítulo I describe los elementos teóricos básicos necesarios para la compresión del trabajo experimental de esta tesis. Brevemente recordamos las principales propiedades de los átomos de Rydberg, incluidos algunos aspectos de los estados circulares; discutimos particularmente la respuesta de estos átomos frente a campos eléctricos y magnéticos. Luego vamos al mecanismo de bloqueo en si mismo. Describimos su principio, las interacciones dipolo-dipolo involucradas, y discutimos la situación para el estado objetivo, 60S. El capítulo termina con simulaciones realizadas para parámetros experimentales razonables.

En el capítulo II, presentamos el setup experimental, incluyendo todas las etapas necesarias para el atrapamiento y enfriamiento del ensamble átomico. El corazón de nuestro experimento es el chip superconductor, que esta ubicado dentro del ambiente criogénico. Usamos el chip para crear la trampa magnética, que es la etapa final del confinamiento de los átomos y el punto inicial para los experimentos con átomos de Rydberg.

El capítulo III esta dedicado a los primeros estudios del campo eléctrico alrededor de la zona de excitación. Primero describimos el sistema de estabilización de los láseres. Presentamos luego el setup para la detección de los iones producto de los átomos de Rydberg producidos, sistema que esta instalado dentro del ambiente criogénico. Finalmente presentamos los primeros espectros y mediciones de las inestabilidades del campo eléctrico, justo frente de la superficie del chip superconductor. Terminamos el capítulo con la solución encontrada para deshacernos de estos campos parásitos.

Finalmente el capítulo IV presenta los principales resultados experimentales de esta tesis. La eliminación de los campos eléctricos parásitos nos permiten realizar espectroscopia de microonda de los átomos de Rydberg generados. Primero, usamos estas transiciones para medir el campo eléctrico a diferentes distancias del chip con el objetivo de caracterizar la zona de excitación. Después de eso, para dos distancias diferentes, 150 μm y 450 μm, realizamos secuencias de Ramsey y de spin-eco, revelando tiempos de coherencia para nuestros átomos de Rydberg en el rango de los milisegundos. Terminamos la parte experimental del manuscrito con algunas paginas dedicadas a las conclusiones y a las perspectivas.

Part I

Experiment: Towards deterministic preparation of single Rydberg atoms

Chapter I

Rydberg atoms and dipole blockade: theory and simulations

This work deals with Rydberg atoms. We will thus briefly recall their principal characteristics. We will in particular focus on two topics, which play a central role in this work, their interaction with electromagnetic fields and their mutual dipole-dipole interaction, leading to the dipole blockade mechanism [12, 17].

A Rydberg level [18] is an excited atom with one electron promoted to a very high principal quantum number n. These levels have many peculiar and useful properties. They are ideally suited, for instance, to research fields as CQED and quantum information processing [3, 19, 2, 12]. They offer indeed a unique blend of interesting properties.

The size of these atoms may be impressive, with for example a radius of the order of one micrometer for $n = 110$. These are obviously orders of magnitude larger than the orbital radius a_0 (Bohr radius) of the Hydrogen ground state. Hence, Rydberg atoms have large electric dipole moments for transitions between neighboring Rydberg states. They are thus excellent candidates for tests of the light-matter interaction, with a coupling with electromagnetic field much larger than for atoms with low n values. Their large electric dipole moments also give rise to a dipole-dipole coupling between Rydberg atoms at the μm scale, which is orders of magnitude larger than the standard van der Waals interaction between ground state atoms. Finally, they have long lifetimes, simple level structures (particularly for the circular states), high polarizability, etc.

In CQED experiment, the circular Rydberg levels are used due to their long lifetime and simple level structure [2, 20]. These levels have a high principal quantum number, but also maximum orbital l and magnetic m quantum numbers, $l = |m| = n - 1$. In classical terms, the electron orbits around the nucleus is a circle and its wavefunction is a thin torus located around the circular orbit of the Bohr model. The lifetime of these levels may reach tens of ms for $n \simeq 50$. We will use these remarkable properties in the theoretical part of this thesis, see V.

The experimental work reported here is realized with low angular momentum Rydberg levels of Rubidium. This alkali has been chosen for its convenient laser transitions. Laser diodes are available with appropriate wavelengths for the whole cooling and trapping pro-

cesses. A simple laser excitation scheme, also based on laser diodes, leads from the ground state $5S$ to our target state $|60S\rangle$, which has a radius of $\langle r\rangle = 4850a_0 = 256.5$ nm. We use the ^{87}Rb isotope, which easily leads to Bose-Einstein condensate since no attractive interactions occur, contrary to the ^{85}Rb case.

This chapter is divided in three sections. In section I.1, we briefly recall all the main features of Rydberg atoms useful for our purpose. This includes the calculation of the relevant levels lifetimes and the behavior of the atoms under static electric or magnetic fields. In section I.2, we focus on the description of the dipole-dipole interaction between Rydberg atoms. We describe the dipole blockade on an atomic ensemble. This section presents numerical calculations of the energy shifts of a reduced system made up of two atoms as a function of the distance between them. We also simulate the blockade effect efficiency (section I.3), considering first the analytic case of a pair of atoms and then the full system with a pure Thomas-Fermi BEC or with an impure BEC surrounded by a thermal cloud. These simulations are performed with realistic experimental parameters.

I.1 Rydberg atoms

To get a good understanding of all the relevant properties of Rydberg atoms, it is very useful to bear in mind the scaling of the different atomic quantities with the principal quantum number n. The most relevant parameters for this work will be discussed in details in this section.

For the simplest Hydrogen atom, the binding energy of the n level is

$$E(n) = -\frac{R_y}{n^2} \tag{I.1}$$

where $R_y = 13.60569251(69)$ eV [21] is the Rydberg constant than can be derived in term of fundamental quantities as follows

$$R_y = \frac{Z^2 e^4 m_e}{32\pi^2 \epsilon_0^2 \hbar^2} \tag{I.2}$$

with $Z = 1$ for H (note that we neglect here the effect of the reduced electron mass). The charge quantum is $+e = 1.602176565(35) \times 10^{-19}$ C [21].

For alkali atoms, the charged core has the structure of a rare gas, much more complex than the single proton of the Hydrogen atom. However, to first order, when the outer electron in far from the nucleus, it is a good approximation to consider that it evolves in a Coulombic hydrogen-like potential, since the internal electrons shield the valence electron from the large charge of the nucleus.

A more realistic description must include corrections to the hydrogen model due to two main effects. First, for states with a very low angular momentum, $l < 3$, the valence electron is, in classical terms, on a very eccentric elliptical orbit. It thus has a non-zero probability to be very near the nucleus and to experience a potential well much deeper than in the Hydrogen case. This effect is the dominant perturbation for low l states, but it

rapidly decreases with increasing l values, as the probability for coming close to the center of force. For non-penetrating orbits (and particularly for the circular states), the dominant perturbation is due to the finite static polarizability of the ionic core, which gets polarized by the outer electron, resulting in an additional term in the interaction.

These complex effects can be represented in a simple way for large enough n values. The binding energy is simply replaced by:

$$E(n,j,l) = -\frac{R_y}{(n-\delta_{n,l,j})^2} = -\frac{R_y}{n*^2} \tag{I.3}$$

where $\delta_{n,l,j}$ is the *quantum defect* [18], a correction to the principal quantum number depending weakly on the level and decreasing rapidly with l. n^* is called the effective principal quantum number. Table I.1 summarizes how some of the Rydberg atoms properties scale as a function on n^*.

Property	*n-dependecy*
Binding energy W	n^{*-2}
Orbital radius	n^{*2}
Energy difference of adjacent levels	n^{*-3}
Polarizability	n^{*7}
Van der Waals coefficient C_6	n^{*11}
Radiative Lifetime (low l)	n^{*3}

Table I.1: Table summarizing the scaling properties of Rydberg atoms with n^*, the effective principal quantum number [18].

The pertinent quantum numbers are n, l, j, and m_j, with $s = 1/2$ being the spin of the electron, and $j = l + s$ the total angular momentum. m_j is associated with the projection of the total angular momentum on the quantization axis. The fine structure is negligible, as the quantum defect, for high $l > 3$ states. In particular, the circular levels are purely hydrogen.

This description of Rydberg atoms does not include the coupling with the spin of the nucleus (hyperfine structure), since the distance between the nucleus and the electron is most of the time very large, making their mutual interaction negligible.

The quantum defect can be expanded as:

$$\delta_{n,l,j} = \delta_{lj,0} + \frac{\delta_{lj,2}}{(1-\delta_{lj,0})^2} + \frac{\delta_{lj,4}}{(1-\delta_{lj,0})^4} + \ldots, \tag{I.4}$$

where the various parameters can be obtained from microwave spectroscopy on transitions between nearby Rydberg levels [22, 23, 24]. It can be shown [25] that this series converges quite fast for $n > 40$, giving the position of the levels with a kHz-range accuracy for a

large set of n values. This rapid convergence makes it possible for us to omit in equation I.4 terms beyond the second order. The quantum defects we use in this work for all simulations and numerical calculation are given in table I.2[26, 27]. The frequencies for the atomic transitions between neighboring Rydberg levels are obtained with a precision better than ≈ 50 kHz in the useful range.

State	$\delta_{lj,0}$	$\delta_{lj,2}$
$nS_{1/2}$	3.1311804(10)	0.1784(6)
$nP_{1/2}$	2.6548849(10)	0.2900(6)
$nP_{3/2}$	2.6416737(10)	0.2950(7)
$nD_{3/2}$	1.34809171(40)	−0.60286(26)
$nD_{5/2}$	1.34646572(30)	−0.59600(18)
$nF_{5/2}$	0.0165192(9)	−0.085(9)
$nF_{7/2}$	0.0165437(7)	−0.086(7)

Table I.2: Quantum defects measured in [26] and [27] for Rudbidium Rydberg states with $n \geq 20$.

Let us now turn to the wavefunction of the valence electron, which will be essential to describe the coupling of the levels to external fields. It is obviously (neglecting the fine structure) a solution of the standard Schrödinger equation, which reads in atomic units

$$\left[-\frac{1}{2\mu}\nabla^2 + V(r)\right]\psi(r,\theta,\phi) = E\psi(r,\theta,\phi) \tag{I.5}$$

where μ is the reduced electron mass, r the radial coordinate, θ and ϕ the angular coordinates, and $V(r)$ the real potential experienced by the electron, taking into account the penetration of the core.

The angular and radial variables can be separated as

$$\psi(r,\theta,\phi) = R_{nl}(r)Y_l^{m_l}(\theta,\phi) \tag{I.6}$$

since the effective potential seen by the outer electron is spherically symmetric.

The angular part of the wavefuntion solution is given by

$$Y_l^{m_l}(\theta,\phi) = \sqrt{\frac{(2l+1)(l-m_l)!}{4\pi(l+m_l)}}P_l^m(cos\theta)e^{im_l\phi} \tag{I.7}$$

where P_m^l are the unnormalized associated Lengendre functions. The $Y_l^{m_l}(\theta,\phi)$s are the normalized spherical harmonics.

For a heavy alkali as Rubidium, the potential V is not well known and the solution $R_{nl}(r)$ of the radial equation is certainly not analytic. We will thus have to use a numerical solution of the radial equation.

The task is simplified since we are mostly interested here in the interaction of Rydberg atoms with fields or in the dipole-dipole interaction. They are all described in terms of dipole-like matrix elements. The electric dipole moment is given in the classical picture by $\mathbf{d} = -e\mathbf{r}$, where $\mathbf{r}$ it the position of the electron relative to the positive core. It characterizes the action of external electric fields on the atom. In the quantum mechanical description, the dipole moment is replaced by the matrix element of the dipole operator between two Rydberg levels. It is given by

$$\mathbf{d}_{nljm_j,n'l'j'm'_j} = \langle nljm_j| - e\mathbf{r}|n'l'j'm'_j\rangle \tag{I.8}$$

where $\mathbf{r}$ is the valence electron position operator. This matrix element describes for instance the Rabi oscillation between two Rydberg levels due to an external resonant electromagnetic field radiation. The strength of the coupling is then characterized by the Rabi frequency defined by $\Omega_{nljm_j,n'l'j'm'_j} = \mathcal{F}d_{nljm_j,n'l'j'm'_j}/\hbar$ with $\mathcal{F}$ being the electric field amplitude. The electric dipole matrix elements are also central in the calculation of transition probabilities, of the polarizability as well as of the levels radiative lifetimes.

The electric dipole moment (I.8) can be separated in a radial and an angular part,

$$\mathbf{d}_{nljm_j,n'l'j'm'_j} = -e\mathcal{R}_{i,f}\mathbf{A}_{i,f} \ , \tag{I.9}$$

where

$$\langle nl|r|n'l'\rangle = \int R_{nl}(r)rR_{n'l'}(r)r^2dr = \mathcal{R}_{i,f}, \tag{I.10}$$

and

$$\mathbf{A}_{i,f} = \langle ljm_j| \left(\sin\theta\cos\varphi, \sin\theta\sin\varphi, \cos\theta\right) |l'j'm'_j\rangle \ . \tag{I.11}$$

In these expressions, the index i, f is an abbreviation to denote the initial and final states.

The angular part reflects the selection rules of a dipole transition. The radial integral is clearly dominated by the part of the radial wavefunctions which are farthest from the core. For high-lying levels, we do not need to know precisely the wavefunctions in the central region, where the actual potential $V(r)$ most differs from the Coulombic one. This feature is represented in figure I.1.

This naturally leads to using the Numerov method for calculating the radial part of the dipole matrix element (see [18] pages $10 - 24$). The calculation relies on the fact that, outside the core of the atom, the potential remains Coulombic. The wavefunction is numerically obtained by an inward integration of the Schrödinger equation, starting with appropriate asymptotic values, and using as the energy the actual energy of the levels of interest, given by the quantum defect formula.

In the special case of circular Rydberg states [2], the electric dipole moment for $n \gg 1$ takes the following form

$$d_n \simeq n^2\frac{qa_0}{\sqrt{2}} \ . \tag{I.12}$$

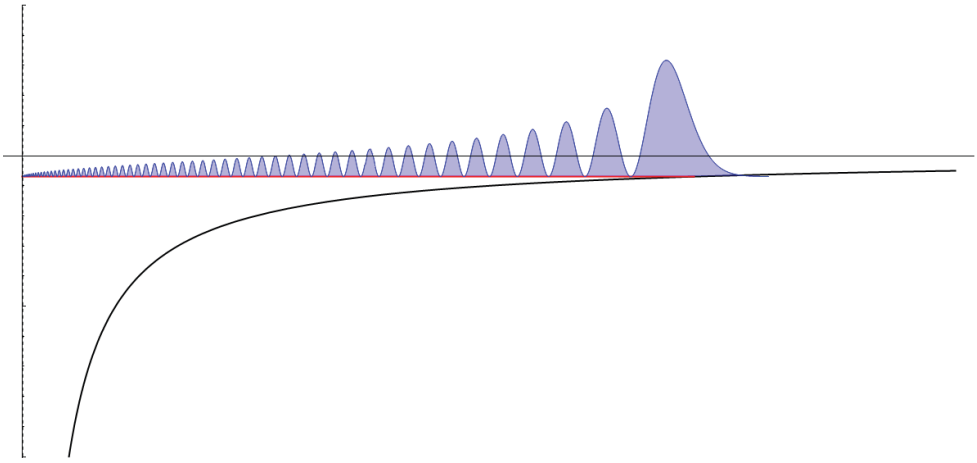

Figure I.1: The probability density $|rR(r)|^2$ is plotted as a function of r for the $60S$ hydrogen level, along with the Coulombic potential. The size of the effective core of a Rubidium atom is shown on scale by a vertical dashed black line, very close to the origin. We can observe that the dipole is determined by the wavefunction in regions far from the core. The red horizontal line shows the extension of the classical orbit, limited by a turning point at $R_y/n^2 = V(r)$.

I.1.1 Lifetime

Rydberg atoms have extremely long lifetimes when compared to their homologous ground states atoms [18, 2]. There is a clear classical picture of this important feature. The outer electron on the weakly bound state has a much lower average acceleration than in the ground state. Hence, the power radiated (through Larmor's formula) is much lower and it takes a much longer time to radiate the excitation energy. This effect is at its maximum for the circular orbits, where the acceleration is constant and at the minimum value compatible with a bound state.

Nevertheless, Rydberg states are highly sensitive to blackbody radiation in the millimeter-wave range, corresponding to transitions between adjacent levels. In our experiment, we work at cryogenic temperatures. However, room temperature blackbody field can enter the experimental zone through the many optical access of the cryostat. We must thus examine the lifetime of the levels of interest as a function of the radiation temperature.

We include in this lifetime calculation the radiative decay to the lower states and also the transitions to the higher lying ones, induced by black body radiation. The spontaneous emission rate may be expressed by the Einstein coefficient A given by :

$$A_{if} = \frac{2e^2\omega_{if}^3}{3\epsilon_0 c^3 h}|d_{if}| \tag{I.13}$$

where i and f denote the initial and final states for the transition with an energy $\hbar\omega_{if}$ (f having a lower energy than i), and d_{if} is the dipole matrix element between them. This emission rate is obtained, through a Fermi Golden Rule argument as the product of

two terms. The first corresponds to the density mode of the electromagnetic waves near resonance at frequency $\nu = \omega_{if}/2\pi$. The second is the square of the atom-field coupling element.

In presence of the background blackbody field, the spontaneous emission rate is enhanced by stimulated emission. The total transition rate from i to the lower level f is then $A_{if}[1 + \bar{n}(\omega)]$, where $\bar{n}(\omega)$ is the mean photon number per radiation mode in free space at thermodynamic equilibrium, given by :

$$\bar{n} = \frac{1}{e^{\hbar\omega/k_B T} - 1} \ , \tag{I.14}$$

where k_B is the Boltzmann constant and T the field temperature. In the thermal field, transitions are also possible towards levels f above level i. The corresponding rate cancels at zero temperature and simply writes $A_{fi}\bar{n}(\omega)$, where A_{fi} is the spontaneous emission rate from f to i.

The total lifetime for the state $|i\rangle$ taking into account all possible final states $|f\rangle$ is thus given by:

$$\frac{1}{\tau_i} = \sum_{f<i} A_{if}[1 + \bar{n}(\omega)] + \sum_{f>i} A_{fi}\bar{n}(\omega_{if}) \ , \tag{I.15}$$

where the two summations extend to the levels lower than or higher than the initial level i.

For the practical calculation of this lifetime, we must take into account the dipole transition selection rule for a single photon emission : $\Delta l = \pm 1$. Figure I.2 presents as a green histogram the spontaneous emission rates from the initial level $i = |60S\rangle$ to the states nP, for each n, summed over the two possible final j values, $j = 1/2, 3/2$. At zero temperature, the emission is thus dominated by optical transitions towards low-lying P states (and mostly towards the first 5P excited state). These optical transitions are obviously quite insensitive to the blackbody background, totally negligible in this frequency domain. The red and blue bars present the transitions rates at 300 K and 4 K respectively towards neighboring Rydberg states. The transitions are concentrated around the initial level, due to the fast decay of the dipole matrix elements when the principal quantum numbers get very different. They are of course extremely dependent upon the temperature: at 300 K the spontaneous emission rate from the $60S$ to the $59P_{3/2}$ is 1.29 ms^{-1} whereas it is less than 0.04 ms^{-1} at 4 K.

The results of the numerical calculations are summarized in table I.3. References can be found in [28, 29]

Let us finally mention briefly the case of the circular atoms. They can only decay by spontaneous or thermally induced millimeter-wave transition towards the neighboring circular state. Their lifetime is thus much longer at low temperature than that of the S levels ([2], page 257):

$$\Gamma_n = \frac{1}{\tau} = \frac{4}{3}\frac{R_\infty}{\hbar}\alpha^3 n^{-5} \tag{I.16}$$

This expression evaluates to 28.5 and 31.5 ms for circular states $n = 51$ and 50 [20]. This result will be of interest for the theoretical part of this work.

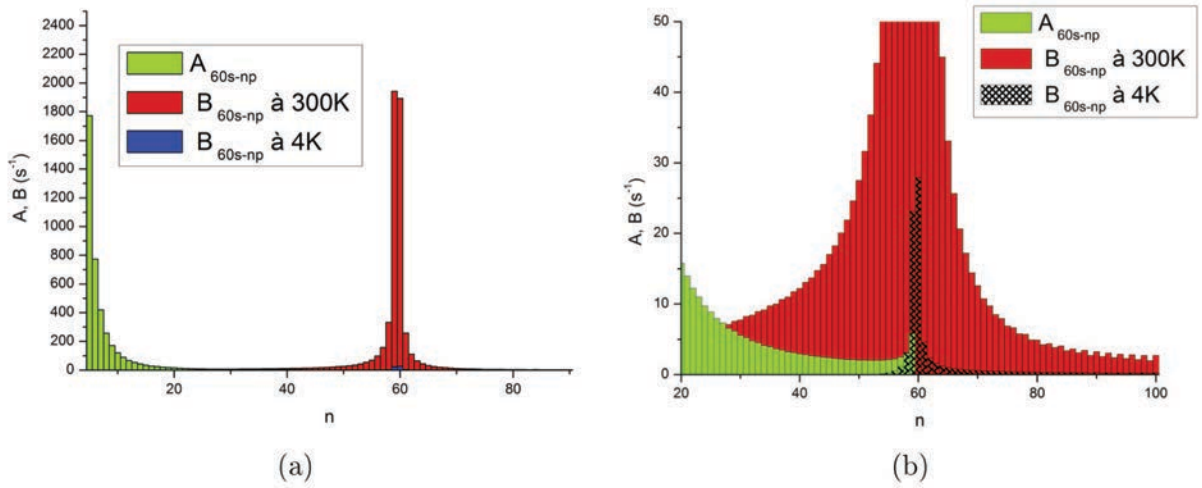

Figure I.2: **(a)** Transition rates between states $|60S\rangle$ and $|nP\rangle$ summed over the final j values, 1/2 and 3/2. Green bars: spontaneous emission rates. Red bars: blackbody induced transition rates at 300 K. Blue bars: blackbody induced transition rates at 4 K. **(b)** Zoom for a better view of the low temperature transition rates.

	$n = 59$	$n = 60$	$n = 61$
Lifetime $nP_{1/2}$ levels (μs)			
0 K	496.474	522.151	548.195
4 K	481.511	506.205	531.228
300 K	129.131	133.84	138.581
Lifetime $nP_{3/2}$ levels (μs)			
0 K	459.826	483.585	507.647
4 K	447.281	470.207	493.413
300 K	126.893	131.531	136.194
Lifetime $nS_{1/2}$ levels (μs)			
0 K	232.281	244.513	257.248
4 K	227.834	239.791	252.241
300 K	95.5404	99.4028	103.337

Table I.3: Lifetime of the Rydberg levels $nS_{1/2}$, $nP_{1/2}$ and $nP_{3/2}$ for n equal to 59, 60 and 61 at 0 K, 4, 2 K and 300 K.

I.1.2 Rydberg atoms in static electric fields: Stark effect

Rydberg atoms are notoriously sensitive to static electric fields. This has pros and cons.

On the positive side, this allows us to tune nearly at will the atomic transition by making use of moderate fields, in the V/cm range. In the same vein, the high sensitivity to electric field leads to the field-ionization method, which offers an excellent efficiency

combined with a nearly perfect state selectivity.

On the negative side, Rydberg atoms are very sensitive to stray electric fields, which must be controlled as carefully as possible in all experiments. It is not unfair to say that most of the experimental work presented in this PhD has been devoted to the control of the stray fields.

In order to quantify properly the stray fields encountered in this work, we need a detailed understanding of the position of the Rydberg levels in an electric and/or magnetic field.

When a Rydberg atom is placed in an external electric field $\mathbf{F}$, a Stark effect term must be added to the Hamiltonian

$$H = -\frac{1}{2}\nabla^2 + V(r) + H_F \tag{I.17}$$

where

$$H_F = -\mathbf{d}\cdot\mathbf{F}. \tag{I.18}$$

The Stark Hamiltonian H_F couples Rydberg levels linked by a dipolar transition (nonzero dipole matrix element). We will of course choose the quantization axis Oz along the field direction. In this condition the Stark Hamiltonian only couples levels with the same m_J value. The spherical symmetry of the Hydrogen atom is lost, but the system remains cylindrically symmetric around the quantization axis. In this symmetry, the angular momentum l is no longer a 'good' quantum number.

For a given n, the states with $l < 3$ are non-degenerate due to their finite quantum defect. The Stark effect thus acts as a second order perturbation, giving rise to a quadratic shift in the energy levels

$$\Delta E = -\frac{1}{2}\alpha\mathcal{F}^2 \tag{I.19}$$

where the polarizabililty α is :

$$\alpha = \sum_{n,l,j\neq n',l',j'} \frac{|\ \langle n,l,j,m_j \mid er \mid n',l',j',m'_j\rangle\ |^2}{E_{n,l,m} - E_{n',l',j'}}\ . \tag{I.20}$$

It scales as n^{*7}, since the numerator, square of the dipole matrix element scales as the square of the orbit extension, i.e. as n^{*4}, and the energy denominator as n^{*-3}.

For the simple Hydrogen atom, taking into account the choice of quantization axis, $d_z = -a_0 e\langle z\rangle$, the energy eigenstates can be obtained analytically [18]. The angular momentum quantum number l is then replaced by the *parabolic quantum number* n_1, which takes all integer values from 0 to $n - |m| - 1$, for a given n and m. The energy of the level $|n, m, n_1\rangle$ admits an expansion up to second order in the electric field, $E = E^{(0)} + E^{(1)} + E^{(2)}$,

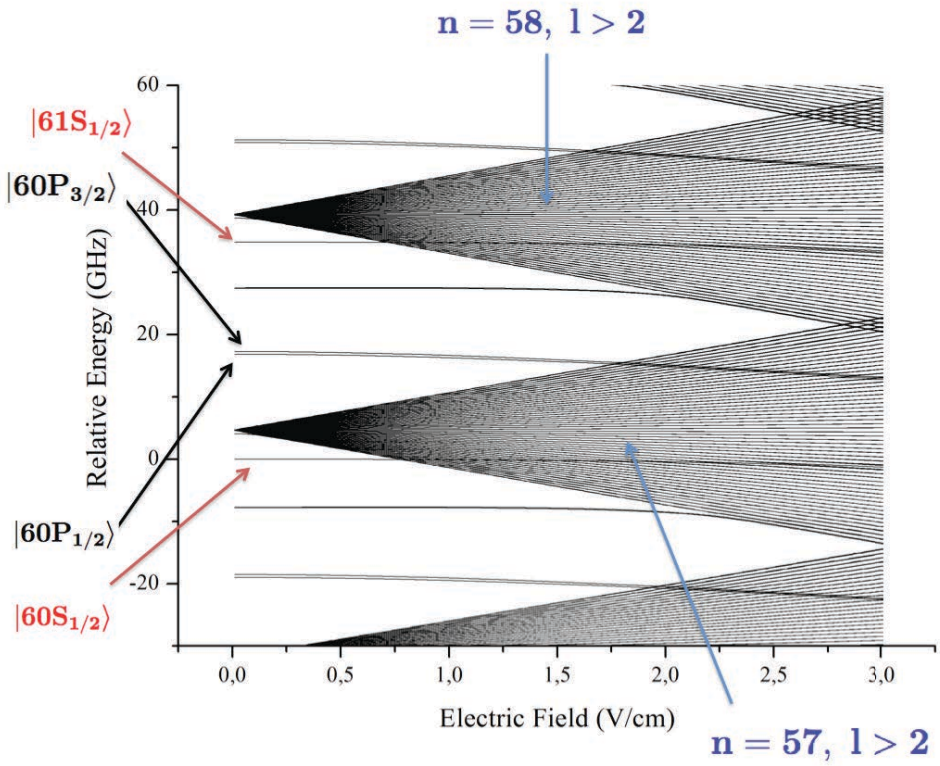

Figure I.3: Map of the Stark levels for a wide region around the target state $60S_{1/2}$. The degeneracy in the l quantum number is lifted, even for zero electric field, due to the quantum defects. The two multiplicities presenting linear Stark effect corresponds to the degenerate high-l levels with principal quantum numbers $n = 57$ and $n = 58$.

given by [30]:

$$E^{(0)} = -\frac{1}{2n^2} \tag{I.21}$$

$$E^{(1)} = \frac{2}{3}kn\mathcal{F} \tag{I.22}$$

$$E^{(2)} = -\frac{1}{16}(17n^2 - 3k^2 - 9m^2 + 19)n^4\mathcal{F}^2 \tag{I.23}$$

with $k = 2n_1 - n + |m| + 1$, where the energies and field amplitudes are expressed in atomic units. In the linear term, nonzero k values are related to states exhibiting a permanent dipole moment $d = -3nk/2$. For the circular Rydberg atoms in particular, $E^{(1)}$ vanishes. As a result, the sensitivity of these levels to electric field is minimized, which makes then convenient tools for cavity quantum electrodynamics experiments. We will use these features in chapter V.

For the alkalis and particularly for small m values (involving levels having an important quantum defect), the Stark spectrum must be computed numerically, based on the

Numerov estimates of the dipole matrix elements. This computation, albeit complex, can be performed with nearly arbitrary precision. Figure I.3, for instance, presents the computed Stark structure for the levels of interest in this work.

For such a numerical calculation, the size of the matrix to be diagonalized should be kept small enough. Due to the Stark coupling selection rules, only states with the same m_j have to be considered. In order to have a good accuracy, we include in the calculation of figure I.3 levels with principal quantum numbers between $n_{min} = 50$ and $n_{max} = 70$. For l we have included the levels with $l \leq 5$ and a maximum energy difference with respect to the 60S level of 200 GHz.

For the levels that will be of interest in the experimental part, the quadratic Stark shift coefficients are:

$$A_{60S_{1/2}} = -89,9 \text{ MHz(V/cm)}^{-2} \tag{I.24}$$

$$A_{61S_{1/2}} = -100,9 \text{ MHz(V/cm)}^{-2} \tag{I.25}$$

$$A_{60P_{3/2},m_j=-1/2} = -676 \text{ MHz(V/cm)}^{-2} \tag{I.26}$$

$$A_{60P_{3/2},m_j=+3/2} = -569 \text{ MHz(V/cm)}^{-2} \tag{I.27}$$

For the P state, the two m_J levels have different Stark shift coefficients, since they are not coupled to the same set of levels.

In most of the experiments reported here, the electric field adds as a little perturbation to the directing magnetic field $\mathbf{B} = B_x\hat{x}$ in the bottom of the trap. The next paragraph thus deals with the Rydberg levels Zeeman effect.

I.1.3 Rydberg atoms under static magnetic fields

The Zeeman effect plays a major role in these experiments, since the atoms are confined in a Ioffe-Pritchard trap, whose minimum magnetic field is different from zero, varying from 4 to 9 Gauss approximately. For such fields, we deal with an intermediate case for the Zeeman effect, in which neither the fine structure nor the Hamiltonian describing the magnetic field contribution dominate.

The Zeeman shift in the LS-coupling picture is given by

$$H_Z = \frac{\mu_B}{\hbar}(L_x + 2S_x)B_x = \frac{g_J\mu_B}{\hbar}m_J B_x \tag{I.28}$$

The factor g_j is the Landé g-factor, μ_B the Bohr magneton. As we have mentioned before, the hyperfine structure can be neglected. For this intermediate case, two basis are equally appropriate, either the $|J, m_J\rangle$ one or that of the uncoupled states $|L\rangle, |m_S\rangle$. Nevertheless, the second makes it more difficult to express the matrix elements of the Hamiltonian of the system without Zeeman or Stark effect. The Landé g_J factor for Rb^{87} can be obtained from the total quantum angular momentum, orbital angular momentum and spin momentum J, L and S, respectively, as:

$$g_J = 1 + \frac{J(J+1) + S(S+1) - L(L+1)}{2J(J+1)}. \tag{I.29}$$

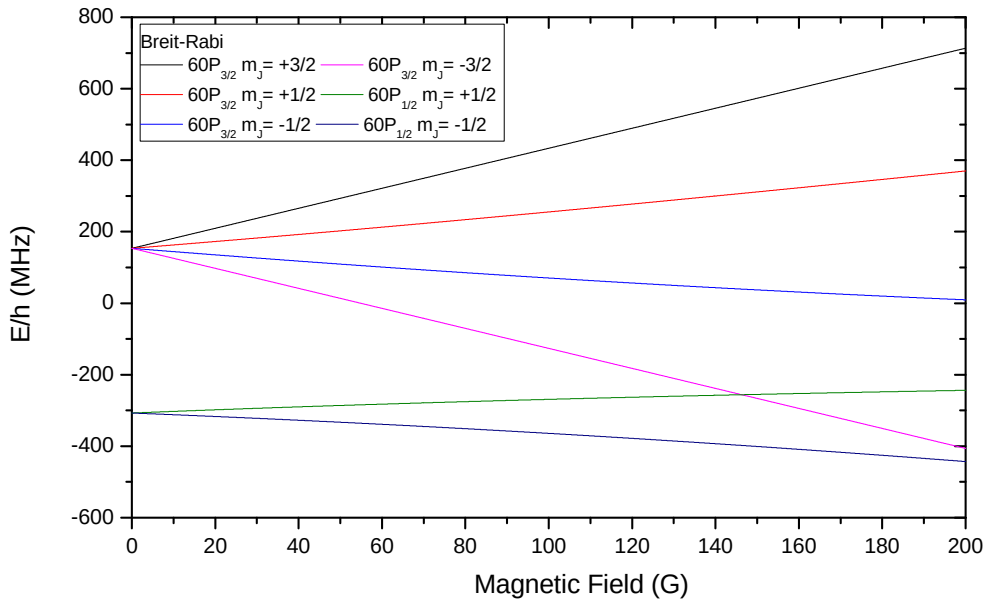

Figure I.4: Zeeman splitting for the states $|60P_{1/2}\rangle$, $m_J = \pm 1/2$ and $|60P_{3/2}\rangle$, $m_j = \pm 3/2, \pm 1/2$ from the Breit-Rabi formula. The quadratic contribution for the useful range of fields is $K^{(2)} = h \cdot 1.03$ kHz/G^2.

If we consider the Zeeman effect for the intermediate magnetic field range, we can make use of the Breit-Rabi formula originally given in the context of the hyperfine coupling [31, 32]. An alternative derivation can be performed when considering the fine structure ([32], page 20),

$$E(J, m_J) = -\frac{\Delta E_{so}}{2(2L+1)} + \mu_B B m_J \pm \frac{\Delta E_{so}}{2}\sqrt{\left(1 + \frac{4m_J x'^2}{2L+1} + x'^2\right)}^{1/2} \tag{I.30}$$

with ΔE_{so} the fine splitting energy and

$$x' = (g_S - 1)\frac{\mu_B}{\Delta E_{so}}$$

with g_S the electron spin g-factor. In figure I.4 we show the Zeeman effect map for the Rydberg levels of interest,$60P, m_J = \pm 1/2$ and $60P, m_J = \pm 3/2, \pm 1/2$. The quadratic contribution for the magnetic field, $K^{(2)}B$, has a value of $K^{(2)} = h \cdot 1.03$ kHz/G^2.

When adding the Stark effect, the Hamiltonian for the system becomes

$$H = -\frac{1}{2}\nabla^2 + V(r) + H_Z + H_F. \tag{I.31}$$

We take the magnetic field direction as the quantization axis and we proceed to perform a full numerical diagonalization of the Hamiltonian. An important parameter for the simulation is the angle between the electric and the magnetic field, which is unknown *a priori* (the electric field is mainly a stray spurious field in our experiments). Nevertheless, the problem can be reduced to the calculation of the quadratic Stark shift either for an electric field parallel $F_x = |\mathbf{F}_x|$ or perpendicular $F_z = |\mathbf{F}_z|$ to the quantization axis.

We consider the magnetic field to be in the x-direction $\mathbf{B} = \mathcal{B}\hat{x}$. We write then the electric field as $\mathbf{F} = \mathcal{F}_x\hat{x} + \mathcal{F}_z\hat{z}$. The Stark interaction Hamiltonian has then the following form:

$$H_F = -e(x\mathcal{F}_x + z\mathcal{F}_z) \tag{I.32}$$

For non-degenerate states, i.e. states with $l < 3$, it contributes to a second order shift. It can be expressed as a perturbation expansion involving a sum over all possible states f coupled to the state of interest i of terms proportional to:

$$|\langle\psi_i|H_F|\psi_f\rangle|^2 \tag{I.33}$$

where $|\psi_i\rangle = |n, l, j, m_j\rangle$. Expanding the expression of the Stark Hamiltonian, we get four terms

$$|\langle\psi_i|x\mathcal{F}_x|\psi_f\rangle|^2 + |\langle\psi_i|z\mathcal{F}_z|\psi_f\rangle|^2 \tag{I.34}$$
$$+ \langle\psi_i|x\mathcal{F}_x|\psi_f\rangle\langle\psi_f|z\mathcal{F}_z|\psi_i\rangle \tag{I.35}$$
$$+ \langle\psi_i|z\mathcal{F}_z|\psi_f\rangle\langle\psi_f|x\mathcal{F}_x|\psi_i\rangle \tag{I.36}$$

Both terms (I.35) and (I.36) vanish due to the selection rules for the spherical harmonics. The problem is thus reduced to summing independently the contributions of the parallel and perpendicular field components. The quadratic Stark shift is then described by two coefficients for the square of the electric field: $A^{(//)}$ associated to $\mathcal{F}_x^2$ and $A^{(\perp)}$ to $\mathcal{F}_z^2$.

In our experiment, we will be mostly interested in the quadratic Stark effect of the two microwave transitions $60S \rightarrow 60P_{3/2}, m_J = -1/2$ and $60S \rightarrow 60P_{3/2}, m_J = 3/2$. The numerical calculation for these levels, taking into account both the Zeeman and the Stark effects, provides the following Stark coefficients in the presence of a magnetic field

$$A^{(//)}_{-1/2} = -676\,\mathrm{MHz(V/cm)}^{-2} \tag{I.37}$$
$$A^{(\perp)}_{-1/2} = -597\,\mathrm{MHz(V/cm)}^{-2} \tag{I.38}$$
$$A^{(//)}_{+3/2} = -596\,\mathrm{MHz(V/cm)}^{-2} \tag{I.39}$$
$$A^{(\perp)}_{+3/2} = -647\,\mathrm{MHz(V/cm)}^{-2}. \tag{I.40}$$

I.2 Dipole Blockade

I.2.1 Principle of the blockade effect

One of the most important consequences of the strong interactions between Rydberg atoms is the possibility of a deterministic excitation of one single atom to a Rydberg level through

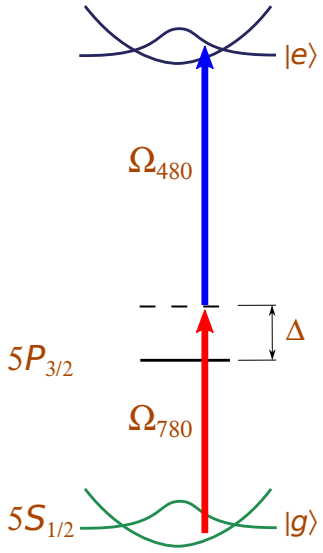

Figure I.5: Two-photon excitation towards the target Rydberg state $60S$. Δ is 540 MHz.

the dipole blockade effect [12, 17], which is a direct consequence of the energy level shifts due to the mutual dipole-dipole interaction of two Rydberg atoms. The unusually large electric dipole moment Rydberg atoms exhibit makes this interaction particularly strong, even at distances in the micrometer range.

In this section, we discuss briefly the theory of the blockade effect. Later, we will focus on the calculations of the dipole-dipole interaction energy.

Let us first discuss a two atoms configuration in a simple qualitative picture to grasp the fundamental principle of dipole blockade. The first atom to be excited is of course, for distances in the micrometer range, impervious to the presence of the second atom in its ground state. However, the excitation lines of the second atom are shifted by the dipole-dipole interaction with the first excited one. Hence, it will be out of resonance for the exciting laser. It is thus quite intuitive that, in a small enough sample, a single Rydberg atom can be excited.

For a deeper understanding of this mechanism, it is important to describe in more details the laser excitation of Rydberg levels. We use the most common excitation scheme, which is presented in figure I.5. We use a two-photon excitation from the $|5S_{1/2}, F = 2\rangle$ ground state of Rb^{87} to the Rydberg state $|e\rangle = |60S_{1/2}, m_J = 1/2\rangle$. The two lasers are a 'red' one at 780 nm and a 'blue' at 480 nm. The excitation involves the intermediate level $|5P_{3/2}, F = 3\rangle$, detuned by $\Delta = 540$ MHz with respect to the 780 nm laser to avoid spurious population of this short-lived intermediate level.

The effective Rabi frequency on the two-photon transition is thus

$$\Omega_{2p} = \frac{\Omega_{780}\Omega_{480}}{2\Delta} \tag{I.41}$$

where Ω_{780} and Ω_{480} are the Rabi frequencies on the detuned one-photon transitions.

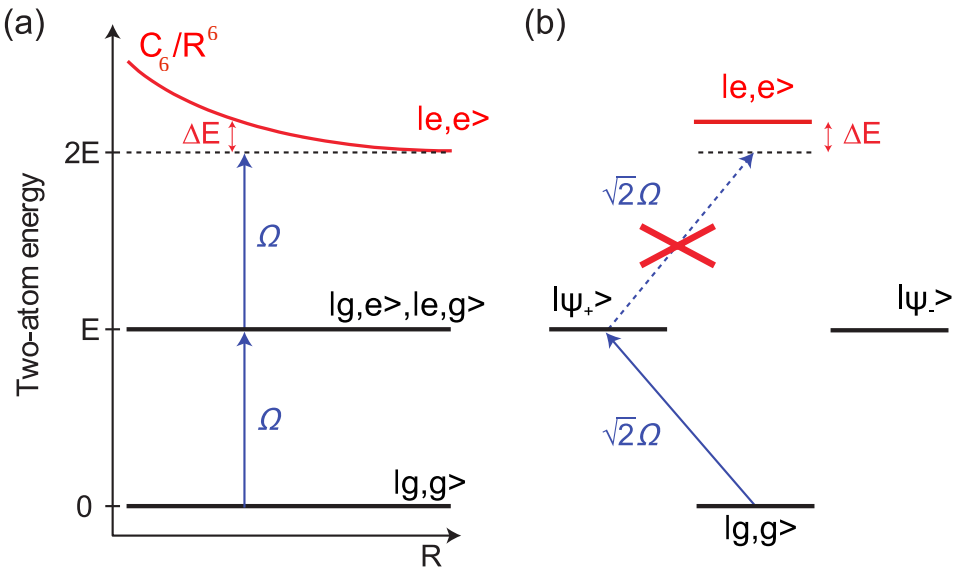

Figure I.6: Pictorial representation of the dipole blockade principle. **(a)** Energy shift as a function of the interatomic distance. **(b)** Case when the dipole-dipole energy shift is larger than the transition linewidth. $|e,e\rangle$ denotes the double excited state, and $|\psi_+\rangle$ and $|\psi_-\rangle$ the symmetric and anti-symmetric states with one excitation only.

Figure I.6 presents a pictorial representation of the dipole blockade mechanism in a simple qualitative analysis for a pair of atoms. The excitation laser (represented here as an effective two-level transition) couples the ground state g with the Rydberg state e. It is tuned at resonance with the atoms when they are isolated. The figure presents the energy of the involved levels as a function of the distance between the atoms. At an arbitrary distance, the doubly excited state $|e,e\rangle$ is shifted by the interaction. The dipole-dipole interaction scale as $1/R^6$ (van der Waals interaction) at long distances and as $1/R^3$ at short distances. For the 60S level, the transition between these regimes is at $\simeq 2.5$ μm. For this state and at distances of the order of a few micrometers, the shifts are in the MHz range.

When the shift is large, the laser is on resonance for the excitation of the states with a single excitation, but detuned from the resonance leading to a second excitation. In these conditions, the dipole blockade is efficient and a single atom can be prepared in the pair.

Of course, this simple picture holds only when the transition width is much smaller that the levels shift. The atomic line width Γ_a and the laser one must be small compared to these shifts. We can thus define a distance R_b, called *effective blockade radius*, which is of the order of a few μm, below which the energy shift induced by the dipole-dipole interactions $\Delta_{dd}(R_b)$ exceeds the laser and atomic line widths:

$$\Delta_{dd}(R_b) > \Gamma_L, \Gamma_a. \tag{I.42}$$

Qualitatively, below the blockade radius, only one atom in the pair can be excited.

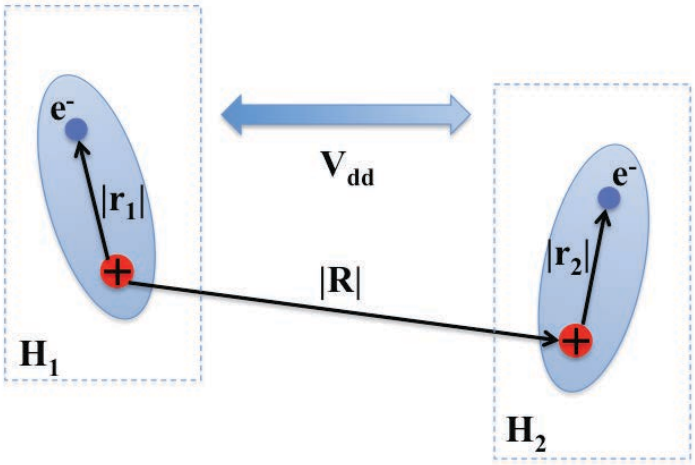

Figure I.7: Two atoms represented by two dipoles 1 and 2 separated by a distance $|\vec{R}|$, much larger than $\vec{r_i}$, with $i = 1, 2$.

If we consider now a cold atom cloud, once an atom has been promoted in r, it defines a sphere with a radius R_b into which no further excitation can take place. Hence, for a deterministic excitation of a single Rydberg atoms, we must maximize the blockade radius and prepare an initial cloud entirely contained in a single blockade sphere.

These conditions set rather demanding conditions on the laser technology and on the control of the stray fields which might act onto the atoms. The characterization and control of these stray fields and the optimization of the laser frequency locking have thus become logically the main objective of this work, on the road towards dipole blockade.

I.2.2 Theoretical description of the dipole-dipole interactions

For a first theoretical insight into the dipole-dipole interaction, we examine here the simple case of two atoms separated by a distance $R = |\vec{R}|$ (scheme show in figure I.7) excited to the Rydberg level $|e_1\rangle, |e_2\rangle = |e_1\rangle \otimes |e_2\rangle$. Precise numerical calculations will be done for the evolution of the pair state $|60S, 60S\rangle$.

We assume that the distance between the two atoms, R, is much larger than the distance between each core and its electron. Hence higher multipole terms can be neglected. The interaction Hamiltonian is then:

$$H = H_1 + H_2 + V_{dd}(r) \tag{I.43}$$

including the interaction term [33]

$$V_{dd}(R) = \frac{q^2}{4\pi\epsilon_0}\frac{1}{R^3}\left[\hat{r}_1 \cdot \hat{r}_2 - 3\left(\hat{r}_1 \cdot \frac{\vec{R}}{R}\right)\left(\hat{r}_2 \cdot \frac{\vec{R}}{R}\right)\right]. \tag{I.44}$$

where $\vec{r_i}$ is the position of each electron with respect of each core. The Hamiltonians H_1 and H_2 are the Coulomb interactions between the core and the electron for each atom and V_{dd} is the dipole-dipole potential.

We neglect here the translational degrees of freedom of the atoms, a good approximation in a cold atom context. The typical atomic velocity in the trap is a few cm/s, and the excitation laser pulse typically lasts at most a few microseconds. The distance between the atoms during this short time interval changes thus by much less than the size of the Rydberg state itself (256.5 nm for $n = 60$).

The interaction Hamiltonian, V_{dd}, can be rewritten as

$$V_{dd} = \sum_{e'e''} [\frac{W_{e'e''}}{R^3} |e_1, e_2\rangle\langle e'_1, e''_2| + \frac{W^*_{e'e''}}{R^3} |e'_1, e''_2\rangle\langle e_1, e_2|], \tag{I.45}$$

with $W_{e'e''} = \langle e'_1, e''_2|\hat{V}_{dd}|e_1, e_2\rangle$. Here, $|e_1, e_2\rangle = |n, l, j, m_{j1}\rangle \otimes |n, l, j, m_{j2}\rangle$ is the state of interest, and $|e'_1, e''_2\rangle$ another pair of states coupled to $|e_1, e_2\rangle$ by electric dipole transitions.

I.2.3 Specific case of the target state: $60S - 60S$

We now turn more specifically to the case of two atoms in the 60S Rydberg state. Of course, we must aim to a numerical diagonalization of the interaction Hamiltonian (I.43), in the unperturbed pair state basis $|e_1, e_2\rangle$ in which the free Hamiltonians H_i are diagonal by construction.

The first problem is the calculation of the matrix elements $W_{e'e''}$ of the interaction term. In the absence of a magnetic or electric directing field, it is convenient for the symmetry of the problem to choose $\mathbf{R}$ as the quantization axis. The interaction potential I.44 can then be written, by separating the angular and radial parts, as

$$\hat{V}_{dd} = -\frac{q^2}{4\pi\epsilon_0} \frac{\hat{r}_1\hat{r}_2}{R^3} \frac{4\pi}{3} \left(\hat{Y_1}^1(\theta_1, \phi_1)\hat{Y_1}^{-1}(\theta_2, \phi_2) + \hat{Y_1}^{-1}(\theta_1, \phi_1)\hat{Y_1}^1(\theta_2, \phi_2) + 2\hat{Y_1}^0(\theta_1, \phi_1)\hat{Y_1}^0(\theta_2, \phi_2) \right) \tag{I.46}$$

When computing the $W_{e'e''}$ matrix elements, the angular part is thus explicit and simple. It enforces the selection rules, and the only levels coupled to $60S, 60S$ are P states, for which the total magnetic number $M = m_{j1} + m_{j2}$ is conserved. The radial integral $\mathcal{R}_{e'e''}$ requires a bit more attention.

The subspace of the coupled pair states with the same M has yet an infinite dimension. We thus need to perform a truncation of the Hilbert space. Since we are expecting a second order level shift, we must include in the calculation the pair levels with a strong enough radial coupling and a small energy difference with the level of interest.

We plot in figure I.8 the radial matrix element $\mathcal{R}$ between levels $60S_{1/2}$ and $nP_{1/2}$, normalized with respect to the value for $n = n_0 = 60$. These radial matrix elements decrease rapidly when n becomes notably different from n_0. It is thus a reasonable approximation to include in the calculation only levels with a principal quantum number four units above and below $n = 60$: $|n - n_0| \leq 4$. Moreover, we keep only those pair states whose energy

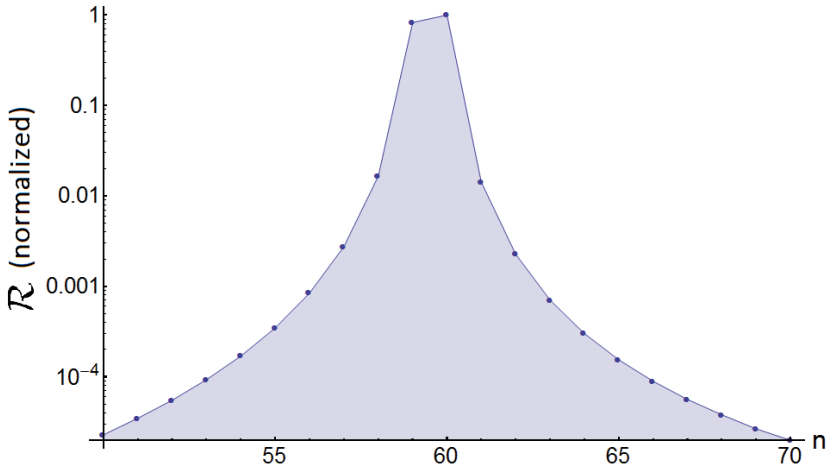

Figure I.8: Variation of the radial part of the interaction matrix element, $\mathcal{R}$, as a function of n between the $60S_{1/2}$ and $nP_{1/2}$ levels, normalized to the value for $n_0 = 60$.

differs from the $60S60S$ one by less than 40 GHz. The final basis thus includes only 523 levels, making diagonalization a quite tractable task for a personal computer. We have checked on a few distances that including more levels only changed the results by less than one percent.

The outcome of these numerical calculations are shown in figure I.9, where we can follow versus the interatomic distance the energies of the states coinciding with the unperturbed pair states in the limit of very large distance. Figure I.10 presents in more details the evolution of the energy of the pair state of interest.

(i) In the large distance regime, above 3 μm, the energy difference between the diatomic state $|e_1', e_2''\rangle$ and $|e_1, e_2\rangle$ is much larger than the corresponding dipole-dipole interaction matrix element:

$$W_{dd} \ll \delta_{|e_1',e_2''\rangle,|e_1,e_2\rangle} \tag{I.47}$$

This is the **Van der Waals regime (vdW)**, and the dipole dipole interaction acts at the second order of perturbation. Hence, the shift is given by

$$\Delta_{dd}^{(2)} = \frac{|\langle e_1, e_2|\hat{V}_{dd}|\mathrm{e}_1'\mathrm{e}_2''\rangle|^2}{E_{e_1',e_2''} - E_{e_1,e_2}} = \frac{|W_{dd}|^2}{\delta_{|e_1',e_2''\rangle,|e_1,e_2\rangle}} \ , \tag{I.48}$$

while the eigenstates are very close to the eigenstates at infinite distance.

The shift is thus proportional to C_6/R^6. The Van der Waals coefficient value for the $|60S, 60S\rangle$ state is $C_6^{60S,60S} = 137.5\mathrm{GHz}\mu\ \mathrm{m}^6$. Since $|\langle e_1, e_2|\hat{V}_{dd}|\mathrm{e}_1'\mathrm{e}_2''\rangle|^2$ scales as n^{*4} and the energy difference $\delta_{|e_1',e_2''\rangle,|e_1,e_2\rangle}$ as n^{*-3}, the van der Waals energy shift scales as n^{*11}. This astoundingly fast variation makes high-lying Rydberg states particularly appealing for the dipole blockade implementation. Of course, the sensitivity to stray electric field also increases rapidly with n.

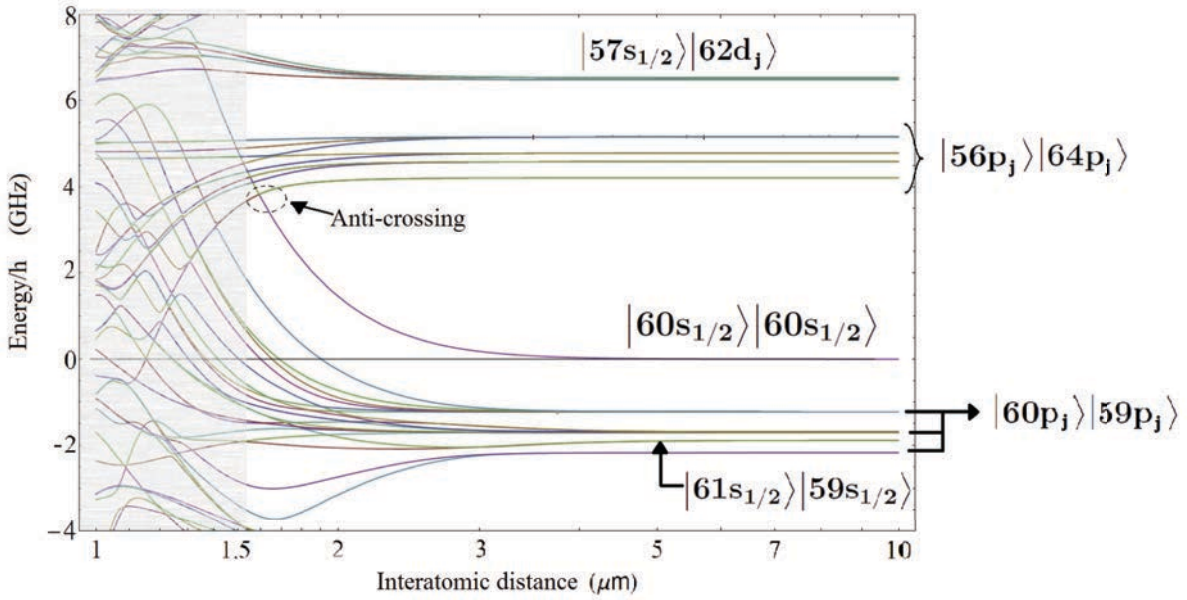

Figure I.9: Energy of the pair states as a function of the distance between the two atoms with respect to the energy of $|60S, 60S\rangle$ at infinite distance. The levels *crossings* are in fact small *anti-crossings*. The grey region marks distances shorter than 1.6 μm, for which the levels start to be mixed up due to an interaction energy larger than the separation between the pair states.

(ii) A second regime is observed in (I.9) and (I.10) for interatomic distances between 3 and 1.6 μm. The dipole-dipole interaction energy is then of the same order of magnitude as the distance between the uncoupled levels. The eigenstates of the full Hamiltonian are completely different from the original pair states. We start entering a regime in which the perturbation acts at the first order, leading to a variation of the shift with distance in C_3/R^3, with C_3 scaling as n^{*4}. However, the $1/R^3$ regime is never exactly reached, since the original level undergoes its first anti-crossing at a distance of 1.6 μm (figure I.9).

(iii) For distances lower than 1.6 μm (grey region in figure I.9), many anti-crossings occur. It we assume that the atoms have been brought adiabatically to the final distance, from an infinite separation, the energy will follow the black line in figure I.10. Of course, the excitation spectrum in this region is extremely complex. In this region, the chosen truncation of the Hilbert space might also be inappropriate.

For the sake of completeness, we give in table I.4, the vdW coefficients C_6 for some diatomic levels $|nS, nS\rangle$, with n near 60. We compare the directly computed van der Waals coefficients with the values deduced from $C_6^{60S,60S}$ and the n^{*11} scaling law.

Bearing in mind these orders of magnitude, the next step is to determine the size of the atomic sample leading to a clear dipole blockade effect and to the excitation of a unique Rydberg atom. We will use for this purpose numerical simulations but, before that, we will discuss in more quantitative terms the dipole blockade itself.

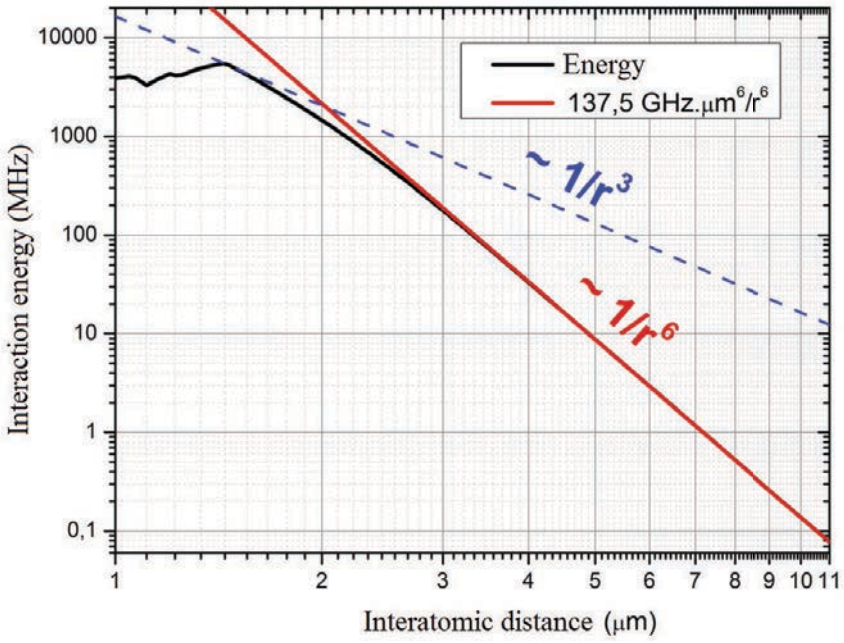

Figure I.10: Energy of the pair state $|60S, 60S\rangle$ as a function of the interatomic distance R (black line). For distances larger than 3 μm the regime is dominated by a vdW interaction varying as $1/R^6$ (red line). When the atoms are separated by 5 μm, the energy shift is 8.8 MHz. For distances shorter than 3 μm, we approach the dipole-dipole regime $1/R^3$ (blue line), but anti crossings with other levels occur. In the case of atoms taken from infinity adiabatically, the energy follows the black curve

	C_6 μm^6 GHz	$C_6^{60S,60S} \times \frac{(n-\delta_{nlj})^{11}}{(60-\delta_{60lj})^{11}}$ μm^6 GHz
$\|57S_{1/2}, 57S_{1/2}\rangle$	73.8	75.8
$\|58S_{1/2}, 58S_{1/2}\rangle$	92.93	92.7
$\|59S_{1/2}, 59S_{1/2}\rangle$	111.5	113, 1
$\|60S_{1/2}, 60S_{1/2}\rangle$	137.5	137.5
$\|61S_{1/2}, 61S_{1/2}\rangle$	167.5	166.6
$\|62S_{1/2}, 62S_{1/2}\rangle$	203.5	201.1
$\|63S_{1/2}, 63S_{1/2}\rangle$	246.3	242.0

Table I.4: Van der Waals coefficients of $|nS, nS\rangle$. The first column shows values from numerical calculations. The second column shows the values calculated from the coefficient of $|60S, 60S\rangle$ and the scaling law $(n - \delta_{nlj})^{11}$.

I.2.4 Dipole blockade effect

Following the ideas presented in section I.2.1, we present briefly here the theoretical background of the dipole blockade effect, by describing the collective excitation of a sample of

N ground state atoms inside a Rydberg level.

We treat the excitation of the ground state g to the Rydberg level e as an effective one-photon process, with a Rabi frequency $\Omega/2\pi$. The laser at frequency $\omega/2\pi$ is assumed to be detuned from the atomic transition by $\delta = \omega - \omega_0$ (positive δ value corresponding to a 'blue' detuning), much smaller that the detuning of the transitions to the nearby Rydberg levels.

If the laser beam waist is much larger than the transverse dimensions of the atomic cloud, all atoms are coupled to the laser with the same Rabi frequency. We will assume that the van der Waals interaction between all pairs of atoms in the sample are additive, a reasonable approximation for not too small interatomic distances. In these conditions, we can write the global Hamiltonian describing the atom-field interaction as:

$$\frac{\hat{H}}{\hbar} = \delta \sum_{j\leq N} |e_j\rangle\langle e_j| + \frac{\Omega}{2}\sum_{j\leq N}(e^{i\mathbf{k}\cdot\mathbf{r}_j}|e_j\rangle\langle g_j| + e^{-i\mathbf{k}\cdot\mathbf{r}_j}|g_j\rangle\langle e_j|) + \sum_{j\leq N,\, k<j} \Delta(r_{jk})|e_k, e_j\rangle\langle e_j, e_k| \ , \tag{I.49}$$

where we have used the Rotating Wave Approximation to remove rapidly oscillating terms. In this Hamiltonian, $\vec{k}$ is the wave vector of the excitation laser field (we cannot consider that the atomic sample is much smaller than the laser wavelength) and $\vec{R}_i$ is the position of the ith atom. Finally, $\Delta(r_{jk})$ is the van der Waals interaction energy between atoms i and k, when they are both promoted to the Rydberg states.

The phase terms, $e^{i\mathbf{k}\cdot\mathbf{r}_j}$, can be easily removed by a proper definition of the excited states phase, since the atoms are assumed to be motionless during the laser excitation. We can thus rewrite the Hamlitonian under the simpler form:

$$\frac{\hat{H}}{\hbar} = \delta \sum_{j\leq N} |e_j\rangle\langle e_j| + \frac{\Omega}{2}\sum_{j\leq N}(|e_j\rangle\langle g_j| + |g_j\rangle\langle e_j|) + \sum_{j\leq N,\, k<j} \Delta(r_{jk})|e_k, e_j\rangle\langle e_j, e_k| \ , \tag{I.50}$$

We shall discuss the Hamiltonian (I.50) in two limiting cases. First, we will consider a very dilute sample for which the van der Waals interaction is negligible ($\Delta(r_j k) = 0$). We will then focus on the strong interaction case $\Delta(r_j k) \gg \sqrt{N}\Omega$.

We thus consider first the **limit without interactions** $\Delta(r_{jk}) = 0$ for all j and k. The ground state of the atomic ensemble writes $|N\,:\,0\rangle = \bigotimes_{j\leq N} |g_j\rangle$. The state with only one excitation in the Rydberg state $|1\rangle$ is:

$$|1\rangle = \frac{1}{\sqrt{N}} \sum_{j=1}^{N} |N-1\,:\,g,\,1\,:\,e_j\rangle \tag{I.51}$$

The state $|1\rangle$ is a superposition with equal weights of states $|N-1\,:\,g,\,1\,:\,e_j\rangle$ and is obviously symmetric with respect to atomic interchange, as is the total Hamiltonian when neglecting the van der Waals terms.

It is easy to generalize the picture to the state with k excited atoms in the sample, $|k\rangle$, with $k \leq N$. Each of them is totally symmetrical with respect to atomic interchange. The

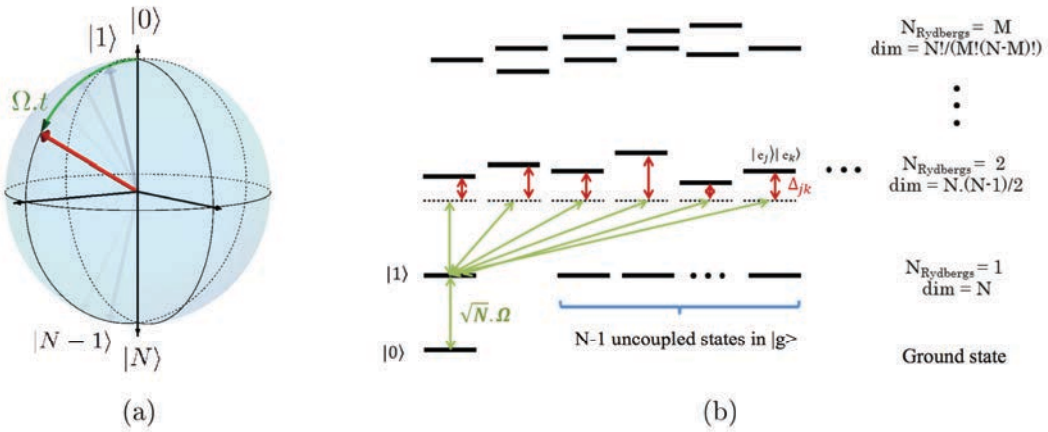

Figure I.11: **(a)** Bloch sphere representation for the collective Rabi oscillation of N atoms coupled to a resonant radiation field. The symmetrical atomic Dicke states generates a $N+1$-dimensional representation of the $SU(2)$ algebra corresponding to the spin $N/2$ system. The Bloch vector representing this spin evolves between the South Pole (ground state with zero excitations $|0\rangle$) and the North Pole (state with N excitation represented by $|N\rangle$), at the Rabi frequency $\Omega/2\pi$. **(b)** Scheme of the 2^N states when the atoms are coupled by dipole-dipole interactions, breaking the symmetry of the Dicke model. The subspaces are sorted by number of excitations.

excited states form thus a ladder of $N+1$ non degenerate equidistant levels. They are known as the **Dicke states** [34]. The coupling symmetry simplifies considerably the problem, since the original Hilbert space, not restricted by this requirement, has a dimension 2^N. Note that we will discuss the Dicke model in much more details in the theoretical part of this thesis.

These $N+1$ levels are also equivalent to a spin $N/2$ evolving in an abstract space. We can thus visualize the Dicke states on a generalized Bloch sphere (see figure I.11). The resonant laser excitation induces a coherent Rabi oscillation on this sphere, leading the system from the ground state to the state with all atoms excited and back: $|0\rangle \rightarrow |1\rangle \rightarrow |2\rangle \rightarrow \cdots \rightarrow |N\rangle$. At any time, the atomic systems is in a so-called Spin Coherent State [35]. In figure I.12(a), we present the populations of the one- and two- excitation states in the case $N = 2$.

Let us now consider the effect of interaction. Such an interaction clearly breaks the symmetry of the Dike model. The evolution is no longer confined to the $N+1$ dimensional spin states ladder, but may reach all of the 2^N levels This awfully complex situation may nevertheless be simplified, trough the dipole blockade mechanism itself.

The figure I.11(b) presents the first manifolds in this complex Hilbert space, with zero, one and two excitations (these manifolds being separated by the atomic excitation energy). In the first manifold, there is no dipole-dipole interaction since there is a single excited state. The symmetry argument thus holds still in this case and the ground state is only coupled to the symmetric excited state $|1\rangle$. It is easy to check that the atomic system

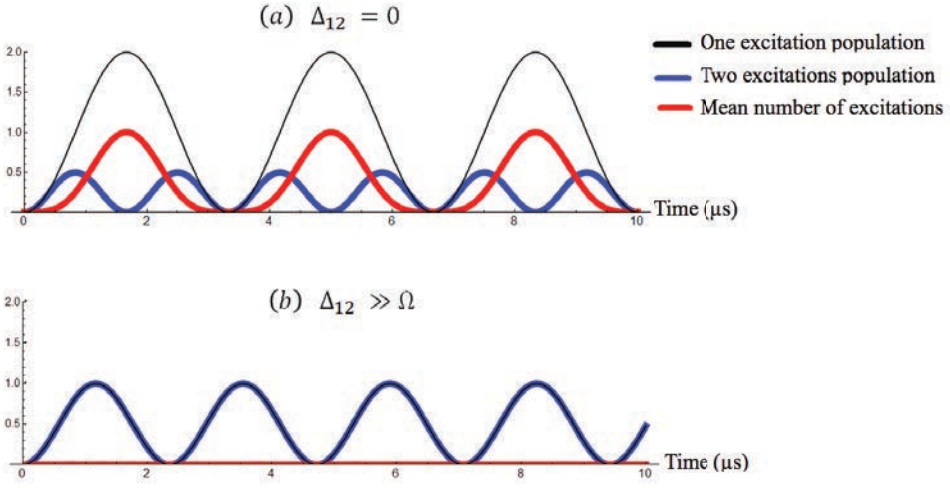

Figure I.12: Analytic solution for the two-atom case. Two limiting cases are shown. **(a)** no interactions, $\Delta_{1,2} = 0$. We observe the Rabi oscillations for the state of one and two excitation, as well as the mean excitation number. **(b)** shows the limit of strong blockade , $\Delta_{1,2} \gg \Omega$. The collective Rabi oscillation frequency between the ground state and the state with one excitation is $\Omega_2 = \sqrt{2}\Omega$. After a time π/Ω_2, a state with one single excitation is generated.

coupling with the laser is then characterized by a collective Rabi frequency $\Omega\sqrt{N}$ (there are N terms in the coupling of the ground state $|0\rangle$ to $|1\rangle$, and each of these terms is equal to $\Omega/\sqrt{N}$: $\langle 1|\hat{H}|N:0\rangle = \hbar\sqrt{N}\Omega = \hbar\Omega_N$.

The situation is much more complex for the second manifold, since $|1\rangle$ is coupled to all levels with two excitations. No clear insight beyond numerical computations can be obtained in this case.

The situation becomes simple again in the case of a **complete blockade** [36], for which $\Delta(r_{jk}) \gg \sqrt{N}\Omega$ for any pair of atoms. As illustrated in figure I.11(b), the laser is then out of resonance for excitation of any of the two-excitation levels, within the transition line width determined by the collective Rabi frequency. We thus expect in this case a simple two-level Rabi oscillation between the ground state and $|1\rangle$, at the collective Rabi frequency Ω_N. Figure I.12(b) illustrates this effect in the simple two-atom case. The state with two excitations is never populated.

The blockade radius: We can now give an expression for the blockade radius [37], which establishes an energy-distance scale, separating the regime of Rabi oscillations and collective oscillations (blocked) . For the van der Waals regime, this radius is given by:

$$R_b = \left(\frac{2\pi C_6}{\Delta\omega}\right)^{\frac{1}{6}}. \tag{I.52}$$

where $\Delta\omega$ is the resonance linewidth. It does not take into account the fact that the

transition width may be affected by external conditions as the effect of stray electric fields. For instance, for the target $|60S\rangle$ state and $\Delta\omega/2\pi = 600$ kHz (laser linewidth), the expected blockade radius is $R_b = 7.8$ μm.

If we consider the case of a dense cloud, where many atoms can be inside the blockade volume, when $\Omega_N = \sqrt{N}\Omega > \Delta\omega$, the radius is defined as:

$$R_b = \left(\frac{2\pi C_6}{\sqrt{N}\Omega}\right)^{\frac{1}{6}}. \tag{I.53}$$

This expression is used in next section.

I.3 Simulations of dipole blockade regime in a small BEC

In order to guide the design of these experiments, we have performed numerical simulations of the dipole blockade mechanism. We used the context of a small Bose Einstein Condensate on the chip, since it provides the highest confinement and density, favorable conditions for the excitation of a single Rydberg state.

We simulate excitation of a small BEC, containing only 300 atoms, with a Thomas-Fermi profile and $r_x, r_y, r_z = (2.34, 1.6, 1.08)$ μm (radius at e^{-1}). The trap frequencies are $(\omega_x, \omega_y, \omega_z) = 2\pi(37(1), 107(1), 121(1))$ Hz corresponding, in the experimental section of this work, to a Ioffe Pritchard trap at 455 μm from the chip surface. The critical BEC temperature T_C in this trap is given by [38]

$$k_b T_C \approx 0.94\hbar\bar{\omega}N^{1/3} \tag{I.54}$$

where $\bar{\omega} = (\omega_x\omega_y\omega_z)^{1/3}$ and k_B is again the Boltzmann constant. For our trap $T_C = 23.6$ nK. Note that the diameter along the z direction of the BEC is below 1.6 μm which is the distance of the first anticrossing. We are there in a situation of complete blockade.

At zero temperature, all atoms are in the condensed phase. At a more realistic finite temperature, $T = 14$ nK, only 80% of the atoms are in the condensed phase. The BEC is thus surrounded by a thermal cloud with dimensions (radius at e^{-1}) given by $r_x, r_y, r_z = (5.37, 1.83, 1.64)\,\mu$m. We will consider in the following simulations both the pure BEC case and the more realistic finite temperature one.

Obviously we cannot compute the total evolution in the 2^{300} dimensional Hilbert space. We will thus restrict ourselves to the manifolds with zero one and two excitations. This will be a reasonable approximation if the numerics show that the population of the manifold with two excitations remains negligible at all times.

We use the frozen gas approximation. We mostly use resonant laser pulse durations shorter than 1 μs. The atomic position variations regarding their initial velocity (at 1 μK, 1.38 cm/s) results in negligible interaction energy variations.

The state, considering up to two excitations can be written as

$$|\psi_{012}\rangle = c_0|0\rangle + \sum_k c_k|\phi_{(k)}\rangle + \sum_{k,l>k} c_{kl}|\phi_{(kl)}\rangle \ , \tag{I.55}$$

$|0\rangle$ being the state without excitations, $|\phi_k\rangle$ the state for the k atom excited to $|60S\rangle$, and $|\phi_{kl}\rangle$ the state for the atom k and l excited. Using the Hamiltonian defined in (I.50), we get the following equations for the probability amplitudes:

$$i\frac{dc_0}{dt} = \frac{\Omega}{2}\sum_k c_k(t) \tag{I.56}$$

$$i\frac{dc_k}{dt} = \delta \cdot c_k(t) + \frac{\Omega}{2}c_0(t) + \frac{\Omega}{2}\sum_{l\neq k} c_{kl}(t) \tag{I.57}$$

$$i\frac{dc_{kl}}{dt} = (2\delta + \Delta(r_{kl}))c_{kl}(t) + \frac{\Omega}{2}c_k(t) + \frac{\Omega}{2}c_l(t) \ . \tag{I.58}$$

The collective Rabi frequency is taken from typical experimental parameters: $\Omega_N = \sqrt{N}\Omega = 2\pi \times 500$ kHz (which implies a $R_b = 8.09$ μm), of the same order of magnitude as the laser linewidth. The laser is at exact resonance $\delta = 0$. The equations have been numerically solved by a C_{++} code using Runge-Kutta method at 4th order. The atomic distribution in the sample is chosen randomly according to the trap parameters. The dipole-dipole interaction terms are then computed, and the equations solved.

Figure I.13(a) presents the evolution of the populations of the three manifolds (zero one and two excitations) versus time for the ideal case of a pure condensate. We observe a nearly perfect blockade effect, with a population of the second manifold below 0.1%.

Figure I.13(b) deals with the more realistic case of a finite temperature. The probability for a pair exception is then up to 10%, a much larger value due to the large average distance between atoms in the thermal cloud. It might even be that more excited levels would be produced in a more complete computation. It is thus of paramount importance to prepare a pure condensate for a proper dipole blockade effect.

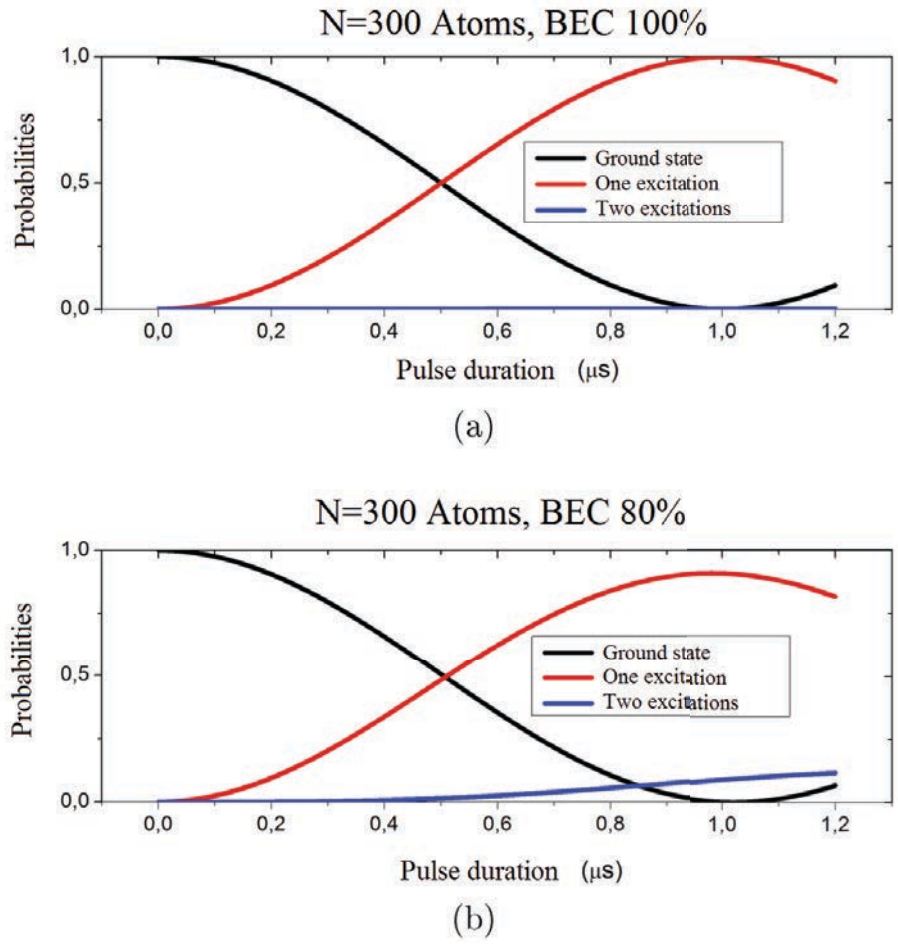

Figure I.13: Evolution of the zero, one and two excitations manifolds for the target state $|60S\rangle$ in a BEC with 300 atoms. **(a)** Pure BEC. **(b)** BEC with 80% of the atoms in the condensed phase and the rest in a thermal cloud. See text for the other parameters.

I.4 Conclusion

We have introduced in this chapter the main theoretical tools that will be needed for this work. We have recalled the main properties of the Rydberg atoms and outlined their high sensitivity to electric fields and their very strong dipole dipole interaction. We have discussed the dipole blockade mechanism, which was the primary initial aim of this work.

This theoretical approach has set the proper conditions for dipole blockade. It should involve an S target state, to make the dipole-dipole interaction independent on the orientation of the interatomic axis with respect to the quantization axis. The principal quantum number should be not too large to limit sensitivity to stray fields, but also large enough for a strong van der Waals interaction. This justifies the choice of the 60S state in all the experiments presented here. We have also shown that the dipole blockade requires an extremely tight control of the atomic and laser line widths. The major part of the

technical efforts described in the next chapters will be devoted to this control. We have finally shown that a very pure BEC with a small number of atoms is mandatory to get a proper blockade. This is a difficult goal, which is still far from being reached.

Chapter II

Experimental setup

In this chapter, we focus on a rapid description of the experimental setup. The optical cooling and trapping techniques used here are already described in details in the PhD works of C. Roux [39] and T. Nirrengarten [40].

The heart of the experiment is a superconducting atom-chip, made up of Niobium wires [41]. With this device, we can confine tightly an atomic ensemble and even realize the Bose-Einstein condensation on-chip [13]. The small sizes and high densities of these on-chip trapped clouds are important assets for the observation of the dipole blockade effect. The chip is placed inside a cryostat, cooled down to 4.2 K. This cryogenic environment is essential for the experiments we are aiming at. In particular, the millimeter-wave transitions between adjacent Rydberg levels are highly sensitive to the blackbody background field, which must be reduced as much as possible to get long levels lifetimes (see section I.1.1).

When I joined the group, the experiment was undergoing a radical upgrade, being basically rebuilt from scratch, except for the cryostat itself. Together with a post doc (Sha Liu) and another PhD student (Raul Celistrino Teixeira), we have entirely rebuilt the optical table providing all the useful laser beams. We have designed and built a new chip in order to get higher critical currents and hence higher confining potentials, reducing even further the dimensions of the traps.

We start by describing the cryogenic environment, then the chip itself and its fabrication procedure (it is only outlined here, more details can be found in Appendix A of [42]. We give a qualitative description of the magnetic Ioffe-Pritchard trap provided by the chip. We summarize the main features of the laser and imaging system. We defer to the next chapter the description of the laser locking system and that of the Rydberg excitation and detection systems.

We finally describe the atomic cooling and trapping sequence, in the order of the events experienced by the atoms. They are first captured in a 2D-MOT outside of the cold environment and sent, in a low-velocity atomic beam arrangement, towards the chip. They are trapped near the chip in a Mirror MOT whose quadrupolar magnetic field is provided by macroscopic superconducting coils. They are then transferred into a mirror-MOT (U-MOT) generated by an on-chip conductor. They are cooled further in an optical molasses

and optically pumped in a level appropriate for the magnetic trap. They are transferred into the magnetic on-chip Ioffe-Pritchard trap, compressed even further to improve collision rates. Finally an evaporative cooling sequence leads at will to ultra-cold thermal atomic cloud or to a BEC.

II.1 Cryogenic environment

The use of a cryogenic environment sets some difficult constraints on the experiment (for instance, a rather narrow optical access). On the other hand, as mentioned earlier, it is essential for the operation of the superconducting chip and for an efficient shielding from the thermal radiation. A final asset is the good quality of the residual vacuum. At 4.2 K, it is rather straightforward to reach pressures smaller than $1 \cdot 10^{-10}$ mbar. This reduces the losses due to collisions with the background gas and very long trap lifetimes can be reached without time-consuming outgasing procedures [43].

A general view of the cryostast is given in figure II.1, along with a sketch of its main components. It consists of three cylindrical shields, the two inner ones made of gold coated copper. The inner one is in contact with the liquid ^4He bath (4.2 K). The intermediate one is thermalized by a liquid nitrogen reservoir (77 K). Finally, the outer cylinder, at room temperature, provides vacuum isolation. The intermediate shield protects the inner one from the intense thermal radiation coming from the outer shield at 300 K. The autonomy without Helium refill is about 2 days. On the outside of the nitrogen shield, the pressure is measured to be $2 \cdot 10^{-8}$ mbar, whereas the vacuum in the inner part, at 4.2 K, which cannot be directly measured, is inferred to be much smaller that $1 \cdot 10^{-10}$ mbar from the lifetime of our atom traps, of the order of a few minutes. For the sake of clarity (see figure II.1), we set the coordinate system of the experiment as follows. The x-direction is horizontal and parallel to the chip, the y-direction is perpendicular to the its surface, and the z-direction is such as that gravity follows $-z$.

We can also see in figure II.1 that each shield is equipped with windows for optical access. The trapping and cooling beams as well as the beams for the imaging system are sent through these ports. For the optical cooling and trapping, we use the two windows in the $\pm x$-direction. They are also used for one of the imaging beams, giving information on the cloud in the yz plane (side view). The windows centered on oblique axes are used for the beams of the mirror-MOTs. They will be from now on called the ± 45 beams since they form an angle of 45^0 with the y axis in the yz plane. The windows aligned on the y axis are used for an imaging beam looking at the atoms from the front, in the xz plane. The Rydberg excitation beams pass through the x windows, as described in more details in the next chapter.

The internal helium shield is covered by a layer of lead, superconducting at 4.2 K, which screens the external magnetic field through the Meissner effect [44]. This layer also considerably reduces the Foucault currents induced in the shields when we rapidly turn off or on the magnetic fields.

It is obviously impossible, in this cryogenic environment, to trap the atoms near the

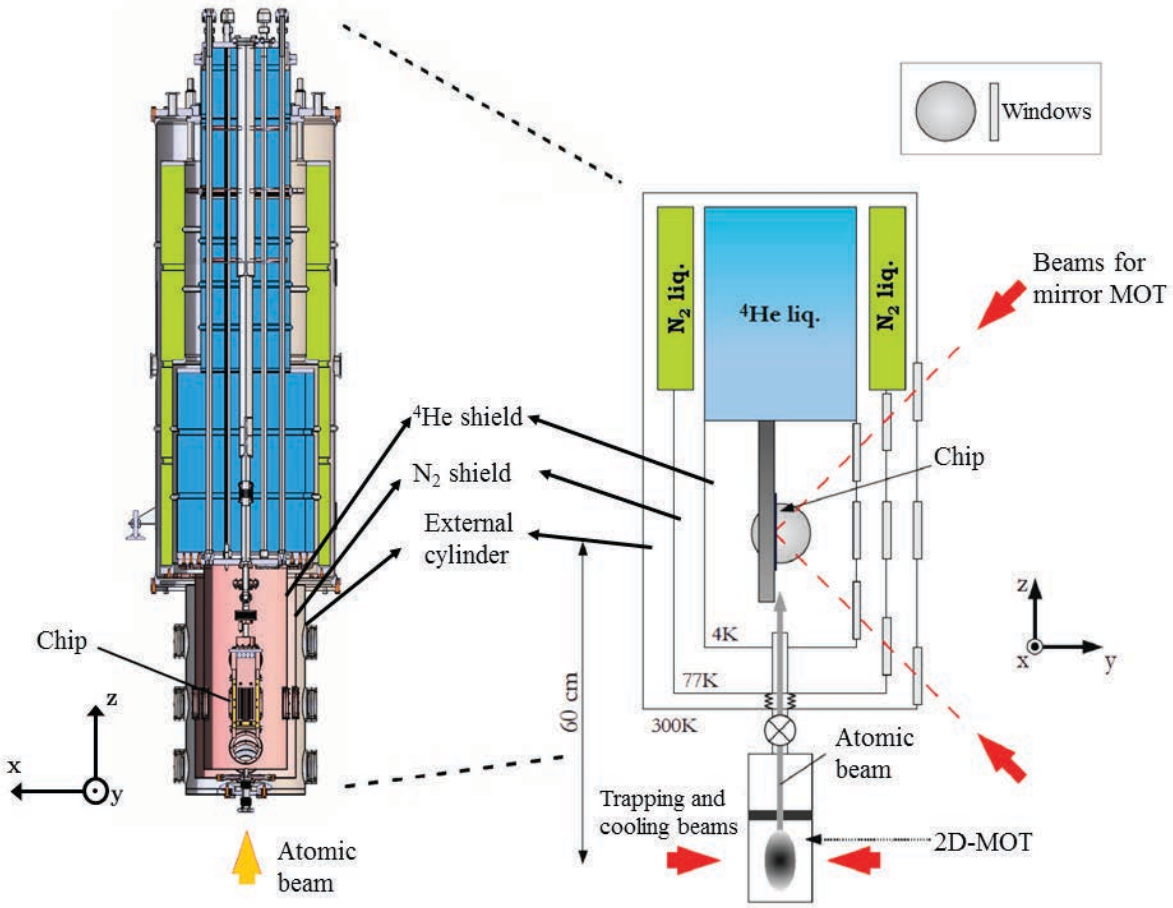

Figure II.1: **Left:** Cut of the cryostat. The point of view is facing the chip. The liquid nitrogen shield is in green, the Helium reservoir in blue. The low velocity atomic beam enters the cryostat from the bottom (yellow arrow). **Right:** scheme of the cryostat viewed in the x direction, parallel to the chip surface. The atoms are first caught in the 2D-MOT trap in the bottom, send towards the chip. They are first trapped and cooled in a mirror MOT in front of the chip.

chip from a thermal vapor. All Rubidium atoms immediately stick forever to the cold surfaces around the chip (this is by the way the key problem we will have to solve to get rid of the stray electric fields). The atoms are thus first captured by a two-dimensional magnetic-optical trap (2D-MOT) operating at room temperature, which can be seen at the bottom of figure II.1. The MOT chamber is connected to the cryostat by a small tube, with a hole diameter of 1.5 mm, to maintain a gradient of pressure between this chamber and the cryostat. The atoms may escape naturally from the trap along the $+z$ direction. They can also be extracted by a pushing laser beam sent in the same direction. They arrive near the chip surface, with a velocity in the 10 m/s range. They are then trapped in a three-dimensional mirror magneto-optical trap (3D-MOT) before being transferred into the on-chip magnetic trap .

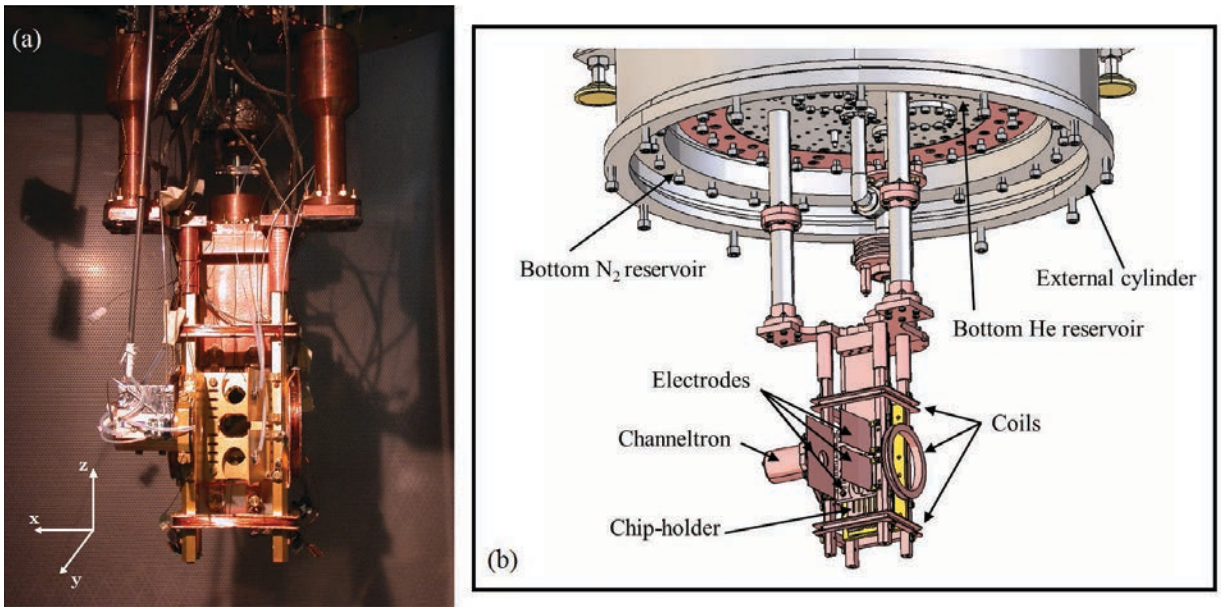

Figure II.2: **(a)** Photograph of the heart of the experiment, attached to the Helium reservoir. **(b)** Technical sketch of the same region.

A more detailed view of the experiment's core is presented in figure II.2, depicting other important components. Panel (a) presents a photograph of the setup and panel (b) a technical sketch of the same region. The superconducting coils aligned on the x and z axis create in the chip region nearly uniform bias fields used, together with that generated by the chip, for the MOT and magnetic trapping. We can also see the electrodes and the channeltron counter of the Rydberg detection system, which will be described in the next chapter.

All the components in figure II.2 are thermalized at 4.2 K by direct contact with the Helium reservoir, except for the Channeltron device which works at 42 K and it is very well isolated from the chip.

II.2 A superconducting atom chip

Figure II.3 presents the geometry of the chip. The wires of the chip are made up of a thin film of Niobium, superconducting material with a critical temperature at 9.2 K for bulk. In the thin films used here, the critical temperature is slightly reduced, in the 7 K region.

The chip was designed bearing in mind the requirements of the dipole blockade effect commented in section I.2 of the first chapter. The central part of the chip surface must be covered by an efficient mirror needed for the mirror MOT operation. We have made the rather obvious choice of gold for the mirror.

The micro-fabrication techniques for producing the chip are rather standard. Their adaptation to our experiment is described in more detail in [40], for an older version of the

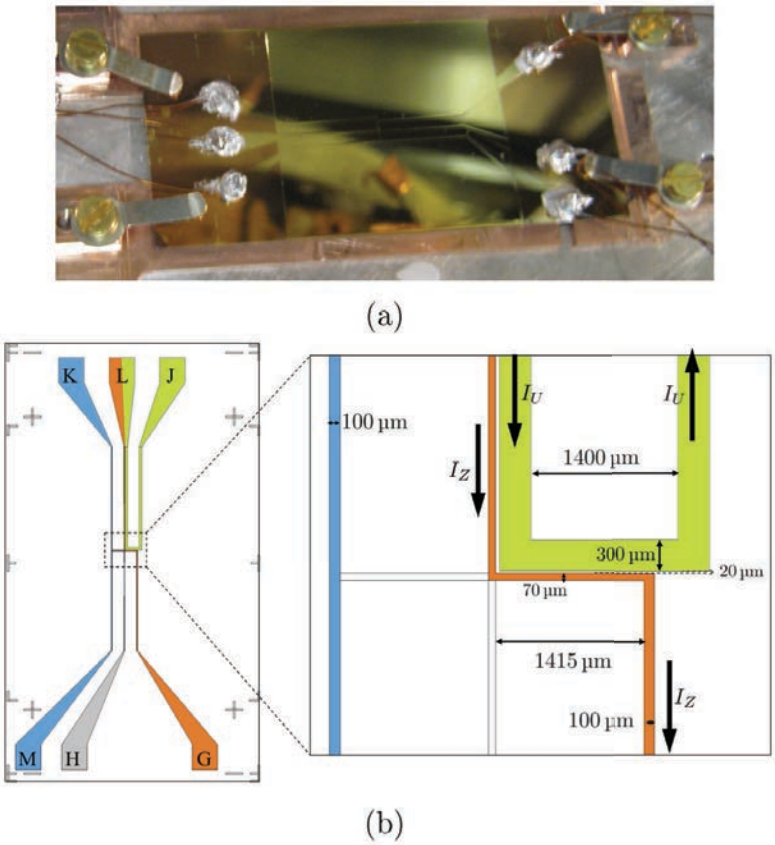

Figure II.3: **(a)**: Photograph of the chip, once installed in its holder. The golden square is the mirror used for the 3D-MOT. The chip wires are visible behind this front gold layer. They are soldered to superconducting current feeds. **(b)**: Chip design with a zoom on the interesting region on the right, turned by 90^0 with respect to the image in panel (a). It is thus shown as actually installed in the cryostat. In green, we see the U-shaped wire, which creates the quadrupole field needed for one of the U-MOT cooling stage. In orange, we have the Z-shaped wire, which is used for the Ioffe-Pritchard magnetic trap. In blue, we show the wire transmitting the radio frequency for the evaporative cooling stage.

chip, and in [42] for the new design used in this work. We give here only a sketch (Fig. II.4) of the chip and a brief description of the fabrication.

The superconducting Niobium film has a thickness of $2\,\mu$m. It can sustain a current of up to 3.5 A for $70\,\mu$m wide wires and up to 8 A for $300\,\mu$m wide ones, without transit into the normal state. The color code in figure II.3(b) identifies the various functions of the wires on the chip. In green, we see the U-shaped wire, which creates, together with a uniform bias produced by the external coils, the quadrupole field needed for the U-MOT stage. It has a width of $300\,\mu$m. In orange, the Z-shaped wire generates the Ioffe-Pritchard magnetic trap. It has a width of $70\,\mu$m, for the upper arm and central path, and $100\,\mu$m for the lower. The U and Z wires have a common entry port at L. In blue, we show the wire

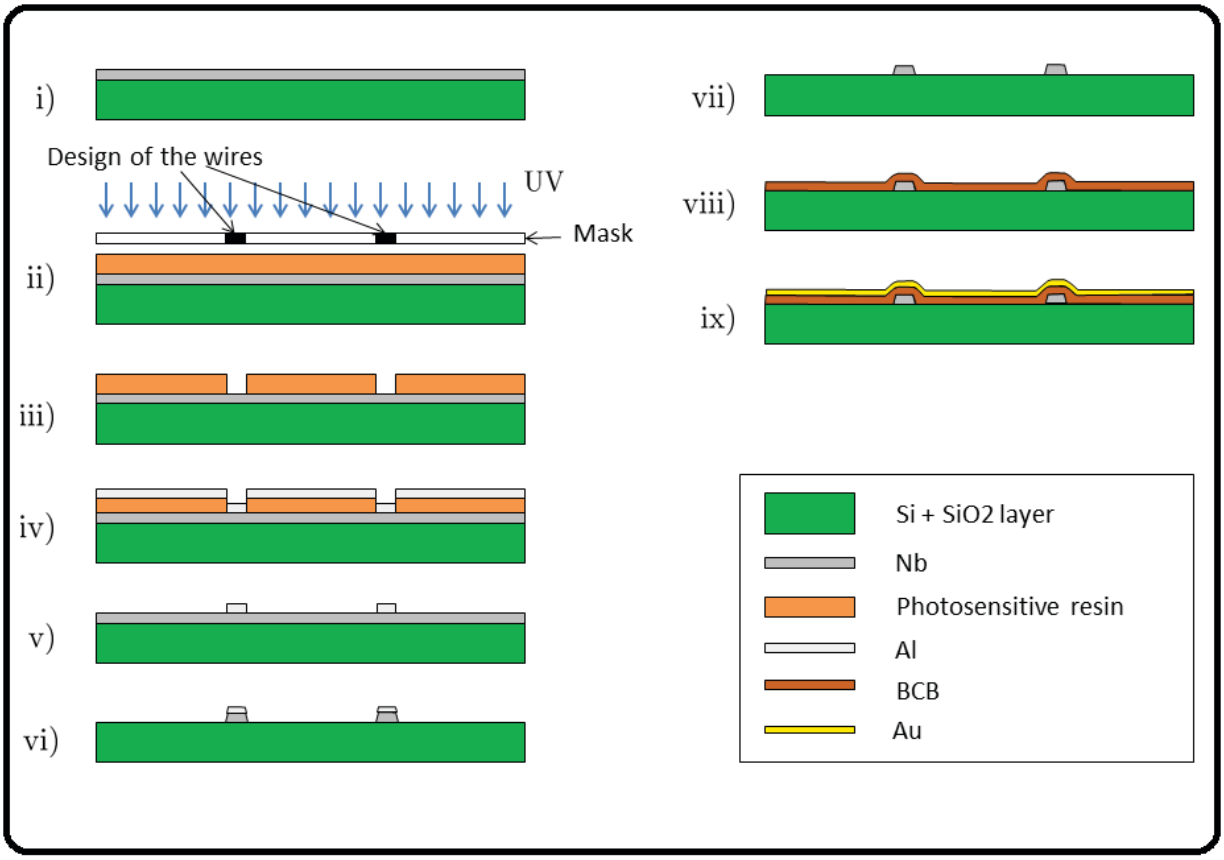

Figure II.4: Fabrication procedure. The S_i/S_iO_2 substrate is cleaned by a mixture of sulfuric acid H_2SO_4 and hydrogen peroxide H_2O_2 (piranha solution), before the deposition of a 2 μm-thick Nb film (stage *(i)*). The stages **(ii)** and **(iii)** describe the standard negative photo-lithographic method used to define the wires and the soldering pads. In stages **(iv)** and **(v)** , an Aluminum film is deposited over the whole surface before removing the unexposed resin (and hence the Al on top of it) by a process called *lift off*. After that stage, Al covers only the parts that will become the wires and the pads for the soldering. The uncovered Nb is then removed by a reactive ion etching (RIE) (stage **(vi)**) and the Aluminum film is dissolved in KOH (stage **(vii)**). Finally, the niobium chip is planarized with benozocyclobutene (BCB) and covered by a 200 nm gold layer deposited onto a 30 nm Titanium layer.

through which the radio frequency (RF) is sent for the evaporative cooling stage leading to the BEC.

The main experiments are performed when the atoms are confined in the Ioffe-Pritchard trap created by the field of the Z wire superposed with a uniform bias. The shape of the Z wire has been designed to optimize the final shape of the trapped atom cloud. It is now in order to discuss the properties of this magnetic trap in more details.

The Zeeman effect for the hyperfine structure of the ground state of Rubidium is given

by

$$H_z = g_z m_F \mu_B |\mathbf{B}(\mathbf{r})| \ , \tag{II.1}$$

where F denotes the hyperfine level and m_F the Zeeman-sublevels, as described in section I.1.3. The quantization axis is defined along the direction of the magnetic field $\mathbf{B}$.

Atoms optically pumped in the $F = 2, m_F = 2$ (Landé factor $g = +1/2$) sublevel thus experience a trapping potential when the modulus of the magnetic field has a local minimum [45]. It is important that the minimum value of $|\mathbf{B}(\mathbf{r})|$ is nonzero, to avoid the Majorana losses due to atomic spin flips when the atom passes in a region of too weak a magnetic field. This is one of the key assets of the Ioffe-Pritchard geometry [46], which provides a clearly defined quantization axis in the bottom of the trap.

Let us discuss first the simple case of a 1-D infinite trap. Figure II.5 shows the field created by a horizontal infinite current line in the $-x$-direction plus a uniform bias field with components B_y and B_z in the plane yz perpendicular to the current. The modulus of the magnetic field cancels at a single point in the perpendicular plane. The distance between the current line and the zero of the field is

$$r_0 = \frac{\mu_0}{2\pi} \frac{I_x}{B_\perp} \tag{II.2}$$

where $B_\perp$ is the modulus of the bias field in the yz plane, $B_\perp = \sqrt{B_y^2 + B_z^2}$ and I_x the current passing through the line. Around this zero, the field behaves as a quadrupole field (green lines in the figure). The gradient in the orthogonal eigenaxes of the quadrupole field is given by

$$|B'(r_0)| = \frac{2\pi}{\mu_0} \frac{B_\perp^2}{I_x}. \tag{II.3}$$

The trapping is of course insensitive to an added uniform bias in the x-direction, B_x. The field in the bottom of the trap can then be nonzero, avoiding Majorana losses.

The Zeeman term (II.1) can be rewritten along one of the quadrupole field eigenaxis $\mathbf{e}_r$ as

$$H_z \approx g_F m_F \mu_B B_x + \frac{g_F m_F \mu_B}{2} \frac{(B'(r_0))^2}{B_x} (r - r_0)^2 \tag{II.4}$$

since the modulus of the field around the minimum in the direction $\mathbf{e}_r$ can be written as

$$B = \sqrt{B_x^2 + (B(r_0))^2} \approx \sqrt{B_x^2 + (B'(r_0)(r - r_0))^2} \approx B_x + \frac{1}{2} \frac{(B'(r_0))^2}{B_x} (r - r_0)^2. \tag{II.5}$$

From the quadratic part in II.4, we see that the trapping potential in this direction is harmonic with a characteristic frequency $\omega_\perp$. The frequency for a motion along the perpendicular eigenaxis is obviously the same. We thus obtain an isotropic harmonic trap. The oscillation frequency can be expressed in term of $B_\perp$ or r_0 as follows

$$\omega_\perp = \sqrt{\frac{g_F m_F \mu_F}{M B_x}} \frac{2\pi}{\mu_0} \frac{B_\perp^2}{I_Z} \tag{II.6}$$

$$\omega_\perp = \sqrt{\frac{g_F m_F \mu_F}{M B_x}} \frac{2\pi}{\mu_0} \frac{I_Z}{r_0^2} \tag{II.7}$$

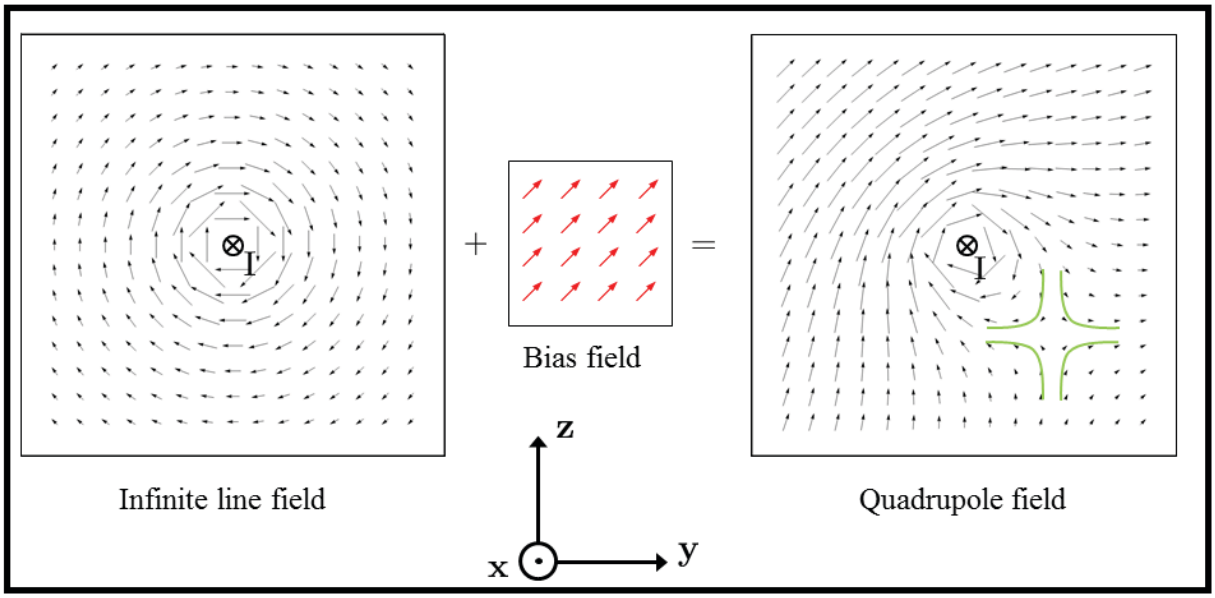

Figure II.5: Magnetic field configuration created by a current flowing in an infinite line in the $-x$ direction, superposed with a uniform bias. A $2D$ quadrupole confinement is created in the yz plane. The green lines represent the quadrupole field lines around the magnetic field minimum.

These expressions are valid as long as the distance of the trap to the Z-wire remains small compared to the length of the line. We observe that the smaller is the bias field in the x-direction, the higher is the atomic confinement. In our experiments, this bias field has a value of 9.5 G. The depth of the trap, in energy terms, is given by

$$\Delta E = g_F m_F \mu_B \sqrt{B_x^2 + B_\perp^2} - B_x \tag{II.8}$$

which is proportional to the difference between the modulus of the total bias field $\sqrt{B_x^2 + B_\perp^2}$ and the magnetic field at the trap center B_x.

In our trap, the confinement in the x-direction is realized by the arms of the Z-shaped wire. Since the current flows in the same direction in the three parts of the Z, the minimum of the field in that direction is already positive. By changing the value of the bias B_x field, we are able to increase the field at the trap center as well as the dimension of the trap and the oscillation frequencies in that direction, as shown in Figure II.6.

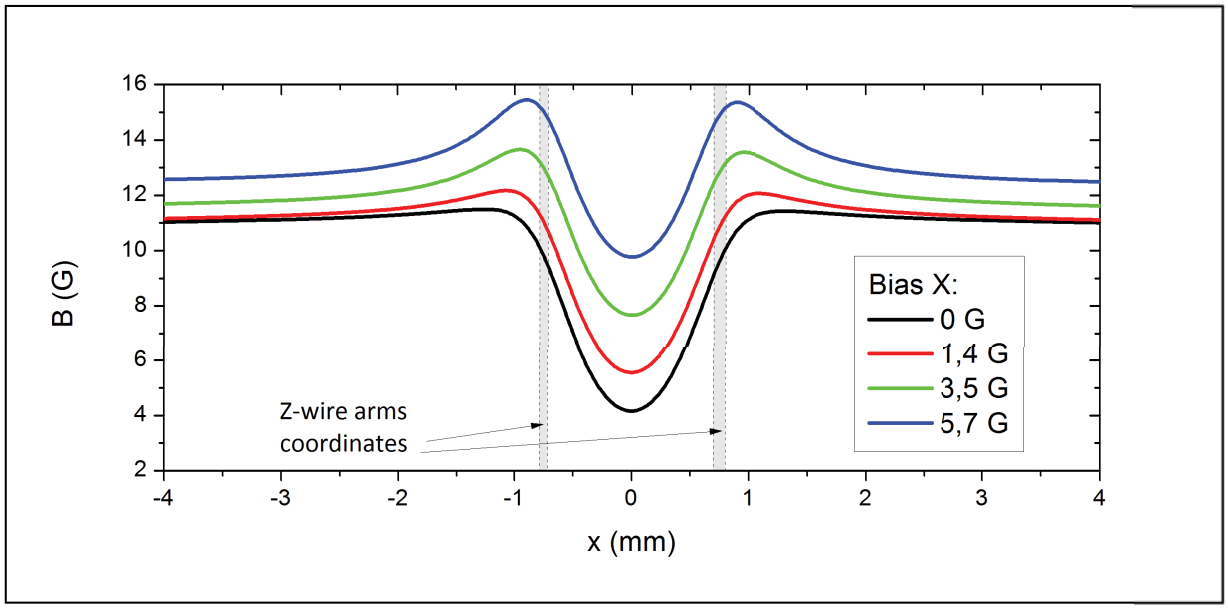

Figure II.6: Trapping potential in the x direction in the Ioffe-Pritchard on-chip trap, for various B_x bias field values. For this calculation, $B_y = 0$ G and $B_z = 11$ G.

II.3 Laser and imaging system

II.3.1 $D2$ transition line of ^{87}Rb.

The Rubidium 87 transitions involved in the cooling and trapping are shown in figure II.7 [31]. We work with the hyperfine transition $|F = 2\rangle \rightarrow |F' = 3\rangle$ of the $D2$ line for all cooling, trapping, imaging and optical pumping process.

The trapping and cooling in the 2D-MOT and 3D-MOT stages are performed with a laser detuned by -20 MHz with respect to the transition $|F = 2\rangle \rightarrow |F' = 3\rangle$. It is called the *cooling beam* in figure II.7. Later in the sequence, in one of the mirror-MOT stages, this detuning is changed in order to increase the density of the atomic cloud in phase space.

A probe bean is set in resonance with the transition mentioned above for observing the atoms. For the optical pumping, which pumps the atoms in the level $|F = 2, m_F = 2\rangle$ of the ground state just after the optical molasses stage and before turning on the magnetic trap, a laser beam is needed at resonance with the $|F = 2\rangle \rightarrow |F' = 2\rangle$ transition. It is referred to as the *Zeeman pumper* in the figure.

In the cooling and trapping process, some atoms can decay in the $F = 1$ state, impervious to the previously mentioned laser beams. Hence, a repumper beam in needed, tuned to the $|F = 1\rangle \rightarrow |F' = 2\rangle$ transition as can be seen in figureII.7.

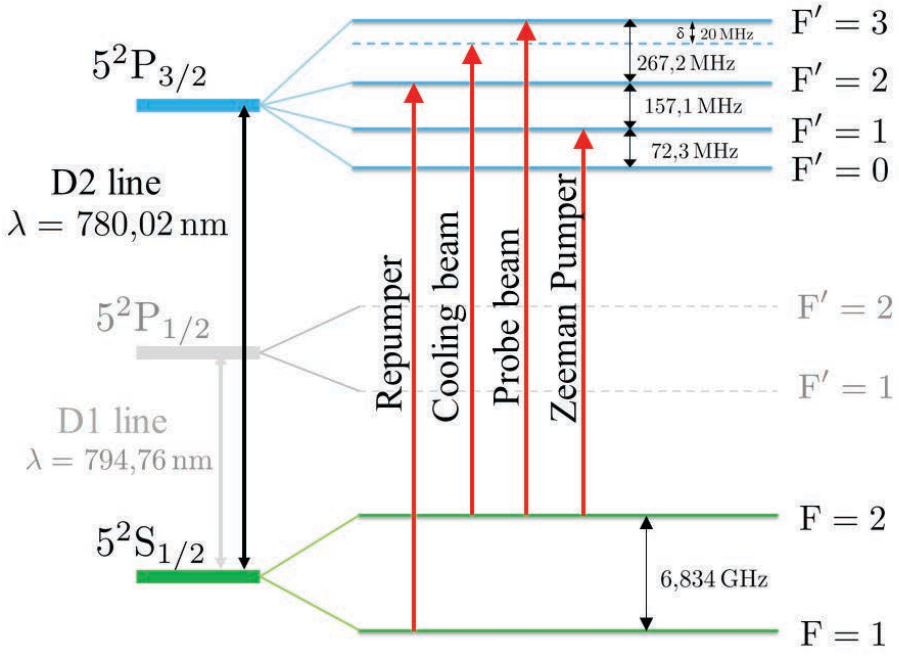

Figure II.7: Fine and hyperfine structure of ^{87}Rb. In our experiment, we make use of the $D2$ line transitions for the optical cooling and trapping, as well as for the imaging system and for the Zeeman optical pumping.

II.3.2 Imaging the atoms

We need to observe the atoms. We use fluorescence and absorption images. Fluorescence is very useful to observe the atomic clouds in real time during the MOT stages. We use it routinely to check if the cooling lasers are properly locked.

For precise measurements of atom number, cloud size, temperature, etc, absorption imaging is preferred. We observe the absorption of a laser beam resonant with the cooling transition $|F = 2 \rightarrow F' = 3\rangle$ as shown in figure II.7. The absorption signal measures the cloud optical density integrated along the beam propagation direction. This signal gives us complete information about the total atom number when the on-resonance cross section is well known.

We use two optical paths in order to observe the atoms either from a front point of view (xz plane) or from the side (yz plane). We have thus installed two CCD cameras, one Micromax and one Photonmax respectively (Princeton Instruments), both designed for low intensity light imaging with low noise and fast image acquisition. Each camera has a pixel matrix of 512×512. The optical paths as well as the cameras are shown in figure II.8. The side-view probe beam enters from the $-x$-window with an angle w.r.t the axis of 6.7^0. This beam is reflected by the chip an exits by the $+x$-window toward the Photonmax camera, where the light is collected and processed. The front-view probe beam enters by

the window directly perpendicular to y axis, with an angle of 5.4^0 with respect to this axis. It is reflected by the surface and goes out by the same window towards the Micromax camera. The characteristics of each probe beam are given in table II.1.

Characteristic	Side-view probe beam	Front-view probe beam
Probe power	100 μW	46 μW
Repumper power	10 μW	6 μW
Radius at e^{-2}	3.5 mm	2.5 mm
Average intensity	0.26 mW/cm^2	0.24 mW/cm^2

Table II.1: Probe beams characteristics. The mean intensity is determined over the radius at e^{-2}.

The scaling factors between the camera pixels and the actual dimensions of the cloud are the following: for Micromax (front view) 7.5 μm/pixel and for Photonmax (side view) 9.2 μm/pixel. As can be seen in figure II.8, all optical elements are placed outside the cryostat, i.e. at more than 150 mm from the atomic position. This is a severe limitation of this cryogenic set-up for the spatial resolution of the imaging system.

Since the probe beam is reflected on the chip surface, we must deal with a double image of the atomic cloud. This effect is explained in figure II.9, which shows how the atomic cloud absorbs the light from the probe beam both before and after its reflexion on the chip, providing information on the cloud to the chip surface distance d. The separation between the two images on the camera is $2d\cos\theta$, where θ is the angle between the probe beam and the chip.

We can thus extract conveniently the cloud-to-chip distance d from the side view imaging on the Photonmax camera. An example is shown in figure II.10, presenting a cloud in an optical molasses. The distance of the molasses to the chip surface is $900\,\mu$m.

For the front view in the Micromax camera, the reflexion effect is also present and we also have two images. However, the projection angle θ' is such that $\cos\theta' = 0.095$. For a cloud at $d = 500\,\mu$m the separation between the two images is $47\,\mu$m only. In most cases, we only observe a fake elongation of the atomic cloud and not a proper separation between the two images.

II.3.2.a Determination of the atom number

Let us make more precise the calibration of the atom number from the absorption image. We consider, for the sake of this discussion only, a laser beam propagating in an abstract z-direction. We consider the case of a laser beam well below the saturation of the atomic transition, i.e. $I \ll I_{sat}$. The light intensity after passing through the atomic cloud is given by the Beer-Lambert law:

$$I(x,y) = I_0(x,y)e^{-\int dz\sigma n(x,y,z)} \tag{II.9}$$

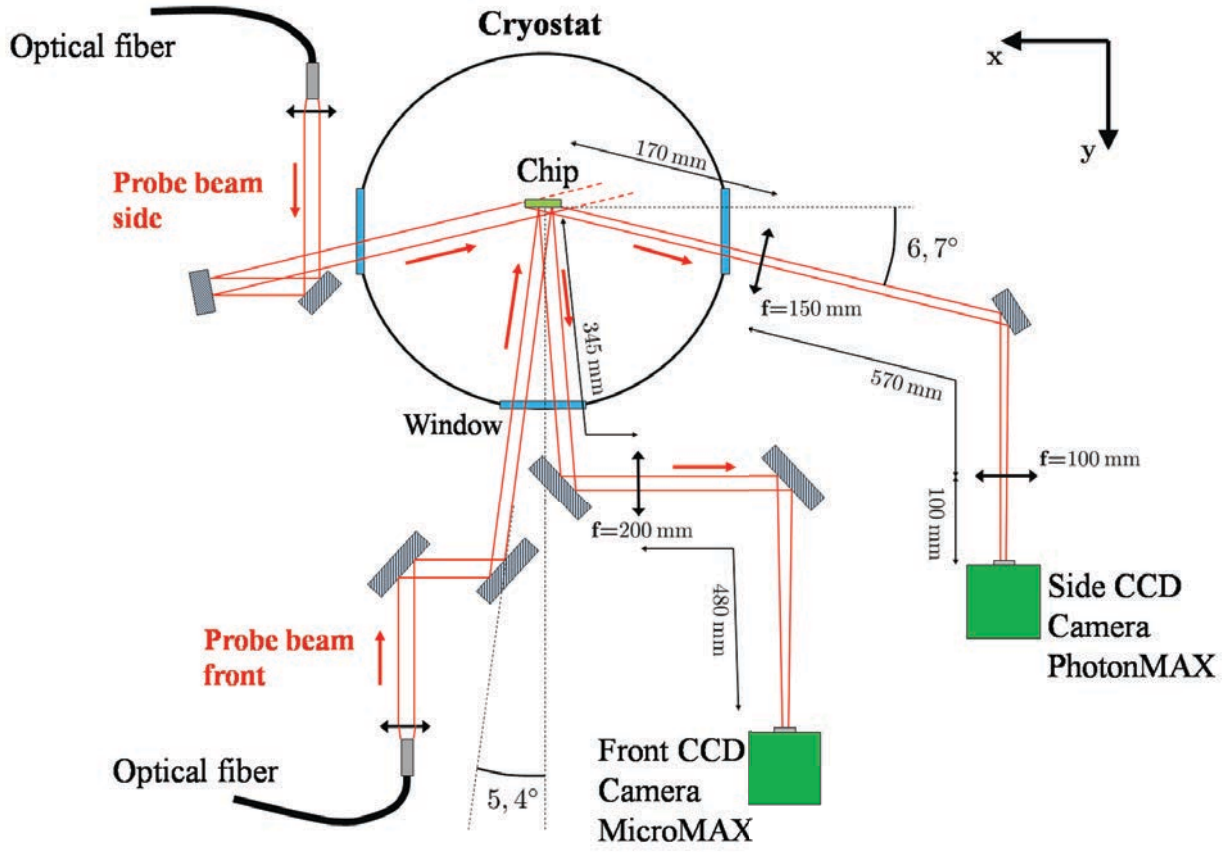

Figure II.8: Complete scheme of the imaging system. Two CCD cameras, Micromax and Photonmax, allow the visualization of the atomic ensemble from the front and the side point of views respectively.

where I_0 is the incident intensity, $\sigma = \sigma(\delta)$ is the atomic cross section, δ the detuning with respect to the resonant transition $|F = 2\rangle \rightarrow |F' = 3\rangle$, and $n(x, y, z)$ is the atomic density at the point (x, y, z). We assume that the probe beam polarization has been optimized. The on-resonance ($\delta = 0$) scattering cross section is given by

$$\sigma(\delta = 0) = \sigma_0 = \frac{3\lambda^2}{2\pi} \tag{II.10}$$

where $\lambda = 780nm$ is the wavelength of the atomic transition.

The absorption images provide thus access to $\int dz\sigma n(x, y, z)$, provided we can get a reliable value for I/I_0. It is necessary to remove the background noise of the camera and the stray light. We thus estimate the density based on three images: the light intensity in the presence of the atoms $I_{at}(x, y)$, the probe beam intensity when atoms are not present, $I_{wo}(x, y)$, and the intensity of the background light I_{BKG}, which is independent of the

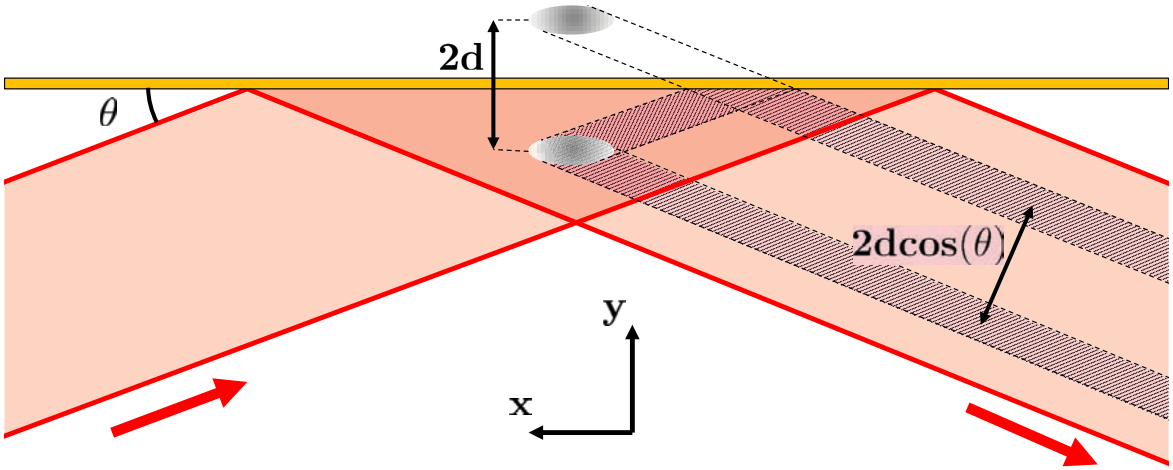

Figure II.9: Scheme explaining the double image formed on the camera due to the reflection on the probe beam on the chip surface.

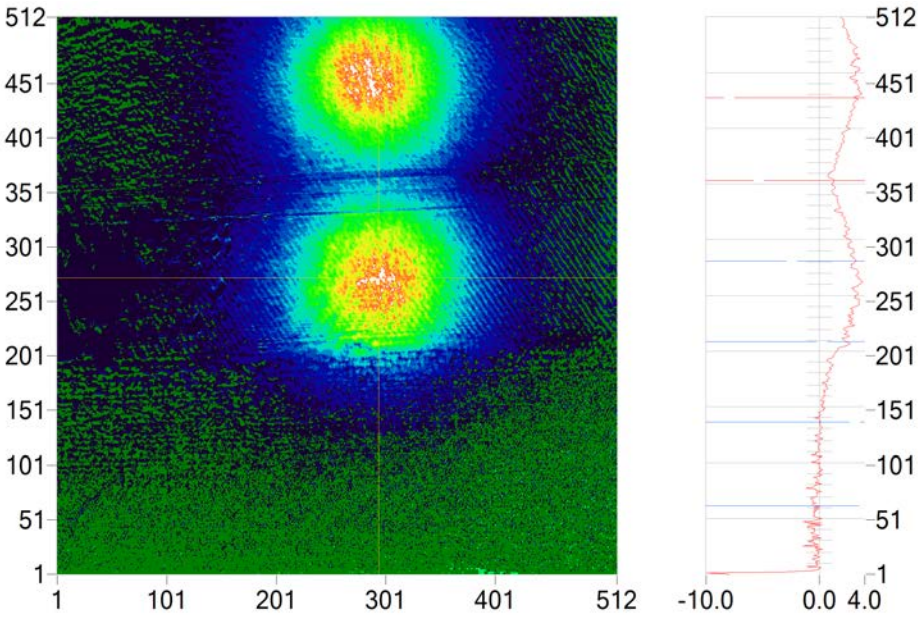

Figure II.10: Absorption image of an optical molasses. It has been taken after a 8 ms time of flight. The chip-to-cloud distance is inferred from this image to be 900 μm.

probe beam. The optical density is the obtained as

$$\text{o.d}(x,y) \equiv \int dz \sigma_0 n(x,y,z) = -ln \frac{I_{at}(x,y) - I_{BKG}(x,y)}{I_{wo}(x,y) - I_{BKG}(x,y)} \tag{II.11}$$

and the density at the point (x, y, z) can be written as

$$\int n(x,y,z)dz = \frac{1}{\sigma_0}\left(ln\frac{I_{wo}(x,y) - I_{BKG}(x,y)}{I_{at}(x,y) - I_{BKG}(x,y)}\right). \tag{II.12}$$

The normalization condition connecting the total atom number with the density is

$$\int n(x,y,z)dxdydz = N_{at} \tag{II.13}$$

and hence, using equation (II.12), we get

$$N_{at} = \frac{1}{\sigma_0}\int\left(ln\frac{I_{wo}(x,y) - I_{BKG}(x,y)}{I_{at}(x,y) - I_{BKG}(x,y)}\right)dxdy. \tag{II.14}$$

[47] shows how to take these effects into account by scaling the absorption cross section, replacing σ_0 by σ_0/α. The calibration of the α scaling factor implies taking absorption images of the same sample for different laser intensities, all above the saturation intensity I_{sat}. The details of the measurements done in order to obtain α are reported in reference [42] chapter II. We have found it to be $\alpha = 2,06 \pm 0.1$. We finally take into account the scaling factor between the camera image and the actual cloud g, 10μm/pix for photonMAX. The atom number is finally given by

$$N_{at} = \frac{g^2\alpha}{\sigma_0}A \tag{II.15}$$

where A is the bidimensional Gaussian fit of the obtained image.

II.3.2.b Temperature measurement

We measure the temperature of the cloud using the *time of flight* technique. After turning off the magnetic fields providing the atomic confinement, the atoms fall down due to the gravity and experience an expansion, which is temperature-dependent. The root mean square velocity the x direction, for instance, is

$$\Delta v_x^2 =< v_x^2 >= \frac{k_B T}{M} \tag{II.16}$$

and the root mean square size of the cloud, after a time of flight t, is

$$\Delta x^2(t) =< x^2 > (t) = \Delta x^2(0) + \Delta v_x^2 \Delta t^2 = \Delta x^2(0) + \frac{k_B T}{M}\Delta t^2. \tag{II.17}$$

By measuring the gaussian profile of the cloud for different times of flight, the temperature can be calculated together with the initial size $\Delta x^2(0)$.

II.4 From the 2D-MOT to the BEC: sequence for the optical cooling and trapping.

In this section, we describe the successive stages for arriving at a Bose-Einstein condensate starting from the atoms trapped in the 2D-MOT. The details of the optimization of each step can be found in [40] and [39].

II.4.1 The source of slow atoms: 2D-MOT

At the very beginning, the atoms are trapped in the x- and y-directions by a 2D-MOT, placed below the cryostat. A more detailed scheme of this trap is shown in figure II.11. It is a commercial device designed and fabricated by the SYRTE laboratory (Systèmes de Référence Temps-Espace) described in details in [48]. The MOT chamber is attached to a drift tube, connected to the cryostat. The connection is made through at 1.5 mm coupling hole, leaving the slow atomic beam pass and providing a differential vacuum isolation between the relatively high pressure in the MOT region and the ultra-high vacuum of the upper part, connected via a pressure-valve to the cryogenic environment. Two ion pumps are connected to the system, one at the top and one at the bottom of the assembly. The ion pump at the bottom indicates typically a pressure of 4×10^{-6} mbar when the Rb cell is heated up to its working temperature $T = 60\ ^0$C. The ion pump at the upper part indicates a much lower pressure, the minimum one 8×10^{-10} mbar for the ion pumps, since it is localized closer to connection point with the cryostat.

Figure II.11(a) presents a detailed scheme of the MOT assembly. We see the coils for the quadrupole magnetic field and the three laser beams with their reflections. The polarizations are indicated in the figure. The 2D-MOT has four windows in the upper part for visualizing the atomic beam by fluorescence, once the atoms have been slowed down in x and y- direction. These slow atoms form a collimated atomic bean which passes through the 60 cm separation between this stage and the chip in less than 100 ms. The laser beams needed for the MOT are carried by two optical fibers as can be seen in figure II.11(b). Both beams are collimated on a diameter of 24 mm (at $1/e^2$). Then, each beam is divided into three beams by identical polarizer beam splitter cubes and half-wave plates, creating three stages of two-dimensional trapping. Quarter-wave plates change the polarization to circular as needed for the trapping (panel (a)). Each fiber input power is of 60 mW of master laser, 7 mW of repumper laser for one arm and 1 mW for the other. The asymmetry in the repumper comes from the construction of the optical table and it has not influence at all on the trapping efficiency.

II.4.2 The mirror MOT

When the atoms arrive in the cryogenic environment, they are trapped in a mirror-MOT [49], loaded from the slow atomic beam for 3s. Figure II.12 shows the scheme of this MOT (with the lasers, their polarization, the coils..) and an actual picture of the set-up. As

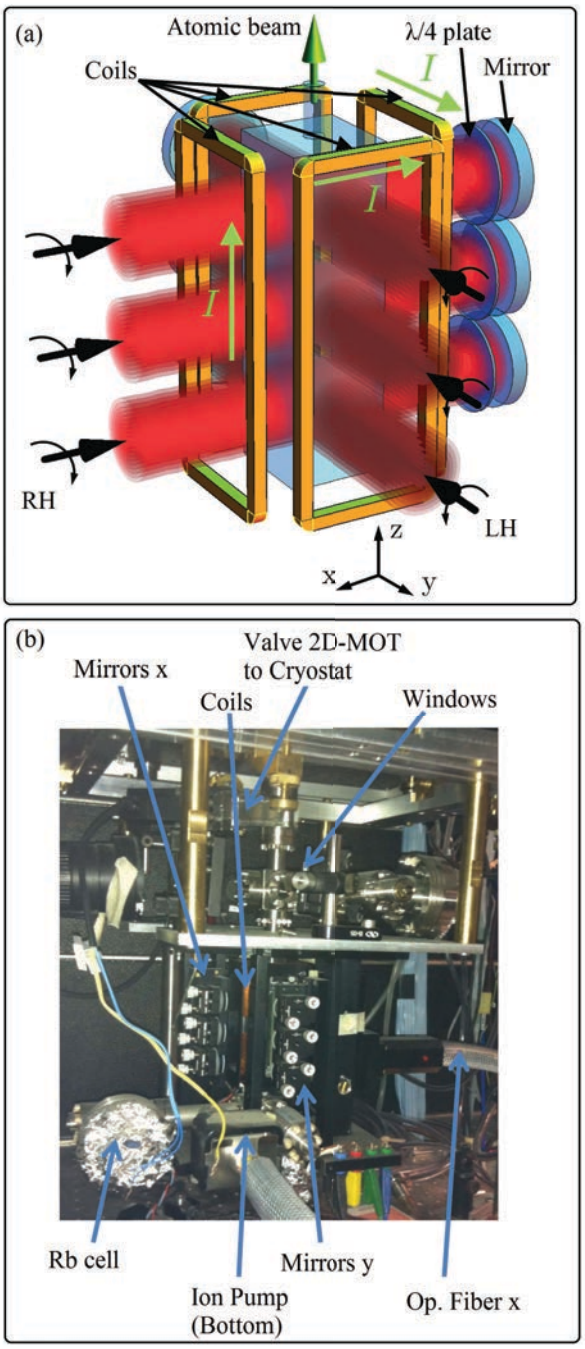

Figure II.11: **(a)** 2D-MOT scheme. It consists in an UHV chamber, connected via a valve to the cryogenic environment, with three laser beam stages. The polarization as well as the direction of the current in the coils are indicated (RH: Right Helicity defined by the light propagation direction). The beams are retro-reflected by mirrors installed beyond the chamber, and the return polarization is controlled by lambda/4 plates. **(b)** Photograph of the 2D-MOT at the bottom of the cryostat. We can see the the ion pump at the bottom (the upper one is hidden by the windows), the windows, the valve, the coils, the *Rb* cell, etc.

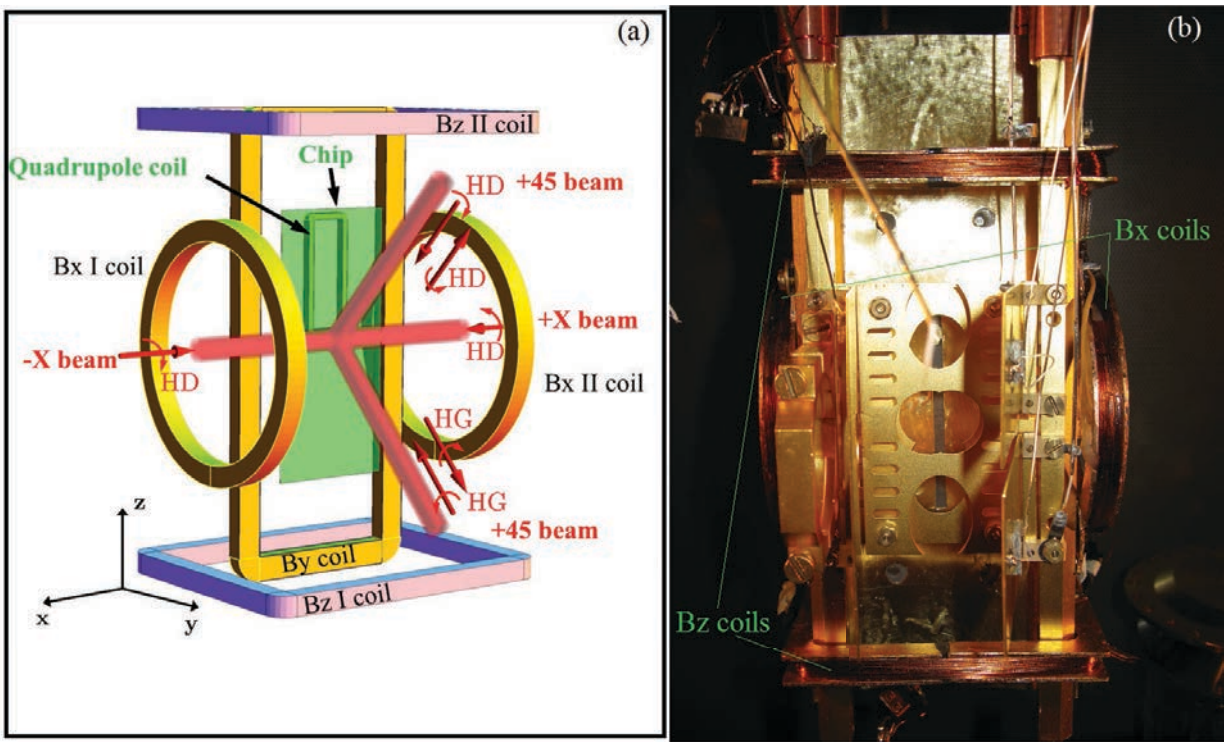

Figure II.12: **(a)** Mirror-MOT scheme with the laser configuration. Polarization is indicated for each beam. RH: Right Helicity and LH: Left Helicity. The coils create a tunable homogeneous bias field at the atomic position aligned in the three space dimensions: one pair of square coils for the z-direction, one pair of circular coils for the x-direction and a single coil for the y-direction, located at 5.4 mm behind the chip. In order to create a magnetic quadrupole field, a *Quadropole Coil* is placed at 2.8 mm behind the chip. **(b)** Photograph of the set-up viewed from the front. The chip, as well as the detection system (Channeltron) and the *Rb* dispenser boxes, were not installed. We observe the coils in the x- and z-direction. The holes in the electrodes (used for the Rydberg atoms detection) allow access for the cooling, imaging and excitation beams.

mentioned before, we use a mirror MOT because it requires only four beams to cool down the atoms, since it uses the chip surface as a mirror. A normal 3D-MOT requires six beams to realize the 3D confinement [50, 43].

Two counter-propagating beams are sent parallel to the chip, in the $\pm x$-direction. Two other counter-propagating beams are sent with an angle of $\pm 45^0$ from the y axis in the yz plane. Both are reflected by the chip. All beams are fibre-coupled to the laser system on the optical table. The power sent in each of the four fibers is 6.8 mW, superposed with 1 mW of repumper light. Each beam has a diameter at $1/e^2$ of 5.7 mm, corresponding to an average intensity of 27 mW/cm^2 in a disk having that diameter.

Figure II.12 shows also the coils generating the magnetic quadrupole field needed for the atomic confinement. The **bias field $\mathbf{B_z}$** is created by two square coils, $B_z\, I$ and

$B_z\,II$, in a Helmholtz configuration with z as their common axis. The lower U-part of the **quadrupole coil**, made of 19 loops and mounted $2,8$ mm behind the chip, creates together with $\mathbf{B_z}$, the required quadrupole field. Additional homogeneous bias fields in the x and y directions can be created by two circular coils aligned on the x axis and a single coil placed at 5.4 mm behind the chip for the y-direction.

Figure II.13(a) shows the magnetic field map created by the lower U-shaped part of the quadrupole coil superposed to a uniform bias field in the z direction. We observe the creation of a quadrupole field in the yz plane. The position of the zero is the trapping location of the atoms. It can be shifted at will by changing the value of B_z or by adding a uniform B_y bias. Similarly, the arms of this coil create a field in the x direction which is represented in figure II.13(b). There again, there is a zero in the field whose position can be adjusted at will by changing the uniform bias field, B_x. In a nutshell, by adjusting the three components of the uniform bias field, we can change nearly at will the position of the atomic cloud trapped in the mirror MOT.

The total number of atoms trapped in a 3 s period is estimated from the fluorescence signal to be of the order of a few 10^8, with a temperature of the order of $400\,\mu$K. Absorption imaging is not possible at this stage since the atoms are too hot and the cloud too large (diameter in the millimeter range) for the magnification of the imaging system. This cloud size is much too large to provide a good transfer to the tight on-chip Ioffe-Pritchard magnetic trap. Another cooling stage in a tighter MOT is thus mandatory.

II.4.3 The U-MOT

The second MOT stage ('U-Mot-far') uses the same laser beams, but the quadrupole field is generated by a current flowing in the U-shaped conductor on the chip (see figure II.3). We turn off the current in the quadrupole trap and turn on simultaneously the current in the on-chip MOT in about 20 ms, while the bias fields are optimized to match the initial positions of the two MOTs. Refer to figure II.14, presenting the timing of the complete sequence, for the precise definition of this switching procedure. The transfer efficiency from the QUAD-MOT to the U-MOT-far is hard to estimate. By the fluorescence images we can infer that it varies from 10 to 40%. A large part of the loss is due to the fact that the spacing between the arms of the quadrupole coil is 11 mm, while the arms of the on-chip U-wire are separated by 1.7 mm only. The trapping volume is thus considerably lower in the U-MOT

The atomic cloud is then compressed and brought nearer to the chip surface, at a $d = 600\,\mu$m distance. This is obtained by changing the parameters of the MOT from the U-MOT-far configuration to a U-MOT-near one. To this aim, we simultaneously reduce the current in the U wire and the bias fields in 20 ms again (figure II.14).

Simultaneously, we increase the laser detuning δ from -3.3Γ to -9Γ, i.e. from -20 MHz to -72 MHz, in order to increase the density in the centre of the trap, a clear asset for the final transfer in the tight Ioffe-Pritchard trap. In fact, in a simple model of the MOT operation [51, 52], the density is proportional to δ. This is due to the competition between the trapping and cooling forces, which range as $1/\delta$, and the repulsive force due to photon

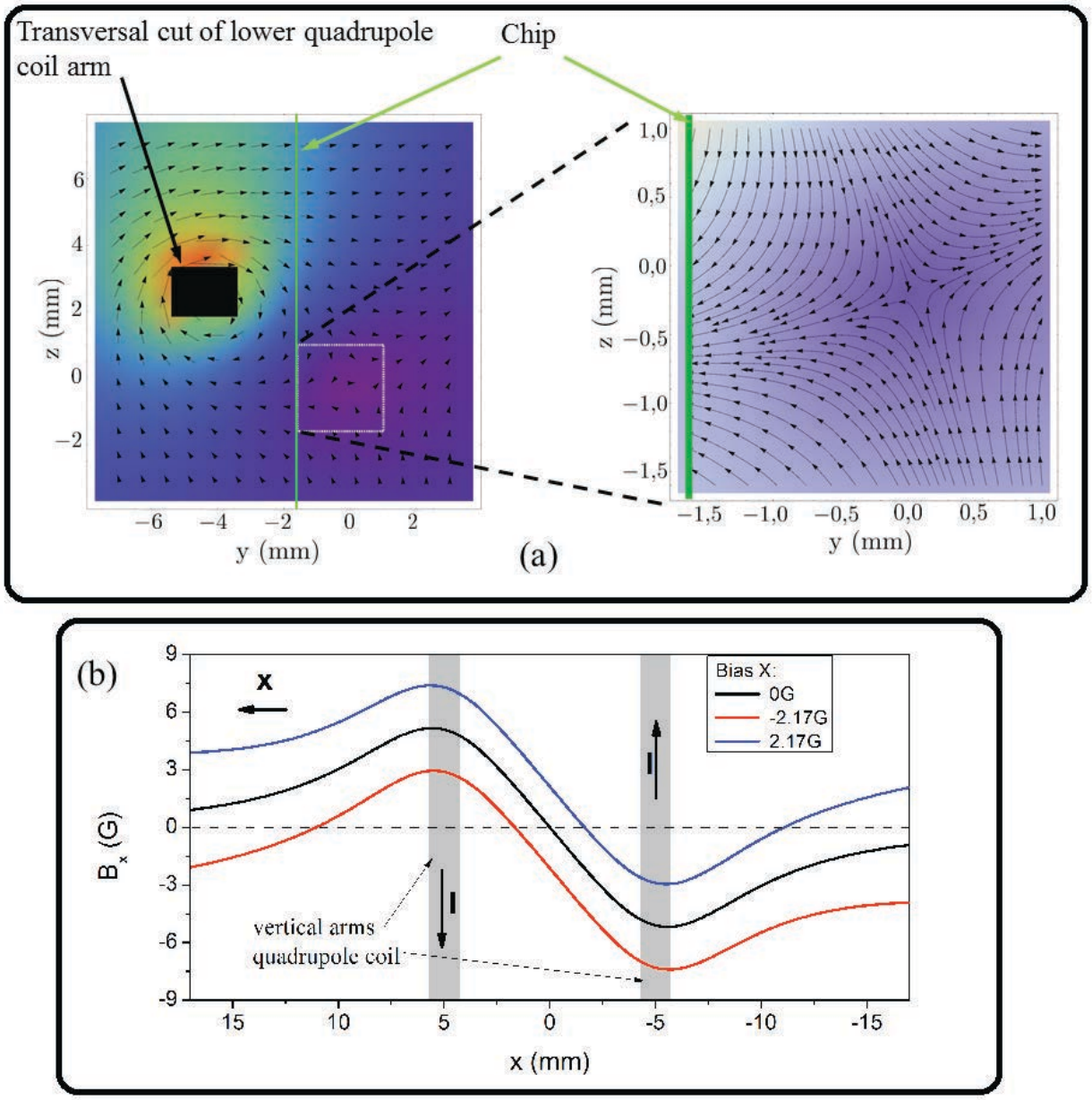

Figure II.13: **(a)** Projection in the plane yz of the quadrupole magnetic field created by the lower part of the Quadrupole Coil (the section of its lower arm is shown in black), with a 3.5 A current and a uniform bias field $B_z = 14.7$ G in the z-direction. The chip is located at the position of the green line. The color scale gives the field modulus projected in the plane. **(b)** Field created by the arms of the quadrupole coil along the x-direction. When the bias field B_x is changed, the zero point of the field in x is changed as well.

diffusion which varies as $1/\delta^2$. The second force is related to the fact that spontaneous photons radiated by an atom can be reabsorbed by a neighboring atom. An optimum in

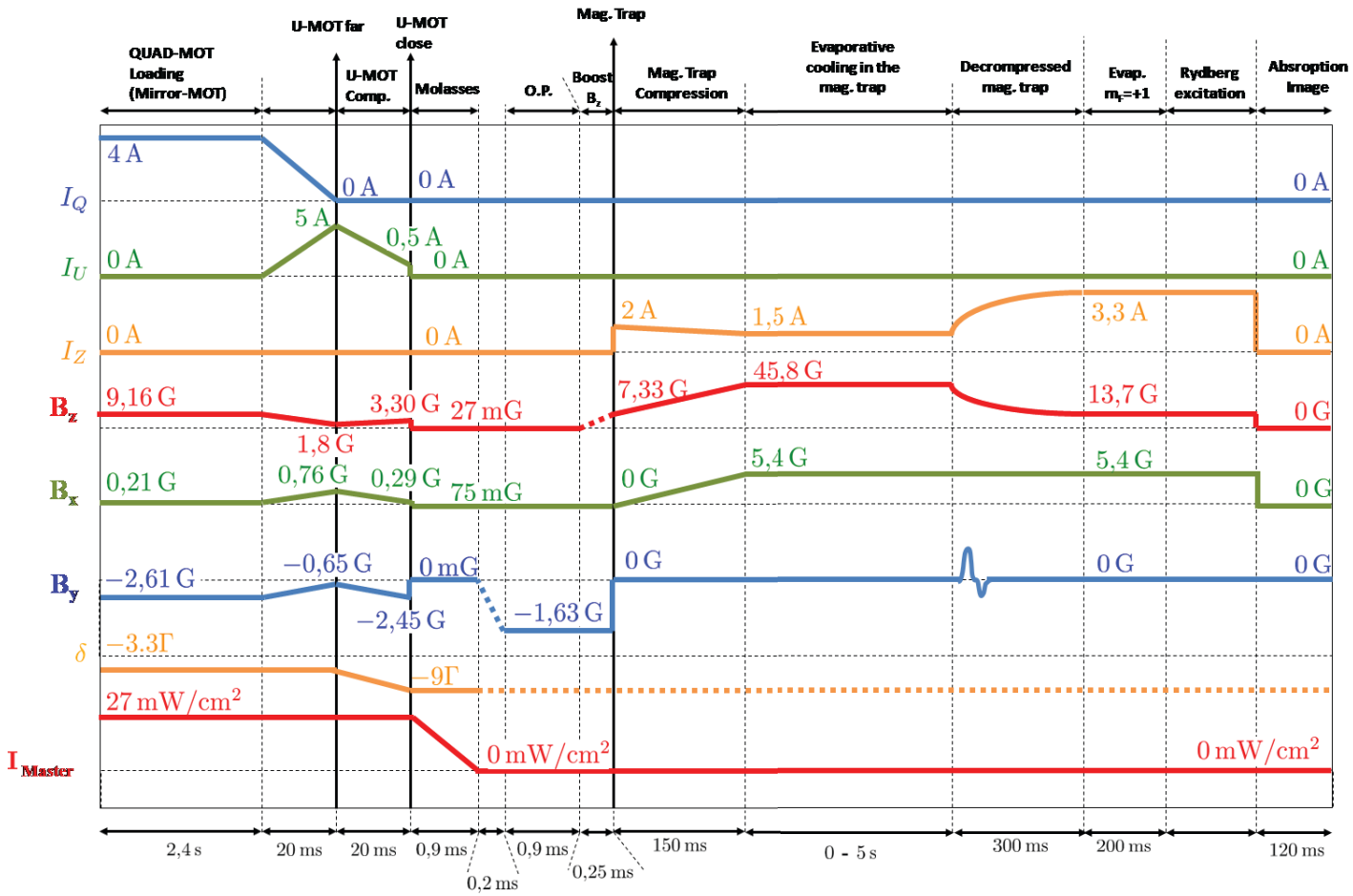

Figure II.14: Complete sequence from the 3D-mirror MOT loading to the BEC, including the Rydberg excitation and the imaging by absorption. The graph shows all relevant currents, bias fields, the detuning δ w.r.t. the $|F = 2\rangle \rightarrow |F' = 3\rangle$ transition and the power of the master laser used for cooling and trapping.

density can thus be found. We have determined it experimentally, by scanning the final value of δ while measuring the transfer efficiency into the final magnetic trap.

II.4.4 Optical molasses and optical pumping

At the end of the compression, an optical molasses [53] of 0.9 ms duration is needed in order to cool the atoms further. During the molasses, the laser power is gradually reduced to zero (figure II.14). Each bias coil is optimized to compensate the residual field at the atomic position, since the molasses require a good cancellation of the magnetic field. At the end of this short molasses sequence, the atomic cloud has a temperature of $13\,\mu$K and contains 6.4×10^7 atoms. Details about the optimization of this part of the sequence can be found in [39].

For the magnetic trapping, it is best to transfer all the atoms into the magnetic sublevel with the largest Zeeman effect, $|F = 2, m_F = +2\rangle$. We thus perform an optical pumping stage, just after the extinction of the molasses lasers. A bias field in the y-direction, $B_y = 1.63$ G, is turned on in order to lift the Zeeman degeneracy A Zeeman pumper beam, in resonance with the transition $|F = 2\rangle \rightarrow |F' = 2\rangle$, is sent for another 0.9 ms along the $-y$-direction. The polarization is σ^+ and the average intensity is $230\,\mu\mathrm{W/cm^2}$. The beam is indeed reflected by the chip but the polarization viewed by the atoms for the reflected beam is also σ^+. The repumper beam is still needed at this stage and is sent along the path of the 3D-MOT beams at very low power.

II.4.5 Transfer into the magnetic trap

After optical pumping, the atoms are transferred to the Ioffe-Pritchard magnetic trap created by the Z-wire. This is a delicate process. In particular, the magnetic field should never cancel (in order to avoid Majorana losses) while switching from the B_y directing field used for the optical pumping stage to the final B_x of the magnetic trap. We thus proceed in the following way. A bias field $B_z = 7.33$ G is rapidly (250 ms) turned on (this bias field together with the current in the Z wire will create the trapping potential). This fast turn on is facilitated by a capacitive boost circuit. The corresponding part of the sequence is thus denoted as 'boost' on figure II.14.

We can then suddenly switch off the bias field in y while we set a current of 2 A in the Z wire to complete the Ioffe-Pritchard trap. The field in the bottom of the trap is non-zero even though we do not apply a current in the B_x coils. The field created by the long parts of the Z-wire in this direction is strong enough to avoid Majorana losses.

The atomic cloud can then be adiabatically compressed and brought closer to the chip. In order to reach the BEC, we compress as much as possible in order to increase the collision rate for the evaporative cooling [54, 55]. The tighter compression sequence lasts 150 ms (figure II.14). We decrease the current in the Z-wire while raising the B_Z bias up to 45.8 Gauss. In the meantime, we apply a 5.4 Gauss uniform bias in the x direction to raise the bottom of the trap. This is important for the evaporative cooling sequence.

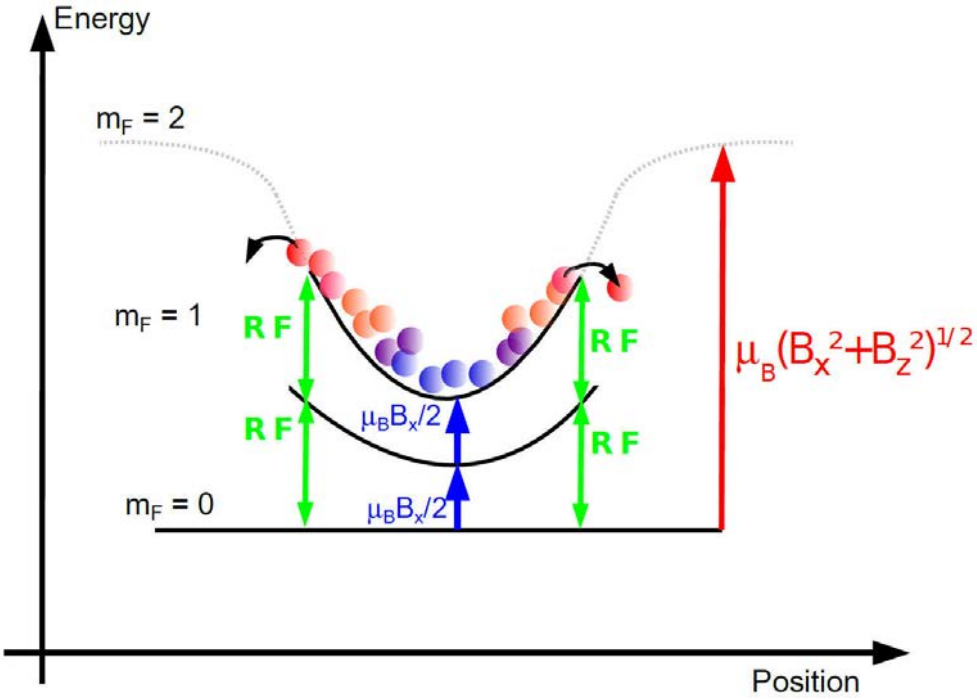

Figure II.15: Scheme for the evaporative cooling. The RF signal is sent through the KM chip wire (figure II.3). This RF induces transitions (green arrows) from the level $|F = 2, mF = +2\rangle$ to the others Zeeman sublevels (we do not show all of them here).

With this sequence, the magnetic field, and hence the quantization axis, has been rotated from the y direction to the z one, and from the z one to the final x direction slowly enough for the atoms to adiabatically follow this rotation. All atoms are thus finally in the $|F = 2, mF = +2\rangle$ state with respect to the x quantization axis. The final trap is located at $80\,\mu m$ from the chip surface, and the trap frequencies are $(w_x, w_y, w_z) = 2\pi \times (24, 3400, 3400)$ Hz. The total atom number is 1.9×10^7, corresponding to a transfer efficiency from the molasses of 30%. The cloud temperature is $45\,\mu$K. The distance from the chip surface is $550\,\mu$m .

II.4.6 Getting a BEC: evaporative cooling

The evaporative cooling technique is ideal to increase the density in the phase-space up to the degenerate state (BEC). It relies on a progressive truncation of the trapping potential in order to get rid progressively of the hottest atoms in the trap, effectively cooling the remaining ones. This principle is outlined in figure II.15. We apply on the atoms a radiofrequency field (RF) inducing transitions between the original trapped level $|F = 2, m_F = +2\rangle$ and the other Zeeman levels. This RF signal passes through the KM wire of the chip (in blue in figure II.3). Since the Zeeman effect is almost linear with the fields at stakes, the RF induces cascade transitions towards levels with zero or negative magnetic

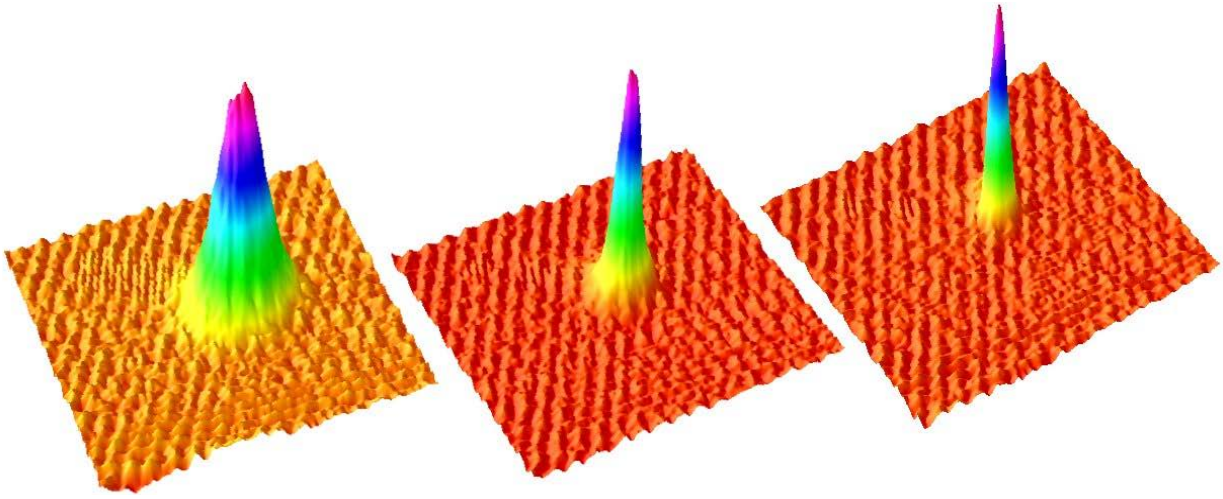

Figure II.16: BEC transition on the superconducting atom chip. Three absorption images are shown (after a time of flight), above, at and well below the Bose Einstein condensation temperature.

quantum numbers which are rapidly expelled from the trap.

At each step of the evaporative cooling, the RF is resonant with the Zeeman transitions in the largest magnetic field experienced by the atoms in the trap. The RF thus only addresses and expels the hottest atoms. The remaining ones are thus, on the average, colder, and rapidly thermalize if the collision rate is large enough (hence the importance of operating in a tightly compressed trap). When the RF frequency is properly slowly decreased, decreasing thus the maximum atomic energy, the cooling is faster than the evaporation and the phase space density increases up to the condensation point. This process is clearly analogous to the cooling of a coffee cup by evaporation, explaining the 'evaporative cooling' name coined for it.

A critical optimization is the time-dependence of the RF frequency. We start with a value 11 MHz above the transition in the minimum magnetic field and reduce it in linear segments down to a value very close to the transition in the bottom of the trap. Each segment in this frequency ramp is carefully optimized by measuring the final phase space density. The procedure and the final ramp chosen, with a total duration of 5s, are described in [39].

Figure II.16 presents absorption images of the Bose Einstein condensation, taken after 16.5 ms time of flight for different values of the final RF frequency. The first image, with a rather high final frequency, is that of a thermal cloud in the trap. The second presents a Bose Einstein condensate immersed in a residual thermal cloud. Finally, the third image, taken for the lowest final RF frequency, corresponds to a nearly pure BEC, containing about 2×10^4 atoms.

The RF spectroscopy is also essential to measure precisely the B_x magnetic field in the bottom of the trap. For this determination, we shine a 200 ms RF pulse, with a fixed frequency and the maximum available power. We decompress the trap and measure the

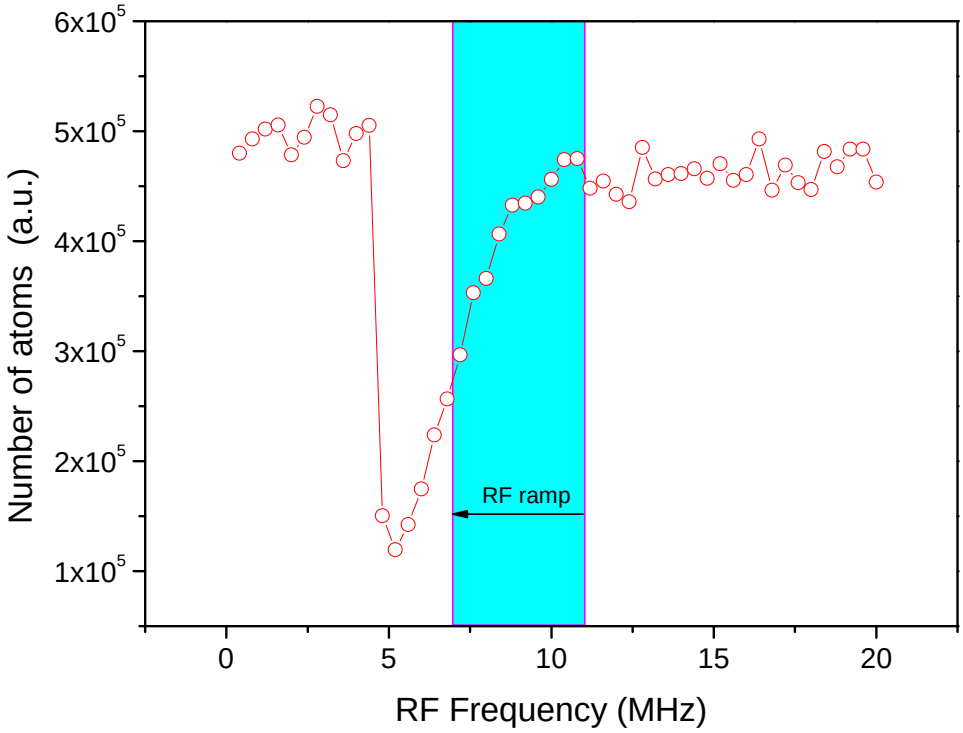

Figure II.17: RF spectroscopy to determine the bottom of the trap. Final atom number versus the frequency of an RF pulse. The blue range corresponds to the span of the RF frequency ramp used for evaporative cooling.

number of atoms remaining as a function of the RF frequency. The results are plotted in figure II.17. We observe a clear resonance in the atomic losses. The minimum frequency corresponds to the evaporation of those atoms which are located near the bottom of the trap. The sharp edge on the low frequency side of this resonance clearly defines the minimum magnetic field in the trap, which we can measure here in frequency units within the width of the RF generator (50 kHz).

II.4.7 Decompressing and moving the magnetic cloud

After the evaporative cooling, we have a very compressed cloud quite close to the chip surface. We need to decompress the magnetic trap and to move it away from the chip to perform systematic studies of the spectroscopy of the atomic cloud. This decompression should be performed in an optimized way to avoid heating the atomic cloud. This is not totally straightforward in our geometry, contrary to previous theoretical [56, 57, 58] and experimental [59] works, since our trap has non degenerate frequencies.

Moreover, we have observed a heating phenomena in the compressed trap. The measured temperature raises linearly by $2\,\mu$K/s. We have not identified the origin of this problem, which is no longer observed at $200\,\mu$m from the chip. The trap decompression

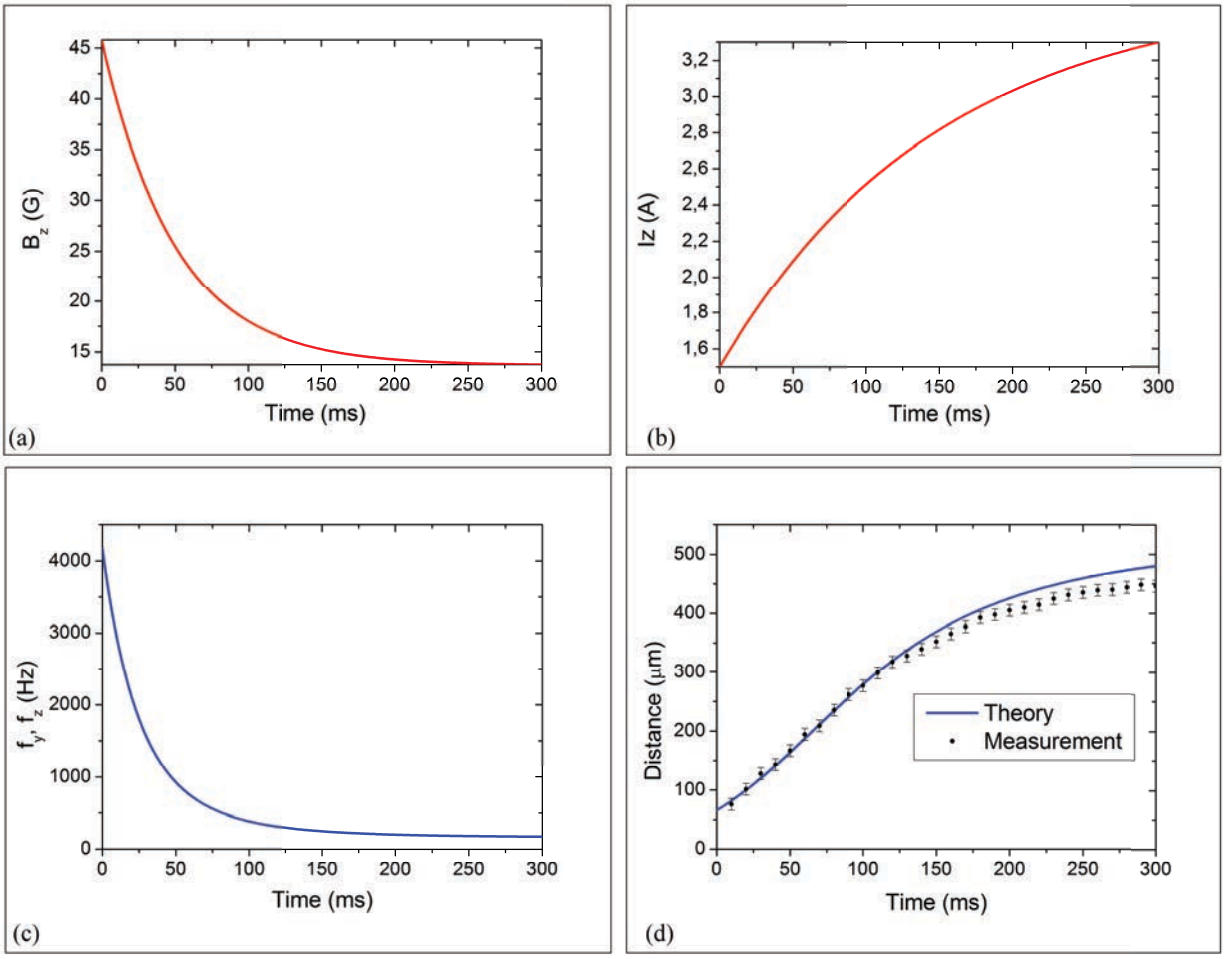

Figure II.18: **(a)** and **(b)** show the ramps for B_z for the current in the Z-shape wire for the trap decompression. **(c)** shows the corresponding evolution of the frequencies $\omega_x/2\pi$ and $\omega_z/2\pi$ ($\omega_\perp/2\pi$). **(d)** shows the atom-to-chip distance d, both calculated from the trap geometry (solid line) and measured by direct imaging (points).

should thus move rapidly away from the chip.

We have painstakingly optimized the decompression stage by minimizing the final temperature and also the residual oscillations of the cloud's center of mass due to a non-adiabatic evolution. Figure II.18 shows typical decompression ramps. They give us a decompressed trap at $d = 455\,\mu$m from the chip surface, with frequencies $(\omega_x, \omega_y, \omega_z) = 2\pi \times (37(1), 107(1), 121(1))\,Hz$. The final currents are $I_z = 3.3$ A and the bias field in z 13.7 G.

As shown in the plots, the decompression ramps are exponentials. There are three parameters to determine: the total time of the ramp T_0, and the decay time constants T_{iZ} and T_{Bz} for the IZ current and the field Bz. The chosen parameters, $T_0 = 300$ ms, $T_{iZ} = 150$ ms and $T_{Bz} = 50$ ms, minimize the heating without exciting oscillations of the center of mass in the y and z direction. Unfortunately, the situation is different for

the x direction. We can observe the effect with the front view camera. This is shown in the panels of figure II.19 (black curves). We observe the projection of the motion in the x/z directions generated by the decompression. We can recognize in both motions one frequency, which corresponds to the x trap frequency of ~ 30 Hz. The projection of the motion along the x-direction shows that this trap frequency is being excited at the very beginning of the decompression ramp. That the oscillations are also seen along the z direction is due to the fact that the eigenaxes of the trap are slightly misaligned from the natural axis of the Z wire.
The motion in the x direction seemed to be inevitable. We have tried to optimize the decompression ramp shape but we couldn't get rid of this very first rough oscillations. This is due to the fact that at the very beginning of the decompression, the trap is 100 times tighter on the y and z directions than on the x direction. The atoms thus feel an acceleration that is nearly adiabatic for the confining directions but not for the x one. Finally we have kept the decompression ramp as initially chosen and we have *slowed* the atoms in the x direction by performing a displacement of the trap center against the motion (and therefore in quadrature with the oscillation of the position of the trap). For this, we have made use of a bias field in y, which changes the x position (as well as the height) of the trap. Along the z direction, the decompression is still adiabatic, but in x we are able to slow the atoms. The red curves in figure II.19 show the improvement of the oscillations in the x direction after a slow down of the atomic sample.

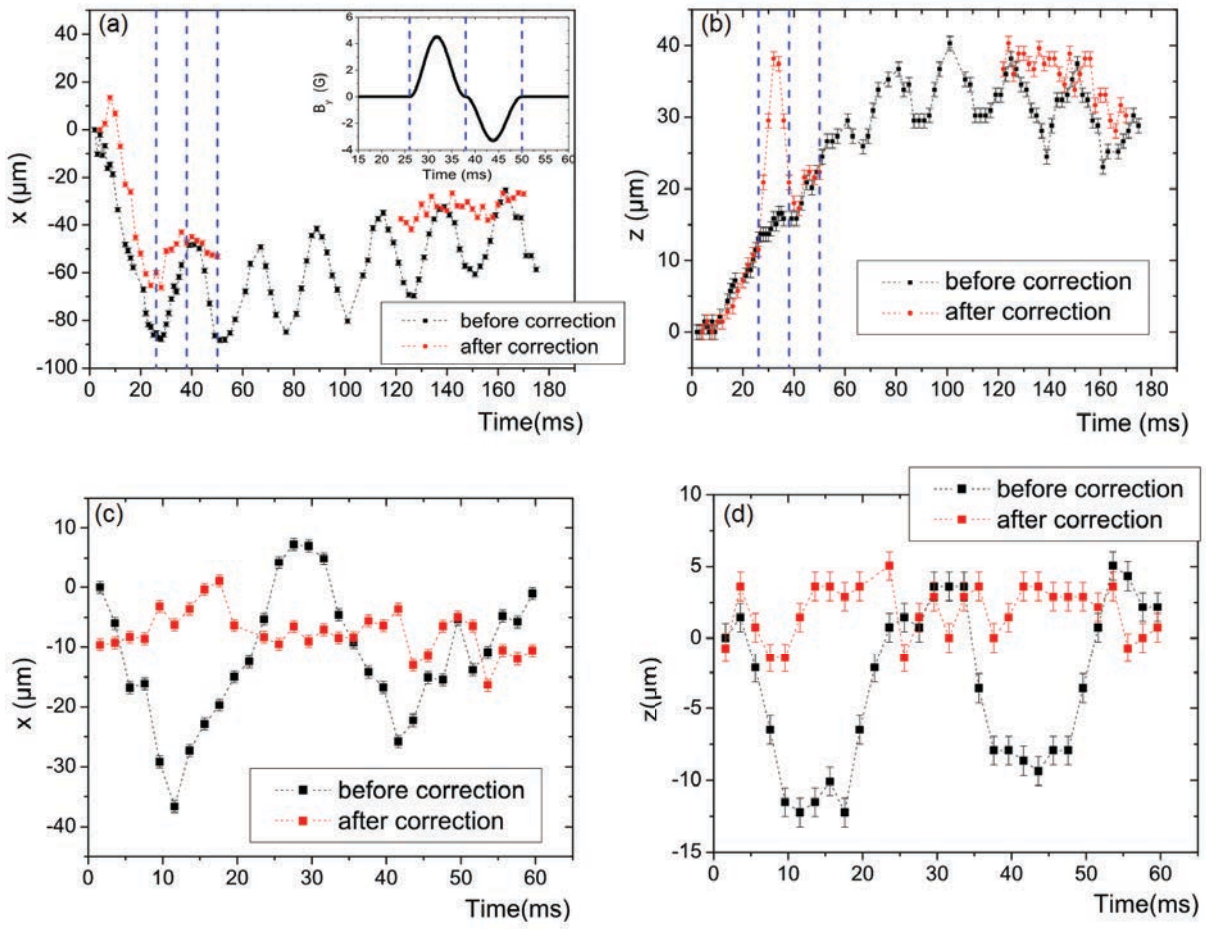

Figure II.19: **(a)** and **(b)** temporal evolution of the x and z coordinates of the atomic cloud for the first 180 ms of the decompression ramp. The black curves are without the function to eliminate the trap oscillation and the red curves are with it. The correction function is plotted in the inset figure at the top of the (a) panel. The function takes place between the times 26 and 50 ms (indicated with blue dashed lines). **(c)** and **(d)** show the oscillations in both directions after the decompression, again with and without the correction.

II.5 Conclusion of the chapter

We have described the main features of the experimental setup, with the cryostat, the laser and imaging system. We have discussed the experimental sequence from loading the atoms from the 2D-MOT outside the cryostat up to the condensation of 20000 of them. The optimization of these various parts has been a rather long work, to which I devoted the first two years of my PhD. Fortunately, we have been able to develop a set-up matching all our initial requirements.

Chapter III

First electric field studies

This chapter is devoted to the first part of our experimental results. It focuses on the study of the electric field near the superconducting atom chip surface. One of the biggest challenges in our complex experimental system is related to stray electric fields. A large part of this work, after reaching the state of the art for the whole cold atom part, was thus centered on the high-precision control of these fields, which can completely destroy the signature of blockade signal (chapter V).

We have observed initially, with a 'fresh' chip (the concept will become clear along the chapter), that these stray electric fields were changing over a time scale of minutes, hours and days. At the beginning of our experiments, it was impossible to get a stable excitation line and to compensate the residual fields. Other groups faced the same difficulty in similar contexts[14, 15]. Together with them, we attributed these stray fields to Rubidium atom deposited onto the chip. This deposition is unavoidable as soon as the experiment is turned on. We tried to control this deposition, to pattern atoms on the surface, but to no avail. Finally, we came out with a quite simple solution. We stabilized the electric field and made it homogeneous through the controlled deposition of a metallic Rubidium layer onto the chip surface by the use of Rubidium dispensers installed inside the cryogenic environment. We will describe this procedure and its impact in details.

The first section III.1 in this chapter will be devoted to the excitation geometry, including some words on the laser stabilization system. We then describe (III.2) the Rydberg atoms detection scheme. Later (III.3), we present the first laser spectroscopy data on the target level $|60S_{1/2}\rangle$. We detail then the first studies of the electric field, and show how it was drifting in time. Then, in section III.4, we present systematic studies of the electric field after our first attempts to make it more homogeneous by depositing *Rb* patches with MOTs. The chapter continues with section III.5, in which the installation of the Rubidium dispensers inside the cryogenic environment is described. We present the most important data of this chapter, exhibiting the considerable improvement in the laser excitation spectra due to this deposition. The chapter ends with the best laser line obtained in this work after a final optimization of the laser locking system.

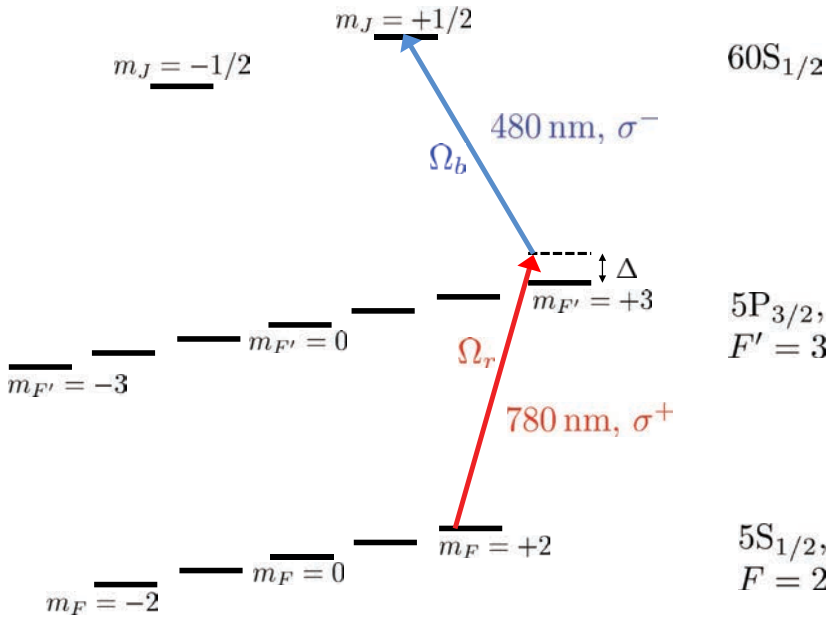

Figure III.1: Rydberg excitation scheme for atoms in the Z-trap, from the level $|F = 2, m_F = +2\rangle$ to the Rydberg state $|60S_{1/2}\rangle$. The polarization of each transition is shown in the figure. Ω_r and Ω_b are the Rabi frequencies corresponding to each transition and Δ the detuning with respect to the intermediate level, equal to 540 MHz. It is large enough to avoid any spurious population of the short-lived $5P$ level.

III.1 Laser stabilization system

The excitation scheme of the Rydberg states has already been introduced in chapter I, (figure I.5). It consists in a two photon transition: one red photon at 780 nm and a blue one at 480 nm. The red laser is blue detuned by 540 MHz with respect to the intermediate level $|5P_{3/2}, F = 3\rangle$ and the blue laser is in resonance for the two-photon transition towards the Rydberg state. For the choice of the beam polarizations, we must bear in mind that the quantization axis for the atoms trapped in the Z-trap (in level $|F = 2, m_F = +2\rangle$) is x, defined by the magnetic field B_x in the bottom of the trap. The excitation scheme including laser polarizations is recalled in figure III.1.

During this work, the geometry of the excitation beams has changed several times. For the most relevant results (reported in chapter IV), both laser are sent parallel to the chip surface in the $+x$-direction, as shown in figure III.3). They are superposed before entering the cryogenic environment. The red laser has a σ^+ polarization and the blue σ^-, in order to address transitions $|5S_{1/2}, F = 2, m_F = +2\rangle \rightarrow |5P_{3/2}, F' = 3, m'_F = +3\rangle$ and $|5P_{3/2}, F' = 3, m'_F = +3\rangle \rightarrow 60_{1/2}, m_J = +1/2\rangle$. The dipole transition moment for the red laser is $2.98931(62)ea_0$ [31], that for the blue laser is $9.9 \times 10^{-3}ea_0$. The maximum power we can get for the blue laser beam is 8 mW, focused in a 22 μm waist at the trap position. For the 780 nm laser, we have much more freedom. The power we have used for

our experiments varies from 100 nW to 2 μW, in order to control the number of Rydberg excitation. The red laser is focused to a 150 μm waist. A summary of the beam properties is given in table III.1.

Characteristic	Red beam	Blue beam
Power	1 μW	8 mW
Radius ($1/e^2$)	150 μm	22 μm
Rabi frequency $\Omega_{r,b}/2\pi$	5.6 MHz	11.3 MHz

Table III.1: Properties of the excitation beams. The powers given here are typical. The fact that $\Omega_r, \Omega_b \ll \Delta$ ensures that population of the intermediate level $|5P_{3/2}\rangle$ is avoided. The power difference between the two beams is due to the fact that they must have equivalent Rabi frequencies (to avoid excessive light shifts), in spite of the small dipole moment on the blue transition. We also choose a low power for the red laser to avoid parasitic heating of the trapped cloud.

Since $\Omega_r, \Omega_b \ll \Delta$ the population in the intermediate level $|5P_{3/2}, F = 3\rangle$ can be neglected and the atom behaves as a two-level system with an effective Rabi frequency given by

$$\Omega_{rb} = \frac{\Omega_r \Omega_b}{2\Delta} \tag{III.1}$$

with $\Omega_r = 2\pi \times 5.6$ MHz and $\Omega_b = 2\pi \times 11.3$ MHz, then $\Omega_{rb} = 2\pi \times 58.5$ kHz.

We should not forget that these values are relevant for individual atoms. As a consequence of the Rydberg blockade effect, collective many-body Rabi oscillation may arise. Then, the Rabi frequency is multiplied by a factor $\sqrt{N}$ where N is the number of atoms in the blockade radius.

Almost all our lasers are diode systems by *Toptica Photonics* (the repumper is an homemade device). For the blue 480 nm laser, we use a **TA-SHG 110** system. For the infrared excitation at 780 nm, we have a **DL pro**. We shall describe briefly in the following paragraphs the locking system of each laser, since their linewidth plays an important role for precise spectroscopy, as discussed in chapter I.

Both laser are stabilized by locking to a Fabry-Pérot (FP) cavity, using the Pound-Drever-Hall (PDH) technique [60]. A general scheme of the optical system for these two lasers is shown in figure III.2.

The 780 nm laser has two stages of stabilization: one locks the laser to the FP-cavity and the other locks the cavity to an usual Doppler-free saturation spectroscopic signal. The optical paths for these locks are phase-modulated at 20 MHz using an EOM (electro-optic modulator, here used as a phase modulator). The reflection signal coming out from the FP-cavity is used to create an error signal for the PDH scheme. The slow part of this signal is used to stabilize, through a PZT, the length of internal cavity of the laser head (from the laser diode surface to the grating). The high frequency part acts directly on the laser diode driving current. This locking to the cavity is performed by a FALC Toptica unit.

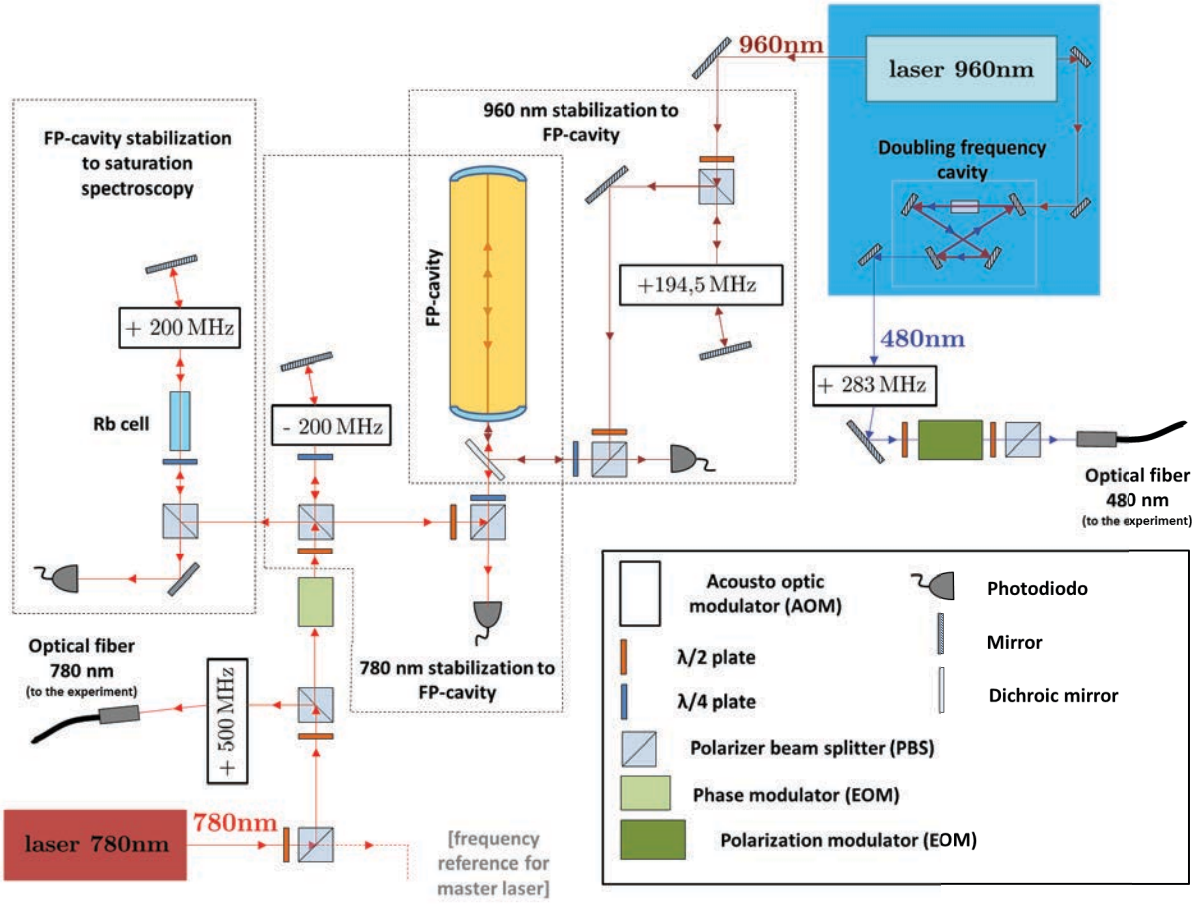

Figure III.2: Laser septup: scheme of the optical path for the stabilization and excitation system. The lenses and the polarization purifiers are not shown. The complete optical table (not shown) is divided in four parts: one for the master laser, a second for the repumper, both used for the optical cooling, trapping and imaging system. A third part is devoted to the 780 nm excitation laser and a fourth to the 480 nm laser (DL 960 nm laser + TA amplification+ SHG cavity). In this figure, we show only the last two parts.

Then, we lock the cavity to one of the crossover hyperfine peaks resolved by the saturation spectroscopy signal of ^{87}Rb atoms. The modulated spectra feeds the same PDH box, which creates another error signal, sent to a PID Toptica unit to stabilize the cavity by feedback action on a piezo mounted behind one of the mirrors.

The system is quite similar for the blue 480 nm laser. The blue light source consists of a diode laser at 960 nm, which is amplified by a tapered amplifier (TA) providing up to 0.9 W. Then, this light passes through a frequency doubler *butterfly*-shaped cavity (second harmonic generation SHG). Here again, there are two stages for the locking system. One locks the frequency and the other locks the doubling cavity. The frequency stabilization is performed on the 960 nm diode laser head, which is stabilized on the same FP-cavity

used for the 780 nm laser, using a PDH system and a FALC unit. The stabilization of the doubling cavity is made also by a PDH technique plus a PID unit. Here, the 20 MHz modulation is applied directly on the current of the 960 nm laser diode.

Several AOM's (acousto-optic modulators) are installed on the optical path to offset the excitation frequencies. They are also used to turn off the laser light when needed during the sequences. The light extinction is carried out in 100 ns after a 400 ns delay from the input TTL signal. For the blue laser, we place along the optical path an EOM for polarization modulation, which makes it possible to realize short pulses and the ultra-fast turning off of the light sent to the experiment. With this device, we can generate blue pulses as short as 10 ns.

The PDH technique provides a laser linewidth (at short times) smaller than 20 kHz, as measured by heterodyne interferometry (Appendix C of [42]). During our work we have observed that the two-photon transition line $|5S, m_F = +2\rangle \rightarrow |60S_{1/2}, m_J = +1/2\rangle$ was moving over time, even after the resolution of the stray field problem. This pointed to a subtle laser stabilization problem than will be addressed at the end of the chapter.

III.2 Detection setup

The two lasers we use to reach the target level, $|60S_{1/2}\rangle$, arrive by optical fibers to the exterior of the cryostat where they are superposed in the $+x$-direction. The detection system by field ionization is installed inside the cryogenic environment. A set of electrodes is placed around the excitation zone in order to: **compensate** for stray electric fields perpendicular to the chip surface, **ionize** the created Rydberg atoms and **guide** the resulting ions to the Channeltron counting unity (SJUTS model KBL 10RS-EDR). We shall describe this procedure in the following.

In figure III.3, we display the scheme of the electrodes and of the Channeltron for the field ionization detection together with the chip and the excitation beams. The field-ionization detection technique relies on the fact that Rydberg atoms are very sensitive to electric fields and therefore very easy to ionize (see section I.1). The ionizing field is different for different Rydberg levels. A ramp of field thus ionizes the involved levels at different times and we can measure their population by recording the channeltron signal.

Once created by the excitation beams, the Rydberg atoms are ionized. This is realized by applying a negative voltage ramp on the two first electrodes called V_{ion1} and V_{ion2}. V_{ion1} is parallel to the chip, at a 16 mm distance and V_{ion2} is located 6 mm after V_{ion1}. The created Rubidium ions are accelerated by the field ramp and guided to the Channeltron by the deflection electrodes V_{defl_1} and V_{def_2}, always on and positively biased at 250 V. A typical ionization ramp and the detected signal are shown in figure III.4. A photograph of the electrodes and of the Channeltron is shown in III.5.

The homemade system generating the voltage ramp for V_{ion1} and V_{ion2} can reach ± 150 V. The circuit is shown in figure III.6 and is explained in the figure caption. The computer transmits an order to a function generator (*Agilent* model 33250*A*) to generate the shape. It is sent to a fast voltage amplifier. We chose a model WMA-300 Falco Systems, with

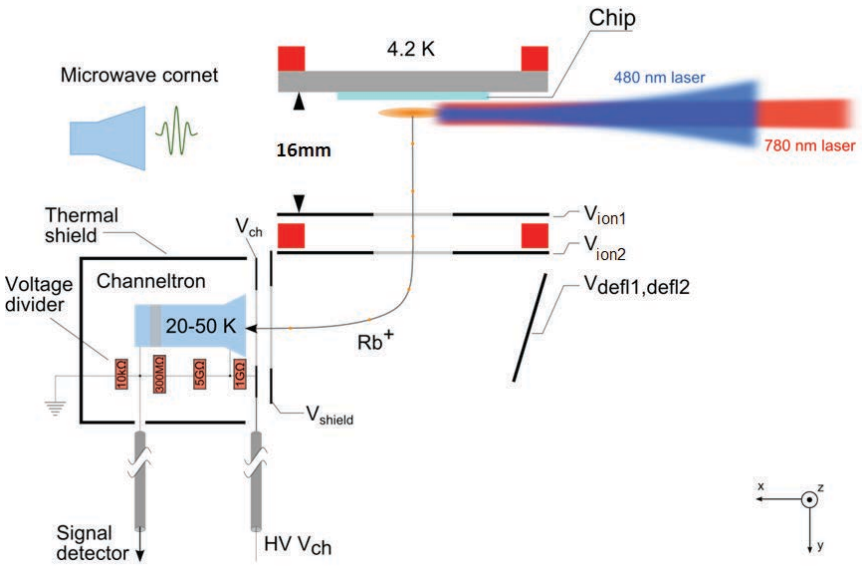

Figure III.3: Scheme of Rydberg atoms detection by field ionization. The point of view is from the top. The distance from the chip to the first electrode V_{ion1} is 16 mm and from this one to the second, V_{ion2}, 6 mm.

a $50X$ amplification, a maximum amplitude of ± 150 V and 5 MHz bandwidth. With such a feature, the ramp can be performed in less than one 1 μs. The computer also sends a trigger TTL signal. The final component is a switch. It commutes a voltage divider between two operating modes. When the trigger TTL is off, the voltage from the the amplifier is divided by a large factor. This makes it more easy to control the small compensation voltage applied onto the ionization electrodes during laser excitation and it reduces the technical noise on this field. When the TTL becomes active at the beginning of the ramp, the optocoupler short-circuits a resistor and the voltage divider is removed from the circuit.

The complete ramp is programmed in advance by a GPIB unit and is triggered 1 μs after laser excitation. The counting windows that will define afterwards the transfer from one Rydberg state to another are carefully set by monitoring the arrival times of the ions. An example of ionization signal is shown in figure III.4b for the $|60S_{1/2}\rangle$ level.

The ionization ramp, after the constant voltage for stray field compensation, is divided into two segments: a fast part and an slow part. The fast part is designed to arrive as fast as possible close to the ionization voltage of the target state. The slope is then changed to have a good temporal resolution of the states to be resolved.

The slew rate of the fast part is nevertheless important, for more subtle reasons. As we can observe in figure III.4(b), the ionization signal for the target state $|60S\rangle$ presents, versus the arrival time, a double peak. A very similar signal is shown in reference [61]. The relative proportion of these two peaks depends upon the slew rate of the fast ramp. We have observed that nearly all the signal appears in the first peak when the fast part

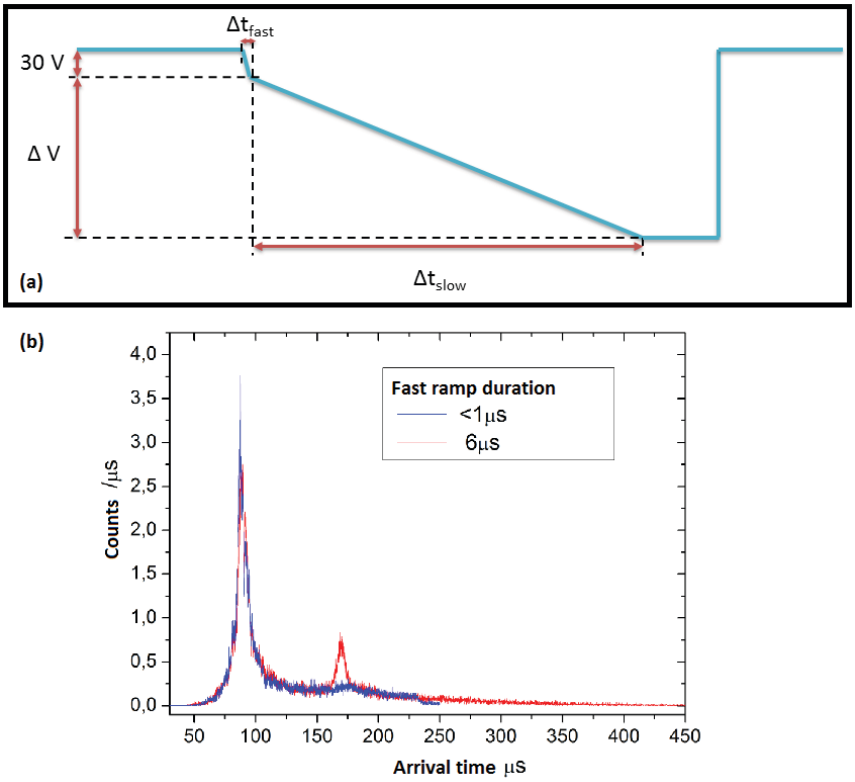

Figure III.4: **(a)** Standard ionization ramp. It is applied to both V_{ion1} and V_{ion2} in parallel. The ionization ramp is superposed to a constant value compensating the stray electric fields in the y-direction during Rydberg excitation. Afterwards, the ramp is divided into two, a fast and a slow part, the slope being changed in order to better resolve the arrival times of different levels. **(b)** Depending upon the duration of the fast ramp, we observe diabatic or adiabatic ionization peaks. The blue line corresponds to a first part of the ionization ramp shorter than 1 μs. The red signal, corresponds to a first part of the ramp lasting 6 μs.

of the ionization ramp is shorter than one microsecond. We have concluded that, for the $60S$ state, this first peak is the result of **diabatic ionization** whereas the second peak is interpreted as resulting from **adiabatic ionization**. Let us describe these process in more details.

While the electric field rises, the eigenenergies and the states of the Rydberg atoms change accordingly due to the Stark effect. A description of this effect has been presented in chapter I with a Stark map around our target state (figure I.3). For alkali atom, this level map presents numerous anti-crossings. If the field rises slowly enough, these anti-crossings will be passed adiabatically, the atomic state following continuously the same level. If the field rises very rapidly, the atom may change level at the anti crossings. It means that the path followed in the Stark map depends in a complex way upon the field's slew rate. The classical ionization threshold, which depends upon the level energies, is thus reached at different times for a diabatic and an adiabatic ionization. This is the reason

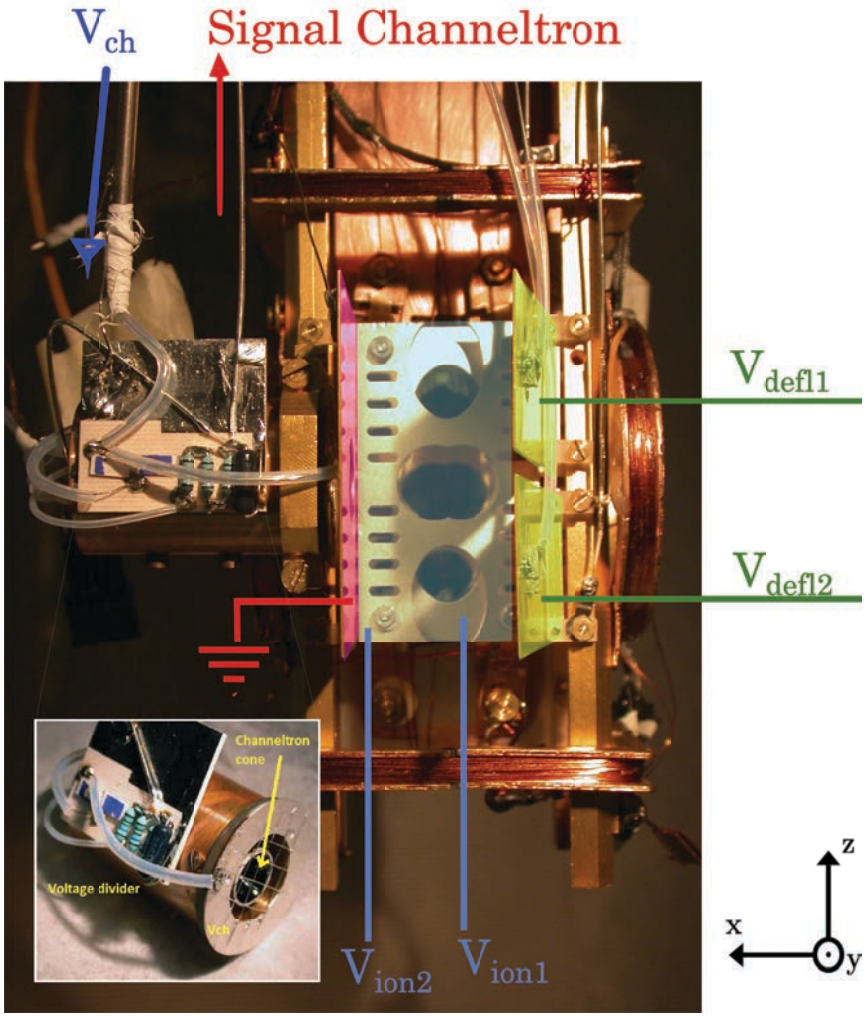

Figure III.5: Photograph of the detection electrodes. The inset presents a photograph of the Channeltron assembly. In blue, we point to the ionization electrodes $V_{ion1,2}$, in green to the deflection electrodes $V_{defl1,2}$ and in pink to the shield electrode V_{sh}, which is always grounded. We can also observe the Channeltron signal cable and its high voltage supply, called V_{ch}. In the inset, we observe from another point of view the Channeltron. We can see the grid which is biased at V_{ch} together with the voltage divider needed for the Channeltron operation.

why the characteristics of the ramp play a fundamental role in the shape of the ionization signal. In order to obtain the simplest ionization signal, making it more easy to measure later transfer rates between Rydberg levels, we thus operate the ionization in the diabatic conditions, as illustrated in Fig. III.4.

The Channeltron detects the ions, multiplies the signal and sends it to a fast counter, a *Hamamatsu* Photon Counting unit, model C9744. The Channeltron can operate at temperatures from 40 K to 60 K. It is therefore thermally isolated from the chip and properly

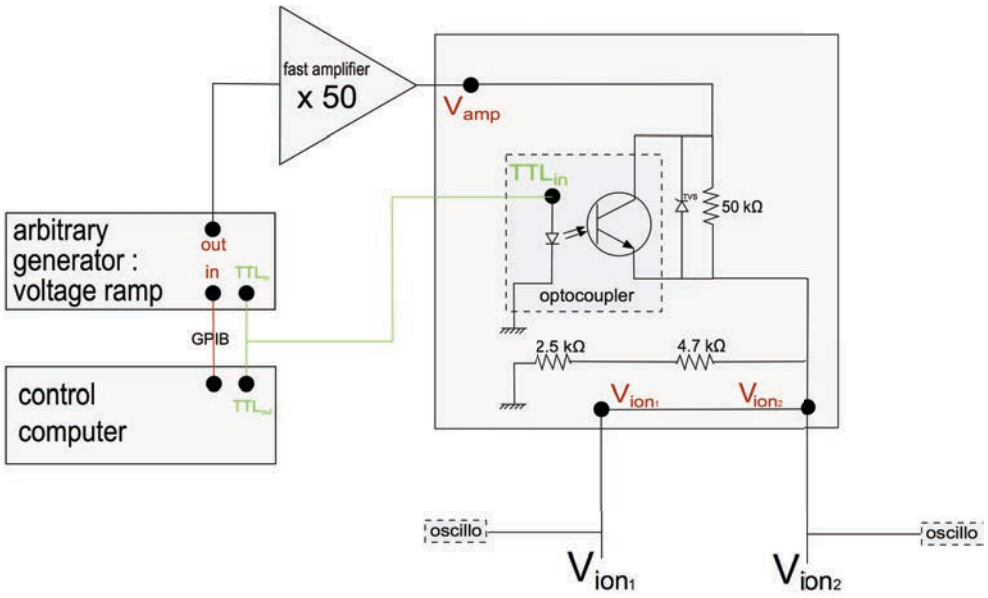

Figure III.6: Circuit for biasing the V_{ion1} and V_{ion2} plates. The amplifier has an amplification of 50X, with a maximum amplitude of ± 150 V. Both electrodes are set with the same voltage during the whole sequence. Before the ionization ramp, an initial small constant value is programmed for the compensation of stray electric fields. During this period, the optocoupler is in the open position. A voltage divider between the resistance $50\,k\Omega$ and $2.5\,k\Omega + 4.7\,k\Omega$ puts the electrodes at voltages $V_{ion1} = V_{ion2} = 7.2/57.2 \times V_{amp}$. Once the Rydberg atoms are created, the ramp is triggered by the TTL signal. Then the optocoupler switches to the closed position, and short-circuits the $50\,k\Omega$ resistance. The electrode voyage is then equal to V_{amp}.

shielded. The electrode V_{shield} (Fig. III.5) is grounded in order to shield the the excitation zone from the high voltage of the Channeltron. We use a voyage divider operating on a high voltage $V_{ch} = -3000$ V, to properly bias the channeltron itself and to bias its input cone with respect to the grid electrode placed in front of it. The counting threshold of the Hamamatsu box is adjusted in order to decrease as much as possible the dark counts without losing the signal. The Channeltron detection efficiency has been measured to be $90 \pm 10\%$ by comparing the Rydberg counts to the loss in the trap measured by absorption imaging. We have checked that we always operate well below the Channeltron saturation.

III.3 First atomic spectrum

For a first coarse exploration of the excitation spectrum, we operated with a steady-state U-MOT at 600 μm from the chip surface, in order to avoid as much as possible any perturbation due to stray electric fields near the surface (broadened transitions). We positioned the red and blue lasers on it and made a broad scan of the blue laser frequency.

Without locking the 960 nm laser system, we can vary the blue laser frequency by several

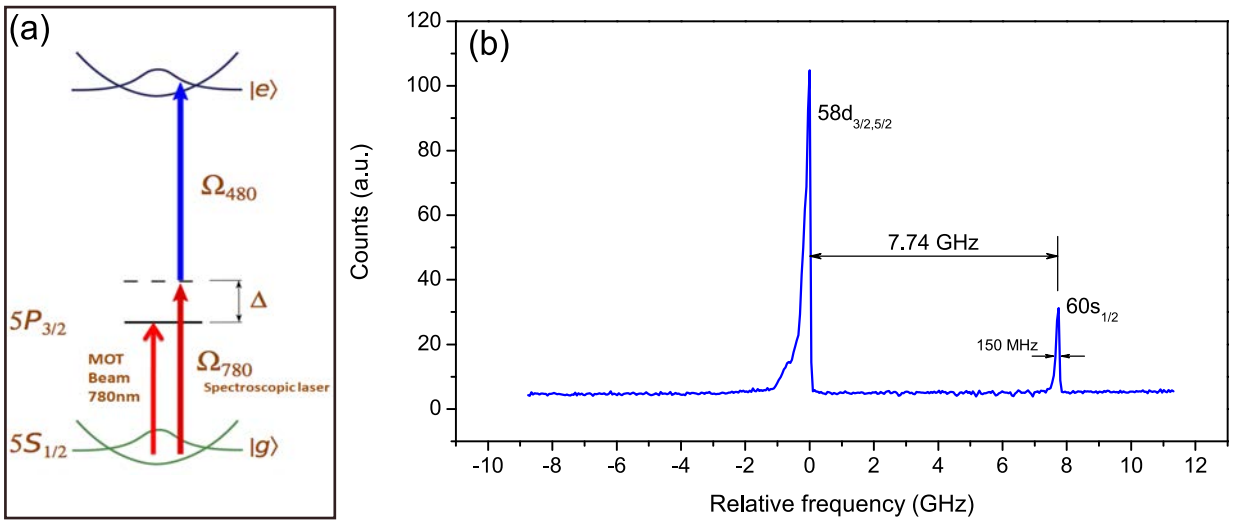

Figure III.7: **(a)** Excitation scheme including the MOT beam. **(b)** Stepwise Rydberg excitation line of atoms trapped in a U-MOT at 600 μm from the chip surface. The two peaks correspond to the two neighboring levels $58D_{3/2,5/2}$ and $60S_{1,2}$.

GHz using the scan control box of the laser diodo where we apply directly a current ramp. The MOT is on during 10 μs and, in this time period, we detect the ions produced by the blue laser. Figure III.7 presents the resulting spectrum when the only 780 nm laser applied on the atoms is that required for the MOT operation, nearly resonant on the transition to the $5P$ level. We thus observe stepwise excitation towards the Rydberg states.

The Rydberg signal shows a structure with two peaks. The distance between them is 7.74 GHz, which corresponds to the expected energy difference from the level $58D_{3/2,5/2}$ to our target state, 60S. The linewidth is 150 MHz, not relevant since the scan of the laser is quite broad and since the laser is free running without any lock. Being familiarized with the landscape of the Rydberg spectrum, we can go further by scanning the blue laser only in the region of interest around the $|60S_{1/2}\rangle$ state. We try to observe the *two-photon transition* line by turning on and off the 780 nm spectroscopic laser, detuned from the intermediate level. We present in figure III.8 the spectra with and without this laser (the MOT resonant laser is always on). We find, when the detuned red is on, a small ionization signal detuned from the resonant stepwise excitation by more than 500 MHz, to the negative frequencies. This line position is consistent with the detuning of 540 MHz from the $5P_{3/2}$ resonance chosen for the red laser.

We can now get rid of the one-photon transition in the MOT cloud, by turning its laser off 1 μs before the the excitation lasers. This time is sufficient to eliminate any light coming from the cooling beams (their switching off takes less than 100 ns), and also to let the atoms fall back into the ground state since the lifetime of the $5P_{3/2}$ is 25 ns. We also proceed to lock the laser to the Fabry-Pérot cavity and scan the frequency by the AOMs, reducing the width of the signal. We furthermore compensate the electric field at the atomic cloud position by scanning the initial value of the ionization ramp. The smaller

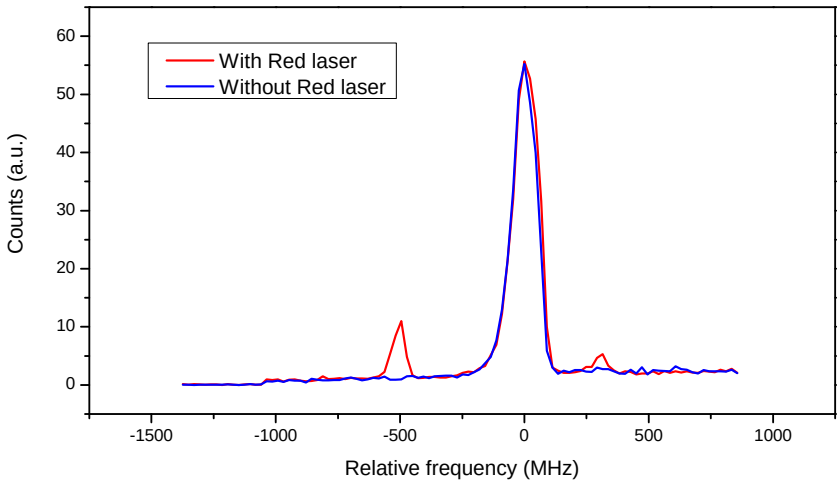

Figure III.8: One and two-photon transition lines for atoms trapped in a U-MOT at 600 μm from the chip surface. The red line corresponds to the case in which the 780 nm spectroscopic laser is on while the MOT is on. We can observe the two-photon transition line to the $|60S_{1/2}\rangle$ Rydberg level on the left side of the spectra. The blue line shows the same signal when the 780 nm laser remains off during the data acquisition. We only observe then the nearly resonant stepwise excitation.

laser linewidth makes it also possible to reduce the power of the excitation beam, avoiding power broadening. The resulting two-photon transition lines will be presented in the next section.

III.4 Fresh chip and deposit of Rubidium via MOTs

We first investigated the two-photon line in the U-MOT trap. The atomic cloud is then rather large (200 μm in the longest dimension), and, contrary to the case of the magnetic trap, the excitation region is mainly defined by the geometry of the laser beams.

During the experiment, we have tried many configurations for the laser excitation. For the results in this section, the blue laser was sent perpendicular to the chip in order to decrease the size of the excitation region and, thus, minimize the influence of the field gradients. The excitation geometry is shown in figure III.9.

Working with this configuration, we observed immediately a drift of the central frequency of the two-photon transition line, as well as a gradual increase of its linewidth over time. This behavior is shown in figure III.10. The two excitation lines in this figure were observed in a U-MOT trap at 550 μm from chip surface. The zero correspond to the expected zero-field line calibrated by microwave transitions. The zero field frequency is inferred from the results of chapter IV.

The black line was observed after minimizing the y electric field. This compensation required the application of 7.835 V on the electrodes V_{ion1} and V_{ion2}, corresponding to

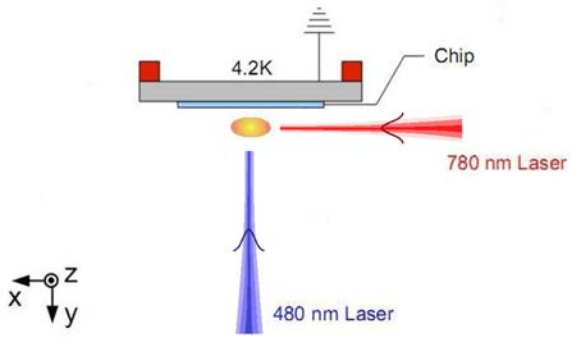

Figure III.9: Excitation scheme with the blue beam perpendicular to the chip surface.

about 3.7 V/cm. In spite of this compensation, the line is rather far from the expected zero field frequency (dashed vertical line). Its width is 30.45 MHz. This is much more than what is expected for all broadening mechanisms evoked in Appendix A, but the quadratic Stark shift. We can thus attribute the linewidth to electric field gradients. Taking into account the dimension of the cloud, this corresponds to an electric field gradient of 12 V/cm^2, and to $\langle E_{\|} \rangle \simeq 0.7$ V/cm.

Only 40 minutes later, we observed the line shown in red. It is even further away from the zero-field frequency (the line center has been shifted by an additional 12.4 MHz) and it is clearly even broader. The width is now 39 MHz corresponding to an electric field gradient of 13.5 V/cm^2. Here the line was not compensated again in the y direction. We observe in many further experiments that the two photon transition line $|5S\rangle \rightarrow |60S\rangle$ was drifting over time scale of minutes, hours and days. By several tests, we have related the problem's origin to the **slow deposition of** *Rb* **on the chip surface** while the experiment is in operation.

Simultanously, other groups also observed this problem and traced it to the same effect [14, 15]. Some concluded that the principle of these experiments was doomed. We concluded that a possible solution was a **controlled deposition of Rubidium on the chip surface**. A first attempt will be described in this section. We refer from now on to a *fresh chip* for the situation before any on purpose Rubidium deposit.

Figure III.12 presents the schematic principle of the situation and the solution we had in mind. The patch deposited on the gold mirror from the QUAD-MOT or from the U-MOT is quite annoying because its size is a fraction of a millimeter to a millimeter, comparable to the cloud to chip distance. With a 2.5V contact potential between gold and Rubidium (a thin layer might not be bulk metal, but the order of magnitude is correct), it clearly generates a large, very inhomogeneous electric field at the location of the atoms. A uniform Rubidium deposit, on the other hand, creates at most a rather uniform field between the chip and the gold ionization electrode, than can easily be compensated by applying the proper bias. We have tried first to decrease the effect of the slow deposition of Rubidium and hence to change the local electric field conditions, without opening the cryostat, by

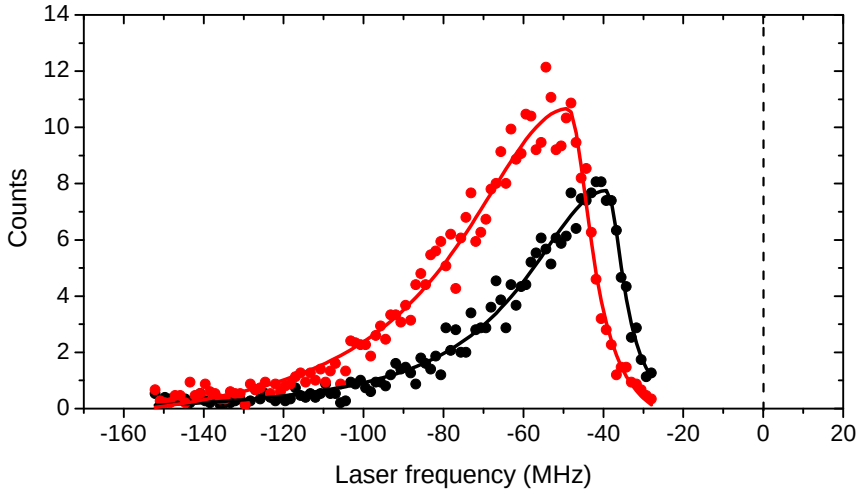

Figure III.10: Laser line $|5S\rangle \rightarrow |60S\rangle$ taken in a U-MOT at $550\mu m$ from the fresh chip surface. The width of the black line recorded first is 30.45 MHz. The red line recorded 37 minutes later, has a width of 39.8 MHz. Both lines were observed with the same compensation voltage, 7.835 V (3.7 V/cm). The difference between the line centers is 12.4 MHz.

depositing on purpose atoms from a QUAD-MOT.

During a long time (one hour or more), we repeatedly captured as many atoms as possible in the QUAD-MOT ($\simeq 10^8$ atoms, as inferred from fluorescence signal) and launched them towards a given point on the chip. After this deposition, we minimized again the y field component and recorded the two-photon excitation line in a U-MOT as a function of the perpendicular blue laser position in the x direction and for a constant z coordinate corresponding to that of the central part of the Z wire.

An example of results for this procedure is given in figure III.11. The maps are taken at 400 μm from the chip surface. The last panel presents the chip geometry and, to scale, in brown, the region in which we deposit atoms from the QUAD-MOT. The first panel in figure III.11 presents the ion signal as a 2D-map, as a function of the laser detuning from the expected zero-field line calibrated by microwave transitions and of the position of the excitation along the x axis after one hour of deposition in the point X_0, defined in panel (d). The second map (b) is after an additional 1 hour deposition at the point X_1 and the third (c) after 4 hours and 30 minutes at the same place. For all graphs, the position of the blue laser is scanned along the dashed yellow line in panel (d). The y field compensation is the same for the three maps, corresponding to a perpendicular field of 6.2 V/cm. Clearly, the line centre at the central x position gets closer and closer to the zero-field frequency when the deposition time is increased. We also observe on the three maps that the residual field has a strong dependence versus x and that it increases rapidly when getting away from the central position, at which the minimization of the y field component has been performed.

As a summary, this deposition procedure certainly changes the local field conditions.

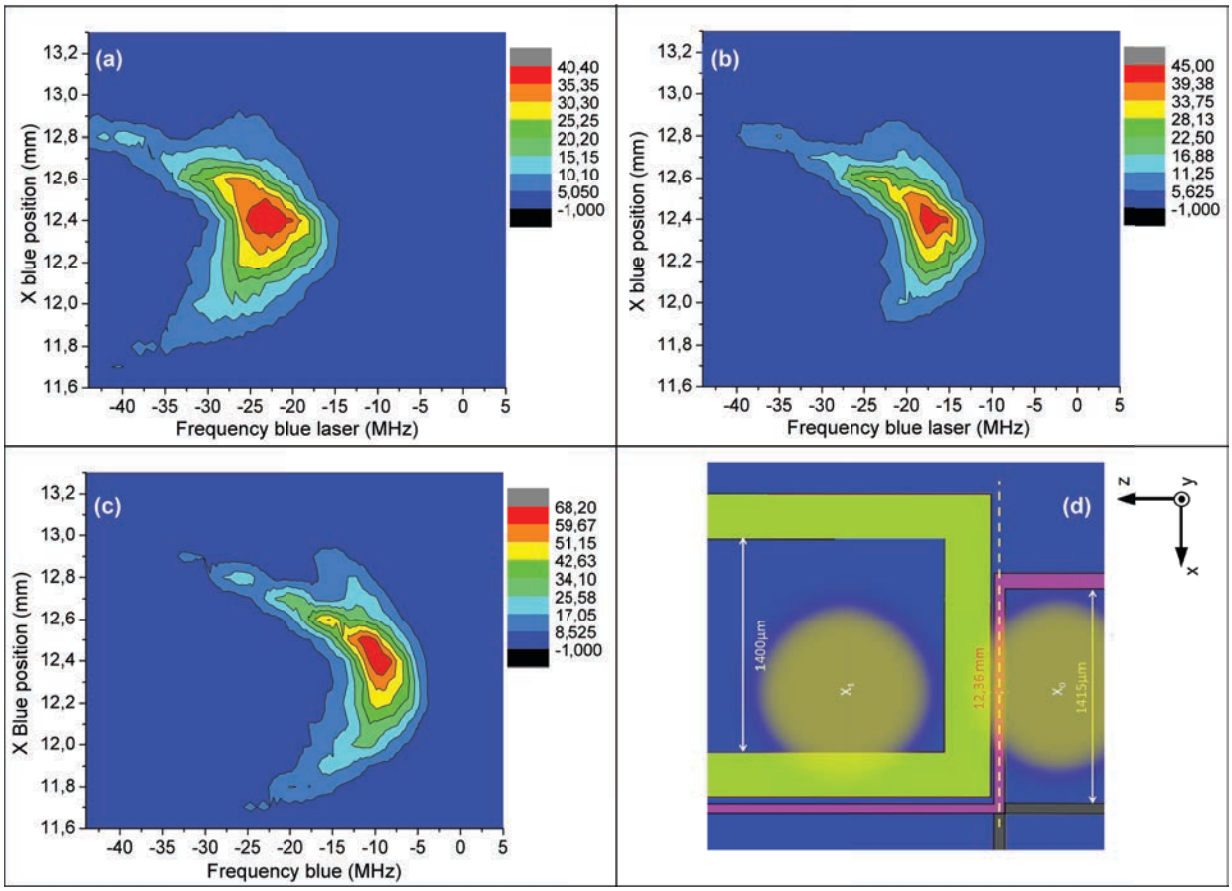

Figure III.11: Evolution of the two-photon transition due to the MOT depositions. (a), (b) and (c) show maps of the Rydberg atoms counts as a function of both the laser detuning w.r.t the zero-field line and of the blue laser x position ($x = 12.36$ mm correspond to the center of the Z-shaped wire). The lines are recorded at 400 μm from the chip surface. The scheme in panel (d) shows the laser position scan (dashed line) and the deposition positions (brown blobs). Note that the chip is turned by 90^0 with respect to the orientation inside the cryostat. (a): after a deposition of one hour in the X_0 point. (b) after a further one hour deposition in the point X_1. (c) after 4h30 minutes also at X_1.

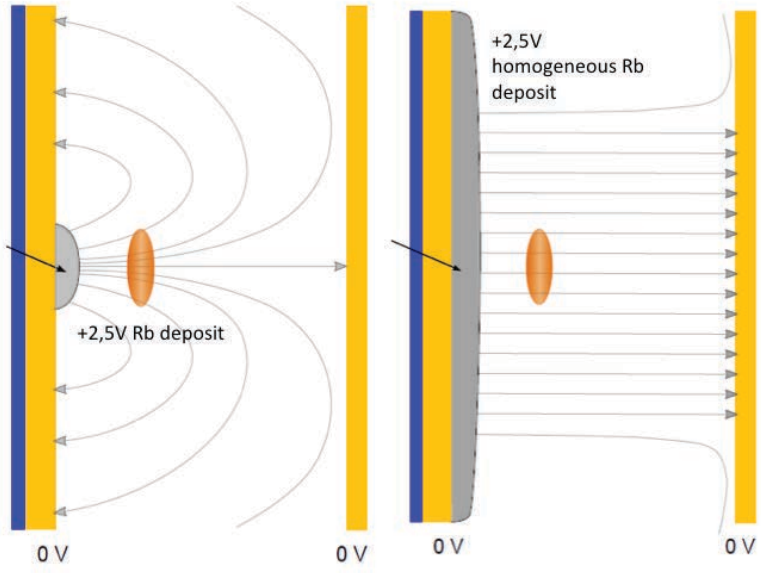

Figure III.12: Illustration of the Rubidium deposit effect. The ellipsoid in the centre of the picture represents the atomic cloud. The deposition of these atoms on the chip creates an extremely inhomogeneous field (left), while a uniform deposit (right) creates at most a uniform field that can be easily compensated for

It is an additional proof that the large line broadening we observe is due to the Stark effect induced by Rubidium deposits onto the surface. We have observed transiently some reduction of the local field. We have repeated this procedure many times, making deposits at different positions with respect to the Z-shaped wire center. However, the solution is not very practical. Hours of deposition are required to create less than a monolayer on a reduced surface, but it is not stable enough. From day to day, the alignment of the lasers slightly change, and thus the position of the parasitic deposit, changing in turn the local field map.

Clearly, we would need to perform large scale thick deposits of Rb to be able to reduce and stabilize the stray fields. This is precisely the final solution we have come to, which is explained in the next section.

III.5 Macroscopic Rubidium deposit

To get rid of the patch effect due to the deposition, the simplest solution is to cover the whole of the chip surface with a metallic Rb layer. The high chemical reactivity (including gold) and the extremely fast oxidation of thin Rubidium layers makes it mandatory to realize the deposition when the cryostat is cold. We have thus chosen to install in the setup two current-activated dispensers from *SAES company* (model **RB/NF/ 3.4/12FT10+10**),

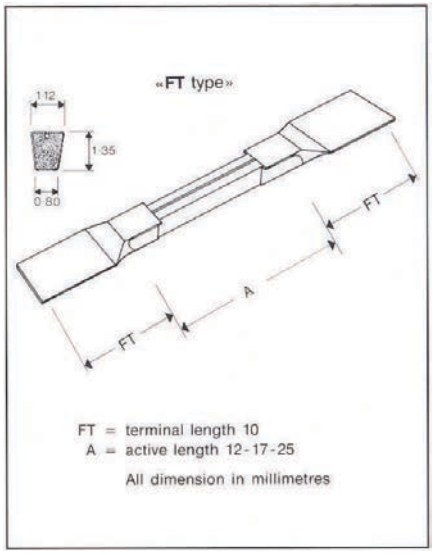

Figure III.13: Rubidium dispenser from *SAES company*.

provided by Jakob Reichel. They are shown in figure III.13. Each contains 4.5 mg of *Rb* to be evaporated.

The activation current is between 4.5 and 7.5 A, when the dispenser is used in a room temperature set-up. The rate of Rb release varies rapidly with the current through the dispenser's operating temperature. This control is very well characterized by the company. We have in principle a precise knowledge of the temperature reached as a function of the current, and of the amount of Rubidium released as a function of time. However, the company had no experience with operation starting at 4 K.

A photograph of one of the dispensers installed in front of the chip is presented in figure III.14. The other dispenser is installed symmetrically in front of the Channeltron. Both dispensers are surrounded by a copper rectangular box in order to hold them and to avoid Rubidium deposits in regions such as the channeltron or the optical windows (a few tens nanometer of Rubidium is enough to make a window opaque). Aiming directly to the chip, the shield box has a slit, 6 mm wide and 30 mm high, allowing deposition on the desired surface.

We cooled down the experiment and proceeded to activate the dispensers. This is a priori a risky task, since the operating temperature of these devices is above 600^0C, quite a detrimental value for a cryogenic environment. We thus proceeded with care, rising progressively the current in the dispensers. We have observed, as expected, a few outgasing peaks at $3.5-4.5$ A before the actual deposition started. When the pressure was down, we continued heating the dispensers, reaching a final current of 6.5 A, quite larger than that used in room temperature experiments. In order to monitor the Rubidium release, we were continuously measuring the absorption of a probe beam in the cryostat. The absorption was small at any time, since the Rubidium atoms released from the chip are expected to stick rapidly on the cold surfaces around them. Note that the temperature of the chip and

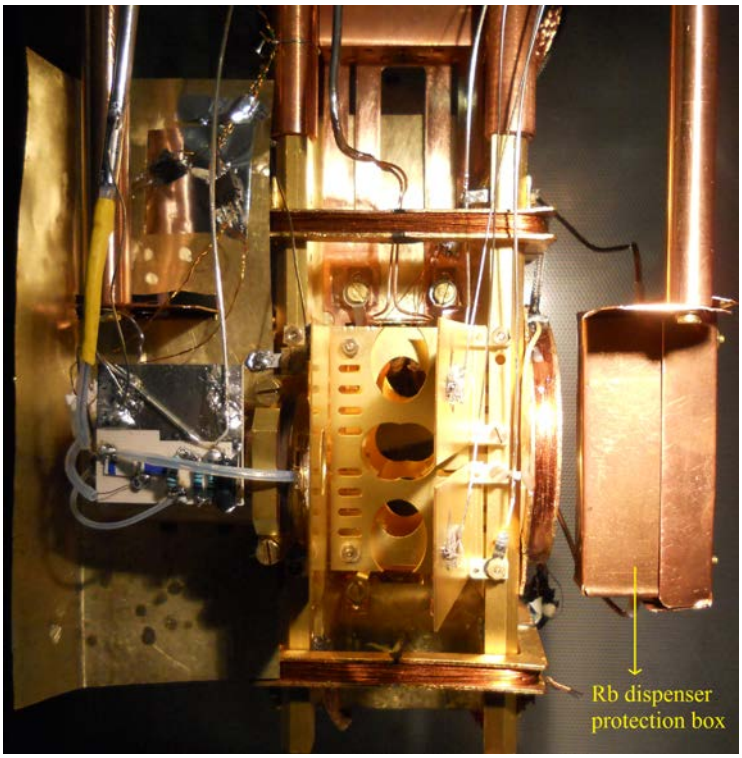

Figure III.14: Photograph of the two Rubidium dispenser box. The dispenser is located inside the rectangular copper box at the right side of the image.

of its surrounding did not heat above 12 K while the dispenser was red-hot. The thermal isolation between the dispenser and the experimental core was thus quite correct.

It is difficult to estimate properly the thickness of the Rubidium deposit. We estimate, from the activation time, from the absorption signal, that most of the available Rubidium has been released. The solid angle determined by a square of 30×30 mm on the ship surface is $\sim 10^0 \times 27^0 = \pi^2/30$ sr. Assuming a non-directional deposition, with an uniform solid angle of 2π sr (half of a sphere, as the filament emits Rubidium just in one side, see figure III.14) and a rate of 100% of sticking on the chip surface, then 1/60 of the dispensers Rubidium has been deposited on the chip. If the whole mass was deposited, considering the density of the metallic Rubidium of 1.5 g cm^3, the thickness of the layer would be 86 nm corresponding to ~ 300 atomic layers. This is far enough to get a metallic film. This is even enough to cover efficiently the few dust particles that were sticking on the chip.

However, we had also evidence that the Rb atoms do not all stick on the first surface they encounter. In the final spectra described in the next chapter, there is no evidence of the expected 2.5 V potential difference between the Rb chip and the gold electrode facing it. We must thus conclude that Rubidium covers the two facing electrodes in similar ways, and thus that the atoms could bounce at least once. The film may thus be a factor ~ 2 thinner.

We then proceeded to measure again the laser excitation line. The blue and red lasers

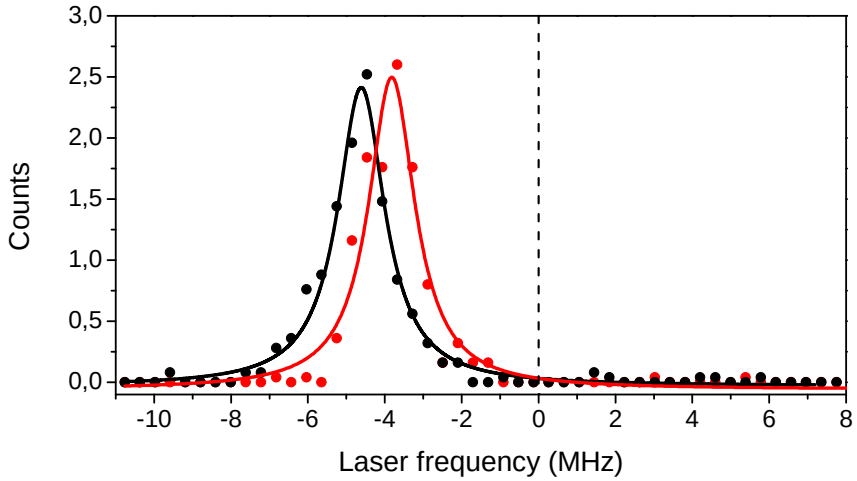

Figure III.15: Laser line $5S \rightarrow 60S$ recorded at a 20 minutes time interval in a QUAD-MOT at 500 μm from the chip surface after the Rubidium deposit. The linewidths are 1.47 MHz and 1.49 MHz respectively. We observe a slow drift of the resonance frequency by 0.794 MHz.

in their final configuration, propagating parallel to the chip surface in the x direction. We have observed that local changes of the magnetic field conditions were much more frequent with the blue laser beam perpendicular to the chip. Indeed, the high blue laser power was able to induce transitions in the superconducting film. This is the main reason why we have changed to the parallel excitation scheme. Figure III.15 shows two resonances recorded at a two hours time interval. They both have a width of 1.5 MHz, corresponding to a gradient of the stray electric field reduced by more than one order of magnitude, down to 1 $(\mathrm{V/cm})^2$. In this two-hours time interval, the line centre drifted by 0.8 MHz only. In fact, we observed a slow oscillation of the line centre with time, that could be rapidly tracked to an imperfection of the laser looking system.

With the narrow spectra obtained after the Rb deposition, we were able to reveal an imperfection of the 780 nm laser locking system, evidenced by the slow drift of the resonance over a sub-MHz interval. The EOM used to create the 20 MHz sidebands on the laser for the PDH lock system was indeed acting as a low-finesse Fabry Perot cavity. The effective length of this cavity was changing over times in the minutes to hours range due mainly to thermal drifts. The signal average level was changing accordingly, leading to a small change in the laser frequency. This imperfection was easily removed by changing slightly the alignment of this component and adding a thermalization cover. The laser stability was considerably increased.

Figure III.16 presents the two-photon transition line $|5S\rangle \rightarrow |60S\rangle$ recorded in a cold magnetic trap with the improved laser system. The laser pulse duration was 10 μs and the two-photon Rabi frequency $\Omega_{rb} = 105$ kHz. The linewidth of each laser was measured by heterodyne interferometry, described in Appendix C of [42]. It was 15(4) and 8.8(16) kHz for the red and blue lasers respectively. The measured width of the two-photon transition

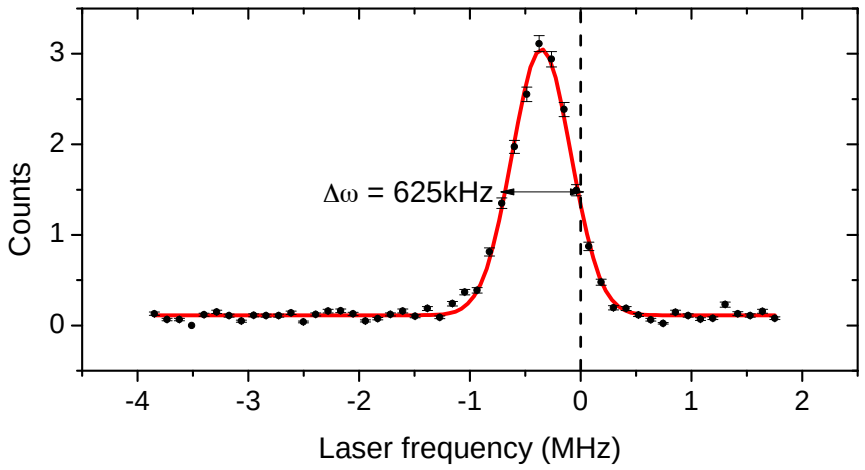

Figure III.16: Laser line $5S \rightarrow 60S$ recorded in a diluted magnetic trap at $300\,\mu$m from the chip surface. The FWHM is 625.6 KHz.

is 625.6 KHz.

We have repeatedly checked the optical line position and its width over a few months time period. We have found no evidence of a systematic drift or of an increase in the field gradients. The Rubidium coating is thus quite stable. Of course, the experiment remained cold during this entire period to avoid Rubidium desorption.

III.6 Conclusion of the chapter

We have introduced the Rydberg atoms detection setup. We have described evidence relating the problem of electrical fields inhomogeneities with a slow Rubidium deposition on the surface of the superconducting chip. We have concluded, from Appendix A, that the width we observed was related to residual electric fields. We have described our first attempts to correct for this problem by depositing *Rb* using the MOTs.

Finally we have shown that the solution was the deposition of Rubidium through dispensers. With this technique, we have estimated a deposition of $\sim$ 86 nm Rubidium on the chip surface and we have finally observed a narrow and stable optical excitation spectrum. This result was encouraging enough to investigate further the atomic coherence by millimeter-wave spectroscopy. These results will be described in the next chapter.

Chapter IV

Long coherence time measurements for Rydberg atoms on an atom-chip

In the previous chapters, we have presented the theoretical basis, the details of the experimental setup and the first measurements of the electric field near the superconducting surface, based on the spectroscopy of the $5S \rightarrow 60S$ two-photon optical transition. After the macroscopic Rubidium deposition on the front surface of the chip (chapter III, section III.5), the stray electric fields were considerably reduced, an essential step in this work. The laser line remained stable for months, providing an experimental setup appropriate for coherent manipulations of the atoms and, later, for the study of the dipole blockade. This chapter is dedicated to microwave spectroscopy near the chip surface, providing detailed insight in the atomic levels coherence.

We have first focused on the $|60S_{1/2}, m_J = 1/2\rangle \rightarrow |60P_{3/2}, m_J = -1/2\rangle$ and $|60S_{1/2}, m_J = 1/2\rangle \rightarrow |60P_{3/2}, m_J = +3/2\rangle$ microwave transitions in six different traps at 150, 245, 338, 445, 555 and 675 μm from the chip surface, all centered at the position of the Z-shaped wire in the x and z directions. From the position of these lines, we deduce the magnetic field (bottom of the trap) for each trap distance as well as the residual electric field. The values of the magnetic field are in good agreement with the independent measurement performed by evaporative RF cooling. An estimation of the field gradients can also be obtained through these measurements. The corresponding results are presented in sections IV.1 to IV.2.3.

Microwave transitions are well suited for the measurement of coherence times. By addressing the $|60S_{1/2}, m_J = 1/2\rangle \rightarrow |61S_{1/2}, m_J = 1/2\rangle$ two-photon transition in two traps, at 150 μm and 450 μm from the chip, we have observed Rabi oscillations, Ramsey sequences and echo sequences in our atomic ensemble. The coherence times deduced from these measurements reach values in the millisecond range. The results are presented in section IV.3.

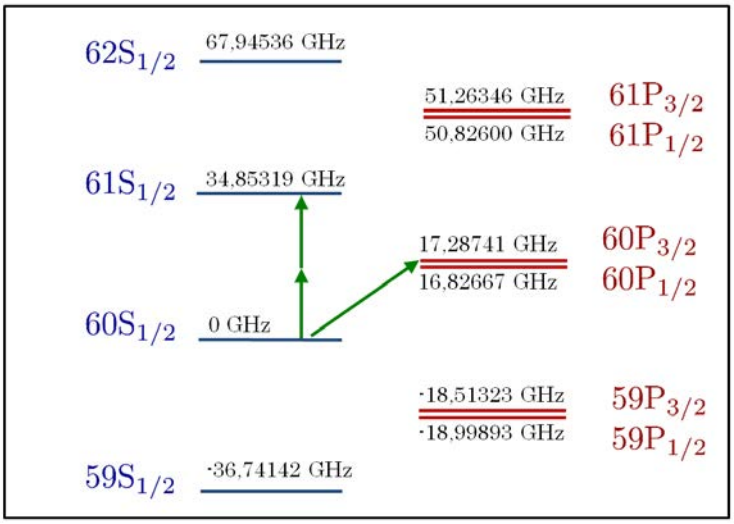

Figure IV.1: Microwave transitions used in this work (green arrows). The $|60S_{1/2}\rangle \rightarrow |61S_{1/2}\rangle$ transition is a two-photon one. The energies are calculated from the quantum defects and they are given with respect to that of the initial state $|60S_{1/2}\rangle$.

IV.1 Experimental conditions of microwave spectroscopy

A detailed energy diagram of the Rydberg levels close to the target state $|60S\rangle$ is presented in figure IV.1.

In order to map the electric field in front of the chip surface, we make use of the precise knowledge of the Rydberg states energies calculated taking into account the quantum defects and the Stark shifts. The Stark constants for the useful transitions are given in chapter I, section I.1.3 for the two limiting case in which the F_x or F_z electric field components are equal to zero.

The differential Stark effect for the $60S \rightarrow 61S$ transition is $-10,95$ MHz $(\mathrm{V/cm})^{-2}$, whereas it is about 50 times larger for the $60S \rightarrow 60P$ transition (for $m_j = 3/2$ and $F_z = 0$, it is $-479,6$ MHz $(\mathrm{V/cm})^{-2}$ and for $F_x = 0$, -557 MHz $(\mathrm{V/cm})^{-2}$). This is the reason why we use the latter transition for measurements of the electric field as a function of the distance to the surface.

For all the measurements, we prepare a cold cloud trapped in a Ioffe-Pritchard magnetic trap, with a temperature in the $T = 1.7 - 9.7\,\mu$K range and a ground state atom number in the $2 - 13 \times 10^4$ range. We operate within this temperature range in order to avoid density effect [62]. For instance, at $y = 455$ μm, the density is of $1.94 \cdot 10^{12}$ at/cm^3. The characteristics of the traps are given in tables IV.1 and IV.2.

The temperature of the atoms in the trap is an important quantity. We cannot determine directly the temperature by the *time of flight* technique (described in chapter II, section II.3) for the traps near the chip, since we cannot turn off suddenly the B_z field when it has a high value. We have thus used the time of flight technique to obtain the temperature of a trap at $y = 455$ μm from the chip surface, at $z = -351.3$ μm. This trap is

T. Dist. μm	$\sim$ # Atoms	# Ryd.	Freq. meas. Hz	Freq. simul. Hz	Temp. μK
150	8.26×10^4	0.37		$(55, 843, 821)$	9.7
245	7.22×10^4	0.42		$(56, 347, 327)$	5.34
338	6.54×10^4	0.315		$(50.6, 202, 188)$	3.6
455	5.1×10^4	0.142	$(37, 107, 121)$	$(41.3, 116, 114)$	2.26
455	1.3×10^5	0.2	$(31.15, 86.3, 63.5)$	$(35, 84.9, 77.8)$	**1.6**
555	5.16×10^4	0.3		$(38.3, 120, 116.6)$	2.34
675	8.94×10^4	0.23		$(33, 85, 75)$	1.72

Table IV.1: Characteristics of the traps. This table gives the number of atoms in the ground state, the number of detected Rydberg atoms, the frequencies of the traps (measured and predicted by simulations), and the calculated temperature. The approximate number of atoms in the ground state is given by absorption images. In bold, we give the average temperature of the trap at $(y, z) = (455, -351)$ μm measured directly by the time-of-flight technique.

Dist. μm	Dimensions μm meas.	Dimensions μm simul.	Position (y, z) μm
150		$(88.15, 5.75, 5.91)$	$(150, -15.2)$
245		$(64.24, 10.37, 11.0)$	$(245, -23.83)$
338		$(58.37, 14.62, 15.71)$	$(338, -29.79)$
455	$(63.25, 21.88, 19.34)$	$(57.9, 20.62, 20.98)$	$(445, -21.28)$
455	$(63.21, 22.82, 31.01)$	$(59.17, 24.39, 26.62)$	$(445, -351.3)$
555		$(62.18, 19.84, 20.42)$	$(555, --)$
675		$(61.87, 24.02, 27.22)$	$(675, -40.3)$

Table IV.2: Dimensions of the traps calculated with the temperature and the trap frequencies (simulated or measured, these two values agreeing within 10%). We give also the relative position of each cloud with respect to the center of the Z-shaped wire center.

particularly important, since we use it for the Rabi, Ramsey, and echo sequences. From the horizontal and vertical expansions, we deduce an average temperature of $T = 1.6 \pm 0.3\,\mu$K. The temperatures of the other traps can be extrapolated from this value. The trap density in phase-space, assuming an harmonic potential, is:

$$\beta = N \cdot \left(\frac{\hbar \bar{\omega}}{k_B T} \right)^3 \tag{IV.1}$$

where N is the atom number and $\bar{\omega}$ is the average harmonic oscillator frequency

$$\bar{\omega} = \sqrt[1/3]{w_x w_y w_z}.$$

For an adiabatic decompression while we move far away from the chip surface, β remains constant. The atom number on the other hand can be considered also constant for all the

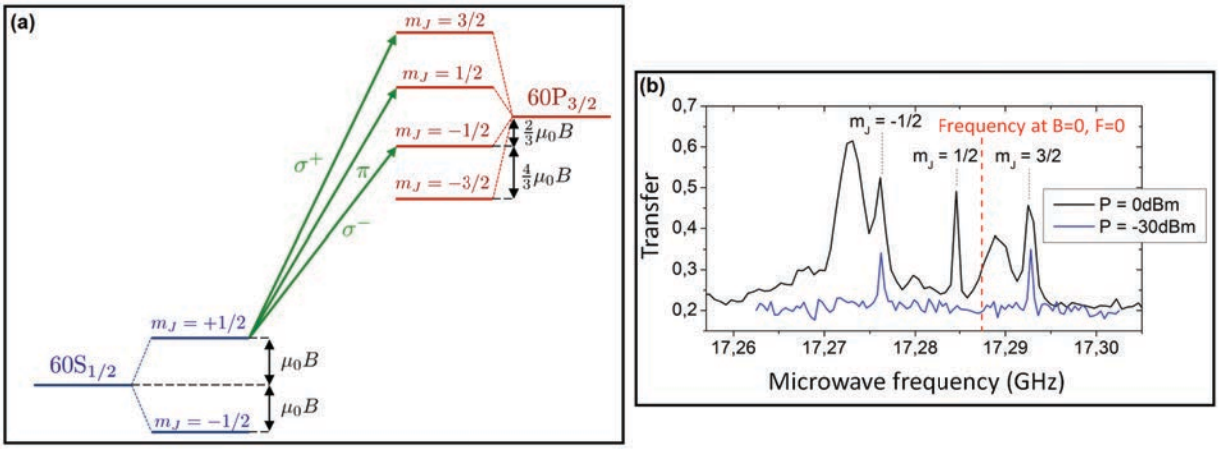

Figure IV.2: **(a)** Zeeman splitting for the transition $|60S_{1/2}\rangle \rightarrow |60P_{3/2}\rangle$. The polarization for each transition is given in the figure. **(b)** First spectrum of the $|60S_{1/2}\rangle \rightarrow |60P_{3/2}\rangle$ transition for two different microwave powers, 0 and -30 dBm. The microwave propagation direction is almost aligned with x, which is the quantization axis defined by the magnetic field of the trap. Due to a slight misalignment with this axis and to the small size of the cryostat windows, the contribution of the π polarization is observable for the highest power.

observed traps. The temperature is thus finally proportional to the trap frequency

$$T \propto \bar{\omega}.$$

For all measurements reported here, the laser beam geometry corresponds to the one given in table III.1. Both lasers are parallel to chip surface as schematized in figure III.3. The power of the red excitation laser varies from 100 nW to 2 μW in order to control the number of Rydberg excitations (up to $\simeq 3$). We prepare only about 0.3 Rydberg atom per shot in order to avoid any broadening of the transition due to dipole-dipole interactions. The probability of excitation thus only depends upon the laser pulse characteristics. The laser pulse duration is 300 ns. This short duration broadens the laser line. This allows us to avoid spatial selection due to electric field inhomogeneities. The Rydberg cloud dimension results thus only from the interplay between the cold atom cloud and laser geometries.

After the laser pulse, we apply a microwave pulse, with a duration of tens of μs, whose frequency is scanned around the $|60S_{1/2}, m_J = 1/2\rangle \rightarrow |60P_{3/2}, m_J = -1/2, \rangle$ and $|60S_{1/2}, m_J = 1/2\rangle \rightarrow |60P_{3/2}, m_J = +3/2, \rangle$ resonances. The duration and the power of the microwave pulse are chosen so that they do not contribute to the width of the transition. These two transitions have different frequencies due to the non-zero magnetic field at the bottom of the trap $B = B_x$, which varies from one trap to the other from 4 to 9 Gauss. The degeneracy of the two $|60P_{3/2}, m_J\rangle$, with $m_j = -1/2$ and $+3/2$, Zeeman sublevels is thus lifted by 15 to 33 MHz. The corresponding energy diagram is shown in figure IV.2(a).

The ionization electrode plates $V_{ion1,2}$ are connected by the circuit given in figure III.6. The timing and the ionization ramp used for this experiment are shown in figure IV.3.

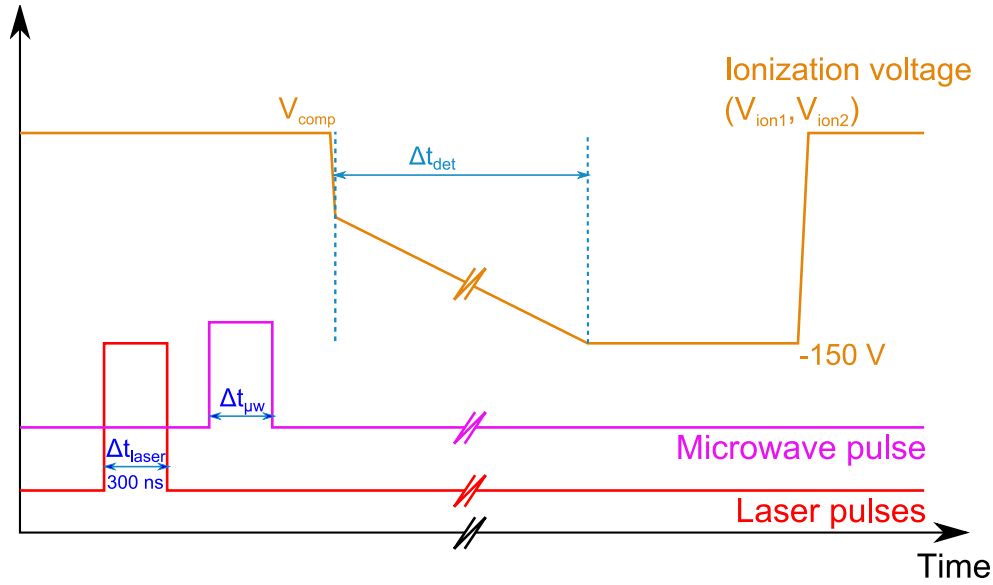

Figure IV.3: Typical voltage ramp sequence with laser and microwave pulses. The slow part of the ramp has a duration $\Delta T_{det} = 50$ μs. The laser pulse is 0.3 μs long and the microwave pulse duration varies from 5 to 20 μs. The microwave pulse lasts a few tens of microseconds. The time interval between the laser pulse and the microwave pulse is 1 μs.V_{comp} is the initial voltage needed for the electric field compensation in the y direction

The difference of ionization thresholds between the $60S_{1/2}$ and $60P_{3/2}$ or $61S_{1/2}$ leads to different arrival times for the ions. We can thus detect these levels selectively, as discussed in chapter III. Typically, we perform $100 - 300$ repetitions of Rydberg excitation and detection, separated by a 3 ms time interval, for each cold atomic cloud prepared. A new cold atomic ensemble is prepared every 8 s. The number of repetitions is limited by the heating of the cloud due to the residual absorption of red photons. We could increase this number by reducing the power of the red laser, but we would reduce also the amount of detected Rydberg atoms.

The microwaves are generated from a commercial *Anritsu* synthesizer stabilized to sub-Hertz level and sent directly through one of the cryostat optical access (figure III.3). The microwave is transmitted through the three windows of the cryostat, propagating near to the x-direction (quantization axis direction) before reaching the atomic cloud. The polarization is linear outside the cryostat. This would mean, for the atoms, a combination of σ_- and σ_+ light. However, the direction of propagation is not perfectly aligned with the x axis and the small size of the windows affects the microwave propagation. The polarization experienced by the atoms contains a little contribution of π-polarization. At high power, we can address three microwaves transitions as shown in figure IV.2(b). The possible transitions (selection rules) are given by the green arrows in IV.2(a).

IV.2 Characterization of residual electric field by microwave spectroscopy

IV.2.1 Electric field perpendicular to the chip surface

For each microwave transition, we cancel the $\mathbf{F}_y$ field component at the cloud position by adjusting the compensation voltage in order to get the highest transition frequency (the quadratic Stark effect of the $60S_{1/2} \rightarrow 60P_{3/2}$ transition is negative). From the calibration of $\mathbf{F}_y$ created at the atomic position as a function of the voltage applied on the electrodes (see appendix B), we can compute the compensation field $\mathbf{F}_y^{comp}$ at each trap distance. The results of these measurements are shown in figure IV.4. The resulting compensation field $\mathbf{F}_y^{comp}$ is independent of y within the error bars. The average value is 0.09 V/cm which is almost two orders of magnitude smaller that the one in the "fresh chip condition", 3.7 V/cm (chapter III).

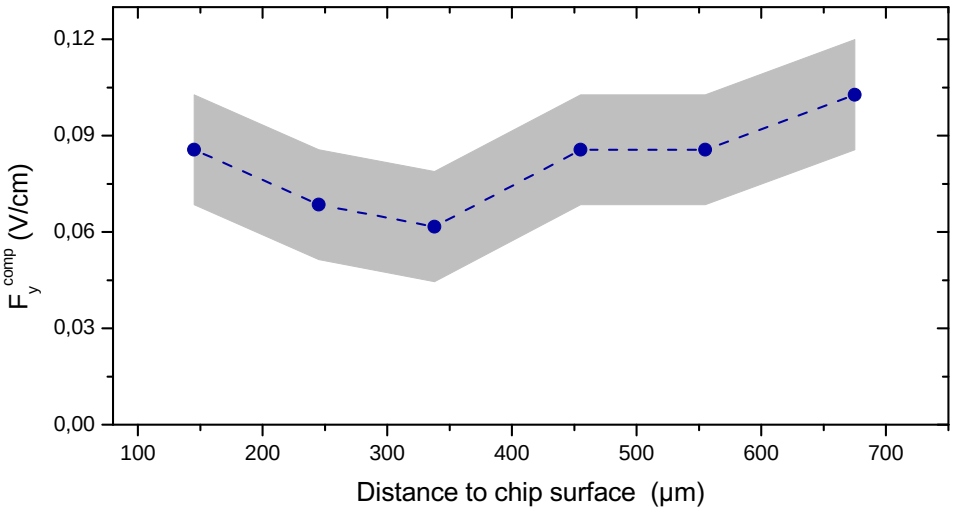

Figure IV.4: Electric field component perpendicular to the chip. On the average, we get 0.09 V/cm, which is almost two orders of magnitude smaller than the value observed before the Rubidium film deposition (3.7 V/cm). Within the error bars defined by the experimental uncertainty, we can conclude that the gradient of the perpendicular field along the y-direction is almost zero.

IV.2.2 Field parallel to the chip surface

Once the perpendicular field component $\mathbf{F}_y$ is properly compensated, we register the spectra of the $|60S_{1/2}, m_J = 1/2\rangle \rightarrow |60P3/2, m_J = -1/2\rangle$ and $|60S_{1/2}, m_J = 1/2\rangle \rightarrow$

$|60P3/2, m_J = +3/2\rangle$ transitions for the six traps. These spectra are presented in figure IV.5, together with Lorentzian fits. The widths of the two lines are proportional, according to the ratio between the Stark shift constants. This ratio depends on whether we consider $\mathbf{F}_x = \mathbf{0}$ or $\mathbf{F}_z = \mathbf{0}$. For the first case, the ratio is $FWHM_{+3/2}/FWHM_{-1/2} \approx 1.1$ and for the second ≈ 0.82. The information about the widths and the frequency transitions is summarized in table IV.4.

From the position of the two lines and the knowledge of the Stark and Zeeman effects for $m_j = -1/2$ and $m_J = +3/2$ sublevels, we compute the magnetic field $B_x = |\mathbf{B}|$ and the residual electric field in the xz plane either assuming $\mathbf{F_z} = \mathbf{0}$ or $\mathbf{F_x} = \mathbf{0}$. We show here the case of $\mathbf{F_z} = \mathbf{0}$, i.e. that of an electric field parallel to $\mathbf{B}$ in the plane xz. We use the following equations

$$f_{-1/2} = f_0 - \frac{5}{3}\mu_0 B + K^{(2)} B^2 + A^{\parallel}_{-1/2} F_x^2 \tag{IV.2}$$

$$f_{+3/2} = f_0 + \mu_0 B + A^{\parallel}_{+3/2} F_x^2 \tag{IV.3}$$

where f_0 is the transition frequency in zero electric and magnetic field and f_{m_j} is the measured frequency transition for $m_J = -1/2$ and $m_J = +3/2$ levels. The quadratic Zeeman constant $K^{(2)}$ is equal to $h \cdot 1.03$ kHz/G^2. Only the $m_J = -1/2$ level affected by a quadratic shift. Solving this system, we get B:

$$A^{\parallel}_{+3/2} K^{(2)} B^2 - \left(A^{\parallel}_{-1/2} + \frac{5}{3} A^{\parallel}_{+3/2} \right) \mu_0 B + A^{\parallel}_{-1/2} \left(f_{+3/2} - f_0 \right) - A^{\parallel}_{+3/2} \left(f_{-1/2} - f_0 \right) = 0 \tag{IV.4}$$

and the electric field F_x by

$$F_x = |\mathbf{F_x}| = \sqrt{\frac{f_{+3/2} - f_0 - \mu_0 B}{A^{\parallel}_{+3/2}}}. \tag{IV.5}$$

The magnetic field is given as a function of y in figure IV.6. We present here the values computed for the two limit orientations of the electric field with respect to the x axis, together with the values deduced from the r.f. spectroscopy in the trap. The best agreement is obtained by assuming the electric field parallel to the quantization axis. Table IV.3, summarizes the measurements of the field at the bottom of the trap. For the trap at 450 μm (spectra in figure IV.5, frame (d)), the magnetic field deduced from the microwave spectroscopy agrees within $\leq 1.5\%$ with the results of the RF spectroscopy. The corresponding value of the uncompensated electric field $|\mathbf{F}_x|$ is shown in figure IV.7.

The uncompensated electric field in the plane xz is largest near the chip surface, with a value always below 0.1V/cm. These measurements show that the electric field is well known and controlled. This mapping of the electric field has been stable for months.

IV.2.3 Electric field gradients

We have estimated the gradient of the electric field in two different ways: first from the electric field measurement given in subsections IV.2.1 and IV.2.2 and second, by moving

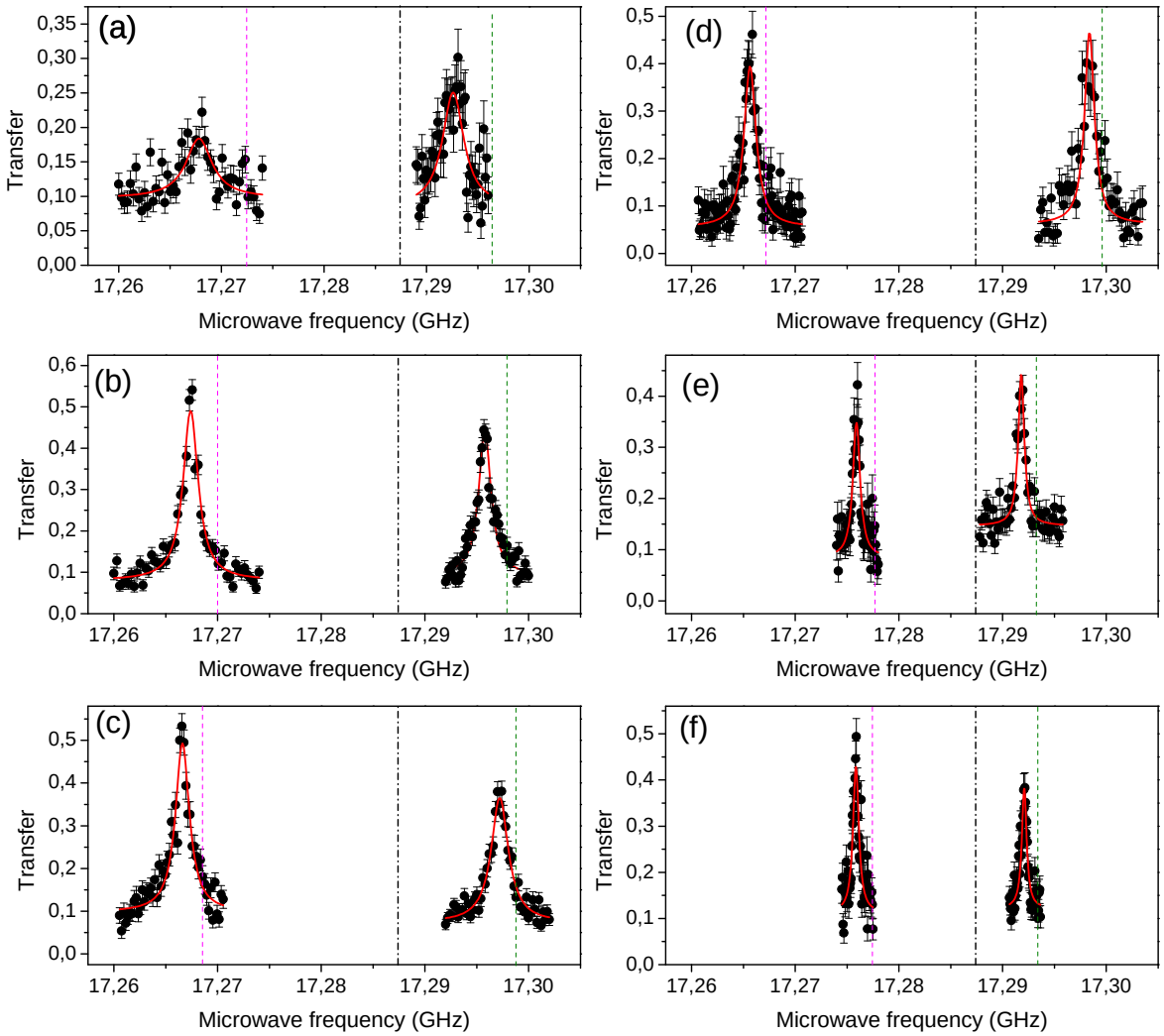

Figure IV.5: Microwave transitions at **(a)** 150 μm, **(b)** 245 μm, **(c)** 338 μm, **(d)** 455 μm, **(e)** 555 μm and **(f)** 675 μm from the chip surface. We observe the transition $|60S_{1/2}, m_J = -1/2\rangle \rightarrow |60P_{3/2}, m_J = +3/2\rangle$ (right), and the transition $|60S_{1/2}, m_J = 1/2\rangle \rightarrow |60P_{3/2}, m_J = -1/2\rangle$ (left). The fit assumes $\mathbf{F_z} = \mathbf{0}$, leading to two linewidths in the ratio $FWHM_{+3/2}/FWHM_{-1/2} \approx 0.82$ (ratio of the Stark shift constants). In black dash-doted line, we give the transition frequency $|60S_{1/2}\rangle \rightarrow |60P_{3/2}\rangle$ at $\mathbf{B} = \mathbf{0}$ and $\mathbf{F} = \mathbf{0}$. In green dashed line, we give the frequency of the transition $|60S_{1/2}, m_j = +1/2\rangle \rightarrow |60P_{3/2}, m_j = +3/2\rangle$ in zero electric field. In magenta, we point the $|60S_{1/2}, m_j = +1/2\rangle \rightarrow |60P_{3/2}, m_j = -1/2\rangle$ transition in zero field.

Trap μm	Bot. trap RF G	Bot. trap **B** $\parallel$ **F** G	Bot. trap **B** $\perp$ **F** G	% $\parallel$ diff.	% $\perp$ diff.
150	6.23	6.42	6.78	3.1	8.8
245	7.46	7.49	7.67	0.4	2.8
338	8.15	8.12	8.26	0.3	1.4
455	8.69	8.71	8.8	0.3	1.5
555	4.09	4.17	4.3	2.1	5.2
675	4.22	4.28	4.39	1.4	4.2

Table IV.3: Comparing measurements of magnetic field.

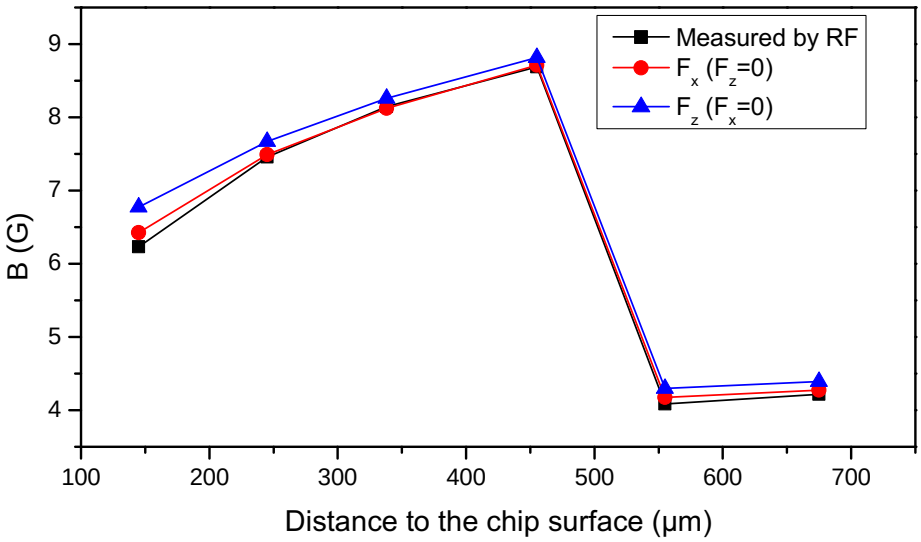

Figure IV.6: Magnetic field calculated for the two possible orientations of $\mathbf{F_{xz}}$. The graph seems to indicate that the electric field is oriented parallel to **B**, since we get a better agreement with the values extracted by RF spectroscopy. Exact values can be found in table IV.3.

the laser position in the z and y direction. The last method is described in Appendix C.

From figure IV.4 we can directly see, within the error bars, that

$$\frac{\partial F_y}{\partial y} = 0. \tag{IV.6}$$

From figure IV.7, and using the width of the transition lines given in table IV.4, we can calculate the gradient of the parallel field for each atomic position along the x and z directions if the width of the lines was only due to electric field inhomogeneties in these directions. For that, we use the half width diameter calculated from table IV.2 for each

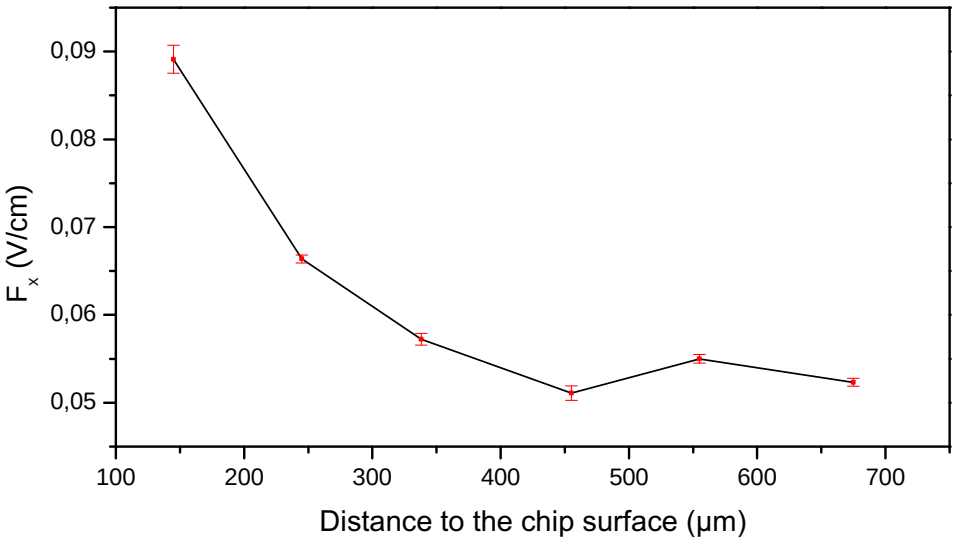

Figure IV.7: Electric field F_x parallel to the quantization axis. We assume the electric field to be along the x-direction since the best agreement for the magnetic field is found for $F_z = 0$. Exact values are given in table IV.4.

Trap μm	FWHM $m_J = -1/2$ MHz	FWHM $m_J = +3/2$ MHz MHz	Transition center $m_J = -1/2$ GHz	Transition center $m_J = +3/2$ GHz	F_x V/cm
150	3.1	2.54	17.26781	17.29259	0.089
245	1.77	1.45	17.26741	17.29578	0.066
338	2.0	1.64	17.26660	17.29721	0.057
455	1.4	1.15	17.26563	17.29835	0.051
555	0.85	0.7	17.27592	17.29180	0.055
675	0.68	0.56	17.27585	17.29208	0.052

Table IV.4: Case $\mathbf{B} \parallel \mathbf{F}$. All values are taken from the fits in figure IV.5. The ratio of the widths of the transition lines is given by the ratio of the Stark shift constants. For the parallel case, we have $A_{+3/2}/A_{-1/2} \approx 0.82$. The width for the Lorentzian fits were set to give this proportion. The magnetic field values can be found in table IV.3.

cloud. We present the gradients in two tables IV.5 and IV.6. The gradient in the z direction is calculated with the excitation region defined by the convolution of the size of the cloud in the y and z directions with the blue laser dimension (see figure IV.8). For the traps whose dimensions are larger than the region defined by the laser beam diameter, we calculate the gradient assuming it to be predominantly in the z-direction.

We calculate also how the parallel field varies as a function of the distance to the chip

Distance μm	d_x μm	$\partial\|F_x\|/\partial x$ V/cm^2
150	207.7	1.4282
245	151.2	1.5038
338	137.5	2.166
455	149.1	1.5659
555	146.5	0.9
675	145.8	0.7601

Table IV.5: Using the width of the transition lines and the diameter of the cloud (d_x is the cloud FWHM) for each trap, we calculate the gradient in the x-direction, calculated assuming the field along the x direction.

Distance μm	$d_\perp$ μm	$\partial\|F_x\|/\partial z$ V/cm^2
150	13.6	21.7144
245	25.2	9.0227
338	25.9	11.5968
455	25.9	9.0112
555	25.9	5.088
675	25.9	4.277

Table IV.6: Using the width of the transition lines and the excitation region diameter defined by the convolution of the size of the cloud in the y and z directions with the blue laser dimension, we calculate the gradient assuming it to be predominantly in the z-direction, calculated assuming the field along the x direction.

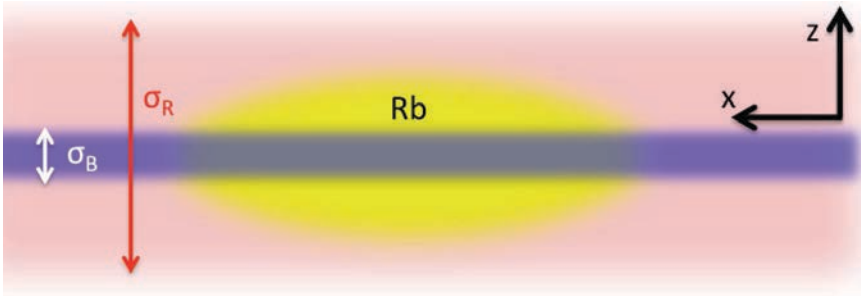

Figure IV.8: Excitation region. Along x, it is defined by the size of the cloud. Along y and z, for the traps from $y = 245$ μm to $y = 675$ μm, the excitation region is defined by the blue laser, which has a half width $\sigma^{(e^{-2})} = 22$ μm.

with the data of the figure IV.7. We get (around $y = 455$ μm):

$$\frac{\partial|F_x|}{\partial y} = \frac{(0.057 - 0.051) \text{ V/cm}}{(455 - 338) \ \mu\text{m}} = 0.5 \text{ V/cm}^2 \tag{IV.7}$$

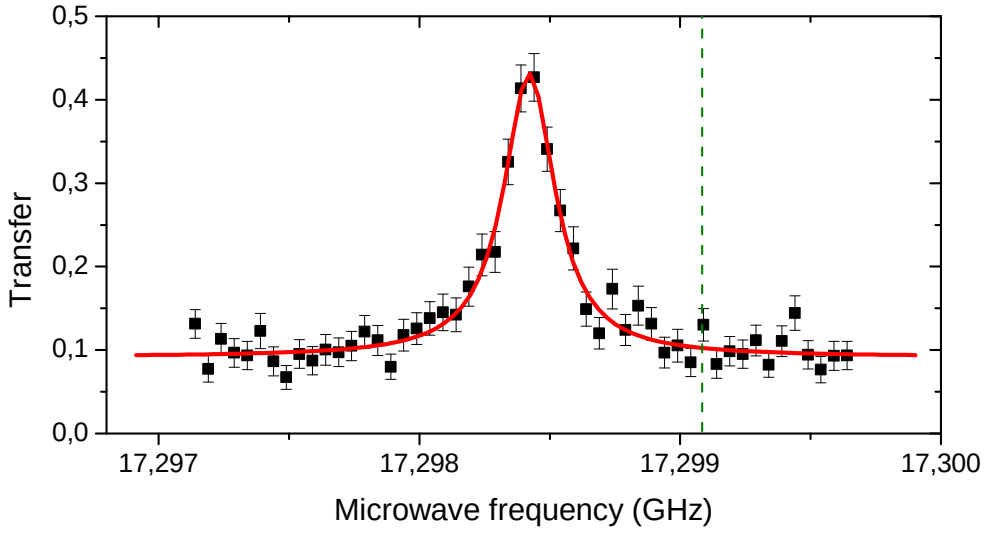

Figure IV.9: $60S_{1/2}, m_J = 1/2 \rightarrow 60P_{3/2}, m_J = +3/2$ transition at 455 μm from the chip surface. The FWHM of the Lorentzian fit is 240 kHz.

which is an upper bound for the actual gradient in this direction.

IV.3 Probing coherence times with Ramsey spectroscopy and spin echo sequences.

We have measured the electric field and estimated the electric field gradient at the cloud position. Now, we want to measure the coherence time of microwave transitions by Ramsey and spin-echo sequences.

We performed these experiments for two traps: one at $y = 150$ μm from the chip, centered with respect to the Z-wire center in the plane xz, and another at $y = 450$ μm from the surface, lowered by $z = -351$ μm with respect to the Z-wire center. For this distance, we have lowered the trap since the measured gradients in the y and z directions (obtained by scanning the blue laser position as reported in Appendix C) are at least two times smaller than those estimated at the Z-wire center. More precisely, at $y = 455$ μm, $z = 0$, the estimated gradient along x is 2 V/cm^2 (see tables IV.1 and IV.2) and $\simeq 10$ V/cm^2 along z. These values are larger than those found by scanning the laser position at $(y, z) = (455, -351)$ μm, $\partial F/\partial z = 1$V/cm^2 ($\partial F/\partial y = 0.5$ V/cm^2) and $\partial F/\partial z = 1$ V/cm^2. With these lower gradients, we get for instance a spectrum on the $S-P$ transition with a FWHM of 240 kHz, much less that the value found at $z \approx 0$ (≈ 1.4 MHz). The corresponding spectrum is shown in figure IV.9.

IV.3.1 Spectra and Rabi oscillations

We investigate first the coherence time of Rydberg atoms by studying the transition $|60S_{1/2}, m_J = 1/2\rangle \rightarrow |61S, m_J = 1/2\rangle$. The relative Stark effect on this two-photon transition between the $60S_{1/2}$ and the $61S_{1/2}$ levels is much smaller than that for the transition to the $60P_{3/2,m_J=+3/2}$ level.

In figure IV.10, we show the spectrum for both traps obtained with a microwave pulse duration of 50 μs, with a Lorentzian fit in red. In frame (a), the transition at 150 μm exhibits FWHM of 41.7 kHz. For the trap at $(y, z) = (455, -351)$ μm, the FWHM is 7.3

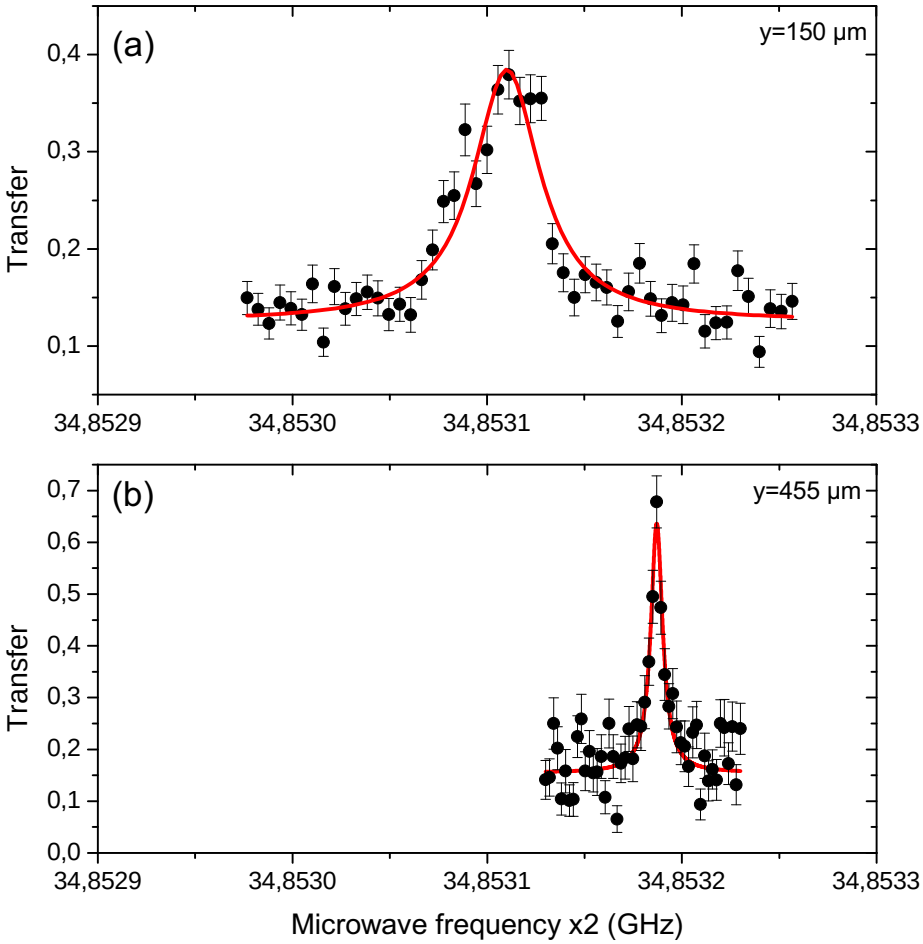

Figure IV.10: **(a):** $60S_{1/2}, m_J = 1/2 \rightarrow 61S, m_J = 1/2$ transition at 150 μm from the chip surface. Microwave pulse duration 50 μs. The red fit is a Lorentzian with FWHM 41.7 kHz.**(b)**: $60S_{1/2}, m_J = 1/2 \rightarrow 61S_{1/2}, m_J = 1/2$ transition at 455 μm from the chip surface. Red line: Lorentzian fit with FWHM 7.3 kHz.

kHz (figure IV.10, frame (b)). Using the gradient measurements at this position (Appendix C), we estimate a Gaussian profile with a FWHM of 3.18 and 151 kHz for the $60S - 61S$

and $60S-60P$, $m_J = +3/2$ transitions respectively. This suggests again that the transition lines are broadened by a noise (slow drift or fast noise) on the electrode used for the electric field compensation along y. Anyway, the widths obtained in Fig IV.10, correspond to a very encouraging coherence time that we proceed to study in more detail in the next sections.

For both traps, we have performed Rabi oscillations experiments. The microwave frequency is kept constant, in resonance with the transition, and the duration of the microwave pulse is scanned. This step is important to calibrate the $\pi/2$ and π pulses used for the Ramsey and spin-echo measurements. The excitation and detection sequence is shown in the figure IV.11.

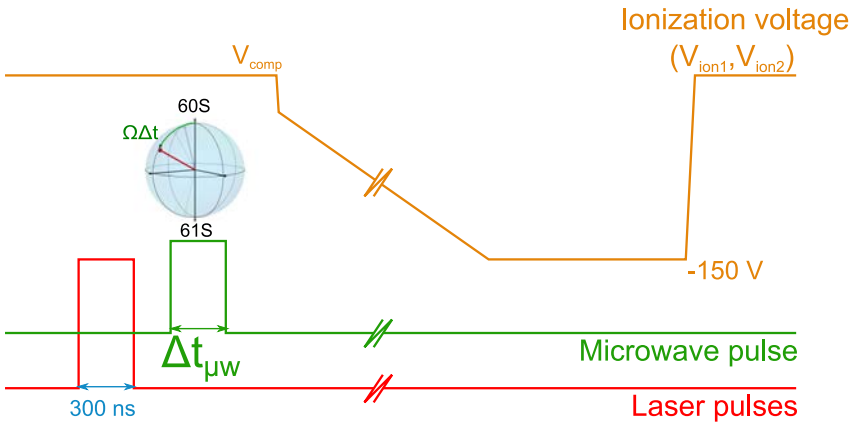

Figure IV.11: Sequence for Rabi oscillations data acquisition.

Two examples are shown. At 150 μm (figure IV.12, frame (a)), we get a Rabi oscillation damping time, defined at $1/e$, $t_{Rabi} = 44.07$ μs. The reason why the oscillations are not centered at 0.5 tranfer value is related to the imperfect discrimination of the $60S$ and $61S$ levels by the field ionization detection.

For the trap at $(y, z) = (455, -351)$ μm, the Rabi oscillations obtained for the $|60s_{1/2}, m_J = 1/2\rangle \rightarrow |61S_{3/2}, m_J = +1/2\rangle$ transition are shown in Fig. IV.12, frame (b). The Rabi oscillation damping time is in this case $t_{Rabi} = 200$ μs.

The decay of the Rabi oscillations gives a timescale, which results from the dephasing of different atoms across the cloud. When performing these measurements, a permanent drive field is applied on the atoms, affecting the decay of the signal. We thus turn to Ramsey spectroscopy to measure the coherence decay associated to the free evolution of our sample.

IV.3.2 Ramsey spectroscopy

The coherence of the superposition between the $|60s_{1/2}, m_J = 1/2\rangle$ and $|61S_{1/2}, m_J = 1/2\rangle$ levels has been probed with a Ramsey interferometry experiment. A $\pi/2$ pulse is applied to

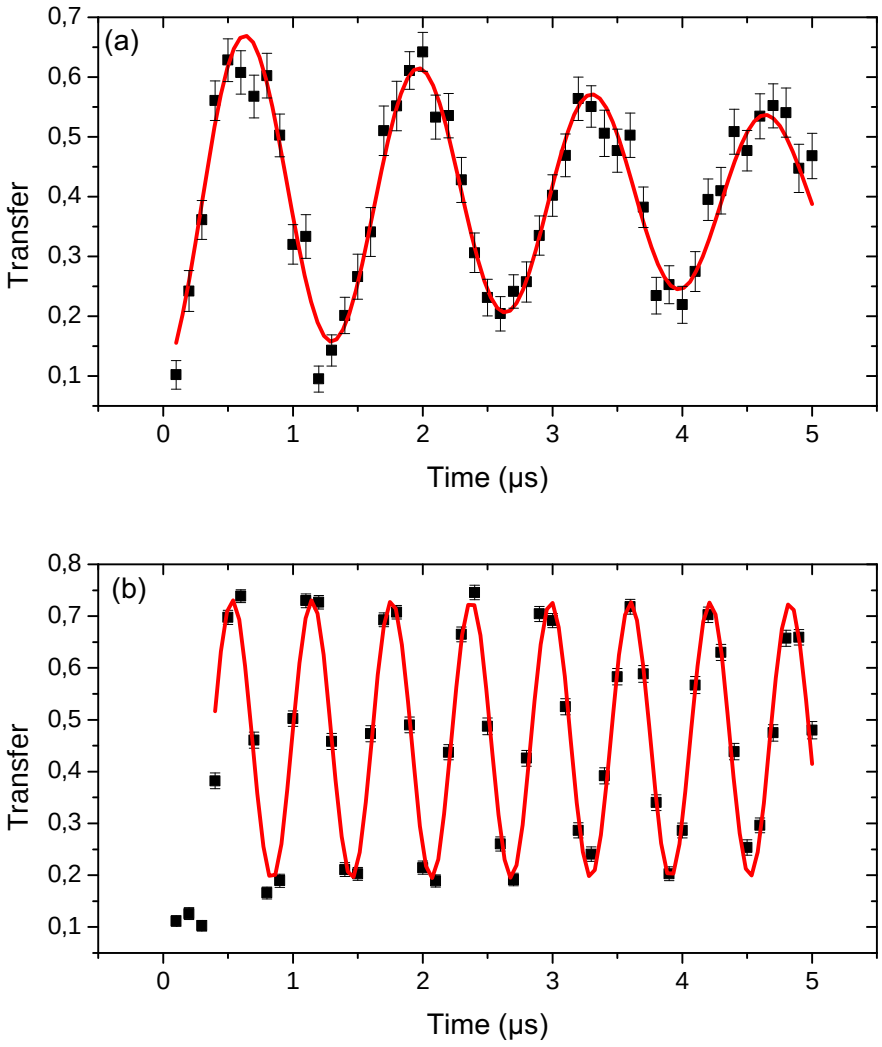

Figure IV.12: Probability of finding the atoms in the excited level as a function of the microwave pulse duration for the $60S_{1/2}, m_J = 1/2 \rightarrow 61S, m_J = 1/2$ transition, at **(a)** 150 μm from the chip surface. The fitting function is an exponentially damped sine. The Rabi oscillation damping time is 44.07 μs, defined at $1/e$. **(b)** Same signal at 450 μm from the chip surface. The Rabi oscillation damping time is 200 μs, defined at $1/e$.

the atoms, preparing them in a superposition of the two Rydberg states. The atoms evolve freely for some time, before another $\pi/2$ pulse is applied to *probe* them. The population in the ground and in the excited level are then measured. A typical sequence is shown in figure IV.13.

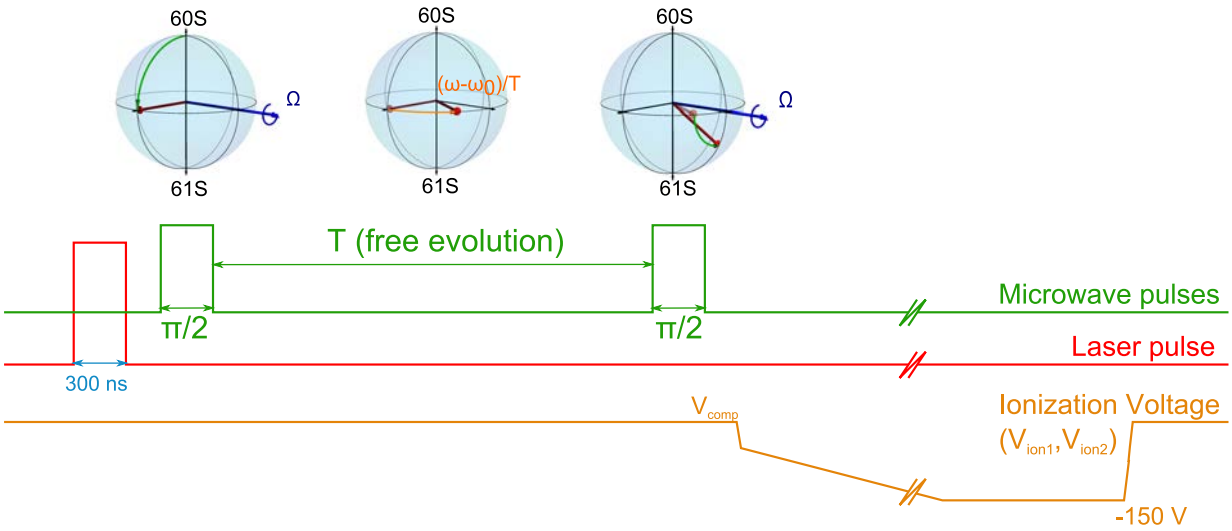

Figure IV.13: Ramsey sequences. A $\pi/2$ pulse with a detuning with respect to the resonant frequency of the $60S - 61S$ transition, prepares the atoms into a superposition state (equator of the Bloch sphere). The phase of the state evolves with a frequency equal to the difference of the transition frequency with the microwave frequency. A second $\pi/2$ pulse applied after a tunable free evolution time T and the final atomic state is read out.

These measurements are less sensitive than the previous ones to possible voltage noise on the electrodes. For instance a rapidly varying noise (within the time scale of the Ramsey sequences) on the compensation voltage can affect the width of the transition lines, but it won't affect Ramsey sequences since all the atoms will accumulate phase on the average in the same way.

For the Ramsey data acquisition, we have varied the number of Rydberg atoms by changing the power of the red spectroscopic laser. We have observed that the contrast of the Ramsey fringes decreases when the density of Rydberg atoms increases, a telltale of the dipole-dipole interaction. The corresponding data are shown in figure IV.14, for the cloud at 455 μm, lowered by 351 μm in the z-direction. In frame (a) we give the transfer signal as a function of the separation, T, between the $\pi/2$ pulses from 90 to 110 μs and in (b) the contrast as a function of the number of detected Rydberg atoms. We discuss this effect in Appendix A, in terms of the broadening of the spectra. Since we are not primarily interested in dipole-dipole interaction for the time being, we have thus chosen to measure spectroscopic data in the region where these dipole-dipole effects are weak (less than 0.3 atom detected per excitation pulse).

For this trap at 450 μm, the $\pi/2$ pulse is performed in 0.3 μs. Figure IV.15 shows the probability of finding the atoms in the excited level $61S$ as a function of the delay between

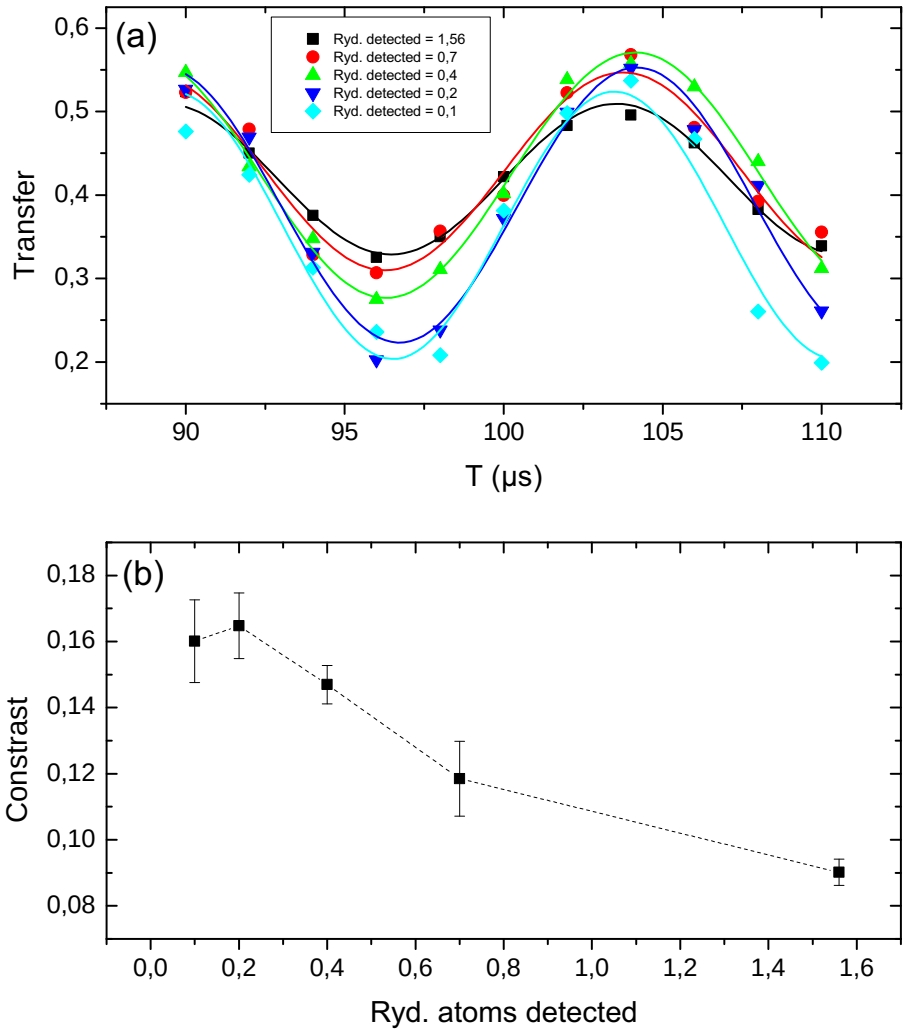

Figure IV.14: **a**: Ramsey fringes between 90 μs and 110 μs for the $60S_{1/2}, m_J = 1/2 \rightarrow 61S_{1/2}, m_J = 1/2$ transition at 455 μm from the chip surface and $z = -351$ μm for different numbers of Rydberg atoms. **(b)** Contrast of the Ramsey fringes as a function of the number of detected Rydberg atoms.

the two microwave pulses. A detuning of 70 kHz from resonance was applied for this sequence. The red curve is a fit on a sine with a Gaussian damping. The decrease of the signal contrast provides a coherence time related to the electric field inhomogeneties. From the fit, we get a coherence time at e^{-1} of 170 μs, which should correspond to a Gaussian line profile with a FWHM of 3.15 KHz. This measurement is in agreement with a rough estimation from the measured gradients (Appendix C), leading to a coherence time at e^{-1} of 165.5 μs and a FWHM of 3.18 kHz.

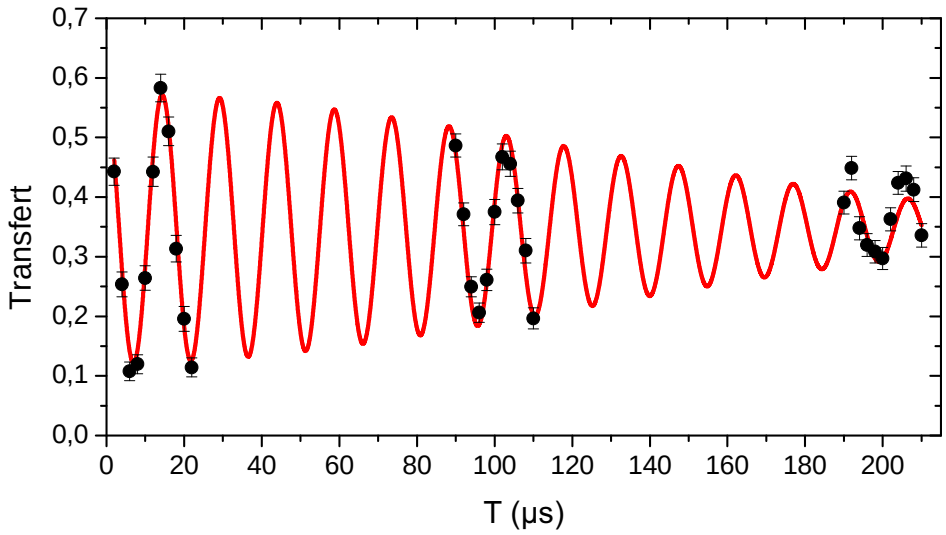

Figure IV.15: Ramsey interferometry. $60S_{1/2}, m_J = 1/2 \rightarrow 61S_{1/2}, m_J = 1/2$ transition at $455\mu m$ from the chip surface. Coherence time at e^{-1} 170 μs (Gaussian fit).

The direct microwave spectra present clearly a Lorentzian profile, corresponding to an exponential decay. The decay time extrapolated from the spectra is faster that what we observe in the Ramsey experiment. In order to understand better the Gaussian shape, the obtained coherence time, and the field gradients involved, we have numerically simulated the Ramsey sequences. We consider an atomic ensemble with a Gaussian position distribution. The electric field at the center is set to 0.056 V/cm, the value measured at $(455, -351)$ μm. The gradients are assumed to be constant in all directions. We randomly choose an atom position. The Bloch vector moves along the equator of the Bloch sphere with an angular velocity given by the detuning of the original $\pi/2$ pulse with respect to the atomic frequency, depending upon the value of the field at the atomic position. After a free evolution time T, we apply the second pulse and compute the detection probabilities. We do that for a large number N of atoms for the same T value and we average the detection results. Our simple numerical model of the evolution of the atomic coherences in a field gradient leads to a Gaussian reduction of the contrast with time. We find from this simulation that a coherence time of 170μs (Gaussian profile at e^{-1}) corresponds

to a field gradient of 0.2 V/cm^2 (0.96 V/cm^2) in the x (z) direction (cloud extension of 60μm, blue beam extension 11μm, see figure IV.8). The gradient in the z direction is in excellent agreement with the measurements reported in Appendix C for the field gradients, $\partial F/\partial z = 1$ V/cm^2.

For the trap at 150 μm, the $\pi/2$ pulse is performed in 0.7 μs, a time interval small compared to the decoherence time. Figure IV.16 shows the probability for finding the atoms in the excited level as a function of the delay between the two microwave pulses. The oscillation is at the chosen 50 kHz detuning between the microwave source and the atomic transition frequency. The contrast is damped, due to the field inhomogeneities. We thus fit the experimental data with a Gaussian decay, and obtain a coherence time of 18 μs for this two-photon transition. This result corresponds to a Gaussian profile with a FWHM of 20.8 KHz. If we fit a Gaussian profile in the S-S transition line (IV.12, frame (a)) we obtain 47.6 kHz. The difference between these values indicates again a source of broadening of the spectral lines, most probably due to a voltage noise on the electrodes.

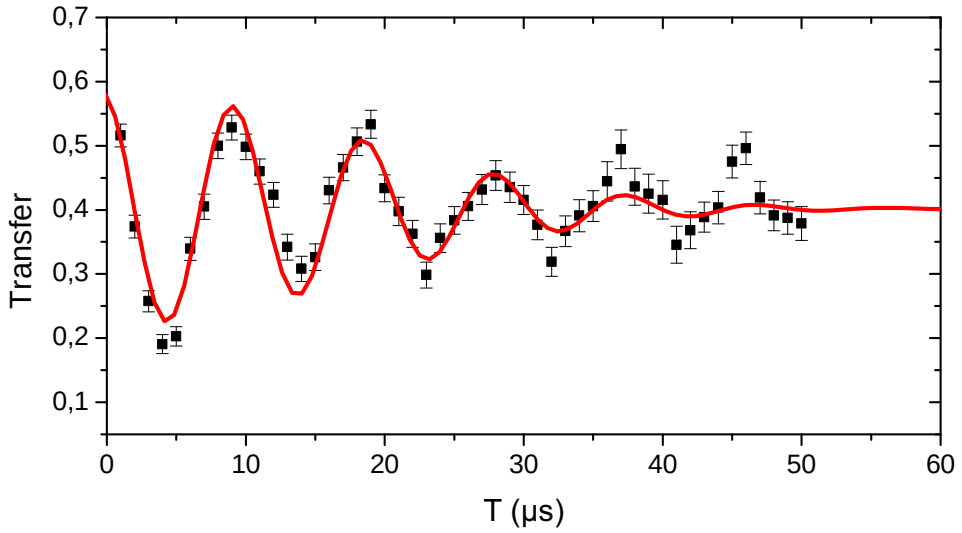

Figure IV.16: Ramsey interferometry. Probability of finding the atoms, trapped at 150 μm from the chip surface, in the excited level as a function of the delay between the $\pi/2$ pulses. The microwave is detuned from resonance by 50 kHz. The red line is a fit on an oscillation with a Gaussian contrast damping. The coherence time found is, at e^{-1}, 25.5 μs.

The situation is more subtle when we analyze the gradients and the coherence time for the trap at 150 μm, since we have not directly measured the gradients by scanning the laser. We only get an upper estimate from the $S-P$ spectroscopy when we assume F to be along x. If we assume, for example, that the gradient along z is 20 V/cm^2, the size of the cloud $\sigma_{yz} = 5.7$ μm, the half width at $e^{-1/2}$ would be $\sigma = 2 \times A_{61S-60S} \times 0.09 \times 0.0114 = 22.5$ kHz which would correspond to a coherence time at e^{-1} of $t_{Ramsey} = 1/(2\pi \times \sigma) = 9.2$ μs,

almost a third of what we have measured (25.5 μs). In order to measure a coherence time of 18 μs, the gradient (considering it in the x (z) direction) should be 0.51 V/cm^2 (7.87 V/cm^2), a factor ~ 2.6 smaller that the ones estimated though spectroscopy. But again, 20 V/cm^2 is an upper bound for the electric field gradient when we assume $F_z = 0$ and it may be grossly overestimated.

From the simulations, a coherence time of 25.5 μs corresponds to a field gradient of 0.2V/cm^2 (7.7 V/cm^2) in the x (z) direction (cloud extension of 88 μm (5.8 μm)). In table IV.7, we present a comparison of the measured coherence times with those expected from the gradients.

Trap (μm)	τ_{Ramsey}	σ estimated	Coherent time predicted
150	18 μs	22.5 kHz	6.5 μs
455	120 μs	1.35 kHz	117 μs

Table IV.7: Transition $60S \longrightarrow 61S$. We compare the measured Ramsey coherence times with those predicted using the electric field gradients and the size of the cloud. We also give the corresponding spectral width for Gaussian profile σ. The coherence times and the σ are given at $e^{-1/2}$ for the correct comparison.

IV.3.3 Spin echo experiment

A spin-echo experiment counteracts some of the dephasing mechanisms present in the Ramsey interferometry experiments. This is particularly the case for the contribution of the inhomogeneities of the electric field, which play an important role, as shown in sections IV.2.1, IV.2.2 and IV.2.3. Spin-echo measurements are also impervious to slow drifts of the electric field.

The principle of Hahn's spin echo is to apply a π Rabi pulse to the atoms in the exact center of the Ramsey sequence. A typical sequence in shown in figure IV.17. The coherence of the superposition between the $60S_{1/2}$ and the $61S_{1/2}$ levels is probed by scanning the starting point of the second $\pi/2$ pulse around the *refocusing time*. In these conditions, the dephasing accumulated in the first half of the free evolution is reversed in the second half. The measured coherence time is expected to be only limited by the residual atomic motion in the field gradient or by electrical noise, with a frequency of the order of $1/T$.

For the trap at 450 μm, figure IV.18 shows two examples of measurements, for $T/2$ equal to 50 and 300 μs . We observe that the error bars for the last measurement ($T/2 = 300$ μs) are considerably larger. This is due to the fact that we reach times of the order of the lifetime of the Rydberg atoms (the measured lifetime of the $60S$ state is 210 ± 4 μs, see Appendix D). After $T/2 = 300$ μs, only about one-third of the prepared atoms are detected. The contrast as a function of the total free evolution time is shown in figure IV.19. A Gaussian envelope for the decay is fitted to the data. The coherence time deduced from this fit is 631 μs at e^{-1}. Note that this time is three times larger than the measured lifetime of the Rydberg atoms.

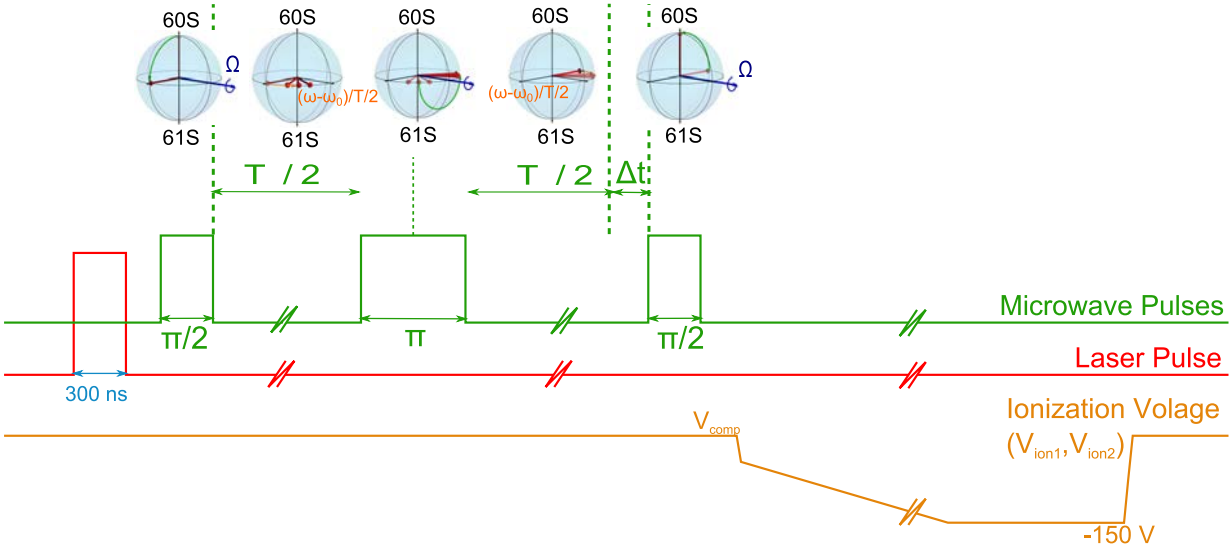

Figure IV.17: Sequence for spin-echo data acquisition. A π pulse is performed in between two $\pi/2$ pulses in order to overcome the decoherence due to electric field inhomogeneities. A π pulse changes the sign of the phase accumulated in the first period of free evolution time lasting $T/2$. The phase is then inverted, and the second free evolution refocuses the state of the atoms at time T. The atomic transfer is measured as a function of Δt. The contrast of the oscillation measures the coherence of the atomic superposition around T.

At 150 μm, figure IV.20 shows two examples of these measurements, for a time separation $T/2$ (figure IV.17) of 20 and 80 μs. The contrast as a function of T is shown in figure IV.21. A Gaussian envelope for the decay was fitted to the data, from which we deduce a coherence time of 116 μs at e^{-1}.

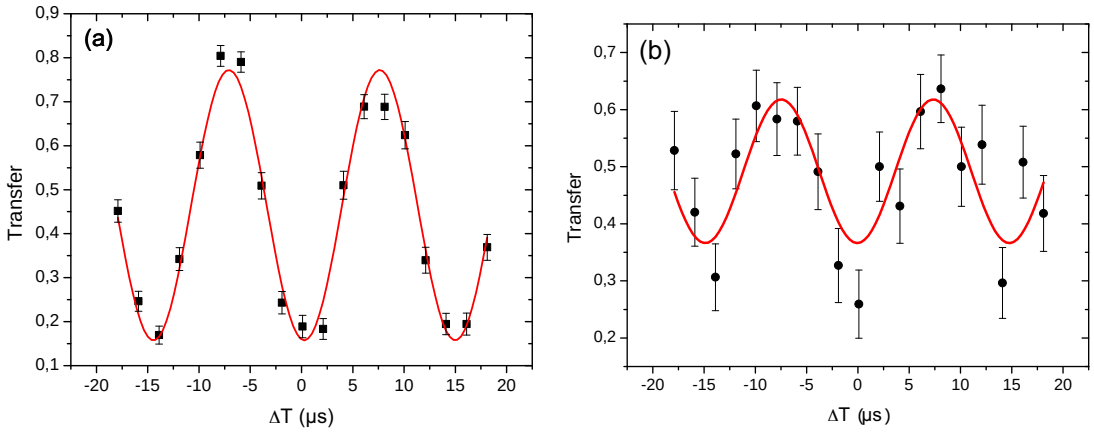

Figure IV.18: Spin-echo experiment at 455 μm. Scan of the probability for the atoms to be found in the $61S_{1/2}$ level as a function of the start of the second $\pi/2$ pulse (Δt of scheme IV.17), for $T/2$ equal to 50 μs (**(a)**) and 300 μs (**(b)**).

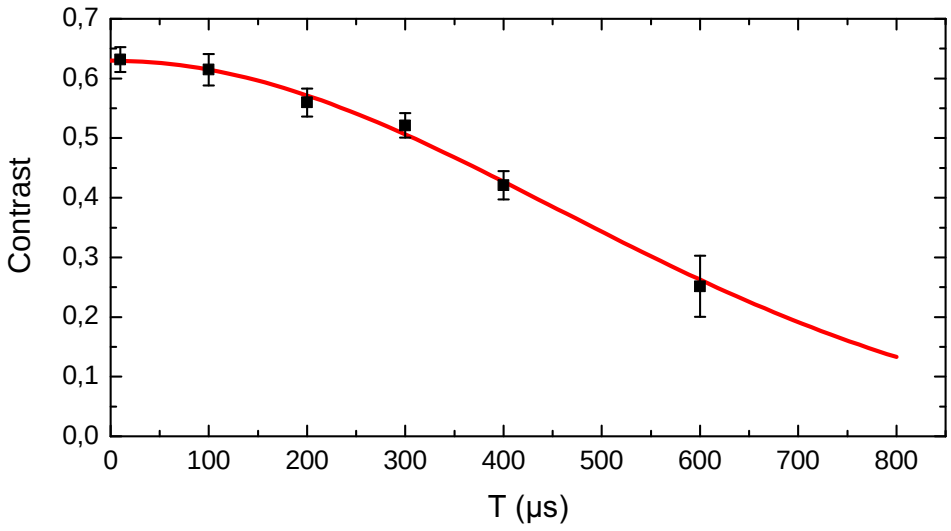

Figure IV.19: Spin-echo experiment at 455 μm. Contrast of the Ramsey interferometer as a function of the total free evolution time. A Gaussian envelope for the decay is fitted to the data (red line). We deduce a coherence time of 631 μs at e^{-1}.

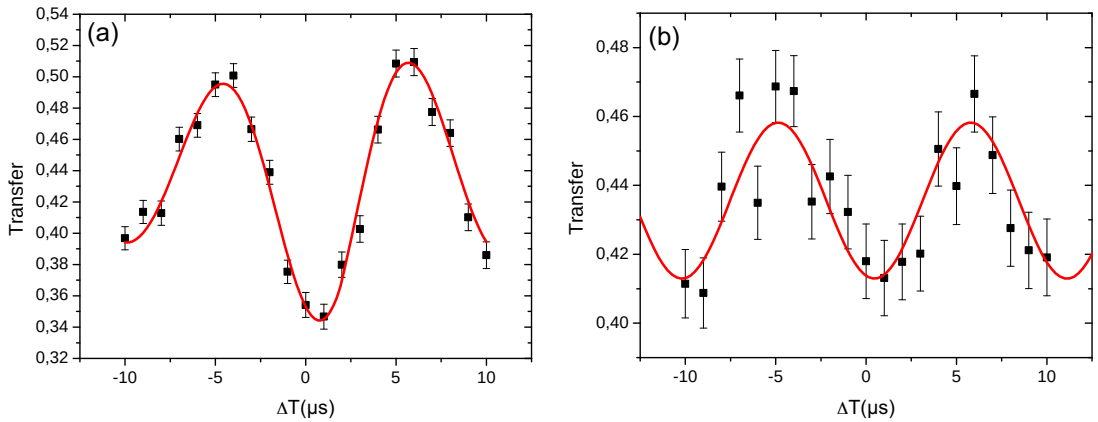

Figure IV.20: Spin-echo experiment at 150 μm. Probability for the atoms to be found in the $61s_{1/2}$ level as a function of the time of the second $\pi/2$ pulse (ΔT in scheme IV.17), for $T/2$ equal to 20 μs **(a)** and 80 μs **(b)**.

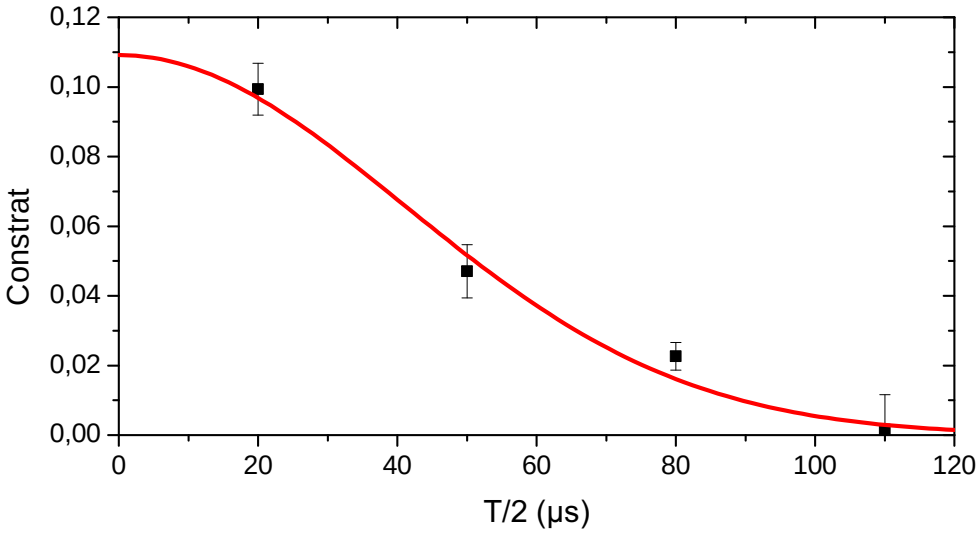

Figure IV.21: Spin-echo experiment at 150 μm. Remaining contrast as a function of the total sequence time $T/2$. A Gaussian envelope for the decay is fitted to the data (red line). We deduce a coherence time of $t_{echo} = 58 \times 2 = 116$ μs at e^{-1}.

Conclusions and perspectives

Within the experimental part of this work, we have presented the study of the electric field near a cold superconducting surface and the coherent manipulation of Rydberg atoms close to it once the stray fields were well compensated. The main problem we had to face, after a nearly complete rebuild of the existing apparatus, was the stray field induced Stark effect. We realized, after painstaking explorations, that this stray field was due to the Rubidium atoms adsorbed on the surface of the chip.

Deposition of Rubidium (a film with an estimated thickness of ~ 86 nm) was a simple solution to overcome this severe limitation. The compensation field in the y-direction, for instance, was reduced from 3.7 V/cm to 0.09 V/cm, nearly two orders of magnitude smaller. The optical spectral lines we have observed after this deposition were not limited anymore by the Stark effect, but rather by the laser itself. They were stable over a few months time scale.

We report in this thesis extremely long coherence times for Rydberg atom microwave transitions, for two different atoms-to-chip distances $y = 150$ μm and $y = 450$ μm. The coherence times obtained are in the millisecond range, exceeding even the atomic lifetimes, two orders of magnitude larger than those observed in reference [16]. These results are extremely encouraging for the exploration of Rydberg-Rydberg interaction and of the dipole blockade mechanism.

We should mention that not all observations are fully understood. First we have observed systematically that the width of the spectral microwave lines were larger that expected, given the coherence time measured by the Ramsey sequences. These times, however, were consistent with the measured gradient. We attribute this problem to a low frequency noise in the electrodes. This noise affects the spectral lines, but not the Ramsey sequences.

The decay of the spin echo signal is not yet fully understood. The residual atomic motion does not seem to explain all of it, since the decay should be of $\propto 1/t^4$ and we have observed a Gaussian decay. Here again we conclude that probably our results are still affected by some voltage noise on the controlling electrodes at a low frequency of the order of $1/T$. If we overcome this problem, we should most probably find even longer coherence times.

Since the completion of this work, we have studied the Rydberg-Rydberg interactions in the cloud. Very interesting results were obtained regarding the mechanical effects of the dipolar interaction of Rydberg atoms. These results are reported in the thesis of Raul

Celistrino Teixeira [42], where all the details and theoretical models may be found. Here we shortly describe the main results of this experiment, in which I took a quite active part.

We have developed a new measurement method to access the energy distribution of a Rydberg atomic ensemble under strong interaction. We consider the excitation of a cloud of atoms by a laser blue-detuned with respect to the atomic transition. Instead of the blockade radius image, relevant at resonance, we are in a situation in which atoms are preferably excited at distances such that the repulsive dipole-dipole interaction compensates the laser detuning (figure IV.22). We have shown that microwave spectroscopy performed on the 60S to 57S two-photon transition provides very interesting insight into the atomic position correlations in this situation. Indeed, the spectrum of the transition directly reveals the spectrum of the interaction energies in the sample. We have observed line broadenings in fair agreement with a simple model. Moreover, the time evolution of the spectra directly reveals the fast motion of the atoms produced by this strong repulsive interaction. We have shown that the 'frozen gas model' breaks down after a very short time, of a few tens of microseconds only. The expansion of the cloud proceeds in an interesting hydrodynamic regime, in which the many-body mutual interaction play an essential role.

A short term perspective for these experiments is the exploration of a 1D trap, which simplifies the entire system and hence the interpretation of the interaction energy spectrum. This situation could lead to interesting studies of quantum excitation transport.

The single Rydberg excitation, the original aim of this work, is also within reach. The best optical transition line obtained, after working on the laser stabilization, had a width of the order of 600 kHz. It means for the $60S$ state a blockade radius of 7.8 μm. The linewidth can be improved further by working on the laser locking system. The cloud size is now quite comparable to the expected blockade radius. We could improve the design of the chip to provide a tighter confinement. Of course, we should simultaneously improve the imaging system. Imaging is one of the main limitations: we cannot observe small BECs (of the order of hundred of atoms). With the current resolution of the imaging system, it is impossible to separate the thermal cloud from the pure BEC fraction for low atom numbers.

We can also consider higher principal quantum number since, then, the blockade radius will be larger. For instance if we consider the Rydberg state $80S$, the broadening due to the Stark effect will be 450 kHz, still smaller that the laser linewidth. The blockade radius (varying with $n^{11/6}$) will increase by a factor 1.7.

With these improvements, the original idea of a deterministic source of atoms for cavity QED experiments would be feasible. We could combine this source with a Stark accelerator to send the atoms trough our high Q cavities.

In the left side of figure IV.23, the Rydberg atoms would be prepared deterministically in an atomic cloud generated in front of the superconducting chip. Then, the atoms would be transferred to the circular state by on-chip fields. They would be accelerated through a Stark accelerator and guided towards the CQED experiment (right of figure).

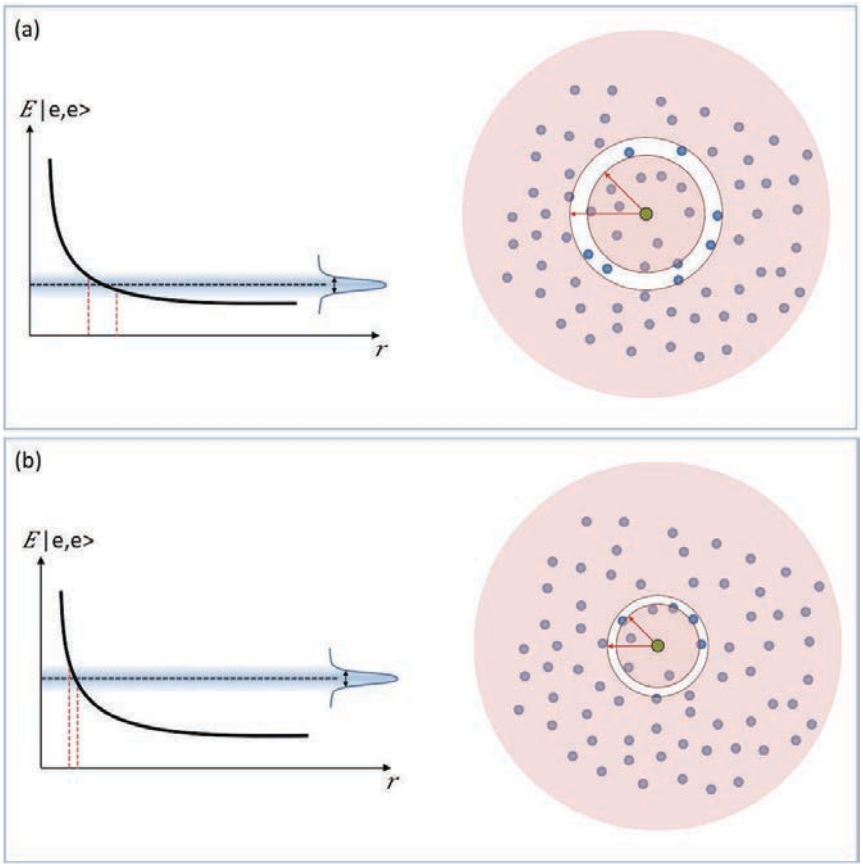

Figure IV.22: Pictorial representation of the action of a positive laser detuning for the excitation of a second Rydberg atom. **(a)** Left: energy of the two atoms in the Rydberg state $|e, e\rangle$ as a function of the distance. Right the situation for a small laser detuning . **(b)** same graphs for a larger detuning. We observe the bands (in white) in which a possible second atom could be excited.

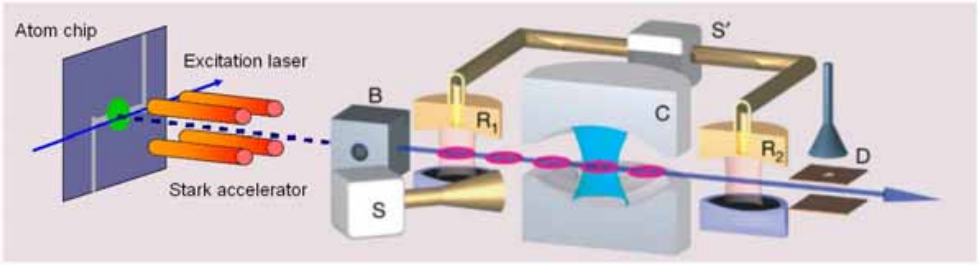

Figure IV.23: Future experimental setup: deterministic source of Rydberg atoms plus current CQED setup.

Part II

Theory: Applications to quantum information processing

Chapter V

Atoms and photons. Theoretical description of the interaction

Basic quantum optics experiments raise a considerable interest. Manipulating atoms and photons in a controlled way makes it possible to test the most intimate behaviors of the quantum world. These experiments also lead to promising perspectives, particularly for the exploration of quantum information communication and processing devices.

The ENS group experiments on cavity QED with circular Rydberg atoms implement the simplest matter-field coupling situation, with a single two-level atom coupled to a single mode of the radiation field, containing only a few photons stored in a modern equivalent of Einstein's photon box [2]. If the experimental challenges are numerous and difficult [63, 20], it is clear that the realization of these experiments sheds light directly onto some still open questions in quantum mechanics.

In particular, this system is well suited for the exploration of the decoherence mechanism, at the border of the quantum and classical worlds. Decoherence is an important process in quantum measurement theory, and explains the conspicuous lack of quantum superpositions at the macroscopic scale. In the ENS decoherence experiments, the interaction of a coherent field stored in the cavity with a single atom casts the field onto a quantum superposition of states with different classical properties. The decoherence of this mesoscopic field state superposition can be directly investigated [3].

The aim of this part is to explore theoretically a scheme for the efficient generation of very large mesoscopic field superpositions (MFSS), based on the simultaneous interaction of two Rydberg atoms with the cavity mode.

We thus start with a first chapter devoted to the introduction of the two basic ingredients in this system: the electromagnetic field and the atom. First, we will briefly recall the formalism of field quantization. It will be followed by the description of the field quantum states and the mathematical representations depicting the field's quantum properties. Afterwards, we will introduce the two-level atom description and its interaction with the quantized field in the resonant and dispersive regimes. We will also recall the basic concepts of decoherence phenomena.

V.1 Quantum description of the electromagnetic field

In this section, we recall the field quantization procedure following the traditional approach starting from the classical Maxwell's equations, identifying the proper coordinates and their conjugate momenta, and defining the operators and the respective commutation relations [64, 65]. The electromagnetic field will be then defined as a quantum object, nothing but a set of uncoupled harmonic oscillators.

V.1.1 Quantization of the electromagnetic field

The objective is to quantize the electromagnetic field in free space. The relations between the magnetic and the electric field $\mathbf{B}(\mathbf{x},t)$ and $\mathbf{E}(\mathbf{x},t)$ are given by Maxwell's equations. In the vacuum they read

$$\nabla \cdot \mathbf{E} = 0 \tag{V.1}$$

$$\nabla \cdot \mathbf{B} = 0 \tag{V.2}$$

$$\nabla \times \mathbf{E} = -\frac{\partial \mathbf{B}}{\partial t} \tag{V.3}$$

$$\nabla \times \mathbf{B} = \frac{1}{c^2}\frac{\partial \mathbf{E}}{\partial t} \tag{V.4}$$

We introduce the *electromagnetic vector and scalar potentials* $\mathbf{A}$ and Φ:

$$\mathbf{E} = -\nabla\Phi - \frac{\partial \mathbf{A}}{\partial t} \tag{V.5}$$

$$\mathbf{B} = \nabla \times \mathbf{A} \tag{V.6}$$

Injecting equations V.5 and V.6 in the Maxwell's equations and using the Coulomb gauge, where $\Phi = 0$ and $\nabla \cdot \mathbf{A} = 0$, it can be easily shown that the vector potential satisfies the wave equation

$$\nabla^2 \mathbf{A} - \frac{1}{c^2}\frac{\partial^2 \mathbf{A}}{\partial t^2} = 0. \tag{V.7}$$

The general solution of this equation is a sum of plane waves with an angular frequency ω_k and a wave vector $\mathbf{k}$ linked by a linear dispersion relation $\omega_k = ck$. Within a total volume V, the solution can be written:

$$\mathbf{A}(\mathbf{x},t) = -i\sum_k \sqrt{\frac{\hbar}{2\omega_k \epsilon_0 V}}\hat{\epsilon}_k A_k(t) e^{-i(\omega_k t - \mathbf{k}\cdot\mathbf{x})} + c.c.], \tag{V.8}$$

where A_k is the amplitude. It is interesting to observe that, in the Coulomb gauge, $\mathbf{A}$ must be perpendicular to the wave vector $\mathbf{k}$. The vector potential is made up of transverse waves. For each $\mathbf{k}$, the possible $\mathbf{A}$ vectors are in a plane, and are generated by two independent polarization directions $\hat{\epsilon}_k = (\epsilon_k^1, \epsilon_k^2)$.

As a consequence of equation (V.8), the electric and magnetic fields are

$$\mathbf{E}(\mathbf{x},t) = \sum_k \sqrt{\frac{\hbar\omega_k}{2\epsilon_0 V}}\hat{\epsilon}_k[A_k e^{-i(\omega_k t - \mathbf{k}\cdot\mathbf{x})} + c.c.] \tag{V.9}$$

$$\mathbf{B}(\mathbf{x},t) = \sum_k \sqrt{\frac{\hbar}{2\omega_k\epsilon_0 V}}(\mathbf{k}\times\hat{\epsilon}_k)[A_k e^{-i(\omega_k t - \mathbf{k}\cdot\mathbf{x})} + c.c.]. \tag{V.10}$$

The quantization is easily obtained when replacing A_k by the operator a_k and A_k^* by $a_k^\dagger$. The operators a and $a^\dagger$ are the annihilation and creation operators, respectively, and they obey the following commutation relations:

$$[a_k, a_{k'}^\dagger] = \delta_{kk'}, \quad [a_k, a_{k'}] = [a_k^\dagger, a_{k'}^\dagger] = 0. \tag{V.11}$$

Then, the quantized electric is given by

$$\mathbf{E}(\mathbf{x},t) = \sum_k \mathcal{E}_0\hat{\epsilon}_k[a_k e^{-i(\omega_k t - \mathbf{k}\cdot\mathbf{x})} + h.c.] \tag{V.12}$$

$$\mathbf{B}(\mathbf{x},t) = \sum_k \frac{(\mathbf{k}\times\hat{\epsilon}_k)}{\omega_k}\mathcal{E}_0[a_k e^{-i(\omega_k t - \mathbf{k}\cdot\mathbf{x})} + h.c.] \tag{V.13}$$

where

$$\mathcal{E}_0 = \sqrt{\frac{\hbar\omega_k}{2\epsilon_0 V}} \tag{V.14}$$

is the electric field amplitude of the vacuum in the mode k and depends only on the geometry and on the frequency of this mode.

The classical Hamiltonian for the field is

$$H_{em} = \frac{1}{2}\int_V d^3x(|E|^2 + |B|^2). \tag{V.15}$$

where the integration is over the volume of the space considered. It follows by replacing equations (V.12) and (V.13) that

$$H_{em} = \sum_k \hbar\omega_k(a_k a_k^\dagger + 1/2) \tag{V.16}$$

The first term in equation (V.16) represents an infinite ensemble of noninteracting quantum oscillators. The second represents the vacuum fluctuation energy. Since we will be interested in situations involving only a few modes, we can eliminate this constant by redefining the zero energy level. Then the Hamiltonian is then simply

$$H' = \sum_k \hbar\omega_k a_k^\dagger a_k \tag{V.17}$$

proportional to the number operator $\hat{N}_k = a_k^\dagger a_k$, which satisfies the following commutation relations:

$$[N_k, a_{k'}] = -\delta_{kk'} a_k, \quad [N_k, a_{k'}^\dagger] = \delta_{kk'} a_k^\dagger. \tag{V.18}$$

With these relations, it is straightforward to get

$$[H, a_{k'}] = -\hbar\omega_k a_k, \quad [H, a_{k'}^\dagger] = \hbar\omega_k a_k^\dagger. \tag{V.19}$$

The energy spectrum of a single quantized electromagnetic field mode is discrete, with a quantum $\hbar\omega_k$.

We restrict to the single mode case. The Hamiltonian eigenstates are eigenstates of N, the Fock states or *number states*, such that $N|n\rangle = n|n\rangle$, with the energy $n\hbar\omega$. The operator a, applied to a Fock state, decreases the energy. Hence the name *annihilation operator*. Analogously, the operator $a^\dagger$ increases the energy and it is a *creation operator*. The action on the Fock states of the creation and the annihilation operators is given by

$$a|n\rangle = \sqrt{n}|n-1\rangle, \quad a^\dagger|n\rangle = \sqrt{n+1}|n+1\rangle. \tag{V.20}$$

and hence

$$|n\rangle = \frac{a^{\dagger n}}{\sqrt{n}}|0\rangle. \tag{V.21}$$

Up to now we have defined some fundamental mathematical objects emerging directly from the field quantization. The *number states* are non-classical states. They are orthogonal with each other. The electric field expectation value $\langle n|E|n\rangle$ in these states is always zero.

To describe the analogue of a classical field in the quantum picture, we need to define another class of states, the so-called *coherent states*.

V.1.1.a Coherent states and displacement operator

A coherent state $|\alpha\rangle$, as introduced by Glauber in 1963 [66], is an eigenstate of the annihilation operator

$$a|\alpha\rangle = \alpha|\alpha\rangle \tag{V.22}$$

where $\alpha = |\alpha|e^{i\varphi}$ is the complex field amplitude. The vacuum is a coherent state with $\alpha = 0$. The coherent states can be expanded over the basis of Fock states:

$$|\alpha\rangle = e^{-\frac{|\alpha|^2}{2}} \sum_{n\geq 0} \frac{\alpha^n}{\sqrt{n!}}|n\rangle \tag{V.23}$$

The probability distribution of the photon number $P(n)$ obeys a Poisson law

$$P(n) = |\langle n|\alpha\rangle|^2 = e^{-|\alpha|^2} \frac{|\alpha|^2}{n!} \tag{V.24}$$

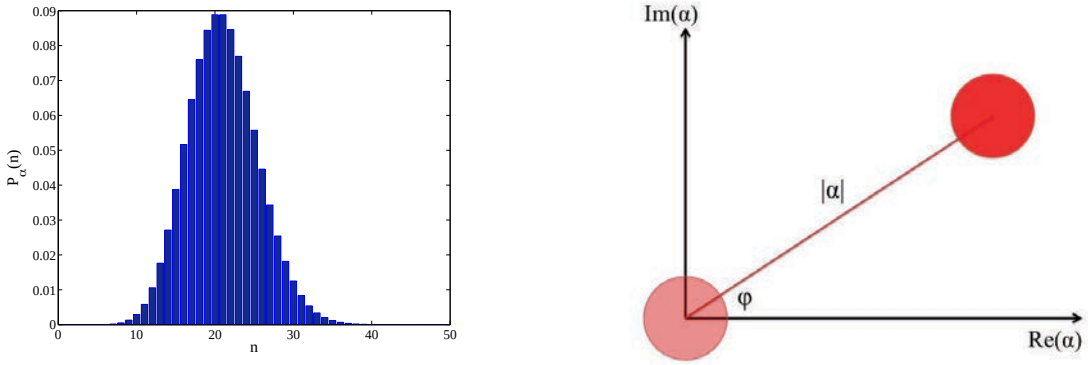

Figure V.1: (a) The photon number distribution of a coherent state $|\alpha\rangle$ with a mean photon number of 20. (b) Pictorial representation of the displacement operator on the vacuum state in the phase space. The uncertainty on the amplitude is represented by the red circles.

with an average photon number given by $\bar{n} = |\alpha|^2$ and a photon number mean square-root deviation of $\Delta N = |\alpha| = \sqrt{\bar{n}}$. Figure V.1 (a) shows the photon number distribution given by this formula.

Using the Hamiltonian (V.16) and the *time evolution operator*, the evolution of the coherent state after a time t takes the form [67]

$$|\alpha, t\rangle = e^{-\frac{i}{\hbar}Ht}|\alpha\rangle \rightarrow e^{-i\omega t/2}|\alpha e^{-i\omega t}\rangle. \tag{V.25}$$

The state remains coherent. The free evolution of the state is a rotation in the phase space at the frequency ω.

These results depict the interest of coherent states to describe semiclassical states of light. In the strong field regime, the coherent state may be considered as description of a classical field.

It is convenient to introduce the *displacement operator*, which generates the coherent states

$$D(\lambda) = e^{(\lambda a^\dagger - \lambda^* a)} \tag{V.26}$$

where λ is a complex number describing the amplitude of the displacement in the phase space. It is an unitary operator, i.e. $D^\dagger D = \mathbb{I}$. The coherent state $|\alpha\rangle$ is generated by the action of the displacement operator on the vacuum state

$$|\alpha\rangle = D(\alpha)|0\rangle. \tag{V.27}$$

A pictorial representation of the action of the operator D is shown in V.1 (b). The action of a classical microwave source (involving large currents and fields) onto the cavity state is faithfully described by a displacement operator. The amplitude α of the produced displacement can be tuned at will by adjusting the source parameters [2].

V.1.2 Quantum states and density operator

In quantum mechanics, a quantum state is a mathematical object that contains all information on a physical system. A definition that can be used is that of Asher Peres ([68], page 24): *A state is characterized by the probabilities of the various outcomes of every conceivable test.* For a mathematical description we have the following postulate

Postulate: To each quantum state corresponds a unique state operator ρ associated with a Hilbert space $\mathcal{H}$ satisfying the following conditions:

1. Normalization condition: $Tr(\rho) = 1$,
2. Hermiticity condition: $\rho = \rho^\dagger$, and
3. Positivity condition: ρ is a non-negative operator, meaning that for a given state $|s\rangle$, $\langle s|\rho|s\rangle \geq 0$ is satisfied.

The three conditions above are sufficient to derive an important number of properties of the density operators. Here we recall the most relevant ones.
Because ρ is self-adjoint, it is possible to find a spectral representation:

$$\rho = \sum_i^D p_i |\phi_i\rangle\langle\phi_i|, \tag{V.28}$$

where the eigenvalues p_i satisfy the conditions $0 \leq p_i \leq 1$ and $\sum_i p_i = 1$.

Another extremely important property is that the expectation value of an observable A in a state represented by a density matrix ρ, is given by

$$\langle A\rangle_\rho = Tr(\rho A). \tag{V.29}$$

Given the above definitions, we proceed to introduce two possible class of states represented by density matrices, the **pure states** and the **mixed states**.

V.1.2.a Pure states

Pure states are represented by $\rho = |\varphi\rangle\langle\varphi|$, i.e., as a projector. The following condition is necessary and sufficient to identify pure states

$$\rho^2 = \rho \Leftrightarrow Tr(\rho^2) = 1 \tag{V.30}$$

In the case of the electromagnetic field for instance, we can choose to work with the number states basis and write the pure state of the field as

$$|\varphi\rangle = \sum_i c_i |i\rangle \tag{V.31}$$

with $c_i = \langle i|\varphi\rangle$. In the simplest case, the expectation value of an observable A will be given by

$$\langle A\rangle = \langle\varphi|A|\varphi\rangle. \tag{V.32}$$

V.1.2.b Mixed states

Most of the experimental procedures for states preparation do not produce pure states but mixed states that are statistical ensembles of pure states. The appropriate density operator to describe this kind of states has the following form

$$\rho_{mix} = \sum_i p_i \rho_i^{pure} = \sum_i p_i |\varphi_i\rangle\langle\varphi_i| \tag{V.33}$$

where $\sum_i p_i = 1$.

It is interesting also to define functions *measuring* how pure a state is. We refer here to two of them: the Von Neumann entropy [69] and the purity of the system. The first is defined as

$$S(\rho) \equiv -Tr(\rho \ln \rho) = -\sum_{i=1}^{D} p_i \ln p_i, \tag{V.34}$$

where the set of p_i are the eigenvalues of the density matrix ρ. The von Neumann entropy can take values from 0, for pure states, up to $\ln D$ for totally mixed states, where D is the dimension of the Hilbert space.

On the other hand, the purity of a state ρ is defined by [69]

$$\mathcal{P}(\rho) \equiv Tr(\rho^2) \tag{V.35}$$

It varies from 1, for pure states, to $1/D$ for completely mixed states.

We now use the entropy and the purity of a state to define the degree of entanglement of a compound system.

V.1.2.c Quantum state of compound systems and degree of entanglement

So far we have considered only systems belonging to a Hilbert space of dimension D. Now, we turn to a bipartite system A and B whose Hilbert space is given by $\mathcal{H}_A \otimes \mathcal{H}_B$. A pure state then can be written as

$$\varphi_{AB} = \sum_{i=1}^{D_A} \sum_{j=1}^{D_B} a_{ij} |u_i\rangle \otimes |v_j\rangle \tag{V.36}$$

or, in term of the density matrix, as

$$\rho_{AB} = \sum_{i,m=1}^{D_A} \sum_{j,n=1}^{D_B} a_{ij} a_{mn}^* |u_i\rangle\langle u_m| \otimes |v_j\rangle\langle v_n| \tag{V.37}$$

where $\{|u_i\rangle\}$ is a basis of the Hilbert space $\mathcal{H}_A$ and $\{|v_j\rangle\}$ is a basis of the Hilbert space $\mathcal{H}_B$.

There are two possible cases: either the density matrix of the compound system has a separable form $\rho_{AB} = \rho_A \otimes \rho_B$, where $\rho_{A,B}$ are the density operator of each system, or it

doesn't. We say then that the state is entangled.
The same concept applies to mixed states. Just as pure states, the mixed states may or not be entangled. When they are not, we can always represent them as an ensemble of product states, weighted by c_i:

$$\rho_{AB} = \sum_i c_i \rho_A^{(i)} \otimes \rho_B^{(i)} \tag{V.38}$$

From this definition, when it is not possible to write the state with the above form we have an entangled mixed state.

We focus on pure states. We define two measures for the degree of entanglement. We consider one of the two reduced density operator ρ_r of the subsystems. We then have the following properties:

- $Tr\rho_r^2 = 1 \Rightarrow \rho_r$ is pure $\Rightarrow$ the compound state is separable
- $Tr\rho_r^2 \leq 1 \Rightarrow \rho_r$ is mixed $\Rightarrow$ the compound state is entangled

The von Neumann entropy (V.34) of ρ_r is maximum for maximally entangled state, and zero when the system is separable.

The so-called *concurrence* is another measure of entanglement. It is directly related to the purity of one of the parts of the system. In particular, we use here the *I-concurrence*, introduced by Rungta *et at.* [70], which is a generalization of the Wootters concurrence [71] for bipartite systems of arbitrary dimension. For pure bipartite states, the I-concurrence is given by

$$C^2 = 2[1 - Tr(\rho_k^2)], \tag{V.39}$$

where $k = A, B$ refers to each subsystem A and B, and $D \equiv min(D_A, D_B)$, with D_A and D_B the dimension of each subsystem respectively. In the case of pure states, the I-concurrence takes values in the range

$$0 \leq C^2 \leq \frac{2(D-1)}{D}. \tag{V.40}$$

For the numerical calculations of next chapter, we use a normalized version of the I-concurrence

$$C' = \frac{D}{D-1}[1 - Tr((\rho_k^2))] \tag{V.41}$$

which can take values from zero for non-entangled states to one for maximally entangled states.

V.1.3 Phase space representation

It is extremely useful to have an intuitive link between classical physics and quantum physics whenever possible. In particular, an appropriate notion of *quantum phase space* is

of great help. One of the fundamental bases of classical statistical physics is the concept of probability distributions in phase space. A system with n degrees of freedom is described by a point in a $2n$-dimensional phase space, the first describing the generalized positions of the state, let's say, of the particle, and the second the conjugate momenta. A point in this space entirely defines the state of the particle. If we consider for example a classical field mode equivalent to an harmonic oscillator, the position and the momentum are the field quadratures.

We consider the case of $n = 1$, a particle undergoing one-dimensional motion. In the classical world the momentum and the position of this particle can be determined precisely and simultaneously. The probability distribution is then a Dirac distribution. If we do not have precise information on the state of the system, we must replace the Dirac distribution associated to this point by a density of probability, $f(x, p)$, positive, normalized and non-zero in a limited region of the space. The statistical average of any observable $O(x, p)$ on the state of the particle is then given by

$$\bar{O} = \int f(x,p)O(x,p)dxdp. \tag{V.42}$$

This classical concept cannot be directly applied to quantum states since the Heisenberg uncertainty relations preclude the precise and simultaneous determination of conjugate variables. For a statistical mixture, the quantum and classical uncertainties are added. A generalization of equation (V.42) for quantum states and observables is then required.

The most useful quantum distribution here is the Wigner function (W). The Wigner function contains all information that is carried by the density matrix, and *vice versa*. Both representations of the quantum state are thus fully equivalent.

There are two other phase space quantum distributions: the P-representation (P), also known as *coherent state representation*, and the Q-representation (Q), also referred as the *Husimi-Q distribution*. We will not use them much in this work.

Any relevant operator can be expanded as a series of a and $a^\dagger$, which are non-commuting. In the *normal* ordering, all creation operators are placed to the left of the annihilation ones. In the *anti-normal* ordering, on the contrary, all annihilation operators are placed to the left of the creation ones. Finally we can also decide to use the *symmetric* ordering, in which all products of the creation and annihilation operators are symmetrized.

The three quasi-probability distributions, P, Q and W, are well suited for calculating average values using normal, anti-normal and symmetrical ordering. They allow us to calculate the expectation value of any observable with formulas very similar to the classical

ones (V.42):

$$\langle a^{\dagger n} a^m \rangle = \int P(\alpha) \alpha^{*n} \alpha^m d^2\alpha \tag{V.43}$$

$$\langle a^n a^{\dagger m} \rangle = \int Q(\alpha) \alpha^{*n} \alpha^m d^2\alpha \tag{V.44}$$

$$\langle \mathcal{S}(a^n a^{\dagger m}) \rangle = \int W(\alpha) \alpha^{*n} \alpha^m d^2\alpha, \tag{V.45}$$

$$\tag{V.46}$$

where $\mathcal{S}(a^n a^{\dagger m})$ denotes the symmetric product of a^n and $a^{\dagger m}$. In particular, we will see that the Wigner function has a very convenient feature: it allows us to compute easily the distributions for any quadrature.

V.1.3.a Characteristic functions

The three functions W, Q and P are the Fourier transform of characteristic functions, which also characterize fully the state of the field. They are linked to the expectation value of the displacement operator D (V.26) in the state described by ρ. These characteristic functions lead to an analytical solution to the energy relaxation problem (see [2] for further details).

The characteristic function for a symmetric ordering is defined by

$$C_S^{[\rho]}(\lambda) = \langle D(\lambda) \rangle = Tr(\rho e^{\lambda a^\dagger - \lambda^* a}) \tag{V.47}$$

where λ is a complex number. For a pure state, this reduces to

$$C_S^{[|\varphi\rangle\langle\varphi|]}(\lambda) = \langle \varphi | D(\lambda) | \varphi \rangle \tag{V.48}$$

the overlap between the state $|\varphi\rangle$ and the same state displaced in the phase space by the action of $D(\lambda)$ (a state auto-correlation function).

The normal and anti-normal-order characteristic functions are defined as

$$C_n(\lambda)^{[\rho]} = Tr(\rho e^{\lambda a^\dagger} e^{-\lambda^* a}) \tag{V.49}$$

$$C_{an}(\lambda)^{[\rho]} = Tr(\rho e^{-\lambda^* a} e^{\lambda a^\dagger}). \tag{V.50}$$

Using the Glauber identity

$$e^A e^B = e^{A+B} e^{[A,B]/2} \tag{V.51}$$

valid when both A and B commute with $[A, B]$, we can relate equations (V.49), (V.50) and (V.48) as follows

$$C_n(\lambda)^{[\rho]} = e^{|\lambda|^2/2} C_S^{[\rho](\lambda)} = e^{|\lambda|^2} C_{an}^{[\rho](\lambda)}. \tag{V.52}$$

V.1.3.b Wigner function

The Wigner function is the two-dimensional Fourier transform of (V.48)

$$W^{[\rho]}(\alpha) = \frac{1}{\pi^2}\int d^2\lambda C_S^{[\rho]}(\lambda)e^{\alpha\lambda^* - \alpha^*\lambda} \tag{V.53}$$

where α and λ are complex numbers [2]. This function is real, normalized, but is not positive definite. It can be written in two equivalent form, one related to the elements of the density matrix and the second to the parity operator.

The first one, probably the most popular form, is given, in the position eigenstates basis, by

$$W(x,p) = \frac{1}{\pi}\int du\, e^{2ipu}\langle x+u/2|\rho|x-u/2\rangle \tag{V.54}$$

which is the Fourier transform of the off-diagonal elements of the density matrix ρ ($\hbar$ has been omitted). Inverting the Fourier transform, we get

$$\langle x+u/2|\rho|x-u/2\rangle = \int dp\, e^{2ipu}W(x,p) \tag{V.55}$$

The knowledge of the Wigner function is thus completely equivalent to that of the density matrix.

An even more compact expression can be found for the Wigner function. It is directly related to the displacement operator D

$$W^{[\rho]}(\alpha) = \frac{2}{\pi}Tr[D(-\alpha)\rho D(\alpha)\mathcal{P}] \tag{V.56}$$

where $\mathcal{P}$ is the hermitian parity operator

$$\mathcal{P} = e^{i\pi a^\dagger a} \tag{V.57}$$

which performs a symmetry in the phase space around the origin as

$$\mathcal{P}|x\rangle = |-x\rangle; \qquad \mathcal{P}|p\rangle = |-p\rangle \tag{V.58}$$

and has the following action in the number states basis

$$\mathcal{P}|n\rangle = (-1)^n|n\rangle. \tag{V.59}$$

Equation (V.56) shows that $W^{[\rho]}(\alpha)$ is the average value of the operator $2\mathcal{P}/\pi$ in the state displaced by $-\alpha$, an operation expressed by $\rho \longrightarrow D(-\alpha)\rho D(\alpha)$. This expression also shows that $-2/\pi \leq W \leq 2/\pi$, since the average of the parity operator is always less than one in modulus.

Main properties of the Wigner distribution

- **Average operator values**: the Wigner function can be used to compute the average value of any operator written in the symmetric ordering O_s (see [64], page 92 and [2] page 575):

$$\langle O_s(a, a^\dagger)\rangle = Tr[\rho O_s] = \int d^2\alpha O_s(\alpha, \alpha^*) W(\alpha) \tag{V.60}$$

  The simple formula (V.60) is very similar to (V.42), which gives the average value of a classical observable. The Wigner function plays the same role in the quantum phase space as $f(x, p)$ in the classical one.

- **Marginal distributions** Using equation (V.55) and taking $u = 0$ we get the probability density for finding the value x for the field quadrature X_0 (position):

$$P(x) = \langle x|\rho|x\rangle = \int dp\, W(x, p) \tag{V.61}$$

  Similarly we get the probability density of finding the value p for the orthogonal quadrature $X_{\pi/2}$ (momentum):

$$P(p) = \langle p|\rho|p\rangle = \int dx\, W(x, p) \tag{V.62}$$

  In other words, we obtain the marginal distributions of x and p by integrating W over the conjugate variable.

  This result can be generalized to any set of conjugate quadratures x', p'

$$P(x') = \int dp'\, W(x', p') \tag{V.63}$$

  The Wigner function is the only quasi probability distribution verifying this useful property.

  When the quadrature probability distribution, $P(x)$ or $P(p)$, presents nodes, the Wigner function must be negative in some regions of phase space. The Wigner function is then not a genuine probability distribution, as $f(x, y)$ in the classical world. Negative W values are the signature of the non-classical features of a state.

V.1.3.c Examples of the Wigner function

We present here the Wigner distribution of a few quantum states. We can divide them into two groups: the group consisting of the state whose Wigner function is always positive called *quasi-classical*, and the group in which the function can take negative values, called *non-classical*.

Coherent states

For a coherent state $|\beta\rangle$, W is

$$W^{[|\beta\rangle\langle\beta|]}(\alpha) = \frac{2}{\pi} e^{-2|\beta-\alpha|^2} \tag{V.64}$$

It is a Gaussian, centered in β, with a width $1/\sqrt{2}$. The coherent state is thus a quasi-classical state since its Wigner function is always positive. Figure V.2 shows the Wigner function for the vacuum state ($\beta = 0$) and a coherent state with a mean photon number $\bar{n} = 20$ ($\beta = \sqrt{20}$).

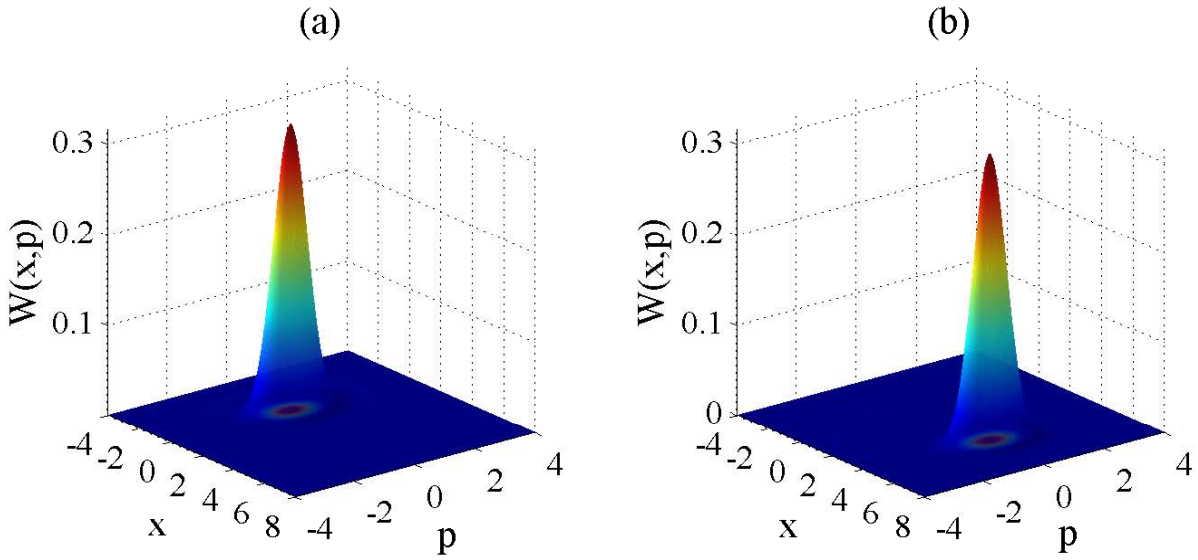

Figure V.2: (a) Wigner function of the vacuum state. (b) Wigner function of a coherent state with $\beta = \sqrt{20}$.

Thermal Field

It is an important state to bear in mind since it is the steady state field in the cavity at a finite temperature. It is also a semi-classical state, since its Wigner distribution is everywhere positive. The density matrix of this thermal state is given by

$$\rho_{th} = \sum_n \frac{n_{th}^n}{(n_{th}+1)^{n+1}} |n\rangle\langle n| \tag{V.65}$$

where n_{th} in the mean number of thermal photons, given by the Bose-Einstein distribution

$$n_{th} = \frac{1}{e^{\hbar\omega_0/k_B T} - 1}. \tag{V.66}$$

In opposition with the coherent state, there is here no coherence between the Fock states: the phase of the thermal field state is completely undefined. The corresponding Wigner function is ([2], page 576)

$$W^{[\rho_{th}]}(\alpha) = \frac{2}{\pi}\frac{1}{2n_{th}+1}e^{-2|\alpha|^2/(2n_{th}+1)} \tag{V.67}$$

which is also a Gaussian, centered at the origin, with a width of $\sqrt{n_{th}+1/2}$. The Wigner function (V.67) is represented in figure V.3 (a).

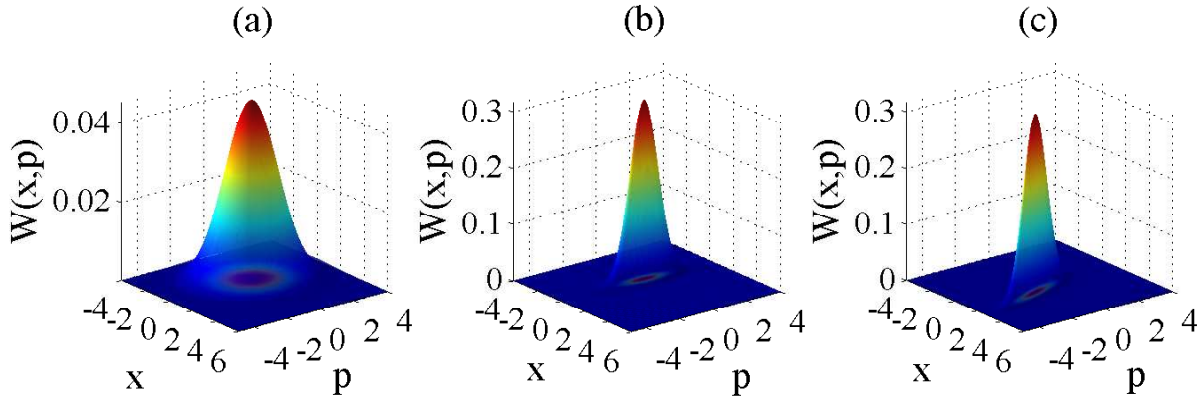

Figure V.3: (a) Wigner function of a thermal field with $n_{th} = 3$. (b) Wigner function of the squeezed vacuum state, with a squeezing parameter $\xi = 0.5$. (c) Wigner function of a general Squeezed state with $\alpha = \sqrt{5}$ and $\xi = 0.5 + 0.5i$.

Squeezed states

The squeezed states are obtained by the action of the squeezing operator defined by

$$S(\xi) = e^{(\xi^* a^2 - \xi a^{\dagger 2})/2} \tag{V.68}$$

and of the displacement operator $D(\alpha)$ on the vacuum state, i.e.,

$$|\alpha, \xi\rangle = D(\alpha)S(\xi)|0\rangle. \tag{V.69}$$

In this state, the fluctuations of one of the field's quadratures are below those of the coherent state (standard deviation of 1/2). Due to the Heisenberg uncertainty relations, this is achievable only at the expense of an increased uncertainty of the conjugate quadrature.

Even though squeezed states are generally considered as non-classical in quantum optics, they have a positive Wigner distribution, which is given, for ξ real and $\alpha = 0$, by ([2], page 577)

$$W^{[sq,\xi]}(x,p) = \frac{2}{\pi}e^{-2\,exp(2\xi)x^2}e^{-2\,exp(-2\xi)p^2} \tag{V.70}$$

This is a non-degenerate Gaussian, plotted in figure V.3 (b) for $\xi = 0.5$. A general squeezed state Wigner function is shown if figure V.3 (c) for $\alpha = \sqrt{5}$ and $\xi = 0.5 + 0.5i$. It also has a Gaussian shape, whose principal axes are now tilted with respect to the x and p ones.

Fock states

The Wigner function of a Fock state has the form ([2], page 578)

$$W^{[|n\rangle\langle n|]}(\alpha) = \frac{2}{\pi}(-1)^n e^{-2|\alpha|^2}\mathcal{L}_n(4|\alpha|^2) \tag{V.71}$$

where $\mathcal{L}_n$ is the nth Laguerre polynomials. In particular, we should note that $\mathcal{L}_n(0) = 1$, which implies that

$$W^{[|n\rangle\langle n|]}(0) = \frac{2}{\pi}(-1)^n \tag{V.72}$$

The Wigner function at the origin, $W(0)$, is $\pm 2/\pi$. It takes the minimum allowed value for odd photon numbers, the maximum one for even photon numbers. The negative values of W make clear that it cannot be interpreted as a probability distribution in phase space. They also evidence the nonclassical nature of the Fock states (different from the vacuum). The Wigner functions of Fock states with 1 and 7 photons are shown in figure V.4.

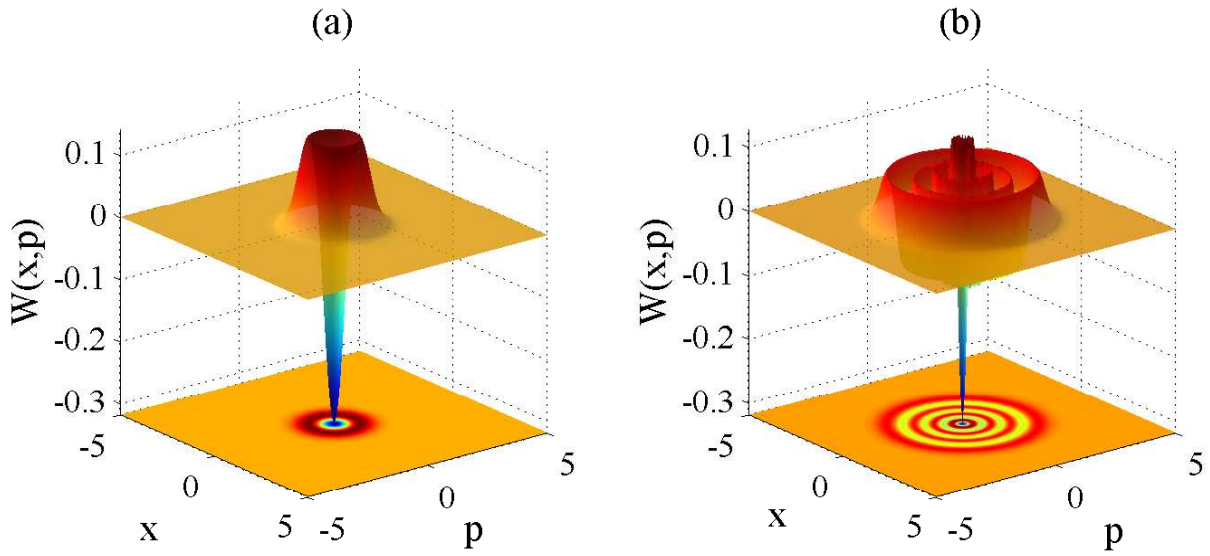

Figure V.4: Wigner function of (a) a one-photon Fock state and (b) of a seven-photon Fock state.

Phase cat states

Another excellent example of non-classical state, and the core of this second part, are the so-called cat states. Here, for the sake of simplicity we will refer to the *phase cat states*, which are superpositions of two coherent states with different phases :

$$|\Psi_{cat}^{\pm}\rangle = \frac{1}{\sqrt{\mathcal{N}_{\pm}}}(|\alpha e^{i\phi}\rangle \pm |\alpha e^{-i\phi}\rangle) \tag{V.73}$$

where $\mathcal{N}_{\pm}$ is a normalization factor given by

$$\mathcal{N}_{\pm} = 2 \pm 2\, Re(\langle \alpha e^{i\phi} | \alpha e^{-i\phi}\rangle). \tag{V.74}$$

For simplicity we will consider here only the simple case of $\phi = \pi/2$ and thus superpositions of coherent states with opposite phases. Setting $i\alpha = \beta$, these states can be expressed in the number states basis as

$$|\Psi_{+}\rangle = \frac{2e^{-|\beta|^2/2}}{\mathcal{N}_{+}} \sum_{n\ even} \frac{\beta^n}{\sqrt{n!}}|n\rangle \tag{V.75}$$

$$|\Psi_{-}\rangle = \frac{2e^{-|\beta|^2/2}}{\mathcal{N}_{-}} \sum_{n\ odd} \frac{\beta^n}{\sqrt{n!}}|n\rangle. \tag{V.76}$$

Their photon number distributions are plotted in figure V.5 (a) and (b) for $\beta = \sqrt{9}$. We observe that they only include photon numbers of a well defined parity. We thus refer to $|\Psi_{+}\rangle$ as even cat, and $|\Psi_{-}\rangle$ as odd cat. This parity selection in the photon number distribution is an indication of the non-classical nature of these cats and is absent for statistical mixtures of $|\beta\rangle$ and $|-\beta\rangle$.

The Wigner function for these cat states is given by for β real ([2], page 579)

$$W^{[cat,\pm]}(\alpha) = \frac{2}{\pi(1 \pm e^{-2|\beta|^2})}[e^{-2|\alpha-\beta|^2} + e^{-2|\alpha+\beta|^2} \pm 2e^{-2|\alpha|^2}\cos(4Im(\alpha)\beta)] \tag{V.77}$$

The function for the odd phase cat state is shown in figure V.6 (a) for $\beta = \sqrt{9}$. It presents an interference patterns between the two cat's components with large negative values near the center of the phase space. This is a clear signature of non-classical behavior, which will be used and analyzed in more detail in next chapter.

Statistical mixture

Let's consider now a statistical mixture of two coherent states

$$\rho_{Mix} = \frac{1}{2}(|\beta\rangle\langle\beta| + |-\beta\rangle\langle-\beta|) \tag{V.78}$$

Its Wigner function is shown in figure V.6 (b). The main difference with the coherent cat state is the absence of the interference pattern. The Wigner function is then positive and the state is classical, with either a phase or the other but not both at once.

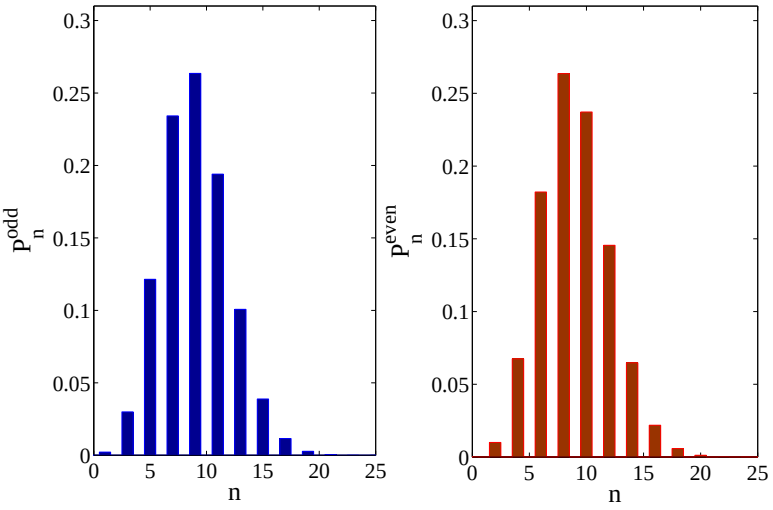

Figure V.5: Photon number distribution for an even (left) and an odd (right) phase cat state $\beta = \sqrt{9}$.

This brief reminder outlines the interest of the Wigner function to evaluate the quantum properties of a state. It is particularly useful for Schrödinger cat states and we will use it thoroughly in this part.

V.2 Two-level atoms

So far we have only described one of the fundamental building blocks of a cavity quantum electrodynamics experiment. It is now necessary to describe the atomic system before addressing its interaction with the field. In this section, we will quickly recall the notion of two-level system, the Bloch sphere, and finally the possible manipulations of the atomic internal state.

V.2.1 Atomic spin and Bloch sphere

The most general state of a two-level system is given by the linear combination

$$|\psi_{at}\rangle = c_e|e\rangle + c_g|g\rangle \tag{V.79}$$

where $|e\rangle$ and $|g\rangle$ (upper and lower states of the two-level atom) form a basis in the Hilbert space. The coefficients c_k are such that $|c_e|^2 + |c_g|^2 = 1$. These modulus squared represent

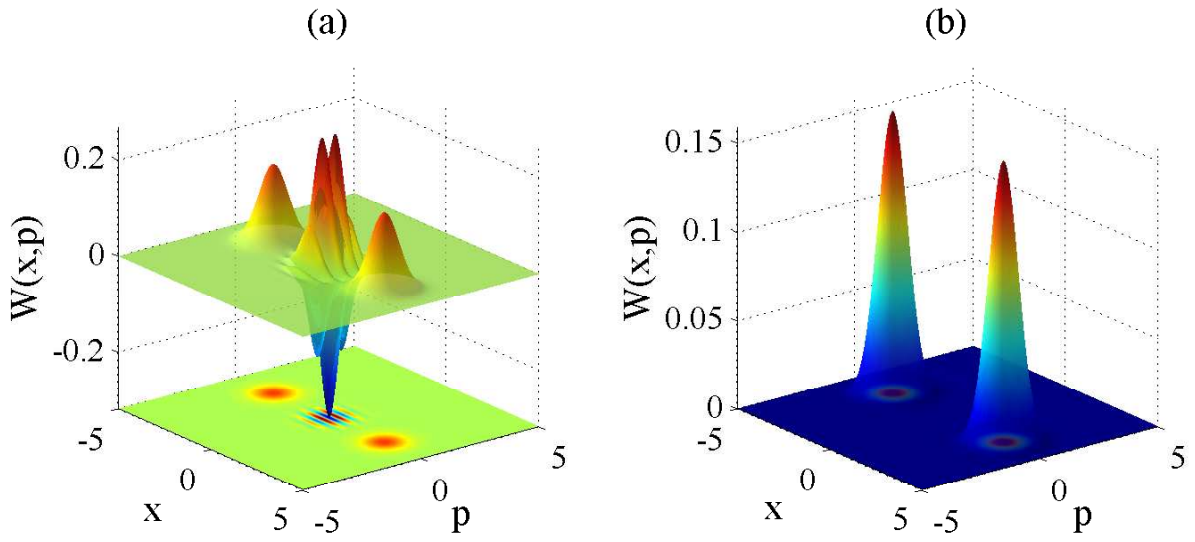

Figure V.6: (a) Wigner function of an even phase cat with $\beta = \sqrt{9}$. (b) Wigner function of a statistical mixture of two coherent states with $\beta = \sqrt{9}$.

the probability to find the atom in the respective state. Without loss of generality, this state can be written within a global phase as

$$|\psi_{at}\rangle = \cos\frac{\theta}{2}|e\rangle + e^{\varphi}\sin\frac{\theta}{2}|g\rangle \tag{V.80}$$

where the two angles are constrained by $0 \leq \varphi \leq 2\pi$ and $0 \leq \theta \leq \pi$.

The Hamiltonian of the atom with eigenstates $|e\rangle$ and $|g\rangle$ can be written as

$$H_{at} = \frac{\omega_{at}\hbar}{2}\sigma_z \tag{V.81}$$

where

$$\omega_{at} = \frac{E_e - E_g}{\hbar}. \tag{V.82}$$

The operator σ_z is one of the Pauli operators defined, in the e, g basis, as:

$$\sigma_x = \begin{pmatrix} 0 & 1 \\ 1 & 0 \end{pmatrix} \quad \sigma_y = \begin{pmatrix} 0 & -i \\ i & 0 \end{pmatrix} \quad \sigma_z = \begin{pmatrix} 1 & 0 \\ 0 & -1 \end{pmatrix}. \tag{V.83}$$

In terms of the energy states, the Pauli operators can be written also as

$$\sigma_x = |g\rangle\langle e| + |e\rangle\langle g|, \quad \sigma_y = i(|g\rangle\langle e| - |e\rangle\langle g|), \quad \sigma_z = |e\rangle\langle e| - |g\rangle\langle g|. \tag{V.84}$$

The atom is equivalent to a spin 1/2 system. We can thus consider the *atomic pseudo-spin* $\mathbf{S} = \hbar\sigma/2$, where σ is Cartesian vector with components $\sigma_{x,y,z}$. When the atom is in the

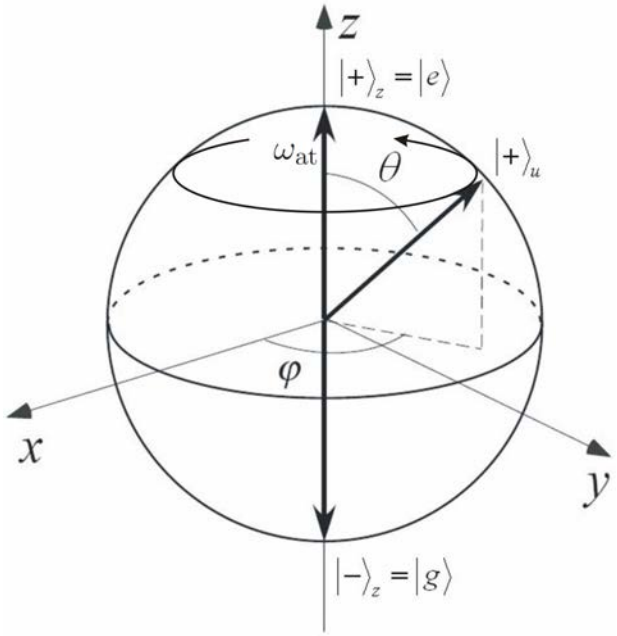

Figure V.7: Bloch sphere representation for the states of a two level system. The states $|\pm\rangle_z$ are associated by analogy to the spin eigenstates. The vector $\mathbf{u}(t)$ rotates with the frequency ω_{at} around the quantization axis z. This is the *Larmor precession* of the atomic pseudo-spin.

superposition state defined in equation (V.80), the average values of each component of the atomic pseudo-spin are:

$$\langle S_x \rangle = \sin\theta\cos\varphi, \quad \langle S_y \rangle = \sin\theta\sin\varphi, \quad \langle S_z \rangle = \cos\theta. \tag{V.85}$$

We can thus represent the atomic pure state as a unit vector with spherical coordinates θ and φ evolving on a sphere, the Bloch sphere, sketched in figure V.7.

The evolution of the state under the Hamiltonian (V.81) is given within a phase by

$$|\psi_{at}\rangle = \cos\frac{\theta}{2}|e\rangle + e^{i(\omega_{at}t+\varphi)}\sin\frac{\theta}{2}|g\rangle, \tag{V.86}$$

In terms of the Bloch sphere, this evolution is a precession (the *Larmor precession*) of the Bloch vector around the quantization axis z.

V.2.2 Manipulation of atomic states

We can define the atomic raising and lowering operators $\sigma_\pm$

$$\sigma_+ = |e\rangle\langle g|; \qquad \sigma_- = |g\rangle\langle e|. \tag{V.87}$$

The hermitian dipole electric operator $\mathbf{d} = q\mathbf{r}$, purely non-diagonal in the energy basis, can be written in term of the $\sigma_\pm$ operators,

$$\mathbf{d} = d(\epsilon_a \sigma_- + \epsilon_a^* \sigma_+), \tag{V.88}$$

where $q\langle g|\mathbf{r}|e\rangle = d\epsilon_a$, ϵ_a being a complex unitary vector related to the polarization of the transition.

For a classical interaction with a classical electric field $\mathbf{E}_r$, the coupling with the atomic dipole is given under the dipole approximation by

$$H_r = -\mathbf{d} \cdot \mathbf{E}_r(t) \tag{V.89}$$

where

$$\mathbf{E}_r(t) = i\mathcal{E}_r(\epsilon_r e^{-i(\omega_r t + \varphi_0 + \varphi')} - \epsilon_r^* e^{i(\omega_t + \varphi_0 + \varphi')}). \tag{V.90}$$

$\mathcal{E}_r$, ω_r and ϵ_r represent the amplitude, angular frequency and polarization of the field respectively. $\varphi_0 + \varphi'$ describe the phase. We switch to the rotating frame at frequency ω_r. The Hamiltonian, under the rotating wave approximation (neglecting fast rotating terms), can be written as:

$$H = \frac{\hbar\Delta_r}{2}\sigma_z - i\frac{\hbar\Omega_r}{2}[e^{-i\varphi'}\sigma_+ - e^{i\varphi'}\sigma_-] \tag{V.91}$$

where $\Delta_r = \omega_{at} - \omega_r$ is the detuning between the driving field classical frequency and the atomic transition frequency. Ω_r is the classical Rabi frequency

$$\Omega_r = \frac{2d}{\hbar}\mathcal{E}_r \epsilon_a^* \cdot \epsilon_r e^{i\varphi_0}. \tag{V.92}$$

The phase φ_0 can be adjusted to make Ω_r real positive (without loss of generality). The phase φ' is a phase offset between the classical field $\mathbf{E}_r$ and the atomic transition $|g\rangle \longleftrightarrow |e\rangle$. The Hamiltonian can be expressed also in the following form:

$$\tilde{H} = \frac{\hbar\Omega_r'}{2}\sigma \cdot \mathbf{n} \tag{V.93}$$

Here, $\Omega_r' = \sqrt{\Omega_r^2 + \Delta_r^2}$ and

$$\mathbf{n} = \frac{1}{\Omega_r'}[\Delta_r \mathbf{e}_z + \Omega_r(-\sin\varphi' \mathbf{e}_x + \cos\varphi' \mathbf{e}_y)].$$

If $\Omega_r = 0$, then $\mathbf{n} \approx \mathbf{e}_z$ and $\Omega_r' \approx \Delta_r$. We get the Larmor precession (there is no interaction – note that the precession occurs at the detuning Δ since we are in an interaction representation with respect to the driving field frequency). If $\Delta_r = 0$ (resonant case) then $\mathbf{n}$ is in the equatorial plane of the Bloch sphere and $\Omega_r' = \Omega_r$. If we consider the atom to be initially in the state $|e\rangle$ or $|g\rangle$, and the interaction is such that

$$\Omega_r t = \pi/2 \tag{V.94}$$

the Bloch vector is rotated to the equatorial plane of the sphere, and the final state is a superposition of the energy eigenstates with equal probabilities

$$|e\rangle \rightarrow \frac{1}{\sqrt{2}}(|e\rangle + e^{i\varphi'}|g\rangle) \quad |g\rangle \rightarrow \frac{1}{\sqrt{2}}(-e^{-i\varphi'}|e\rangle + |g\rangle). \tag{V.95}$$

The condition (V.94) corresponds to a $\pi/2$ *pulse*, an important operation on the internal atomic state. A π *pulse* performs the interaction for a time $2t$ and exchanges the atomic states

$$|e\rangle \rightarrow e^{i\varphi'}|g\rangle \quad |g\rangle \rightarrow -e^{-i\varphi'}|e\rangle. \tag{V.96}$$

The resonant interaction with a classical field is a basic ingredient in our CQED experiments. It is used in the Ramsey zones denoted by R_1 and R_2 in figure 1 in the introduction of this manuscript. Within these classical interaction zones, the state of the atoms can be manipulated at will before of after interaction with the high-finesse cavity C [2, 20, 63]. We have also made use of such pulses for the Ramsey and spin-echo sequences described in chapter IV.

V.3 Light-matter interaction: quantum theory

In this section, we will describe the interaction in the simplest matter-field system: one two-level system interacting with a field confined in a cavity mode. We will study two important regimes: the resonant one, when the atom and the field are at exact resonance, and the dispersive one, when the atom-field detuning is large compared to the coupling.

V.3.1 Jaynes & Cummings Model

The Jaynes & Cummings Model describes exactly our situation, a two-level system interacting with a quantized mode of a radiation field. Under the dipole and rotating wave approximations, the Hamiltonian can be written:

$$H_{JCM} = \frac{\hbar\omega_{at}}{2}\sigma_z + \hbar\omega_c\left(a^\dagger a + \frac{1}{2}\right) - ig(\sigma_+ a - \sigma_- a^\dagger) \tag{V.97}$$

with

$$g = \frac{\hbar\Omega_0}{2} \tag{V.98}$$

where we introduce the vacuum Rabi oscillation pulsation, Ω_0. The Hamiltonian includes three terms. The first is related to the atom, the second to the quantized field and the third to the interaction between them. Inside a cavity, the atom-field coupling generally depends upon the position of the atom in the mode and we have thus:

$$H_{int} = -i\frac{\hbar\Omega_0}{2}(\sigma_+ a - \sigma_- a^\dagger) \tag{V.99}$$

The evolution of the system is quite simple if we do not include any source of decoherence. The Hamiltonian of equation (V.97) couples the states $|e,n\rangle$ and $|g,n+1\rangle$ for $n \geq 0$. The subspace $S_n = \{|e,n\rangle, |g,n+1\rangle\}$ remains closed (the state $|g,0\rangle$ does not couple to any other and does not evolve at all). The evolution is thus described as separate evolutions in a set of dimension 2 manifolds. This suggests using directly the eigenstates of the whole Hamiltonian, the dressed states.

Dressed states:

In the subspace S_n, the complete Hamiltonian is, in matrix form,

$$H_n = \hbar \begin{pmatrix} \omega_c(n+1) + \Delta/2 & -i\Omega_0\sqrt{n+1}/2 \\ i\Omega_0\sqrt{n+1}/2 & \omega_c(n+1) - \Delta/2 \end{pmatrix}, \tag{V.100}$$

whose eigenstates are given by

$$|+,n\rangle = \cos\frac{\theta_n}{2}|e,n\rangle + i\sin\frac{\theta_n}{2}|g,n+1\rangle \tag{V.101}$$

$$|-,n\rangle = \sin\frac{\theta_n}{2}|e,n\rangle - i\cos\frac{\theta_n}{2}|g,n+1\rangle. \tag{V.102}$$

where θ_n is defined as

$$\tan\theta_n = \frac{\Omega_0\sqrt{n+1}}{\Delta} \tag{V.103}$$

varying between $0 \leq \theta_n < \pi$. These eigenstates are called the *dressed states*. Their eigenenergies are

$$E_{\pm,n} = \hbar\omega_c(n+1) \pm \frac{\hbar}{2}\sqrt{\Omega_0^2(n+1) + \Delta^2}. \tag{V.104}$$

This two level system is formally equivalent to a spin placed in a magnetic field [2]. The energies of the dressed states are represented in figure V.8 as a function of the detuning for a given value of the 'n-photon Rabi frequency' $\Omega_n = \Omega_0\sqrt{n+1}$. We observe two qualitatively different regimes, for a large or for a small detuning compared to Ω_n.

For $|\Delta| \gg \Omega_n$, the uncoupled bare states remain good approximations of the dressed states, denoted in the figure by the thick black lines. When $\Delta = 0$, the degeneracy of the bare states is lifted by the coupling Hamiltonian. This results in an energy gap given by the Rabi frequency Ω_n between the two dressed states.

V.3.1.a Resonant quantum Rabi Oscillation

We first consider the resonant evolution of the atom in a field stored in the cavity. The initial state reads

$$|\psi(0)\rangle = \sum_n [c_{e,n}|e,n\rangle + c_{g,n+1}|g,n+1\rangle] \tag{V.105}$$

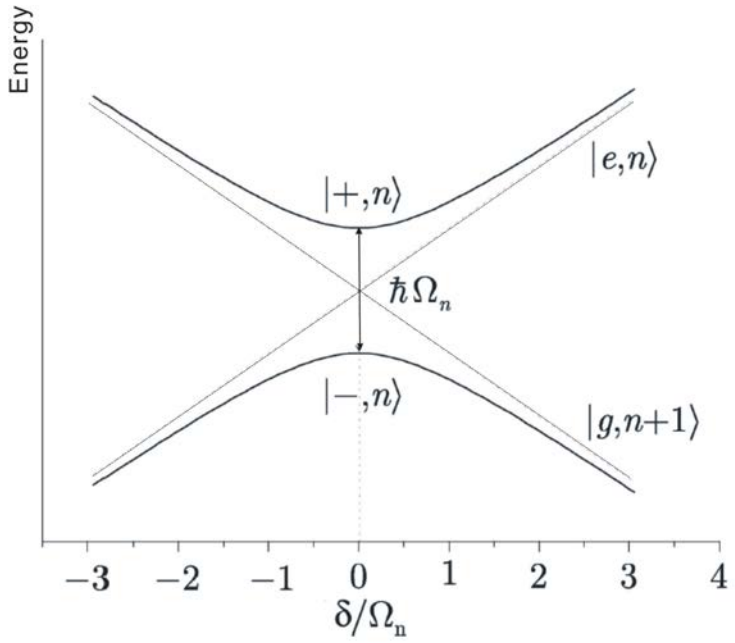

Figure V.8: Energies of dressed states as function of the ratio between detuning Δ and the 'n-photon Rabi frequency' $\Omega_n = \Omega_0\sqrt{n+1}$.

For the sake of definiteness, we will consider the case of an initially excited atom in a coherent field. We have then $c_{e,n} = c_n(0)$, with $|c_n(0)|^2 = P(n)$ defined in equation V.24 for an initial coherent state, and $c_{g,n+1} = 0$.

The evolution is straightforward at resonance using the dressed states picture. We do not give here the detailed calculation. It merely amounts in expressing the initial state in the basis of the dressed states, eigenstates of the total Hamiltonian. For $\Delta = 0$, the angle θ_n is equal to $\pi/2$ for all n values and the dressed states are then given by

$$|\pm, n\rangle = [|e, n\rangle \pm i|g, n+1\rangle]/\sqrt{2}. \tag{V.106}$$

Their evolution is trivial, and we rewrite at the end of the evolution the wavevector on the atomic energy states. The final expression for the atomic population inversion is thus

$$W(t) = \sum_{n=0}^{\infty} P(n)\cos(\Omega_n t) \tag{V.107}$$

Rabi oscillations of the atomic inversion at frequency Ω_0 take place even for an initial field in the vacuum state. This result is notoriously different from the one predicted by the semiclassical description of the interaction (two-level system and classical field). Vacuum Rabi oscillation is thus a genuinely quantum effect.

For larger initial fields, the inversion is a sum of terms oscillating at $\Omega_0\sqrt{n+1}$, weighted by the probability of finding the photon number n in the initial coherent state. For a

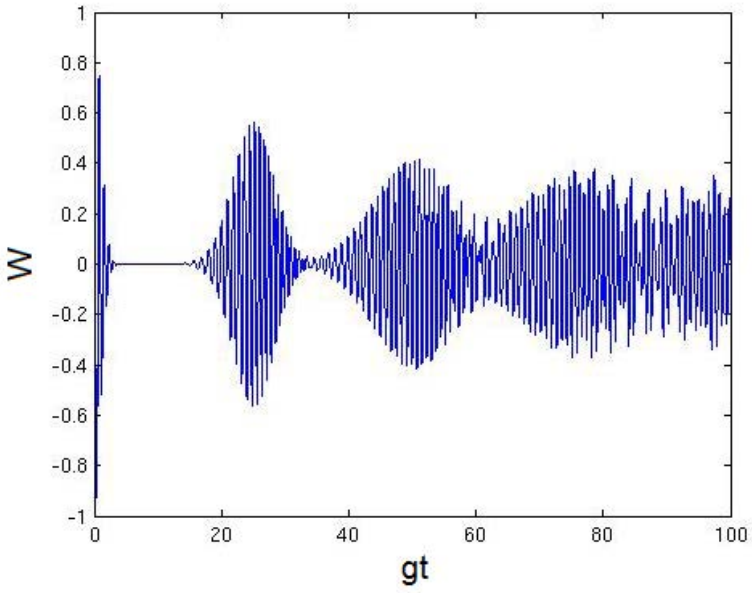

Figure V.9: Collapses and revivals for the atomic inversion W described by the JCM model, for an initial coherent state with $\bar{n} = 16$ photon and the atom in the excited state.

mesoscopic initial coherent field, the evolution is more complex than a simple oscillation. Figure V.9 shows the evolution of W, with an average initial photon number $\bar{n} = 16$. We observe a collapse and a revival of the Rabi oscillations, the first at a time $t_C \approx \pi/\Omega_0$ and the second at $t_R \approx 4\pi\sqrt{\bar{n}}/\Omega_0$, [2, 64, 72]. This collapse and revival sequence is repeated for increasing interaction times, but the amplitudes of the revivals decrease and their duration increases, up to a point when they overlap. We then observe a chaotic oscillation with an average frequency $\Omega_0\sqrt{\bar{n}}$.

Quantum revivals are a pure quantum phenomenon. It can be shown that they are not restricted to an initial coherent field (Rempe 1987, [73]). The quantum revival is a direct manifestation of field quantization. That explains the massive interest that this simple model has raised since the early times of quantum optics, both experimentally and theoretically.

One of the most interesting points is the fact that the atom and the field get entangled during the collapse phase, leading to mesoscopic field state superpositions (MFSS). Those state are the focus of this theoretical part. We thus discuss next the resonant generation of MFSS before addressing their generation by dispersive atoms.

V.3.1.b Resonant MFSS generation

The resonant interaction between a single atom and a mesoscopic field state leads to the efficient production of *phase cat states*. It has been first proposed by Gea-Banacloche

in the nineties [5, 6] and, independely, by Buzek and Knight [7]. It has been realized experimentally for the first time in our group, in the context of microwave CQED [8, 9]. The dynamics of the atom-field entanglement is strongly linked to the quantum collapse and revival of Rabi oscillations. Indeed we will see that atom and field disentangle at revival times and that Rabi oscillation collapses when they are entangled [2].

We consider now an atom initially excited and a a cavity containing initially a coherent field $|\beta\rangle = \sum_n c_n|n\rangle$. The initial state is

$$|e\rangle \otimes |\beta\rangle = \frac{1}{\sqrt{2}} \sum_n c_n[|-,n\rangle + |+,n\rangle]. \tag{V.108}$$

After evolution for some time t_i, the state is

$$|\psi(t_i)\rangle = \frac{1}{\sqrt{2}} \sum_n c_n \left[e^{i\phi_r(n)}|-,n\rangle + e^{-i\phi_r(n)}|+,n\rangle\right] \tag{V.109}$$

with

$$\phi_r(n) = \frac{\Omega_0 t_i \sqrt{n+1}}{2} \tag{V.110}$$

The state (V.109) can be conveniently rewritten as the sum of two states:

$$|\psi(t_i)\rangle = (|\psi_1\rangle + |\psi_2\rangle)/\sqrt{2} \tag{V.111}$$

where

$$|\psi_1\rangle = \frac{1}{\sqrt{2}} \left[\sum_n c_n e^{i\Omega_0\sqrt{n+1}t_i/2}(|e,n\rangle - i|g,n+1\rangle)\right] \tag{V.112}$$

$$|\psi_2\rangle = \frac{1}{\sqrt{2}} \left[\sum_n c_n e^{-i\Omega_0\sqrt{n+1}t_i/2}(|e,n\rangle + i|g,n+1\rangle)\right] \tag{V.113}$$

From this point on, the idea is to try to factor these two states, $|\psi_1\rangle$ and $|\psi_2\rangle$, into an atom and field contribution. For that goal, we make the assumption that the average photon number and its standard deviation $\Delta N = \sqrt{\bar{n}}$ are much larger than one. After some calculations, it is possible to write the state of the atom-field system [2]

$$|\psi(t_i)\rangle \approx \frac{1}{\sqrt{2}}[|\Psi^+_{ac}\rangle + |\Psi^-_{ac}\rangle] \tag{V.114}$$

with

$$|\Psi^+_{ac}\rangle = |\psi^+_{at}(t_i)\rangle \otimes |\psi^+_c(t_i)\rangle \tag{V.115}$$

$$|\Psi^-_{ac}\rangle = |\psi^-_{at}(t_i)\rangle \otimes |\psi^-_c(t_i)\rangle. \tag{V.116}$$

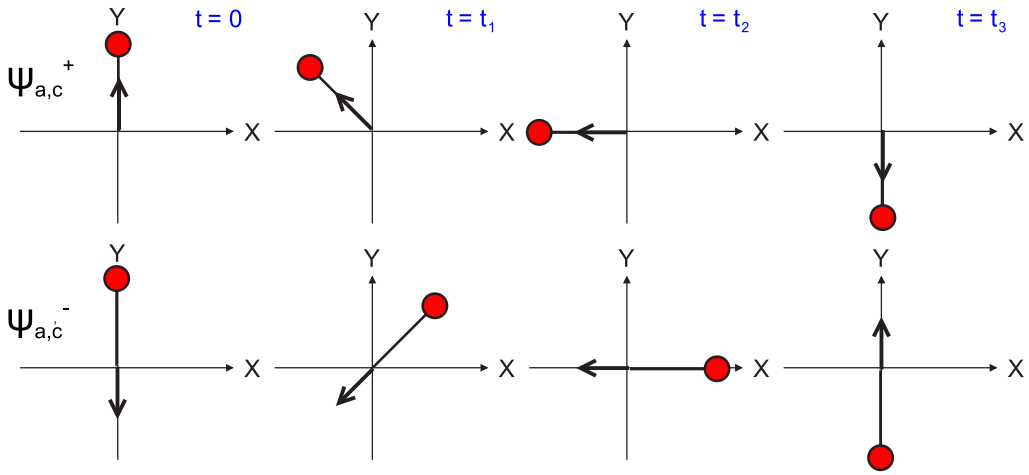

Figure V.10: Evolution for four different interaction times of the atomic and field states represented by vectors in the Bloch equatorial plane mapped of the Fresnel plane. On the top row, we represent $|\psi_{at}^{+}\rangle$ by a thick arrow and $|\psi_{c}^{+}\rangle$ by an arrow ending with a disk (uncertainty disk). The figures correspond to the interaction times $t = 0$, $t_1 = t_r/4 = \pi\sqrt{\bar{n}}/\Omega_0$, $t_2 = t_r/2 = 2\pi\sqrt{\bar{n}}/\Omega_0$ and $t_3 = t_r = 4\pi\sqrt{\bar{n}}/\Omega_0$. The lower row presents $|\psi_{at}^{-}\rangle$ and $|\psi_{c}^{-}\rangle$.

The state (V.114) is generally entangled. The atomic states are in the equatorial plane of the Bloch sphere, given by

$$|\psi_{at}^{\pm}(t_i)\rangle = \frac{1}{\sqrt{2}} e^{\pm i\Omega_0\sqrt{\bar{n}}t_i/2}\left[e^{\pm i\Omega_0 t_i/4\sqrt{\bar{n}}}|e\rangle \mp i|g\rangle\right] \tag{V.117}$$

and the field states are phase-shifted coherent states

$$|\psi_{c}^{\pm}(t_i)\rangle = e^{\mp i\Omega_0\sqrt{\bar{n}}t_i/4}|\beta e^{\pm i\Omega_0 t_i/4\sqrt{\bar{n}}}\rangle. \tag{V.118}$$

The interaction with the atom has split the coherent field into two coherent components with opposite phase shifts. As a consequence, we generate a MFSS. Figure V.10 presents a pictorial representation of the atom-field evolution. The plane used in this figure maps at the same time the equatorial plane of the Bloch sphere for the atom and the Fresnel phase plane for the field. The atomic states are represented as Bloch vectors (thick arrows). The field states are represented with an uncertainty disk centered at the tip of an arrow representing the classical amplitude of the coherent components. The atomic system at $t = 0$ involves the states $|\psi_{at}(0)^{+}\rangle = (|e\rangle - i|g\rangle)/\sqrt{2} = -i|0\rangle_Y$ and $|\psi_{at}(0)^{-}\rangle = (|e\rangle + i|g\rangle)/\sqrt{2} = +i|1\rangle_Y$.

The evolution is shown for four times, all expressed in terms of the revival time for the Rabi oscillations, $t_r = 4\pi\sqrt{\bar{n}}/\Omega_0$. The states $|\psi_{at}^{+}\rangle$ and $|\psi_{c}^{+}\rangle$ are rotating together at the angular frequency $\Omega_0/4\sqrt{\bar{n}}$ in the anti-clockwise direction and remain parallel at all times.

The states $|\psi_{at}^{-}\rangle$ and $|\psi_{c}^{-}\rangle$ rotate at the same frequency in the other direction and remain anti-parallel at all times. The global state is in general an entangled state, since the two field components represented by the uncertainty disks most of the time do not overlap.

Something particularly interesting happens for the time $t_2 = 2\pi\sqrt{\bar{n}}/\Omega_0$, half of the revival time. We can observe it directly in the pictorial representation of figure V.10. The states of the atom, $|\psi_{at}^{\pm}\rangle$, then coincide,

$$|\psi_{at}^{\pm}(t_2)\rangle = \pm\frac{i}{\sqrt{2}}e^{\pm i\pi\bar{n}}(|e\rangle - |g\rangle) = \pm e^{\pm i\pi\bar{n}}|\psi_{at}^{0}\rangle \tag{V.119}$$

The total state of the system factorizes as

$$|\psi(t_2)\rangle = |\psi_{at}^{0}(t_2)\rangle \otimes |\psi_{c}^{0}(t_2)\rangle, \tag{V.120}$$

where the state of the field is given by a MFSS of two coherent states with opposite phases

$$|\psi_{c}^{0}(t_2)\rangle = \left(e^{i\pi\bar{n}/2}|i\beta\rangle - e^{-i\pi\bar{n}/2}|-i\beta\rangle\right). \tag{V.121}$$

The collapse and revival of the Rabi oscillation are directly linked to the atom-field entanglement unveiled here. The signal we have presented in figure V.9 can be considered as a quantum interference between the atomic states $|\psi_{at}^{\pm}\rangle$. This interference only arises when the correlated field states are undistinguishable. The collapse of the Rabi oscillations appears then as a complementarity effect. It occurs when the components of the field become distinguishable. The field then carries information about the state of the atom. After a π rotation in the plane ($t_i = t_r$), the field states overlap again, and the entanglement vanishes. The oscillations revive, since the field state carries no information about the state of the atom.

Resonant MFSS have been realized experimentally for the first time by the group in the context of cQED with circular Rydberg atoms and superconducting cavities in the millimeter-wave regime [8, 9].

V.3.1.c Dispersive MFSS generation

MFSS can also be realized through the atom-field interaction in the dispersive regime. We focus thus in this paragraph on the far detuned regime when $\Delta \gg \Omega_n = \Omega_0\sqrt{n+1}$. In this case, the bare states remain good approximations for the dressed states. The eigenenergies of the Hamiltonian H_n asymptotically join the uncoupled system values (figure V.8):

$$|+,n\rangle \simeq |e,n\rangle \quad \text{and} \quad |-,n\rangle \simeq |g,n+1\rangle \quad \text{if } \Delta > 0 \tag{V.122}$$

$$|+,n\rangle \simeq |g,n+1\rangle \quad \text{and} \quad |-,n\rangle \simeq |e,n\rangle \quad \text{if } \Delta < 0 \tag{V.123}$$

The corresponding energies are modified at the second order in Ω_n/Δ

$$E_{e,n} = E_{e,n}^{0} + \frac{\hbar\Omega_0^2}{4\Delta}(n+1) \tag{V.124}$$

$$E_{g,n+1} = E_{g,n+1}^{0} - \frac{\hbar\Omega_0^2}{4\Delta}(n+1) \tag{V.125}$$

where the E^0 notation denotes the energies of the bare states. The shifts of the dressed levels are known as *light shift*. These shifts can be described by an effective Hamiltonian

$$H_{JC}^{disp} = H_c + \frac{\hbar}{2}\left(\omega_{at} + \frac{\Omega_0^2}{2\Delta}\left(a^\dagger a + \frac{1}{2}\right)\right)\sigma_z \tag{V.126}$$

where H_c is the cavity Hamiltonian. The second term of H_{JC}^{disp} can be considered either as an energy shift of the field or of the atomic system. On the one hand, the atomic frequency in the field of n photons is displaced by,

$$\Delta\omega_{at}(n) = \frac{\Omega_0^2}{2\Delta}\left(n + \frac{1}{2}\right) \ . \tag{V.127}$$

For $n = 0$, this term describes the *Lamb shift* due to the vacuum field fluctuations.

As a consequence, the dispersive interaction lasting a time t_i for an atom with a field containing n photons, will result in a relative phase accumulated between states $|e\rangle$ and $|g\rangle$,

$$\Delta\omega_{at}(n)t_i = \phi_0\left(n + \frac{1}{2}\right) \equiv \phi(n) + \frac{\phi_0}{2} \tag{V.128}$$

with

$$\phi_0 = \frac{\Omega_0^2 t_i}{2\Delta} \tag{V.129}$$

being the *phase shift per photon* ($\phi_0/2$ is the phase shift due to the Lamb shift). This phase shift is represented in the Bloch sphere picture in figure V.11.

We consider the initial atomic state $(|e\rangle + |g\rangle)/\sqrt{2}$. After an interaction time t_i, the state of the atom is transformed according to

$$(|e\rangle + |g\rangle)/\sqrt{2} \rightarrow (|e\rangle + e^{i\phi(n)}|g\rangle)/\sqrt{2}. \tag{V.130}$$

In simple terms, the phase shift imprinted onto the atomic state carries information about the number of photons. This effect is used in the group to realize Quantum Non Demolition measurements of the photon number.

On the other hand, we consider the action of the atom onto a coherent state $|\alpha\rangle$ initially prepared in the cavity. The evolution of the atom-cavity state is straightforwardly given by:

$$|e, \alpha\rangle \rightarrow e^{-i\phi_0/2}|e, \alpha e^{-i\phi_0/2}\rangle \tag{V.131}$$

$$|g, \alpha\rangle \rightarrow |g, \alpha e^{i\phi_0/2}\rangle, \tag{V.132}$$

where $|j, \alpha e^{-i\phi_0/2}\rangle = |j\rangle \otimes |\alpha e^{-i\phi_0/2}\rangle$. The states $|e, \alpha\rangle$ and $|g, \alpha\rangle$ are represented in figure V.12.

When the initial atomic state is $(|e\rangle + |g\rangle)/\sqrt{2}$, then the final atom-field state is given by

$$|\Xi_1\rangle = \frac{e^{-i\phi_0/2}}{\sqrt{2}}|e, \alpha e^{-i\phi_0/2}\rangle + \frac{1}{\sqrt{2}}|g, \alpha e^{i\phi_0/2}\rangle, \tag{V.133}$$

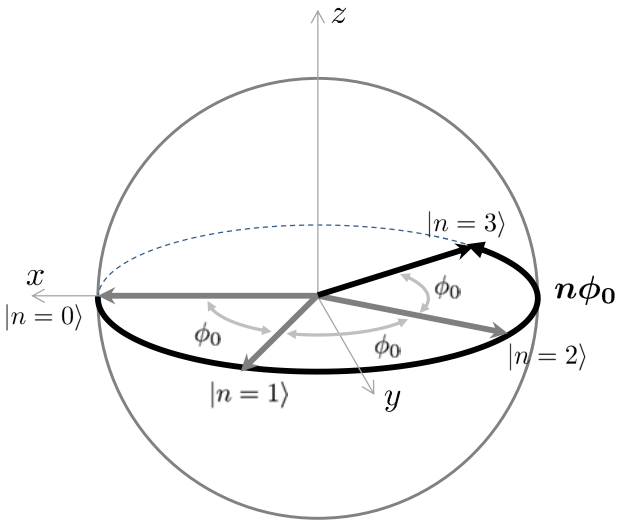

Figure V.11: Evolution of the Bloch vector representing the atomic state after a dispersive interaction with the cavity field prepared in a Fock state $|n\rangle$. The global phase $\phi_0/2$ is not shown in the scheme.

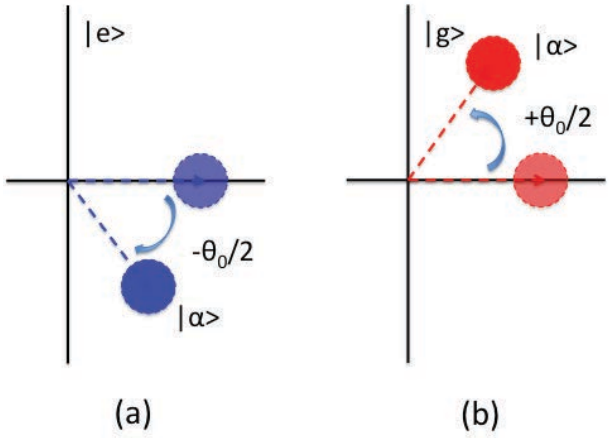

Figure V.12: Evolution of the states **(a)**:$|e,\alpha\rangle$ and **(b)**:$|g,\alpha\rangle$ in the Fresnel plane.

which is again a state reminiscent of the Schrödinger cat situation. In this entangled state, the projection by a direct measurement of the atomic state leads to only one of the field components. A much more interesting situation is obtained if a $\pi/2$ pulse is applied to the atom after the interaction with the cavity. This pulse implements the transformations

$$|e\rangle \to (|e\rangle + e^{i\varphi}|g\rangle)/\sqrt{2}, \qquad |g\rangle \to (|g\rangle - e^{-i\varphi}|e\rangle)/\sqrt{2}. \tag{V.134}$$

The atom-field state becomes then

$$|\Xi_2\rangle = \frac{e^{-i\phi_0/2}}{2}|e\rangle \otimes [|\alpha e^{-i\phi_0/2}\rangle - |\alpha e^{i\phi_0/2}\rangle] + \frac{1}{2}|g\rangle \otimes [|\alpha e^{-i\phi_0/2}\rangle + |\alpha e^{i\phi_0/2}\rangle] \tag{V.135}$$

where we have chosen to set φ equal to $\phi_0/2 = \Omega_0^2 t_i/4\Delta$. In the state $|\Xi_2\rangle$, the field state is projected after atomic detection in either states onto a MFSS $[|\alpha e^{-i\phi_0/2}\rangle \pm |\alpha e^{i\phi_0/2}\rangle]/\sqrt{2}$. If $\phi_0/2 = \Omega_0^2 t_i/4\Delta = \pi/2$, the final field states are the even and odd π-phase cat states, $|\gamma\rangle \pm |-\gamma\rangle$, with $\gamma = -i\alpha$.

There are obviously some differences between the resonant and dispersive generation of MFSS. In the dispersive regime, the separation of the two MFSS components occurs at a relatively low rate. This limits strongly the application of the method to large MFSSs (the preparation time should be much shorter than the decoherence time scale). The resonant generation of MFSS is slightly simpler (no initial atomic state superposition) and it is the fastest method. It is thus optimal for the preparation of MFSS with many photons, if the preparation time (till the half revival) can be kept shorter than the decoherence time scale.

V.4 Decoherence process

The MFSS generated by the resonant atom-field interaction are obviously very interesting. First, their appearance is directly linked to the collapse and revival of the Rabi oscillations, a genuinely quantum effect and a direct consequence of complementarity. Moreover, they sit at the boundary between the classical and the quantum world. Their study might lead to some insight into one of the mysteries of quantum physics, the conspicuous lack of quantum superpositions at the macroscopic scale. Obviously, these MFSS are strongly coupled to their environment and cannot be considered as an isolated, closed quantum system. This coupling results in a fast decoherence process, transforming the fancy MFSS into mundane statistical mixtures of fields with different classical attributes.

In this section we will describe shortly a simple approach to the decoherence process for field MFSS. We also recall the Lindblad equation formalism, which will be instrumental in next chapter.

We take as initial state ($t = 0$) a MFSS

$$|\psi_{cat}(0)\rangle = \frac{1}{\sqrt{2}}(|\alpha\rangle + |\beta\rangle) \tag{V.136}$$

with $\alpha = \sqrt{\bar{n}}e^{i\phi}$ and $\beta = \sqrt{\bar{n}}e^{-i\phi}$.

The environment E can be described as an ensemble of oscillators linearly coupled to the cavity mode. We index these oscillators by i. In the interaction picture, the evolution of an empty environment with a coherent initial field $|\gamma\rangle$ is described by

$$|\psi^E_{|\gamma\rangle}(t)\rangle = |\gamma(t)\rangle \otimes \prod_i |\epsilon_i(t)\rangle \tag{V.137}$$

with $\gamma(t) = \gamma e^{-\kappa t/2}$ and $\epsilon_i(t)$ the complex amplitude of the ith oscillator in E at time t. The cavity energy damping rate is κ, related to the cavity relaxation time T_c by $\kappa = 1/T_c$. Since energy must be conserved, the number of quanta in the environment E must be equal to the number of photons lost by the field at any time. This condition can be expressed as

$$\sum_i |\epsilon_i(t)|^2 = \bar{n}(1 - e^{\kappa t}). \tag{V.138}$$

The global system + environment state at time t is then given by

$$|\psi_{cat}^{E}(t)\rangle = \frac{1}{\sqrt{2}}\left[|\alpha(t)\rangle \otimes |E^{+}(t)\rangle + |\beta(t)\rangle \otimes |E^{-}(t)\rangle\right] \tag{V.139}$$

where the two states of the environment are

$$|E^{+}(t)\rangle = \prod_i |\epsilon_i(t)e^{i\phi}\rangle; \qquad |E^{-}(t)\rangle = \prod_i |\epsilon_i(t)e^{-i\phi}\rangle. \tag{V.140}$$

The two components of the initial MFSS are thus disseminating tiny copies of themselves in the environment. At time t, each mode of the environment involves a quantum superposition of two fields with the same phase relation as the initial cat states. Information about the initial state is thus leaking out of the cavity. We are of course interested only in the reduced density matrix of the cavity field, obtained by tracing over the environment. Tracing the entangled pure state above results, for the field, into a statistical mixture whose density operator is

$$\rho_{cat} = Tr_E \rho_{cat}^{E} = \frac{1}{2}\left\{|\alpha(t)\rangle\langle\alpha(t)| + |\beta(t)\rangle\langle\beta(t)| + \langle E^{-}(t)|E^{+}(t)\rangle|\alpha(t)\rangle\langle\beta(t)| + h.c.\right\} \tag{V.141}$$

where the overlap

$$\langle E^{-}(t)|E^{+}(t)\rangle = \exp\left[-\sum_i |\epsilon_i(t)|^2(1-e^{2i\phi})\right] = \exp[-\bar{n}(1-e^{-\kappa t})(1-e^{2i\phi})] \tag{V.142}$$

is very rapidly damped to zero with time. In particular, if we assume $\alpha = -\beta$, then

$$\rho_{cat}(t) = \frac{1}{2}\left\{|\alpha(t)\rangle\langle\alpha(t)| + |-\alpha(t)\rangle\langle-\alpha(t)| + e^{-2\bar{n}(1-e^{-\kappa t})}(|\alpha(t)\rangle\langle-\alpha(t)| + |-\alpha(t)\rangle\langle\alpha(t)|)\right\}. \tag{V.143}$$

For interaction times very small compared with the cavity relaxation time $t \ll T_c$ we get:

$$\rho_{cat}(t) \approx \frac{1}{2}\left\{|\alpha(t)\rangle\langle\alpha(t)| + |-\alpha(t)\rangle\langle-\alpha(t)| + e^{-2\bar{n}\kappa t}(|\alpha(t)\rangle\langle-\alpha(t)| + |-\alpha(t)\rangle\langle\alpha(t)|)\right\}. \tag{V.144}$$

The non-diagonal contributions to the density operator are thus damped with a characteristic decoherence time

$$T_D = \frac{1}{2\bar{n}\kappa} = \frac{T_c}{2\bar{n}} \tag{V.145}$$

after which the MFSS has become a statistical mixture. We can conclude that the decoherence process becomes faster and faster as the mean photon number increases.

In the general case (not restricted to π phase cats), T_D can be written as ([2], page 423-424),

$$T_D = \frac{2T_c}{D^2} \tag{V.146}$$

inversely proportional to the distance squared D^2 of the coherent components in phase space $D^2 = 4\bar{n}\sin^2\phi$.

V.4.1 Master equation

A more general description of decoherence is provided by the Lindblad equation. This equation will be thoroughly used in the next chapter to treat the realistic generation of large MFSS by resonant atomic ensembles.

Speaking in very general terms, we consider a system S coupled with an environment E. The detailed coupling of S and E is quite complex, since E is a very large system with a huge number of degrees of freedom. We can nevertheless get a simple picture if E is large enough to be impervious to the interaction with S (Born hypothesis) and if the Markov hypothesis applies (memory time scale of the environment much shorter than that of the system evolution). We can then write an equation for the evolution of the system S alone, described by the density matrix ρ_S, the Lindblad or 'Master' equation:

$$\frac{d\rho_S}{dt} = -\frac{i}{\hbar}[H, \rho_S] + \mathbf{L}\rho_S, \tag{V.147}$$

with

$$\mathbf{L}\rho_S = \sum_\mu \left(L_\mu \rho_S L_\mu^\dagger - \frac{1}{2} L_\mu^\dagger L_\mu \rho_S - \frac{1}{2} \rho_S L_\mu^\dagger L_\mu \right). \tag{V.148}$$

The first term is the r.h.s. of the first equation describes the Hamiltonian evolution of the system S, which is generally written in the interaction picture. The second term given by $\mathbf{L}$ describes the decoherence process. The L_μ are the operators describing the change occurring in the system under the influence of the environment. They can be obtained either through a detailed model of the coupling or by more qualitative arguments.

Relaxation of a cavity field in a thermal environment

We consider in our calculation only field decoherence, since atomic relaxation is a minor effect in the experimental context of circular Rydberg atoms. We must find the appropriate operators L_μ for the cavity field evolution.

The only possible events for the cavity field are the loss of a photon in the environment, or the gain of a thermal photon out of the thermal fluctuations of E at a finite temperature. We associate these two process to the the 'jump operators' L_- and L_+, both proportional to the annihilation and creation photon operators,

$$L_- = \sqrt{\kappa_-}a, \qquad L_+ = \sqrt{\kappa_+}a^\dagger \tag{V.149}$$

At thermal equilibrium, the jump rates $\kappa_\pm$ are related by

$$\frac{\kappa_-}{\kappa_+} = \frac{1 + n_{th}}{n_{th}} \tag{V.150}$$

where n_{th} is the average thermal photon number. The probabilities to gain or to lose a photon per unit time are given by

$$p_+ = Tr(L_+^\dagger L_+ \rho) = \kappa_+ Tr(aa^\dagger \rho) = \kappa_+(1 + n_{th}) \tag{V.151}$$

$$p_- = Tr(L_-^\dagger L_- \rho) = \kappa_- Tr(aa^\dagger \rho) = \kappa_- n_{th}. \tag{V.152}$$

A simple thermodynamical equilibrium consideration shows that the two rates are proportional to a unique cavity relaxation rate κ according to $\kappa_+ = n_{th}\kappa$ and $\kappa_- = (n_{th}+1)\kappa$. We can thus write the Lindblad equation for the cavity field as:

$$\frac{d\rho_f}{dt} = -i\omega_c[a^\dagger a, \rho_f] - \frac{\kappa(1+n_{th})}{2}(a^\dagger a\rho_f + \rho_f a^\dagger a - 2a\rho_f a^\dagger) - \frac{\kappa n_{th}}{2}(aa^\dagger\rho_f + \rho_f aa^\dagger - 2a^\dagger\rho_f a). \tag{V.153}$$

The first term can be eliminated by switching to the interaction picture (the other two terms are not modified). The evolution is entirely due to relaxation with

$$\mathbf{L}\rho_f = -\frac{\kappa(1+n_{th})}{2}(a^\dagger a\rho_f + \rho_f a^\dagger a - 2a\rho_f a^\dagger) - \frac{\kappa n_{th}}{2}(aa^\dagger\rho_f + \rho_f aa^\dagger - 2a^\dagger\rho_f a) \tag{V.154}$$

V.5 Conclusion

In this chapter, we have recalled the properties of the components of the atom-field system. We have introduced the standard formalism for the quantization of the field, and the various representations of the field sates. We have in particular described the Wigner function that will be used to present the theoretical results in the next chapter.

We have described the atom as a two-level system within the context of circular Rydberg states. We have introduced the Jayne-Cummings model and we have discussed the resonant and dispersive atom-field interaction regimes. For both of them, we have analyzed the generation of mesoscopic field states superpositions.

Then, we described the decoherence of these cat states and discussed the different time scales associated with it. We have also introduced the Lindblad Master equation and its form for cavity dissipation.

Chapter VI

Fast generation of mesoscopic field states superpositions in CQED

In this chapter, we present the main theoretical results of this work. We propose a simple scheme for the fast generation of MFSS in cavity QED. The generation of these cat states relies on the simultaneous interaction of two two-level atoms with a coherent field stored in the cavity. The detection of the atomic system in the appropriate final state projects the field onto the desired MFSS.

The generation of the MFSS is thus conditioned to the proper atomic detection. Nevertheless, all the required final states of the atomic system are obtained with a high probability, near 30%. The scheme proposed here is more efficient than those we have studied in the previous chapter using a single atom. The discussion of the method will be performed within the context of cavity QED experiment, using the parameters of our present experiment. However, the proposal it also highly relevant for the circuit-QED domain, where these kind of manipulation can be performed with artificial atoms.

We recall first the Dicke model [75] or Tavis and Cummings [34] model for an ensemble of A atoms interacting with the field. We also describe the 'factorization approximation' [10, 11, 74]. We discuss the method in the CQED context by an exact analytical solution first for $A = 2$ atoms without relaxation. We then include decoherence by numerical approaches using the Master equation. We study the maximum cat size, the fidelity with respect to an ideal cat state. Then we study also the $A = 4$ case using the factorization approximation.

VI.1 Dicke model

The Dicke model [75, 34] generalizes the JCM for the case of A atoms simultaneously interacting with a single mode. Collective emission and cooperative behaviors make this model richer than the standard JCM. We consider here only a simple version, in which all the atoms are coupled in the same way with the cavity field. This is a reasonable hypothesis for microwave cavity QED, since the atomic sample can be made much smaller

that the wavelength. The interatomic distances are nevertheless large enough so that the dipole-dipole interaction between the atoms is negligible (we are considering here a few atoms in a mm^3, a density much smaller than those encountered in the experimental part of this work).

The Hamiltonian, in the rotating wave and dipole approximation can be written as:

$$\hat{H} = \hbar\omega(\hat{n} + \hat{S}_z) + g(a\hat{S}_+ + a^\dagger \hat{S}_-) \tag{VI.1}$$

where $\omega = \omega_c = \omega_{at}$, since we focus on the resonant regime, and $g = \hbar\Omega_0/2$ is the coupling constant, the same for all the atoms. The collective atomic operators for the A identical two-level atoms are given by:

$$\hat{S}_\pm = \sum_{j=1}^{A} \sigma_\pm^{(j)} \qquad \hat{S}_z = \frac{1}{2}\sum_{j=1}^{A} \sigma_z^{(j)}. \tag{VI.2}$$

They obey the usual commutation relations

$$[\hat{S}_z, \hat{S}_\pm] = \pm\hat{S}_\pm; \quad [\hat{S}_+, \hat{S}_-] = 2\hat{S}_z. \tag{VI.3}$$

Is very convenient to work in the symmetrical subspace for the atomic system. The *Dicke states* $|k\rangle_{at}$ (or excitation number states) are eigenvectors of $\hat{S}_z$:

$$\hat{S}_z|k\rangle_{at} = (k - A/2)|k\rangle_{at}, \quad 0 \le k \le A \tag{VI.4}$$

$$\hat{S}_+|k\rangle_{at} = \sqrt{(k+1)(A-k)}|k+1\rangle_{at} \tag{VI.5}$$

$$\hat{S}_-|k\rangle_{at} = \sqrt{k(A-k+1)}|k-1\rangle_{at} \tag{VI.6}$$

where k is the number of excitations in the atomic system $0 \le k \le A$. The operator describing the total number of excitations of the complete system

$$\hat{N} = \hat{n} + \hat{S}_z$$

commutes with the Hamiltonian.

The collective atomic system undergoes Rabi oscillations in a mesoscopic coherent field, which present also, as in the $A = 1$ case of the JCM, quantum collapse and revivals [72].

VI.1.1 Factorization approximation

Let us consider the interaction of A atoms with a strong coherent state, where the initial mean photon number is much larger that the number of atoms $\bar{n} \gg A$. The initial state of the system can be written as a product state:

$$|\Psi(0)\rangle = |\alpha\rangle \otimes |\psi_A\rangle, \tag{VI.7}$$

where $|\alpha|$ and $|\psi_A\rangle$ correspond to the state of field and the atomic system respectively. We want to find an expression for the evolution of the global state $|\Psi\rangle$ at an interaction time

t. For that, we perform a basis change for the atomic subsystem. We use the vectors $|\underline{p}\rangle$ as basis, the so-called 'semiclassical atomic states', defined as the eigenstates of $\hat{S}_x$

$$\hat{S}_x|\underline{p}\rangle = \lambda_p|\underline{p}\rangle \tag{VI.8}$$

with $\lambda_p = A - 2p$ and $0 \leq p \leq A$.

The Dicke states can be written in terms of the semiclassical atomic states:

$$|k\rangle = \sum_{p=0}^{A} C_p^k|\underline{p}\rangle \tag{VI.9}$$

where the matrix elements C_p^k are given by [76]

$$C_p^k = \left[\frac{k!p!}{2^A(A-k)!(A-p)!}\right]^{1/2} \sum_{j=0}^{min(p,k)} \frac{(-2)^j(A-j)!}{j!(k-j)!(p-j)}, \tag{VI.10}$$

the standard expressions for the rotation of a spin $A/2$.

Within these conditions, the evolution of the initial state $|\alpha\rangle \otimes |\underline{p}\rangle$ can be approximately written at time t as

$$|\Phi_p(t)\rangle \otimes |A_p(t)\rangle, \tag{VI.11}$$

where the states are given by [10]

$$|\Phi_p(t)\rangle = \exp\left[-igt\lambda_p\sqrt{\hat{n} - A/2 + 1/2}\right]|\alpha\rangle \tag{VI.12}$$

$$|A_p(t)\rangle = \exp\left[-i\frac{gt\lambda_p}{2\sqrt{\bar{n}_N}}\left(\hat{S}_z + A/2\right)\right]|p\rangle \tag{VI.13}$$

with $\bar{n}_N = \bar{n} - A/2 + 1/2$. This is the 'factorization approximation' and it holds for short times compared to $\sim 2\bar{n}/\Omega_0$. The atomic state $|\Phi_p(t)\rangle$ results from the action of a rotation around the Z axis on the semi-classical initial state. The field state $|A_p(t)\rangle$ can be simplified by using the expansion

$$\sqrt{\hat{n} - A/2 + 1/2} \simeq \sqrt{\bar{n}_N} + \Delta\hat{n}/2\hat{n}_N^{1/2} - (\Delta\hat{n})^2/8\bar{n}_N^{-3/2} \tag{VI.14}$$

with $\Delta\hat{n} = (\hat{n} - \bar{n})$. The first term results in a global phase factor for the field state. The second transforms, within a global phase again, the coherent state $|\alpha\rangle$ into $|\alpha \cdot \exp(-i\Omega_p^{(A)}t)\rangle$. It thus describes a rotation of the coherent field amplitude around the origin of the phase space at an angular frequency

$$\Omega_p^{(A)} = \left(\frac{A}{2} - p\right)\frac{\Omega_0}{2\sqrt{\bar{n}_N}}. \tag{VI.15}$$

The third term is responsible for distortions of the coherent components due to an intensity-dependent phase shift. We will observe this action directly on the numerically computed Wigner function.

Taking now the initial state of the atomic system to be $|\psi_A\rangle$ and writing it in terms of the semiclassical states, we obtain an entangled atom-field state at time t

$$|\Psi(t)\rangle \simeq \sum_{p=0}^{A} C_p^k |\Phi_p(t)\rangle \otimes |A_p(t)\rangle. \tag{VI.16}$$

This state can be rewritten in term of the eigenstates of the operator S_z,

$$|\Psi(t)\rangle \simeq \sum_{k=0}^{A} |k\rangle \otimes |\Psi_k(t)\rangle \tag{VI.17}$$

where the state of the field is

$$|\Psi_k(t)\rangle = \sum_{p=0}^{A} D_p^k |\Phi_p(t)\rangle \tag{VI.18}$$

with

$$D_p^k = C_p^A C_k^p e^{i\frac{k\Omega_0(p-A/2)t}{2\bar{n}_N^{1/2}}}. \tag{VI.19}$$

The final state of the field, given by equation (VI.18), is a MFSS involving $A+1$ components. These components have the same energy and different phases [10, 74, 77].

For the simplest case of $A = 1$, Eq. (VI.12) reproduces the result of Gea-Banacloche for the JCM [6]. The field components in (VI.18) are two coherent states, equally weighted, rotating in opposite directions at the angular velocities $\Omega_p = \pm\Omega_0/4\bar{n}^{1/2}$.

The $A = 2$ situation is more interesting. We expect *a priori* a three-component state. Let us assume that both atoms are initially in the excited state, i.e. $k = 2 \longrightarrow \Psi_{at}(0) = |e,e\rangle = |2\rangle$. After interaction with the field, the atomic system can be in the following states $|k\rangle = |0\rangle$, $|1\rangle$, $|2\rangle$, where $|0\rangle = |g,g\rangle$ and $|1\rangle = (|e,g\rangle + |g,e\rangle)/\sqrt{2}$. If we restrict to the case in which we detect only one excited atom (the other being in the ground state), the final atomic state corresponds to $k = 1$. For this k value, the coefficient C_1^1 (and thus D_1^1) exactly cancel and we are left with only two field components which are phase-shifted with respect to the initial coherent field by

$$\pm \frac{\Omega_0 t}{2(\bar{n}-1/2)^{1/2}} \simeq \pm\Omega_0 t/2\bar{n}^{1/2} = \pm\Omega_0^{(2)} t \tag{VI.20}$$

twice as much as in the single-atom case. We can thus use the interaction with two atoms to generate two-component MFSS, albeit with a rate twice as fast as for the one atom case.

Let us compare in more details the MFSS generation process for one and two atoms. We are interested in the maximum size we can generate and in the time required for this generation. For short enough interaction times ($\Omega_0 t \ll \sqrt{\bar{n}}$), the size of the cat state,

$D^2 = 4\bar{n}\sin^2\Omega_0^{(2)}t$, is independent of the initial photon number and grows up quadratically with time

$$D^2 \simeq (\Omega_0 t)^2 \tag{VI.21}$$

This growth is four times faster than in the case of interaction of a single atom with the cavity. The maximum cat size is $4\bar{n}$. This maximum size is reached for an interaction time

$$t_{\pi/2} = \frac{\pi}{2\Omega_0^{(2)}} = 2\sqrt{\bar{n}}t_{vac}^{\pi/2} \tag{VI.22}$$

where $t_{vac}^{\pi/2} = \pi/2\Omega_0$ is the duration of a vacuum $\pi/2$ Rabi pulse. Again, $t_{\pi/2}$ is twice as short as in the $A = 1$ atom case. Even if short, this time must be much shorter than the final state decoherence time. This sets a limit to the mean photon number in the cat state. We set a rather arbitrary condition $t_{\pi/2} < T_{\bar{n}}/10$, which qualitatively corresponds to a $\approx 10\%$ fidelity reduction due to decoherence during preparation. The maximum size of the MFSS is then given by

$$D_{max}^2 \approx 4\left(\frac{T_c}{40t_{vac}^{\pi/2}}\right)^{2/3}. \tag{VI.23}$$

It is larger by a factor 1.6 than the maximum size obtained with a single atom in the same conditions.

VI.2 Two atoms interacting with a cavity field without dissipation. Exact calculation.

We have analyzed so far the factorization approximation for the case of two atoms. The object of this Section is to test the quality of this approximation by a direct comparison with the exact solution without decoherence. We will then compute the full evolution including cavity dissipation. This comparison will reinforce our trust in the factorization approximation, that we will use later to address the $A > 2$ case.

Figure VI.1 shows the setup of the ENS cavity QED experiments (our scheme could be extended for instance to circuit QED, but we consider only this context for the sake of definiteness). Circular Rydberg atom samples are prepared by laser and radio frequency excitation of a thermal rubidium atomic beam in box B (the atomic beam oven is not shown). The velocity of the atomic samples is $v = 150$–250 m/s. They interact with the superconducting cavity C, cooled down to 0.8 K. It is made up of two spherical niobium mirrors, sustaining a Gaussian standing wave mode. The cavity damping time T_c can be as large as 130 ms. The cavity is tuned at resonance with the 51.1 GHz transition between the circular states $|e\rangle$ and $|g\rangle$, with principal quantum numbers 51 and 50. The vacuum Rabi frequency is then $\Omega_0/2\pi = 49$ kHz. The R_1 and R_2 zones form a Ramsey interferometer where we can manipulate the internal atomic states. The atoms are finally counted in the state-resolving field-ionization detector D. A voltage V applied across the cavity mirrors is

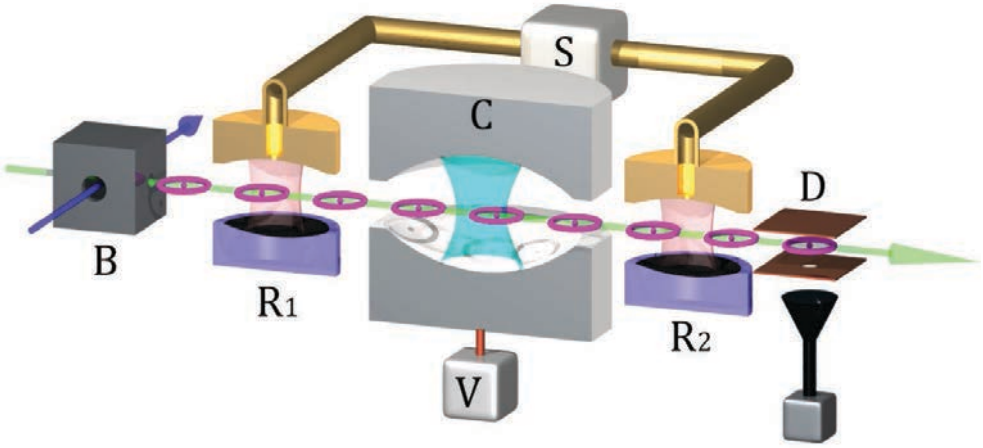

Figure VI.1: Scheme of the cavity QED setup. The circular Rydberg atoms are prepared in the box B and detected in D. The high finesse cavity C stores the coherent field. The cavity C is placed in between two Ramsey zones R_1 and R_2, which form a Ramsey interferometer.

used to tune rapidly the atomic frequency out of the cavity resonance, through the Stark effect. This allows us to define interaction times shorter that the atomic transit through the cavity mode.

The number of atoms prepared by laser excitation in each sample obeys a Poisson statistics. In order to operate with single atoms, we keep generally the average atom count very low. For the scheme presented here, we must operate with samples containing exactly $A = 2$ atoms.

Selecting the atom number can be achieved in several ways. The simplest consist in a post-selection scheme. We count the number of atoms in the sample after it has interacted with C. The counting may be based on direct field-ionization, with a near unit efficiency, or on more sophisticated schemes based on the interaction of the sample with a second cavity [78]. Also, as discussed in the first part of this manuscript, the dipole blockade mechanism makes it possible to prepare selectively two-atom states, by tailored laser excitation of a cold, dense ground-state atomic sample [79, 80]. The two resulting Rydberg atoms can be later accelerated, using the Stark effect [81] to velocities compatible with a propagation through the apparatus during their 30 ms lifetime. Note that, in all cases, the expansion of the atomic sample during its transit towards the cavity makes the direct dipole-dipole interaction between the atoms negligible while they interact with the cavity field, making all the approximations used for the Dicke model valid.

In these conditions, the Hamiltonian in the dipole and rotating-wave approximation, reads ($\hbar = 1$):

$$H = \omega_0 \frac{\sigma_z^1}{2} + \omega_0 \frac{\sigma_z^2}{2} + \omega_c a^\dagger a + g(a\sigma_+^1 + a^\dagger \sigma_-^1) + g(a\sigma_+^2 + a^\dagger \sigma_-^2) \tag{VI.24}$$

where $\sigma_z^{1,2}$ and $\sigma_\pm^{1,2}$ are the Pauli operators for the atom 1 and 2 obeying the usual $SU(2)$ commutation relations:

$$[\sigma_z^{(j)}, \sigma_\pm^{(j)}] = \pm\sigma_\pm^{(j)} \qquad [\sigma_+^{(j)}, \sigma_-^{(j)}] = 2\sigma_\pm^{(j)}. \tag{VI.25}$$

The atomic and field frequencies are given by ω_0 and ω_c, respectively. We assume that the atoms and the field are in resonance, $\omega = \omega_0 = \omega_c$. In the interaction picture, the Hamiltonian is:

$$H_I = g(a\sigma_+^1 + a^\dagger\sigma_-^1) \otimes \mathbb{I}_2 + \mathbb{I}_1 \otimes g(a\sigma_+^2 + a^\dagger\sigma_-^2). \tag{VI.26}$$

A basis for the atomic system is made up of the four state $(e_1e_2), (e_1g_2), (g_1e_2), (g_1g_2)$ where the notation i_1j_2 refers to the atomic states $|j_1\rangle \otimes |i_2\rangle$. The Hamiltonian can be written in matrix form over this basis as:

$$H_I = g \begin{bmatrix} 0 & a & a & 0 \\ a^\dagger & 0 & 0 & a \\ a^\dagger & 0 & 0 & a \\ 0 & a^\dagger & a^\dagger & 0 \end{bmatrix}. \tag{VI.27}$$

The evolution operator of the compound atoms-field system has been derived in Ref. [82]:

$$U(t) = \begin{bmatrix} \mathcal{A} & -ia\mathcal{S} & -ia\mathcal{S} & \mathcal{B} \\ -i\mathcal{S}a^\dagger & \mathcal{D} & \mathcal{E} & -i\mathcal{S}a \\ -i\mathcal{S}a^\dagger & \mathcal{E} & \mathcal{D} & -i\mathcal{S}a \\ \mathcal{B}^\dagger & -ia^\dagger\mathcal{S} & -ia^\dagger\mathcal{S} & \bar{\mathcal{A}} \end{bmatrix} \tag{VI.28}$$

where we use the following definitions:

$$\mathcal{A} = 1 + \frac{a(\mathcal{C}-1)a^\dagger}{\Lambda} \qquad \mathcal{B} = \frac{a(\mathcal{C}-1)a}{\Lambda}$$

$$\mathcal{D} = \frac{1}{2}(1+\mathcal{C}) \qquad \mathcal{E} = -\frac{1}{2}(1-\mathcal{C})$$

$$\mathcal{C} = \cos(\sqrt{2}gt\sqrt{2\hat{n}+1}) \qquad \mathcal{S} = \frac{\sin(\sqrt{2}gt\sqrt{2\hat{n}+1})}{\sqrt{2}\sqrt{2\hat{n}+1}}$$

$$\Lambda = 2\hat{n}+1 \qquad \bar{\mathcal{A}} = 1 + \frac{a^\dagger(\mathcal{C}-1)a}{\Lambda}.$$

For simplicity (without loss of generality), we assume that the initial conditions belong to the symmetrical atomic subspace, which includes the states:

$$|0\rangle = |g_1g_2\rangle \tag{VI.29}$$

$$|1\rangle = \frac{(|e_1g_2\rangle + |g_1e_2\rangle)}{\sqrt{2}} \tag{VI.30}$$

$$|2\rangle = |e_1e_2\rangle. \tag{VI.31}$$

The evolution operator restricted to this subspace can be written as

$$U(t) = \begin{bmatrix} A & -\sqrt{2}iaS & B \\ -\sqrt{2}iSa^\dagger & (D+E) & -\sqrt{2}iSa \\ B^\dagger & -\sqrt{2}ia^\dagger S & A^\dagger \end{bmatrix}. \tag{VI.32}$$

Let us assume now that the atomic and the field state are respectively initially prepared in the excited state $|2\rangle$ and in a coherent field $|\alpha\rangle$, $|\psi(t=0)\rangle = |2\rangle \otimes |\alpha\rangle$. Then, the state at time t is given by [82]

$$|\psi(\phi)\rangle = |0\rangle|\psi_0\rangle + |1\rangle|\psi_1\rangle + |2\rangle|\psi_2\rangle \tag{VI.33}$$

where $\phi = \Omega_0 t/\sqrt{2}$ ($\phi = \pi/2$ correspond to $t = t_{vac}^{\pi/2} = 5$ μs) is a dimensionless time. The (unnormalized) field states corresponding to the three possible atomic states are

$$|\psi_0\rangle = a^\dagger \frac{\left(\cos\left(\phi\sqrt{2\hat{n}+1}\right)-1\right)}{2\hat{n}+1} a^\dagger |\alpha\rangle, \tag{VI.34}$$

$$|\psi_1\rangle = -i\frac{\sin\left(\phi\sqrt{2\hat{n}+1}\right)}{\sqrt{2\hat{n}+1}} a^\dagger |\alpha\rangle, \tag{VI.35}$$

$$|\psi_2\rangle = \left(1 + a\frac{\left(\cos\left(\phi\sqrt{2\hat{n}+1}\right)-1\right)}{2\hat{n}+1} a^\dagger\right)|\alpha\rangle. \tag{VI.36}$$

In figure VI.2, we plot the atomic purity and the concurrence as a function of the interaction time for an initial mean photon number $\bar{n} = 25$. The concurrence is defined as $C = D(1 - Tr(p_a^2))/(D-1)$ (V.41) [70, 71, 83], where D is the Hilbert space dimension. We observe that the concurrence reaches values close to the maximum (one). It means that the atoms-field system reaches a maximum degree of entanglement.

The maximum entanglement occurs within the first collapse of the Rabi oscillations, as shown in figure VI.3. We observe here the rapid oscillations of each atomic level populations ($k = 0,\ 1$, and 2). They correspond to the Rabi oscillation of the spin-1 system driven by the resonant cavity field. These oscillations rapidly collapse, due to the dispersion of field amplitudes in the initial coherent state, as is the case for a single atom. The steady state of the three populations after the collapse of the oscillations are of the order of 1/3. Revivals are also expected, but they happen for much longer times [77, 72], and they are not our focus for the time being. We are more interested into the field states prepared by short interaction times, within the collapse period.

Figure VI.4 shows the Wigner function $W(\beta)$ of the the cavity field states (equations VI.34 to VI.36) after the atomic system is detected either in $|0\rangle$ (frame **(a)**), $|2\rangle$ (frame **(b)**) or $|1\rangle$ (frame **(c)**) . The detection of the three atomic states occur with comparable probabilities. The interaction is halted at $t = 15$ μs.

The three frames in figure VI.4 show clearly that he cavity field is projected into a mesoscopic superposition with nonclassical features. The most interesting situation is obtained for the detection in the state $k = 1$. We can immediately identify a MFSS made

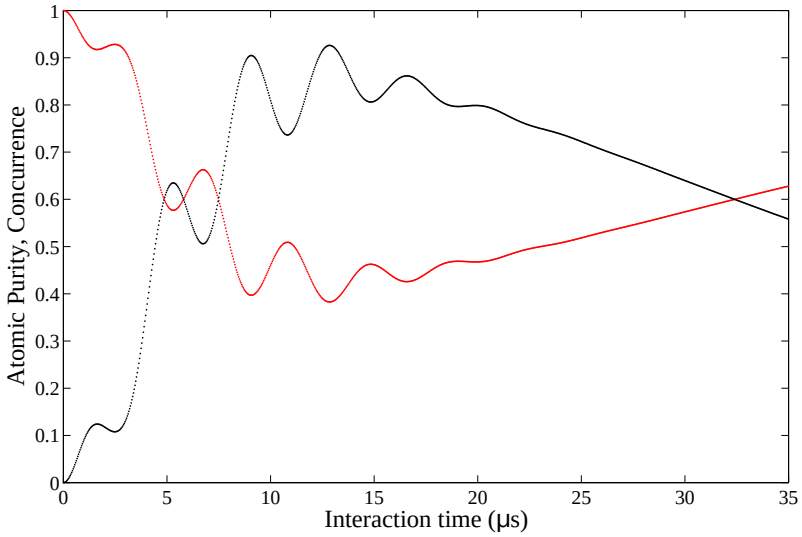

Figure VI.2: Atomic purity (red) and atoms-field concurrence (black) as a function of the interaction time. The atoms and the field are assumed to be initially prepared in the state $|e_1, e_2\rangle \times |\alpha\rangle$ with $\alpha = \sqrt{25}$.

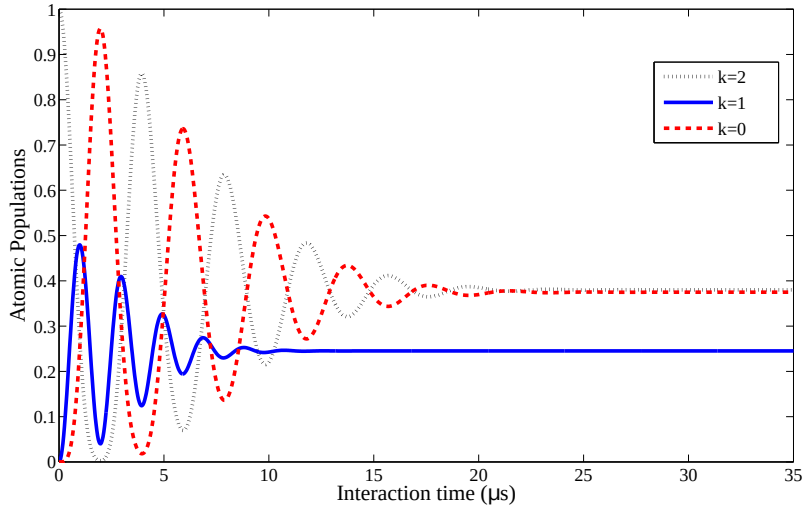

Figure VI.3: Atomic level populations as a function of the interaction time t during the collapse of the quantum Rabi oscillation. Dashed gray, solid blue and dotted red lines correspond to the states $|2\rangle$, $|1\rangle$ and $|0\rangle$ respectively.

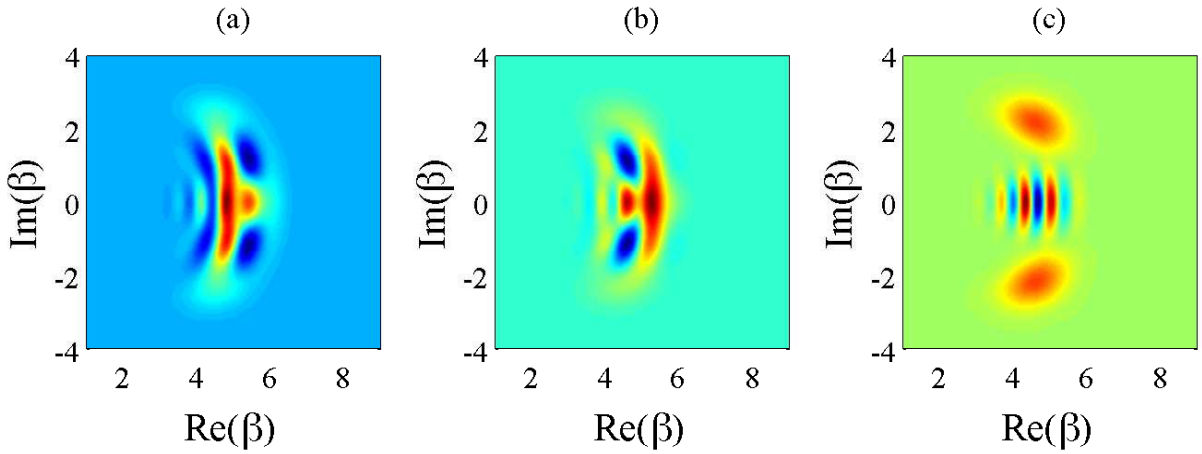

Figure VI.4: Wigner function $W(\beta)$ of the field states conditioned to the atomic detection in states **(a)** $|0\rangle$, **(b)** $|2\rangle$ and **(c)** $|1\rangle$ after an interaction time $t = 15$ μs. The initial conditions are the same as in figures VI.2 and VI.3. For $k = 1$, the field is left in a cat-like state with a small distortion of its coherent components.

up of two nearly coherent components with opposite phase shifts, as predicted by the factorization approximation. The slight distortion of the coherent components observed in the Wigner function is due to higher order terms in the expansion of (VI.14).

The exact field state can be compared with the results of the factorization approximation. We obtain a fidelity $F = 99\%$, where F is defined by [84]

$$F(\rho_1, \rho_2) = \left(Tr \left[\sqrt{\sqrt{\rho_1}\rho_2\sqrt{\rho_1}} \right] \right)^2, \tag{VI.37}$$

where ρ_1 and ρ_2 are the density operators to be compared.

VI.2.1 MFSS size and fidelity with respect to an ideal cat

The MFSS obtained here can also be compared with an ideal cat state, a quantum superposition of two coherent states:

$$|\psi\rangle = c|\delta\rangle + be^{i\varphi}|\gamma\rangle, \tag{VI.38}$$

with $c^2 + b^2 = 1$ and $|\delta - \gamma| \gg 1$. Figure VI.5 shows a direct comparison between the MFSS obtained though the exact two-atom field interaction ($\bar{n} = 25$, interaction time $t = 15$ μs – frame **(a)**) and the ideal cat (frame **(b)**). The amplitudes δ and γ, the coefficients c and b, and the phase φ are adjusted to maximize the fidelity F (equation VI.37) between the ideal cat and the real MFSS. The values resulting from this fit are $\delta = 4.62 + 2.18i$, $\gamma = 4.62 - 2.18i$, with $b = -0.71$ and $\varphi = 0.54$ πrad. The final fidelity w.r.t the original state is 98%. The size of the prepared MFSS, defined as $D^2 = |\delta - \gamma|^2$ reaches $D^2 = 19$.

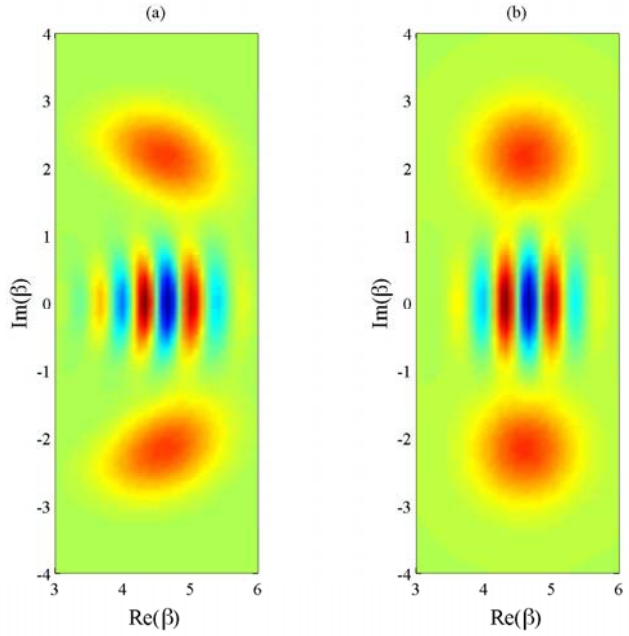

Figure VI.5: Wigner function of the MFSS presented in figure VI.4 **(c)** and again here in frame **(a)**. **(b)** Ideal superposition of two coherent states fitted to the exact state. The mutual fidelity is 98%. The ideal cat components are given by $\delta = 4.62 + i2.18$ and $\gamma = 4.62 - i2.18$. The other parameters of the fit are given in the text. The final MFSS size is $D^2 = 19$.

Note that the cavity is prepared in a pure state by the atomic detection. The slight reduction of fidelity is only due to the small distortion of the two coherent components.

The size of the cat state depends on the interaction time and on the initial mean photon number. In figure VI.6, we show the MFSS size D^2, the fidelity F w.r.t an ideal cat state, and the probability of detecting the state $|k = 1\rangle$ for three initial mean photon numbers $\alpha^2 = 10,\ 20$ and 30 as a function of the interaction time t. We can observe that the MFSS size grows initially quadratically with time. It reaches rapidly (in a time of the order of $2\pi/\Omega_0$) a rather large value. This value nevertheless varies very slowly with the initial photon number, as expected from the factorization approximation results. A similar effect is also observed for a single atom [2, 8]. In frame **(b)**, we observe that the fidelity slightly drops for large initial photon numbers, but always remains above 90%. This drop in fidelity is again entirely due to the small distortion of the coherent components components.

Frame **(c)** shows that the probability to measure the atom in state $|1\rangle$ remains close to 30% for all interaction times in this range. This is an important point for this method. In the single atom case, the generation of the MFFS is unconditional if the interaction time exactly corresponds to the half revival. Here, we generate a superposition for much shorter

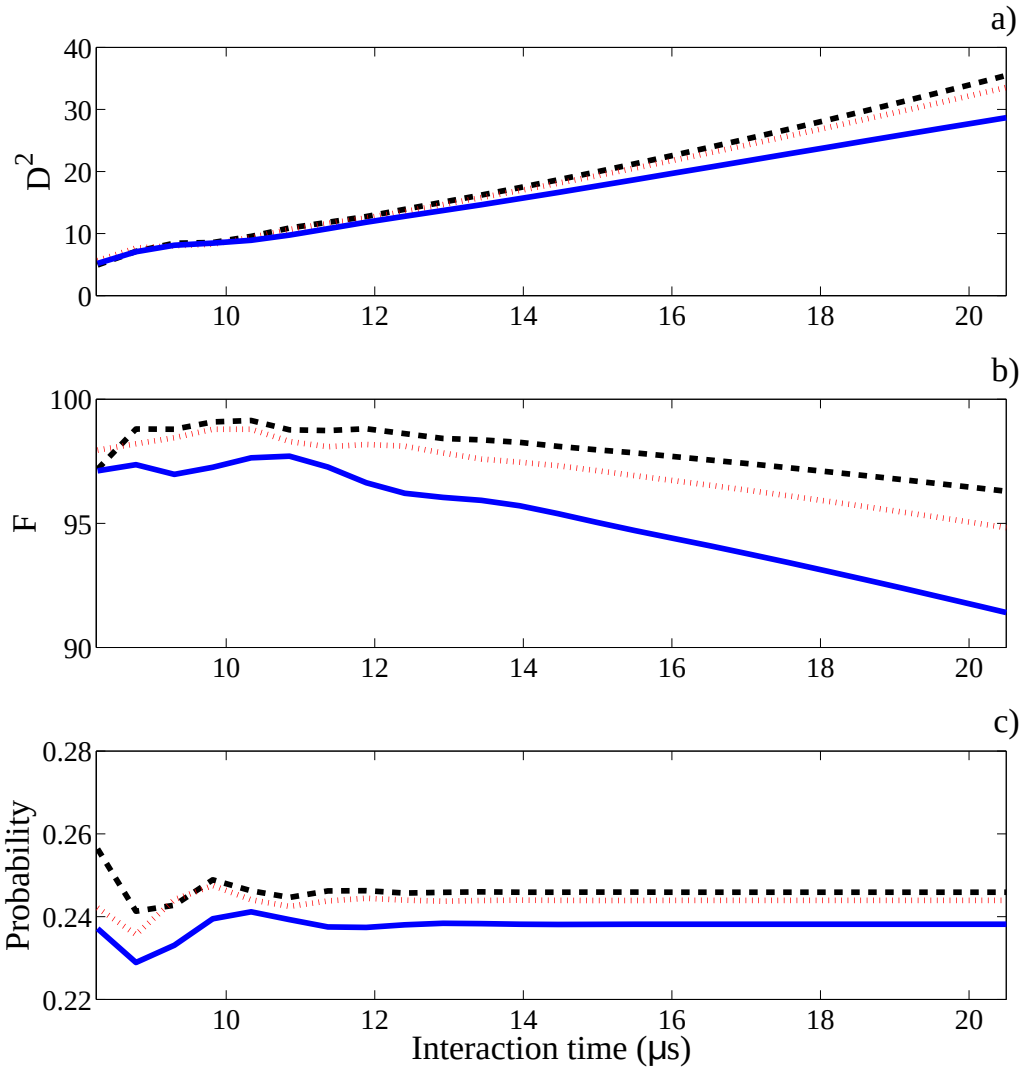

Figure VI.6: Behavior for different initial mean photon numbers $\alpha^2 = 10,\ 20$ and 30 of **(a)** the cat size D^2, **(b)** the fidelity with respect to an ideal cat F and **(c)** the probability for detecting the state $|1\rangle$ as a function of the interaction time .

times, at the expense of a detection of the atoms in the proper state. A high probability of occurrence of this state is essential. We also plot in figure VI.7 a 'movie' of the evolution of the MFSS from 0.5 μs to 16 μs for 25 equally spaced times.

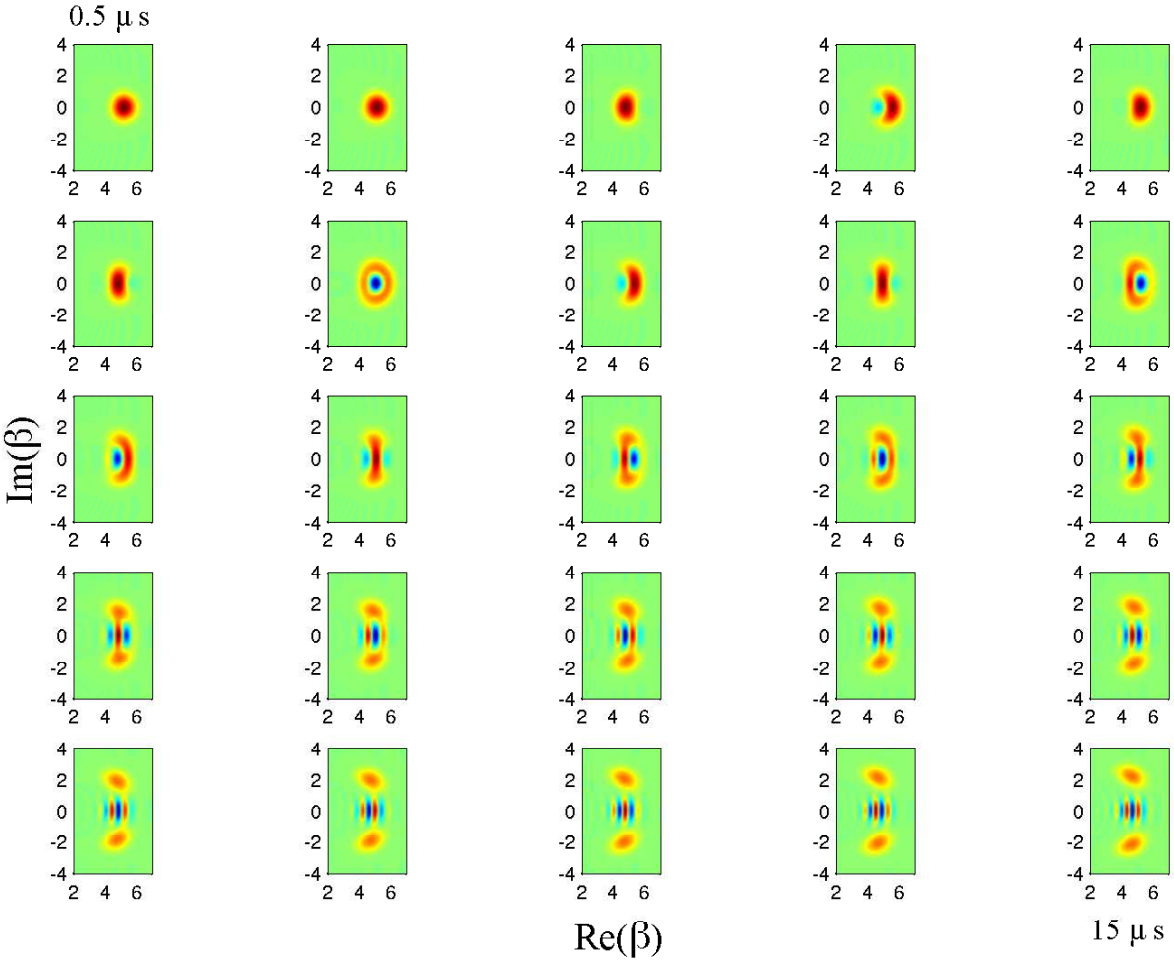

Figure VI.7: Wigner function W for the field state conditioned to the atomic detection in $|1\rangle$ for interaction times from 0.5 μs to 15 μs at 25 equally spaced time steps. $\alpha^2 = 25$. The evolution is from left to right.

VI.2.2 Case of an Initial atomic state $|1\rangle$

Cat-like state can be generated for different initial atomic states. We consider here for instance briefly the initial atomic state $|k=1\rangle$. Of course, the initial preparation of state $|1\rangle$ is much more difficult than that of two excited atoms $|2\rangle$. We only treat this case for the sake of completeness, but it is clear that the experimental implementation of the protocol requires the initial state $|2\rangle$.

After an interaction time t, the states of the cavity field conditioned to the detection of the atoms in $|0\rangle$, $|1\rangle$ and $|2\rangle$ are

$$|\xi_0\rangle = -ia\frac{\sin(\phi\sqrt{2\hat{n}+1})}{\sqrt{2\hat{n}+1}}|\alpha\rangle, \tag{VI.39}$$

$$|\xi_1\rangle = \cos(\phi\sqrt{2\hat{n}+1})|\alpha\rangle, \tag{VI.40}$$

$$|\xi_2\rangle = -ia^{\dagger}\frac{\sin(\phi\sqrt{2\hat{n}+1})}{\sqrt{2\hat{n}+1}}|\alpha\rangle. \tag{VI.41}$$

We show the Wigner functions of these states in figure VI.8. We observe that these three MFSS are very similar to each other, as can be directly inferred from (VI.39) to (VI.41). In other to see more clearly the slight differences between these states, we present in figure (VI.9) the photon number distribution $P(n)$ for these three states.

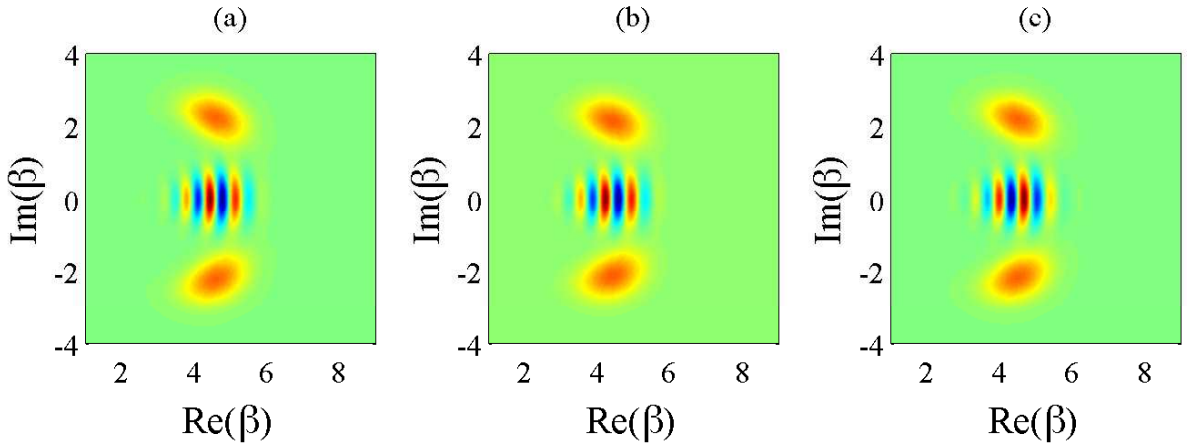

Figure VI.8: Wigner function $W(\beta)$ of the field states conditioned to the atomic detection in states **(a)** $|0\rangle$, **(b)** $|2\rangle$ and **(c)** $|1\rangle$ after an interaction time $t = 15$ μs. The initial conditions are a coherent field with 25 photons on the average and an atomic state in $k = 1$. Cat's-like states are produced whatever the detected atomic state.

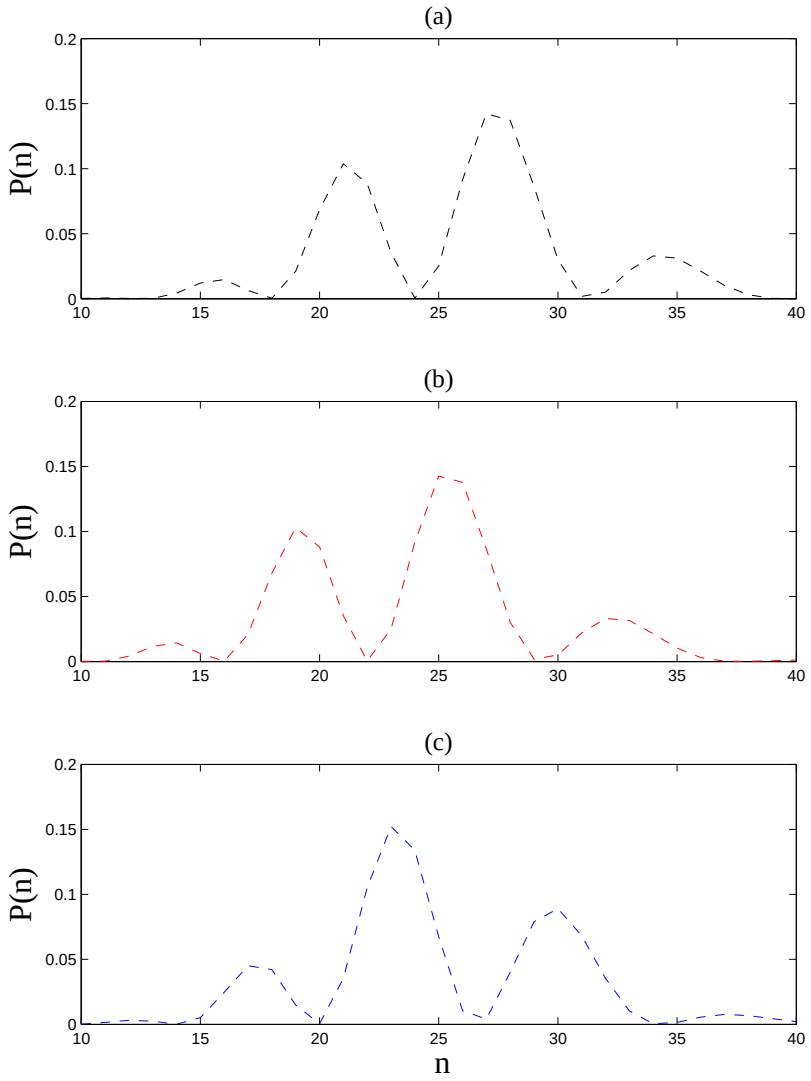

Figure VI.9: Photon number distribution $P(n)$ of the field states conditioned to the atomic detection in states **(a)** $|0\rangle$, **(b)** $|2\rangle$ and **(c)** $|1\rangle$. The initial conditions are the same as for figure VI.8.

VI.3 Numerical simulation: two atoms-field interaction including field dissipation.

So far we have considered only short interaction times at the scale of the cavity damping time. We have seen that the proposed method for the generation of MFSS is efficient within this time scale. It is nevertheless interesting to see how far we can go, in terms of the maximum size of the generated state. In order to do that properly, we must include the effect of cavity dissipation. As we will see in this Section, very large cats are within reach in spite of decoherence, a very encouraging result.

In order to include relaxation process, we assume that the field is in contact with a thermal reservoir at a finite temperature T, and we integrate the Lindblad equation for the atomic-field matrix system ρ_{af}, introduced in Chapter V,

$$\begin{aligned}\frac{d\rho_{af}}{dt} &= -\frac{i}{\hbar}\left[V_{int},\rho_{af}\right] \\ &- \frac{\kappa}{2}\left(n_{th}+1\right)\left(a^{\dagger}a\rho_{af} - 2a\rho_{af}a^{\dagger} + \rho_{af}a^{\dagger}a\right) \\ &- \frac{\kappa}{2}n_{th}\left(aa^{\dagger}\rho_{af} - 2a^{\dagger}\rho_{af}a + \rho_{af}aa^{\dagger}\right)\end{aligned} \tag{VI.42}$$

We use the following parameter values: cavity damping time $T_c = 1/\kappa = 130$ ms, mean thermal photon number $n_{\rm th} = 0.05$ and Rabi frequency $\Omega_0/2\pi = 49$ kHz. Figure VI.10 presents the infidelity $1-F$ of the generated field state at 15 μs w.r.t. an ideal coherent MFSS as a function of the cavity damping time T_c. It shows that the method is quite insensitive to the losses, provided the damping time is at least of the order of 1 ms for this interaction time scale.

What is the largest MFSS we can realistically envision? Taking into account the large $T_c/t_1 = 26000$ value, we can expect, from the qualitative discussion based on the factorization approximation, to generate MFSS with $D^2 \simeq 300$ in a time of the order of 86 μs, starting from a 75 photons coherent state, a quite large cat indeed. Note that this interaction time correspond to atoms crossing the cavity at 87 m/s.

We have numerically computed the evolution, including cavity relaxation, for such a large initial coherent field. Figure VI.11 presents the Wigner function of the MFSS generated for these conditions with $Tc = 0.13$ s. The exact cat size is $D^2 = 324$, measured between the centers of the distorted coherent components. The fidelity with respect to an ideal coherent state superposition is $F \simeq 50\%$. This ideal cat state has a distance squared $D^2 \simeq 300$. The fidelity reduction is in part due to the conspicuous deformation of the components, but also to relaxation. Performing similar calculations for $A = 1$ atom, we find that, the generation time being longer, the maximum distance is limited to $D^2 \simeq 180$.

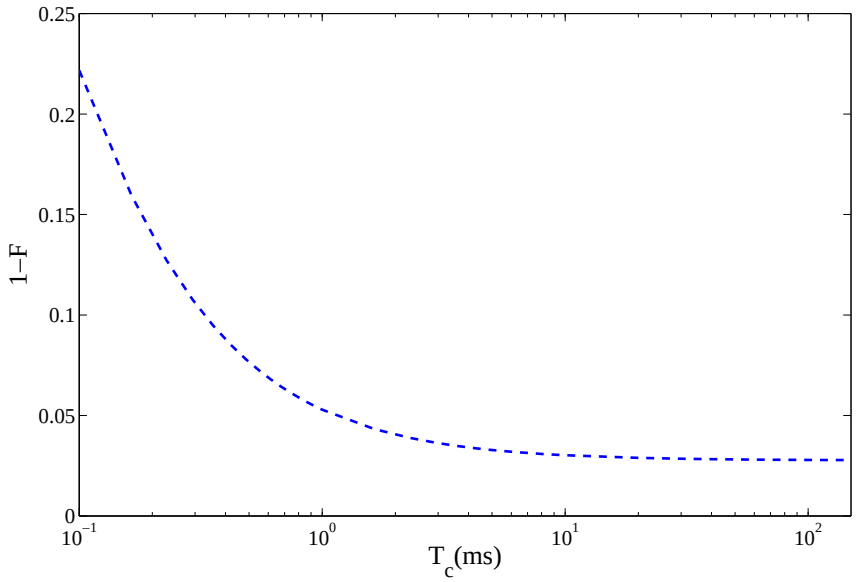

Figure VI.10: Infidelity $1-F$ of the prepared MFSS w.r.t an ideal superposition of coherent states versus the cavity damping time T_c for an initial mean photon number $\alpha^2 = 20$.

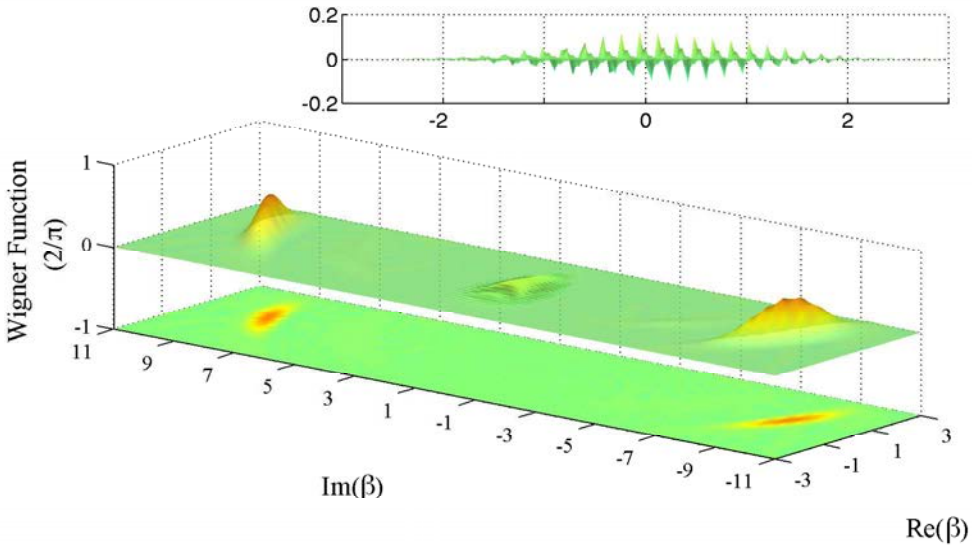

Figure VI.11: Wigner function of the largest cat state ($\alpha^2 = 75$). The size is $D^2 \approx 324$, reached for an interaction time $t = 86$ μs. D^2 is larger than $4\alpha^2$ since it is measured between the centers of the distorted coherent components. Inset: detail of the interference fringes near the origin in phase space.

VI.4 Case of more than two atoms

The achieved results show the interest of the collective interaction for the generation of sizable MFSS and reinforces our trust in the factorization approximation. We now use it to investigate the interaction with the cavity of larger atomic samples. We consider here, for the sake of definiteness, the case $A = 4$ for an initial coherent field with $\hat{n} = 25$ photons. We assume that all atoms are in the excited state at the beginning of the interaction (the atomic state is then $|k = 4\rangle$). We get five possible atomic states at detection time ($k = 0$ to $k = 4$). We thus expect the creation of superpositions of five rotated coherent states.

As in the $A = 2$ case, a simplification occurs for a final atomic state detection in $|k = A/2\rangle$. Two of the D_p^k coefficients vanish. We observe this in figure VI.12, where the central frame representing the field left by a detection in $k = 2$ after a 15 μs interaction time involves only three coherent components, one at the center of the phase space, and the two others phase-shifted four time as much as in the $A = 1$ case. The size of the generated MFSS grows 16 times faster than in the single atom case.

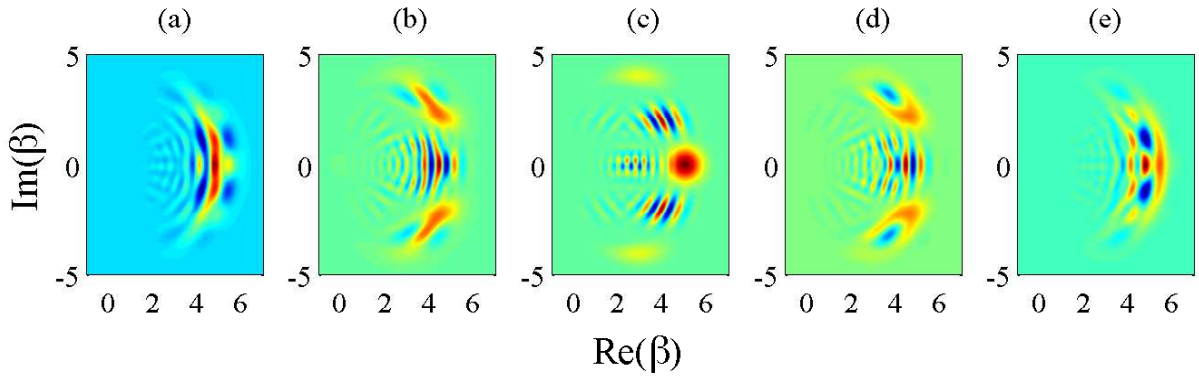

Figure VI.12: Factorization approximation for $A = 4$. The initial field amplitude is $\alpha = 5$ and the interaction time 15 μs. The five frames (a), (b), (c), (d) and (e) present the Wigner functions of the field generated after $l = 0, 1, 2, 3, 4$ atoms have been detected in the upper state, respectively.

Conclusions and perspectives

The theoretical part of this work was devoted to the study of the resonant interaction of two two-level atoms with a coherent field stored in a high finesse cavity, within the frame of CQED experiments with circular Rydberg atoms and superconducting cavities. In the last chapter, we have demonstrated that the conditional detection of the appropriate atomic state after the interaction with the cavity within a quite short time scale projects the field state into a large MFSS.

The generation of these Schrödinger cat-like states is more efficient than the usual method based on a single atom interaction, either in the resonant or dispersive regime. For short interaction times, we have shown that the maximum MFSS size is reached, with two atoms, within a time twice as short as in the case of the single atom. Accordingly, the maximum MFSS size that may be reached is larger by a factor 1.6 when the interaction is with two atoms instead of one.

We have discussed the generation of very large MFSS using the proposed scheme, including a full description of the decoherence process due to cavity losses, based on the Master equation. In the frame of realistic CQED experiments, the interaction time required for the generation of very large MFSS ($D^2 \approx 300$) does not exceed a hundred of microseconds (for an initial $\bar{n} = 75$) and decoherence in this short time interval does not destroy the field state coherence.

This technique is also promising for circuit QED, in which it is pretty easy to control the number of artificial atoms interacting with the cavity mode. The ratio $T_c/t_{vac}^{\pi/2} = 26000$ is even larger is this context, allowing the generation of even larger cats and interesting explorations of quantum-classical boundary.

Concerning the practical implementation of this proposal in the cavity QED context, the preparation of two atoms could be obtained with a post-selection scheme provided the atomic detection efficiency is high enough. In the present set-up, the atomic velocity is at least of the order of 200 m/s, limiting the interaction time and making it difficult to generate very large MFSS.

Much larger field amplitudes could be handled in an experiment under development. This new version will work with slower atoms allowing longer interaction times. A scheme of the new setup is shown in figure VI.13. It relies on a slow atomic beam, in a fountain arrangement. The atoms are prepared in the circular state, interact with the cavity, and are finally detected close to the turning point of their trajectory. This leads to very long interaction times, in the tens of ms range, and would thus allow us to prepare and study

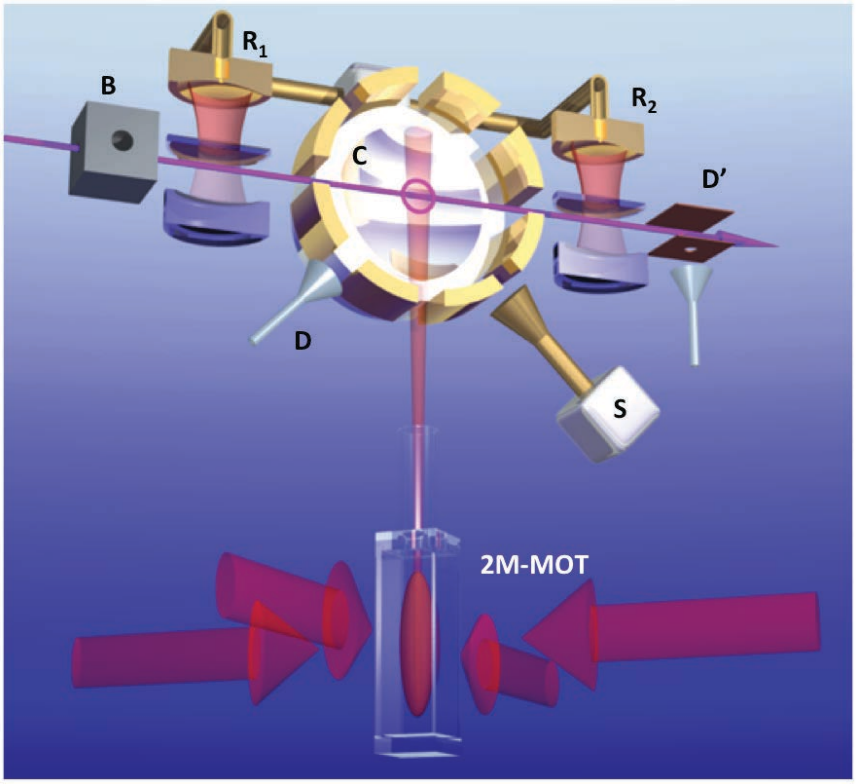

Figure VI.13: New experimental setup for CQED experiment with a low velocity atomic source. The source of slow atoms, a 2D-MOT trap is at the bottom of the picture. These atoms fly upwards towards the high finesse cavity C, where they are prepared in a circular state one at a time and finally detected. The other components are the same as in the usual setup already described.

fairly large MFSS

Another direction for theoretical and experimental explorations is that of non-local MFSS, with two cavities instead of one. A proposal to study Bell's inequalities was published in 2005 by P. Milman et al. [85]. In this paper, a CQED experiment to test Bell's inequalities violations using mesoscopic non-local states (NLMS) shared by two cavities was proposed. The mesoscopic state is generated by the dispersive interaction of both cavity modes with a single atom. A Bell-type inequality violation could be tested. It is expressed in terms of the Wigner function of the entangled two-field mode system at four points in the phase space. This inequality, proposed in [86], was generalized by Jeong et al. [87] and is given by:

$$\mathcal{B} = |\Pi(\alpha', \beta') + \Pi(\alpha, \beta') + \Pi(\alpha', \beta) - \Pi(\alpha, \beta)| \leq 2 \tag{VI.43}$$

with $\Pi(\alpha, \beta) = (\pi^2/4)W(\alpha, \beta)$ being proportional to the two-mode Wigner function $W(\alpha, \beta)$ at one point of the four-dimensional phase space defined by the complex amplitudes α and β. The maximum value of $\mathcal{B}$ is $2\sqrt{2}$ in the quantum realm.

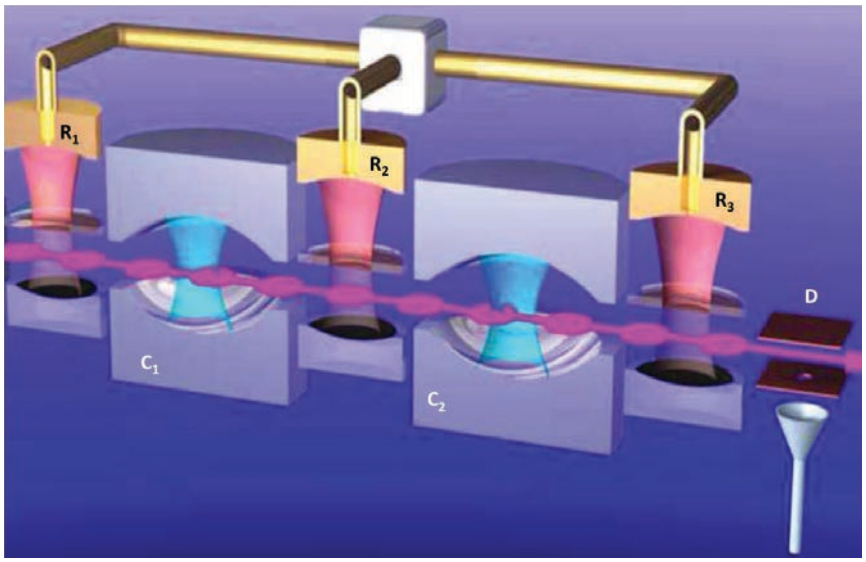

Figure VI.14: Setup with two consecutive high finesse cavities. The middle Ramsey zone between the cavities was not used in the original proposal [85].

Through a single atom dispersive interaction with both cavities, the following Bell states may be prepared

$$|\Psi^{\pm}\rangle = \frac{1}{N_{\Psi^{\pm}}}(|\pm\gamma,\gamma\rangle + |\mp\gamma,-\gamma||) \tag{VI.44}$$

$$|\Phi^{\pm}\rangle = \frac{1}{N_{\Phi^{\pm}}}(|\pm\gamma,-\gamma\rangle - |\mp\gamma,-\gamma||). \tag{VI.45}$$

depending upon the final detected atomic states and the transformation undergone by the atom in the intermediate Ramsey zone.

For realistic experimental conditions including cavity decoherence, [85] has shown that Bell inequalities could be violated and that decoherence very rapidly returns the system to a classical situation, with $\mathcal{B} \leq 2$. This interplay between non-locality and decoherence would be very interesting to study. Of course, this early proposal, based on dispersive interaction, was limited. We would like to explore the resonant interaction of two circular Rydberg atoms with the two cavities. We hope to be able to generate a non-local MFSS in a shorter time than through the dispersive interaction.

Appendix A

Broadening sources

In this appendix, we briefly describe the various sources of spectral broadening that can affect the two-photon excitation of the Rydberg states (see figure I.5). The excitation was discussed in chapter I and in chapter III. For some of the sources described here, we will use the beam characteristics shown in table III.1.

Power broadening: when the Rabi frequencies Ω_r and Ω_b are much smaller than the detuning Δ from the intermediate level, the Rabi frequency relevant for the power broadening if the effective two-photon one, Ω_{rb}, equal to $2\pi \times 58.5$ kHz in our typical operating conditions. This is completely negligible with respect to the broadening we have observed in chapter III and IV.

Light shift broadening: Let us denote by ω_r the frequency of the red laser, by ω_b the blue one. ω_0 is the frequency of the two-photon transition $|5S\rangle \rightarrow |60S\rangle$ and Δ is again the detuning with the intermediate level $5P$, which is blue shifted for the red laser. The resonant condition for the two-photon transition is given by ([88], page 95-97)

$$\omega_r + \omega_b = \omega_0 - \frac{\Omega_r^2}{4\Delta} + \frac{\Omega_b^2}{4\Delta}. \tag{A.1}$$

For our typical conditions, in the centre of the laser beams, $\Omega_r^2/(4\Delta) = 2\pi \times 15$ kHz and $\Omega_b^2/(4\Delta) = 2\pi \times 59$ kHz. These values give us an upper limit for the broadening we may be observing. Again these values are negligible with respect to the width of the signals observed in chapter III and IV.

Broadening due to Doppler effect: When both lasers propagate in the $+x$-direction (figure III.3), the frequency experienced by the atoms is:

$$\nu_D(v_x) = \nu\left(1 - \frac{v_x}{c}\right) \tag{A.2}$$

where v_x is the atomic velocity along the light propagation direction and $\nu = \omega/2\pi$ the light frequency. In general, the atomic velocity distribution is given by

$$\eta(v_x, v_y, v_z) = \frac{1}{(2\pi)^{3/2}}\left(\frac{M}{k_B T}\right)^{3/2} e^{-\frac{1}{2}\frac{Mv_x^2}{k_B T} - \frac{1}{2}\frac{Mv_y^2}{k_B T} - \frac{1}{2}\frac{Mv_z^2}{k_B T}} \tag{A.3}$$

which has a Gaussian shape and is a function of the cloud temperature according to the Maxwell-Boltzmann density law.

The velocity distribution is associated to a frequency distribution, whose width is given by

$$\Delta\nu_D = \sqrt{\frac{8k_BT}{mc^2}\ln 2}(\nu_b + \nu_r), \tag{A.4}$$

with $\nu_{r,b}$ being the red and blue laser frequency respectively. This broadening in a cold magnetic trap at 1 μK is 77 kHz and, for a MOT at 400 μK, which is the usual temperature, 1, 6 MHz. In chapter III we have shown the signal on a MOT (figure III.10) but there, 1.7 MHz is still very small compared with the observed widths of several tens of MHz. After that, we worked only in cold magnetic traps with negligible Doppler effects.

Broadening due to the inhomogeneous Zeeman effect: We may also have a broadening of the line due to the Zeeman effect, introduced in chapter I. This effect exists only in a MOT and not in a magnetic trap. In a magnetic trap, the levels $|5S, F = 2, m_F = +2\rangle$ and $|60S, m_j = +1/2\rangle$ have the same magnetic dipole moment. This means that they are shifted in the same way due to the Zeeman effect. Hence, there is no broadening due to magnetic fields. For a MOT, the situation is different since the atoms do not have a well-defined state. Thus, the magnetic field gradients broaden the line. For instance, for figure III.10, the current in the U-wire is 5 A and the bias field in the z-direction is 11 G. The magnetic field gradient is 25 G/mm. The MOT largest dimension is 200 μm, which results in a broadening of 7 MHz (assuming the same probability transitions to the final states for the initial states with different magnetic numbers), which is still smaller that the width reported in those conditions in chapter III.

Broadening due to quadratic Stark effect: Electric fields can significantly affect the signal we are observing both in a magnetic trap and in a MOT. As introduced in section I.1.2, the frequency difference is proportional to the square of the electric field times a Stark shift constant A. This constant is -89.9 MHz $(\mathrm{V/cm})^{-2}$ for the $5S \to 60S$ transition. The line broadening due to stray electric fields can be tens of MHz if the conditions are not proper. These order of magnitudes are the ones observed in chapter III, particularly in figure III.10. Stark effect is the dominant source of broadening for the observations of chapters III and IV.

Broadening due to dipole-dipole interactions: Rydberg-Rydberg interactions can affect the width of our signals when working with Rydberg densities comparable to $1/R_b^3$, where R_b is the blockade radius. In chapter III, we were not limited by this effect (figure III.10, MOT diameter 200 μm, average distance between two Rydberg atoms 85 μm, which makes their interaction energy completely negligible). Nevertheless, in chapter IV special care was taken to avoid the effect.

Appendix B

Calibration of perpendicular electric field

For the electric field calibration, it is important to know the precise value of the field created by the $V_{ions1,2}$ plates. For this calibration, we use a magnetic trap at 675 μm and 350 nK. We address the $60S_{1/2} \rightarrow 61S_{1/2}$ and $60S_{1/2}\, m_j = +1/2 \rightarrow 60P_{3/2}$, $m_j = -1/2$ transitions. The bottom of this trap is 4.2 G, as measured by RF evaporation. We change the voltage applied on electrodes $V_{ion1} + V_{ion2}$ which, by direct measurement, is given, in Volts, by

$$V_{ion1} + V_{ion2} = (5.928 \cdot V_{pc} + 0.067) \tag{B.1}$$

where V_{pc} is the output signal from the computer, which controls the driving circuit of the electrodes (see figure III.6). We then deduce the electric field:

$$F_y^{V_{ion1}+V_{ion2}} = (5.928 \cdot V_{pc}) \times 0.644 = 3.818 \times V_{pc} \tag{B.2}$$

The factor $0.644\, V/cm$ has been obtained by simulating the electrodes geometry with the *SIMION* software (geometry details in chapter III).

We vary V_{pc} and we determine the center frequency of the microwave transition. The central frequencies, relative to the zero field one (figure IV.1), are plotted as a function of the applied field given by the above expression. With these data, we are able to obtain the relative Stark shift shown in figures B.1 and B.2.

We observed a slight difference between the fit and the calculated Stark shift constants given in equations (I.24), (I.25) and (I.38). The ratio between the calculated values and the ones obtained here leads to

$$\sqrt{\frac{A_{61S-60S}^{Measured}}{A_{61S-60S}^{Calculated}}} = \sqrt{\frac{8.62}{10.96}} = 0.89$$

and

$$\sqrt{\frac{A_{60P_{3/2,\, m_J=1/2}-60S}^{Measured}}{A_{60P_{3/2,\, m_J=1/2}-60S}^{Calculated}}} = \sqrt{\frac{413.9}{507}} = 0.904$$

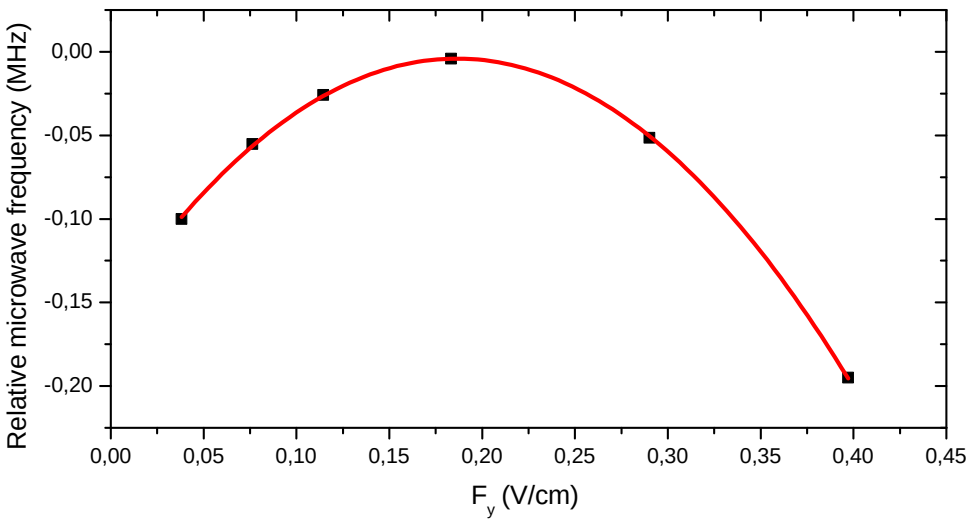

Figure B.1: Relative microwave frequency with respect to the transition in zero field as a function of the electric field applied on $V_{ion1} + V_{ion2}$. From the quadratic fit (solid line) we get a relative Stark constant $A_{61S-60S} = -8.62$ MHz/(V/cm)^2.

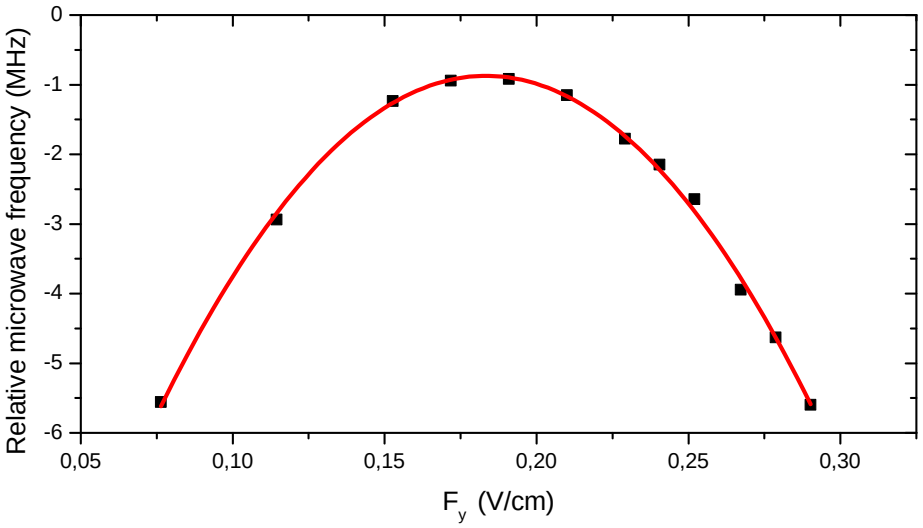

Figure B.2: Relative microwave frequency with respect to the zero field $60S_{1/2}\, m_j = +1/2 \rightarrow 60P_{3/2},\ m_j = -1/2$ transition as a function of the electric field applied on V_{ion}. We extract a relative Stark constant $A_{60P_{3/2},\, m_J-1/2-60S} = -414$ MHz/(V/cm)^2.

This difference clearly originates in the uncertainty of the calibration of the electric field w.r.t. V_{pc}. We are either mistaken in the real voltage applied to the electrodes, or by the geometry itself or by some other elements around the chip that could contribute to decreasing the value of the field at the atomic cloud position. For the two transitions, the difference on the electric field is 11% and 10% respectively. We must thus rely on these Stark shift measurements to determine the proper calibration.

For each transition, using the fit of the curves shown in B.1, we obtain

$$\begin{aligned} |F_y^{60S\to 61S}| &= \sqrt{\frac{A_{measured}}{A_{60S}-A_{61S}}}\cdot(5.928\cdot V_{pc})\times 0.644 \\ &= 0.89\times((5.928\cdot V_{pc})\times 0.644 \\ |F_y^{60S\to 61S}| &= [3.398\times V_{pc}]\ (V/cm) \end{aligned}$$

and similarly for $60S \to 60P_{3/2,m_J=-1/2}$:

$$\begin{aligned} |F_y^{60S\to 60P3/2}| &= \sqrt{\frac{A_{measured}}{A_{60S}-A_{61S}}}\cdot(5.928\cdot V_{pc})\times 0.644 \\ &= 0.904\times((5.928\cdot V_{pc})\times 0.644 \\ |F_y^{60S\to 60P3/2}| &= [3.451\times V_{pc}]\ (\mathrm{V/cm}) \end{aligned}$$

These values are in reasonable agreement and we finally use the average of these measurements to get the perpendicular electric field $F_y = F_\perp$ as a function of V_{pc},

$$|F_y| = [3.425\times V_{pc}]\ (\mathrm{V/cm}) \tag{B.3}$$

Appendix C

Measurement of Electric field gradients

In chapter IV, section IV.2.3, we have estimated the field gradients at a cloud position centered w.r.t the Z-shaped wire. However, we have observed that by moving the trap in the z direction, we can get narrower spectral lines, particularly for $z \approx -350$ μm. We have measured the field gradients around this position by moving the excitation blue laser.

The measurement of the gradients were performed on the magnetic trap we use for the Rabi, Ramsey and spin-echo sequences. It has coordinates $(y, z) = (455, -351.3)$ μm with respect to the center of the Z-shaped wire. The spectrum for the $|60S_{1/2}, m_J = 1/2\rangle \rightarrow |60P_{3/2}, m_J = +3/2\rangle$ transition was taken at that position with a blue laser aligned on the atomic cloud position. We compensated the field component perpendicular to the chip. The residual field is thus of the form $\mathbf{F} = F_x\hat{x} + F_z\hat{z}$. Then, we move the laser position in the y and z directions. For each laser position, we record a microwave spectrum and we measure the central frequency. Note that the y component compensation is performed only once, when the blue laser is centered on the cloud.

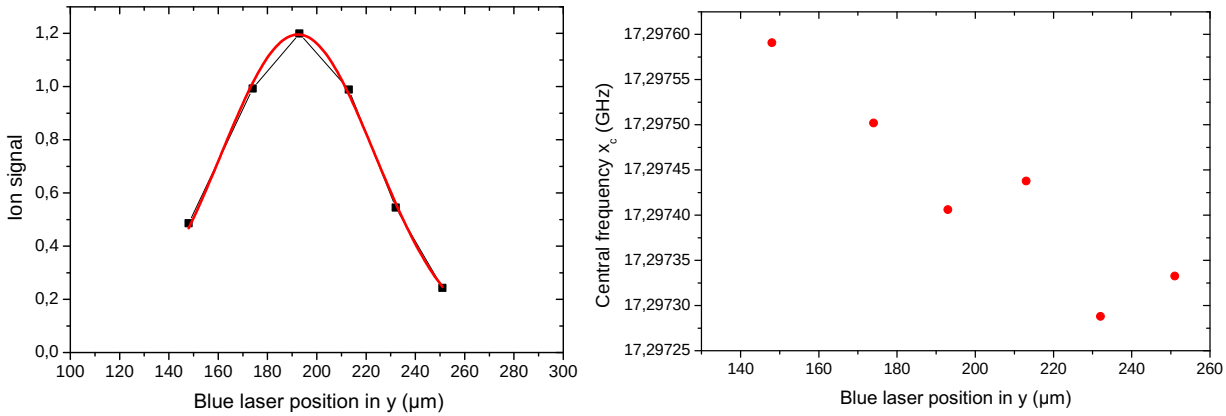

Figure C.1: **(left)**: variation of the total counts detected as a function of the laser position. The width of this curve is 62.34 μm, a convolution between the actual cloud size along y and the laser profile. **(right)**: Variation of the line frequency as a function of the laser position in the y direction.

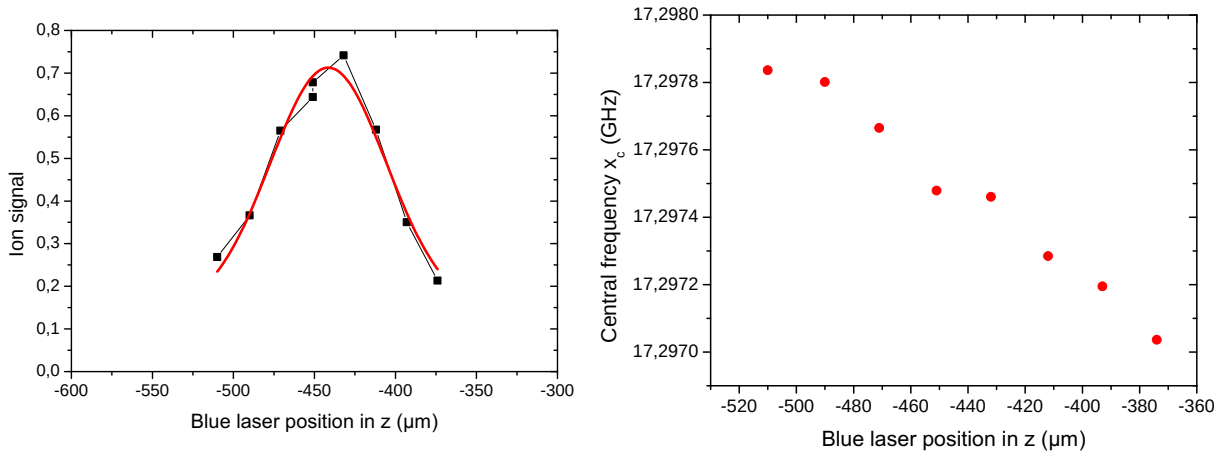

Figure C.2: **(left)**: variation of the total counts detected as a function of the laser position. The width of this curve is 80.7 μm, a convolution between the actual cloud size along z and the laser profile. **(right)**: Variation of the line frequency as a function of the laser position in the z direction.

By this technique, we are able to map the electric field. Taking into account the magnetic field contribution, we calculate the electric field considering it to be either along the x-direction (parallel $\mathbf{F} \parallel \mathbf{B}$) or along the z-direction (perpendicular $\mathbf{F} \perp \mathbf{B}$):

$$|F_x| = \sqrt{\frac{f_{+3/2} - f_0 - \mu_0 B}{A^{//}_{+3/2}}} \tag{C.1}$$

$$|F_z| = \sqrt{\frac{f_{+3/2} - f_0 - \mu_0 B}{A^{\perp}_{+3/2}}} \tag{C.2}$$

where the bottom of the trap is $B = 8.3$ G and the transition frequency at zero electric and magnetic field is $f_0 = 17287.41$ MHz. For each direction of the blue laser motion, we register the variation of the total counts and the transition central frequency. The graphics are shown in figures C.1 and C.2. The results regarding the electric field at each blue laser position are shown in figure C.3 and C.4. We find, by a linear fit on the variation of the electric field as a function of distance y and z, the following gradients:

$$\frac{\partial |F_x|}{\partial y} = 0.484 \pm 0.098 \text{ V/cm}^2 \tag{C.3}$$

$$\frac{\partial |F_z|}{\partial y} = 0.461 \pm 0.094 \text{ V/cm}^2 \tag{C.4}$$

$$\frac{\partial |F_x|}{\partial z} = 1.087 \pm 0.055 \text{ V/cm}^2 \tag{C.5}$$

$$\frac{\partial |F_z|}{\partial z} = 1.037 \pm 0.053 \text{ V/cm}^2 \tag{C.6}$$

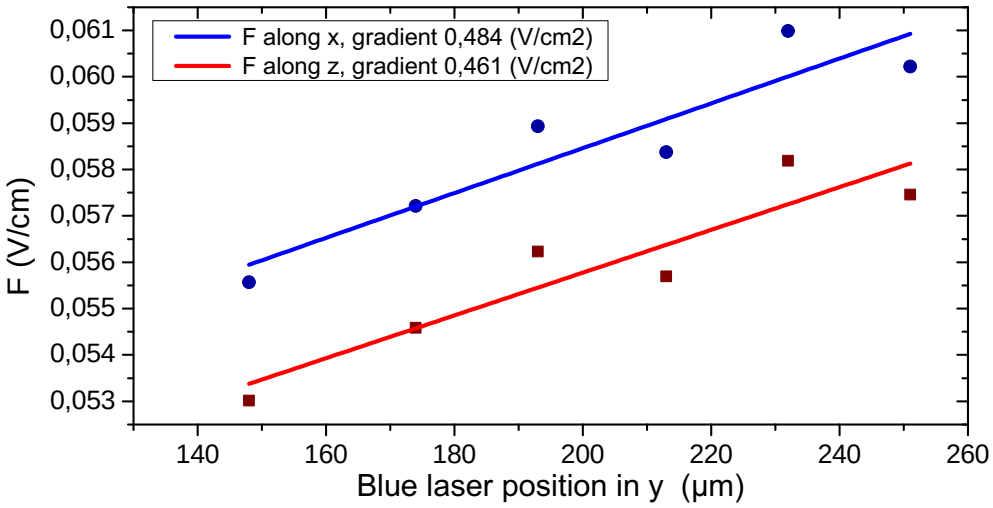

Figure C.3: Variation of the electric field in the y direction.

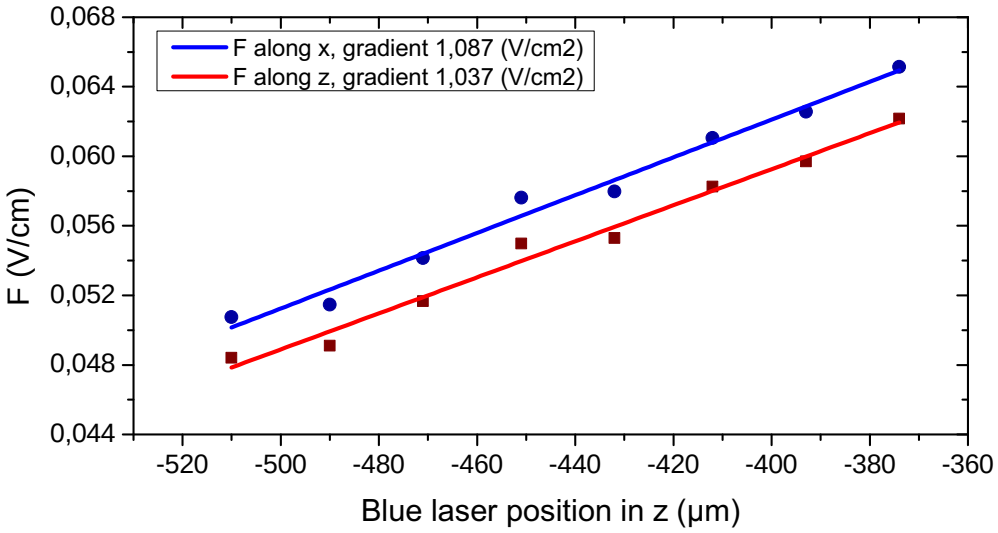

Figure C.4: Variation of the electric field in the z direction.

By observing the total detection signal as a function of the laser position, we can also estimate the effective size of the atomic ensemble, assuming that the atom cloud and the laser have both Gaussian profiles and that the detection signal is proportional to the power of the laser and to the density of the atoms, a reasonable assumption in the case of this experiment.

The width of the curves shown in the left hand-side of figures C.1 and C.2 is a convolution of the width of the blue laser and of the width of the cloud. We find for the y direction

$$\sigma^{y}_{(1/e^2)_{cloud}} = \sqrt{\sigma^2_{fit} - \sigma^2_{laser}} = \sqrt{62,34^2 - 22^2} = 58.33\ \mu\text{m}$$

which means at $1/e^{1/2}$, 29.17 μm. For the z direction, we have

$$\sigma^{z}_{(1/e^2)_{cloud}} = \sqrt{\sigma^2_{fit} - \sigma^2_{laser}} = \sqrt{80.7^2 - 22^2} = 77.6\ \mu\text{m}$$

which means at $(1/e^{1/2})$, 38.80 μm.

The cloud dimensions we get in this way are different from those calculated using the measured temperature $1.6\,\mu$K and measured trap frequencies $(31.15, 86.3, 63.5)$ Hz, giving $(\sigma_x, \sigma_y, \sigma_z) =\sim (63, 23, 31)$ μm. This disagreement (21% in y and 20% in z) can be attributed to a misalignment of the blue laser with respect to the main axis of the trap. Through the trap simulation, we have calculated the angles between the long axis of the trap and the coordinate axes. We have obtained 10.4^0 and 10.6^0 with respect to the planes xz and xy. Taking this 10^0 angle into account, the apparent radius of the trap is

$$\sigma_y^{10^0} = \sigma^y \times \cos(10^0) + \sigma_x \times \sin(10^0) = 33.6\,\mu\text{m}$$
$$\sigma_z^{10^0} = \sigma^z \times \cos(10^0) + \sigma_x \times \sin(10^0) = 41.5\,\mu\text{m}$$

which is different by $\sim 13\%$ and $\sim 6.5\%$ from the values $\sigma_y = 29.2$ and $\sigma_z = 38.8$ μm found by the laser scan. The agreement is better when we take into account the angles.

Considering the size of the excitation region in the z direction (figure IV.8, chapter IV) to be given by the half width of the blue laser beam, $\sigma(e^{-1/2}) = 11$ μm and taking into account the field gradient, we estimate the half width at $e^{-1/2}$ for the $60S \longrightarrow 61S$ transition to be 1.35 kHz, corresponding to a 117 μs coherence time at $e^{-1/2}$. This estimation is in excellent agreement with the coherence time measurement given by the Ramsey sequence presented in section IV.3.2 of chapter IV.

Appendix D

Lifetime measurement

We briefly present the measurement of Rydberg atoms lifetime in the $60S$ level. During the Ramsey interferometry experiments, the lifetime of the Rydberg atoms has been measured directly on the number of Rydberg atoms detected after some free evolution time. We have found a decay time of (210 ± 4) μs. A calculation taking into account all possible decay channels, and the density of blackbody radiation in free, infinite space, yields a lifetime of 239.8 μs for the $60S_{1/2}$ level at a temperature of 4 K and 99.4 μs at 300 K (see chapter I). The experimental lifetime is just slightly reduced from the expected 4 K value. The reduction is due to the 77 K and 300 K radiation entering the excitation region at 4.2K through the optical windows. A complete calculation should take into account the complete geometry of the system. We thus only estimate an effective background microwave temperature of 36 K.

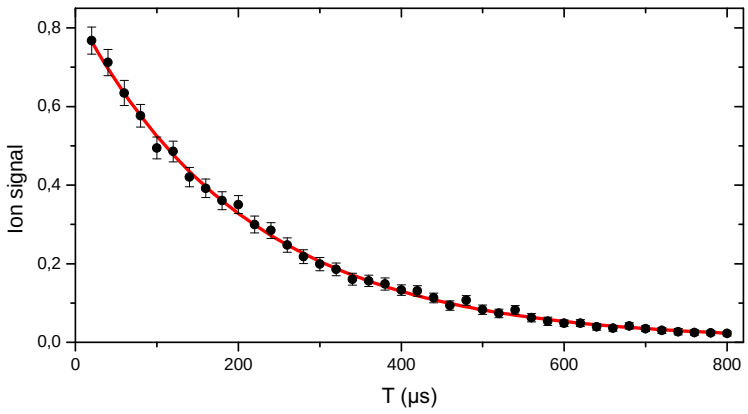

Figure D.1: Lifetime measurement in the $60S_{1/2}$ level. The exponential decay time is $(210 \pm 4)\mu s$.

Bibliography

[1] M. Brune, S. Haroche, J. M. Raimond, L. Davidovich, et N. Zagury. "Manipulation of photons in a cavity by dispersive atom-field coupling: Quantum-nondemolition measurements and generation of "schrödinger cat" states". *Phys. Rev. A*, **45**, 5193 (Apr 1992). URL `http://link.aps.org/doi/10.1103/PhysRevA.45.5193`.

[2] S. Haroche et J.-M. Raimond. *Exploring the Quantum. Atoms, Cavities, and Photons.* Oxford University Press (2006).

[3] S. Deléglise, I. Dostenko, C. Sayrin, J. Bernu, M. Brune, J.-M. Raimond, et S. Haroche. "Reconstruction of non-classical cavity field states with snapshots of their decoherence". *Nature*, **455**, 510 (2008).

[4] E. Jaynes et F. Cummings. "Comparison of quantum and semiclassical radiation theories with application to the beam maser". *Proceedings of the IEEE*, **51**, n° 1, 89 (1963). URL `http://dx.doi.org/10.1109/PROC.1963.1664`.

[5] J. Gea-Banacloche. "Collapse and revival of the state vector in the jaynes-cummings model: An example of state preparation by a quantum apparatus". *Phys. Rev. Lett.*, **65**, 3385 (Dec 1990). URL `http://link.aps.org/doi/10.1103/PhysRevLett.65.3385`.

[6] J. Gea-Banacloche. "Atom- and field-state evolution in the jaynes-cummings model for large initial fields". *Phys. Rev. A*, **44**, 5913 (Nov 1991). URL `http://link.aps.org/doi/10.1103/PhysRevA.44.5913`.

[7] V. Bužek, H. Moya-Cessa, P. L. Knight, et S. J. D. Phoenix. "Schrödinger-cat states in the resonant jaynes-cummings model: Collapse and revival of oscillations of the photon-number distribution". *Phys. Rev. A*, **45**, 8190 (Jun 1992). URL `http://link.aps.org/doi/10.1103/PhysRevA.45.8190`.

[8] A. Auffeves, P. Maioli, T. Meunier, S. Gleyzes, G. Nogues, M. Brune, J. M. Raimond, et S. Haroche. "Entanglement of a mesoscopic field with an atom induced by photon graininess in a cavity". *Phys. Rev. Lett.*, **91**, 230405 (Dec 2003). URL `http://link.aps.org/doi/10.1103/PhysRevLett.91.230405`.

[9] T. Meunier, S. Gleyzes, P. Maioli, A. Auffeves, G. Nogues, M. Brune, J. M. Raimond, et S. Haroche. "Rabi oscillations revival induced by time reversal: A test of mesoscopic quantum coherence". *Phys. Rev. Lett.*, **94**, 010401 (Jan 2005). URL `http://link.aps.org/doi/10.1103/PhysRevLett.94.010401`.

[10] J. C. Retamal, C. Saavedra, A. B. Klimov, et S. M. Chumakov. "Squeezing of light by a collection of atoms". *Phys. Rev. A*, **55**, 2413 (Mar 1997). URL `http://link.aps.org/doi/10.1103/PhysRevA.55.2413`.

[11] C. Saavedra, A. B. Klimov, S. M. Chumakov, et J. C. Retamal. "Dissipation in collective interactions". *Phys. Rev. A*, **58**, 4078 (Nov 1998). URL `http://link.aps.org/doi/10.1103/PhysRevA.58.4078`.

[12] M. D. Lukin, M. Fleischhauer, R. Côté, L. M. Duan, D. Jaksch, J. I. Cirac, et P. Zoller. "Dipole blockade and quantum information processing in mesoscopic atomic ensembles". *Phys. Rev. Lett.*, **87**, 037901 (Jun 2001). URL `http://link.aps.org/doi/10.1103/PhysRevLett.87.037901`.

[13] C. Roux, A. Emmert, A. Lupascu, T. Nirrengarten, G. Nogues, M. Brune, J.-M. Raimond, et S. Haroche. "Bose-einstein condensation on a superconducting atom chip". *EPL (Europhysics Letters)*, **81**, n° 5, 56004 (2008). URL `http://stacks.iop.org/0295-5075/81/i=5/a=56004`.

[14] A. Tauschinsky, R. M. T. Thijssen, S. Whitlock, H. B. van Linden van den Heuvell, et R. J. C. Spreeuw. "Spatially resolved excitation of rydberg atoms and surface effects on an atom chip". *Phys. Rev. A*, **81**, 063411 (Jun 2010). URL `http://link.aps.org/doi/10.1103/PhysRevA.81.063411`.

[15] J. D. Carter, O. Cherry, et J. D. D. Martin. "Electric-field sensing near the surface microstructure of an atom chip using cold rydberg atoms". *Phys. Rev. A*, **86**, 053401 (Nov 2012). URL `http://link.aps.org/doi/10.1103/PhysRevA.86.053401`.

[16] J. D. Carter et J. D. D. Martin. "Coherent manipulation of cold rydberg atoms near the surface of an atom chip". *Phys. Rev. A*, **88**, 043429 (Oct 2013). URL `http://link.aps.org/doi/10.1103/PhysRevA.88.043429`.

[17] M. Saffman et T. G. Walker. "Creating single-atom and single-photon sources from entangled atomic ensembles". *Phys. Rev. A*, **66**, 065403 (Dec 2002). URL `http://link.aps.org/doi/10.1103/PhysRevA.66.065403`.

[18] T. F. Gallagher. *Rydberg Atoms*. Cambrigbe University Press (1994).

[19] S. Gleyzes, S. Kuhr, C. Guerlin, J. Bernu, S. Deléglise, U. B. Hoff, M. Brune, J.-M. Raimond, et S. Haroche. "Quantum jumps of light recording the birth and death of a photon in a cavity". *Nature*, **446**, 297 (2007).

[20] B. Peaudecerf. *Mesure adaptative non destructive du nombre de photons dans une cavité*. Thèse de doctorat, Université Paris VI (2013).

[21] P. J. Mohr, B. N. Taylor, et D. B. Newell. "Codata recommended values of the fundamental physical constants: 2010". *Rev. Mod. Phys.*, **84**, 1527 (Nov 2012). URL http://link.aps.org/doi/10.1103/RevModPhys.84.1527.

[22] C. Fabre, S. Haroche, et P. Goy. "Millimeter spectroscopy in sodium rydberg states: Quantum-defect, fine-structure, and polarizability measurements". *Phys. Rev. A*, **18**, 229 (Jul 1978). URL http://link.aps.org/doi/10.1103/PhysRevA.18.229.

[23] P. Goy, J. M. Raimond, G. Vitrant, et S. Haroche. "Millimeter-wave spectroscopy in cesium rydberg states. quantum defects, fine- and hyperfine-structure measurements". *Phys. Rev. A*, **26**, 2733 (Nov 1982). URL http://link.aps.org/doi/10.1103/PhysRevA.26.2733.

[24] D. Meschede. "Centimeter-wave spectroscopy of highly excited rubidium atoms". *J. Opt. Soc. Am. B*, **4**, n° 3, 413 (Mar 1987). URL http://josab.osa.org/abstract.cfm?URI=josab-4-3-413.

[25] M. J. Seaton. "Quantum defect theory". *Reports on Progress in Physics*, **46**, n° 2, 167 (1983). URL http://stacks.iop.org/0034-4885/46/i=2/a=002.

[26] W. Li, I. Mourachko, M. W. Noel, et T. F. Gallagher. "Millimeter-wave spectroscopy of cold rb rydberg atoms in a magneto-optical trap: Quantum defects of the ns, np, and nd series". *Phys. Rev. A*, **67**, 052502 (May 2003). URL http://link.aps.org/doi/10.1103/PhysRevA.67.052502.

[27] J. Han, Y. Jamil, D. V. L. Norum, P. J. Tanner, et T. F. Gallagher. "Rb nf quantum defects from millimeter-wave spectroscopy of cold rb85 rydberg atoms". *Phys. Rev. A*, **74**, 054502 (Nov 2006). URL http://link.aps.org/doi/10.1103/PhysRevA.74.054502.

[28] R. Löw, H. Weimer, J. Nipper, J. B. Balewski, B. Butscher, H. P. Büchler, et T. Pfau. "An experimental and theoretical guide to strongly interacting rydberg gases". *Journal of Physics B: Atomic, Molecular and Optical Physics*, **45**, n° 11, 113001 (2012). URL http://stacks.iop.org/0953-4075/45/i=11/a=113001.

[29] I. I. Beterov, I. I. Ryabtsev, D. B. Tretyakov, et V. M. Entin. "Quasiclassical calculations of blackbody-radiation-induced depopulation rates and effective lifetimes of rydberg ns, np, and nd alkali-metal atoms with n≤80". *Phys. Rev. A*, **79**, 052504 (May 2009). URL http://link.aps.org/doi/10.1103/PhysRevA.79.052504.

[30] H. A. Bethe et E. E. Salpeter. *Quantum mechanics of one- and two-electron atoms*. Plenum, New York, NY (1977). Based on an article publ. in Handbuch der Physik Bd.35, 1957.

[31] D. A. Steck. "Rubidium 87 d line data". *Phys. Rev. A* (2001). URL `http://george.ph.utexas.edu/~dsteck/alkalidata/rubidium87numbers.pdf`.

[32] S. Svanberg. *Atomic and Molecular Spectroscopy*. Springer, Lund Institute of Technology, 3 édition (2001).

[33] J. D. Jackson. *Classical Electrodynamics*. John Wiley & Sons, Inc., New York, 3 édition (1999).

[34] M. Tavis et F. W. Cummings. "Exact solution for an n-molecule—radiation-field hamiltonian". *Phys. Rev.*, **170**, 379 (Jun 1968). URL `http://link.aps.org/doi/10.1103/PhysRev.170.379`.

[35] J. M. Radcliffe. "Some properties of coherent spin states". *Journal of Physics A: General Physics*, **4**, n° 3, 313 (1971). URL `http://stacks.iop.org/0022-3689/4/i=3/a=009`.

[36] A. Gaetan, Y. Miroshnychenko, T. Wilk, A. Chotia, M. Viteau, D. Comparat, P. Pillet, A. Browaeys, et P. Grangier. "Observation of collective excitation of two individual atoms in the rydberg blockade regime". *Nature Physics*, **5**, 115 (2009).

[37] R. Heidemann, U. Raitzsch, V. Bendkowsky, B. Butscher, R. Löw, L. Santos, et T. Pfau. "Evidence for coherent collective rydberg excitation in the strong blockade regime". *Phys. Rev. Lett.*, **99**, 163601 (Oct 2007). URL `http://link.aps.org/doi/10.1103/PhysRevLett.99.163601`.

[38] C. J. PETHICK et H. SMITH. *Bose-Einstein Condensation in Dilute Gases*. Cambridge University Press, New York, 3 édition (2002).

[39] C. Roux. *Condensation de Bose-Einstein sur une puce à atomes supraconductrice*. Thèse de doctorat, Université Paris VI (2008).

[40] T. Nirrengarten. *Piégeage magnétique d'atomes de Rubidium au voisinage d'une surface supraconductrice*. Thèse de doctorat, Université Paris VI (2008).

[41] T. Nirrengarten, A. Qarry, C. Roux, A. Emmert, G. Nogues, M. Brune, J.-M. Raimond, et S. Haroche. "Realization of a superconducting atom chip". *Phys. Rev. Lett.*, **97**, 200405 (Nov 2006). URL `http://link.aps.org/doi/10.1103/PhysRevLett.97.200405`.

[42] R. Celistrino Teixeira. *Effets mécaniques de l'interaction dipolaire des atomes de Rydberg sondés par spectroscopie microonde*. Thèse de doctorat, Université Paris VI (2014).

[43] E. L. Raab, M. Prentiss, A. Cable, S. Chu, et D. E. Pritchard. "Trapping of neutral sodium atoms with radiation pressure". *Phys. Rev. Lett.*, **59**, 2631 (Dec 1987). URL http://link.aps.org/doi/10.1103/PhysRevLett.59.2631.

[44] W. Meissner et R. Ochsenfeld. "Ein neuer effekt bei eintritt der supraleitfähigokeit". *Naturwissenschaften*, **21**, n° 44, 787 (1933). URL http://dx.doi.org/10.1007/BF01504252.

[45] W. H. Wing. "On neutral particle trapping in quasistatic electromagnetic fields". *Progress in Quantum Electronics*, **8**, n° 3-4, 181 (1984). URL http://www.sciencedirect.com/science/article/pii/0079672784900120.

[46] D. E. Pritchard. "Cooling neutral atoms in a magnetic trap for precision spectroscopy". *Phys. Rev. Lett.*, **51**, 1336 (Oct 1983). URL http://link.aps.org/doi/10.1103/PhysRevLett.51.1336.

[47] G. Reinaudi, T. Lahaye, Z. Wang, et D. Guéry-Odelin. "Strong saturation absorption imaging of dense clouds of ultracold atoms". *Opt. Lett.*, **32**, n° 21, 3143 (Nov 2007). URL http://ol.osa.org/abstract.cfm?URI=ol-32-21-3143.

[48] P. Cheinet. *Conception et réalisation d'un gravimètre á atomes froids*. Thèse de doctorat, Université Paris VI (2006).

[49] J. Reichel, W. Hänsel, et T. W. Hänsch. "Atomic micromanipulation with magnetic surface traps". *Phys. Rev. Lett.*, **83**, 3398 (Oct 1999). URL http://link.aps.org/doi/10.1103/PhysRevLett.83.3398.

[50] C. G. Townsend, N. H. Edwards, C. J. Cooper, K. P. Zetie, C. J. Foot, A. M. Steane, P. Szriftgiser, H. Perrin, et J. Dalibard. "Phase-space density in the magneto-optical trap". *Phys. Rev. A*, **52**, 1423 (Aug 1995). URL http://link.aps.org/doi/10.1103/PhysRevA.52.1423.

[51] M. Drewsen, P. Laurent, A. Nadir, G. Santarelli, A. Clairon, Y. Castin, D. Grison, et C. Salomon. "Investigation of sub-doppler cooling effects in a cesium magneto-optical trap". *Applied Physics B*, **59**, n° 3, 283 (1994). URL http://dx.doi.org/10.1007/BF01081396.

[52] J. Dalibard. *Atomes ultra-froids*. Cours du M2 de physique quantique Paris VI (2006). URL http://www.phys.ens.fr/~dalibard/.

[53] P. D. Lett, W. D. Phillips, S. L. Rolston, C. E. Tanner, R. N. Watts, et C. I. Westbrook. "Optical molasses". *J. Opt. Soc. Am. B*, **6**, n° 11, 2084 (Nov 1989). URL http://josab.osa.org/abstract.cfm?URI=josab-6-11-2084.

[54] H. F. Hess. "Evaporative cooling of magnetically trapped and compressed spin-polarized hydrogen". *Phys. Rev. B*, **34**, 3476 (Sep 1986). URL http://link.aps.org/doi/10.1103/PhysRevB.34.3476.

[55] D. Guéry-Odelin. *Dynamique collisionnelle des gaz d'alcalins lourds : du refroidissement évaporatif á la condensation de Bose-Einstein.* Thèse de doctorat, Université Paris VI (1998).

[56] R. Reichle, D. Leibfried, R. Blakestad, J. Britton, J. Jost, E. Knill, C. Langer, R. Ozeri, S. Seidelin, et D. Wineland. "Transport dynamics of single ions in segmented microstructured paul trap arrays". *Fortschritte der Physik*, **54**, n° 8-10, 666 (2006). URL `http://dx.doi.org/10.1002/prop.200610326`.

[57] E. Torrontegui, S. Ibáñez, X. Chen, A. Ruschhaupt, D. Guéry-Odelin, et J. G. Muga. "Fast atomic transport without vibrational heating". *Phys. Rev. A*, **83**, 013415 (Jan 2011). URL `http://link.aps.org/doi/10.1103/PhysRevA.83.013415`.

[58] E. Torrontegui, S. I. nez, S. Martínez-Garaot, M. Modugno, A. del Campo, D. Guéry-Odelin, A. Ruschhaupt, X. Chen, et J. G. Muga. "Chapter 2 - shortcuts to adiabaticity". Dans P. R. B. Ennio Arimondo et C. C. Lin (rédacteurs), *Advances in Atomic, Molecular, and Optical Physics*, tome 62 de *Advances In Atomic, Molecular, and Optical Physics*, p. 117 – 169. Academic Press (2013). URL `http://www.sciencedirect.com/science/article/pii/B9780124080904000025`.

[59] A. Walther, F. Ziesel, T. Ruster, S. T. Dawkins, K. Ott, M. Hettrich, K. Singer, F. Schmidt-Kaler, et U. Poschinger. "Controlling fast transport of cold trapped ions". *Phys. Rev. Lett.*, **109**, 080501 (Aug 2012). URL `http://link.aps.org/doi/10.1103/PhysRevLett.109.080501`.

[60] E. D. Black. "An introduction to pound drever hall laser frequency stabilization". *American Journal of Physics*, **69**, n° 1 (2001).

[61] T. H. Jeys, G. W. Foltz, K. A. Smith, E. J. Beiting, F. G. Kellert, F. B. Dunning, et R. F. Stebbings. "Diabatic field ionization of highly excited sodium atoms". *Phys. Rev. Lett.*, **44**, 390 (Feb 1980). URL `http://link.aps.org/doi/10.1103/PhysRevLett.44.390`.

[62] J. B. Balewski, A. T. Krupp, A. Gaj, D. Peter, H. P. Buchler, R. Low, S. Hofferberth, et T. Pfau. "Coupling a single electron to a bose-einstein condensate". *Nature*, **502**, 664 (Oct 2013). URL `http://dx.doi.org/10.1038/nature12592`.

[63] S. Gleyzes. *Vers la préparation de cohérences quantiques mésoscopiques: réalisation d'un montage á deux cavités supraconductrices.* Thèse de doctorat, Université Paris VI (2006).

[64] M. O. Scully et M. S. Zubairy. *Quantum Optics.* Cambridge University Press (1997).

[65] A. Delgado et G. Rubilar. *Mecánica Cuántica: Apuntes para el curso del programa de Doctorado en Ciencias Físicas Facultad de Ciencias Físicas y Matemáticas*. Universidad de Concepción (2007).

[66] R. J. Glauber. "Coherent and incoherent states of the radiation field". *Phys. Rev.*, **131**, 2766 (Sep 1963). URL http://link.aps.org/doi/10.1103/PhysRev.131.2766.

[67] J. J. Sakurain. *Modern Quantum Mechanics*. Pearson Education (2009).

[68] A. Peres. *Quantum Theory: Concepts and Methods*. Kluwer Academic Publishers (2002).

[69] M. A. Nielsen et I. L. Chuang. *Quantum Computation and Quantum Information*. Cambridge University Press (2004).

[70] P. Rungta, V. Bužek, C. M. Caves, M. Hillery, et G. J. Milburn. "Universal state inversion and concurrence in arbitrary dimensions". *Phys. Rev. A*, **64**, 042315 (Sep 2001). URL http://link.aps.org/doi/10.1103/PhysRevA.64.042315.

[71] W. K. Wootters. "Entanglement of formation of an arbitrary state of two qubits". *Phys. Rev. Lett.*, **80**, 2245 (Mar 1998). URL http://link.aps.org/doi/10.1103/PhysRevLett.80.2245.

[72] A. B. Klimov et S. M. Chumakov. *Tópicos de óptica cuántica*. Universidad de Guadalajara (2005).

[73] G. Rempe, H. Walther, et N. Klein. "Observation of quantum collapse and revival in a one-atom maser". *Phys. Rev. Lett.*, **58**, 353 (Jan 1987). URL http://link.aps.org/doi/10.1103/PhysRevLett.58.353.

[74] S. Chumakov, A. Klimov, et J. Sanchez-Mondragon. "Collective atomic dynamics in a strong quantum field". *Optics Communications*, **118**, nº 5-6, 529 (1995). URL http://www.sciencedirect.com/science/article/pii/0030401895001655.

[75] R. H. Dicke. "Coherence in spontaneous radiation processes". *Phys. Rev.*, **93**, 99 (Jan 1954). URL http://link.aps.org/doi/10.1103/PhysRev.93.99.

[76] M. Kozierowski, A. A. Mamedov, et S. M. Chumakov. "Spontaneous emission by a system of n two-level atoms in terms of the su(2)-group representations". *Phys. Rev. A*, **42**, 1762 (Aug 1990). URL http://link.aps.org/doi/10.1103/PhysRevA.42.1762.

[77] T. Meunier, A. Le Diffon, C. Ruef, P. Degiovanni, et J.-M. Raimond. "Entanglement and decoherence of n atoms and a mesoscopic field in a cavity". *Phys. Rev. A*, **74**, 033802 (Sep 2006). URL http://link.aps.org/doi/10.1103/PhysRevA.74.033802.

[78] P. Maioli, T. Meunier, S. Gleyzes, A. Auffeves, G. Nogues, M. Brune, J. M. Raimond, et S. Haroche. "Nondestructive rydberg atom counting with mesoscopic fields in a cavity". *Phys. Rev. Lett.*, **94**, 113601 (Mar 2005). URL http://link.aps.org/doi/10.1103/PhysRevLett.94.113601.

[79] T. Pohl, E. Demler, et M. D. Lukin. "Dynamical crystallization in the dipole blockade of ultracold atoms". *Phys. Rev. Lett.*, **104**, 043002 (Jan 2010). URL http://link.aps.org/doi/10.1103/PhysRevLett.104.043002.

[80] M. Ebert, A. Gill, M. Gibbons, X. Zhang, M. Saffman, et T. G. Walker. "Atomic fock state preparation using rydberg blockade". *Phys. Rev. Lett.*, **112**, 043602 (Jan 2014). URL http://link.aps.org/doi/10.1103/PhysRevLett.112.043602.

[81] E. Vliegen, S. D. Hogan, H. Schmutz, et F. Merkt. "Stark deceleration and trapping of hydrogen rydberg atoms". *Phys. Rev. A*, **76**, 023405 (Aug 2007). URL http://link.aps.org/doi/10.1103/PhysRevA.76.023405.

[82] M. Orszag, R. Ramírez, J. C. Retamal, et C. Saavedra. "Quantum cooperative effects in a micromaser". *Phys. Rev. A*, **49**, 2933 (Apr 1994). URL http://link.aps.org/doi/10.1103/PhysRevA.49.2933.

[83] S. Hill et W. K. Wootters. "Entanglement of a pair of quantum bits". *Phys. Rev. Lett.*, **78**, 5022 (Jun 1997). URL http://link.aps.org/doi/10.1103/PhysRevLett.78.5022.

[84] R. Jozsa. "Fidelity for mixed quantum states". *Journal of Modern Optics*, **41**, n° 12, 2315 (1994). http://dx.doi.org/10.1080/09500349414552171, URL http://dx.doi.org/10.1080/09500349414552171.

[85] P. Milman, A. Auffeves, F. Yamaguchi, M. Brune, J. M. Raimond, et S. Haroche. "A proposal to test bell's inequalities with mesoscopic non-local states in cavity qed". *The European Physical Journal D - Atomic, Molecular, Optical and Plasma Physics*, **32**, n° 2, 233 (2005). URL http://dx.doi.org/10.1140/epjd/e2004-00171-6.

[86] K. Banaszek et K. Wódkiewicz. "Testing quantum nonlocality in phase space". *Phys. Rev. Lett.*, **82**, 2009 (Mar 1999). URL http://link.aps.org/doi/10.1103/PhysRevLett.82.2009.

[87] H. Jeong, W. Son, M. S. Kim, D. Ahn, et i. c. v. Brukner. "Quantum nonlocality test for continuous-variable states with dichotomic observables". *Phys. Rev. A*, **67**, 012106 (Jan 2003). URL http://link.aps.org/doi/10.1103/PhysRevA.67.012106.

[88] C. F. A. Aspect et G. Grynberg. *Optique Quantique 1 : Lasers.* Tome I. Ecole Polytechnique (2006).

Préparation déterministe d'atomes de Rydberg uniques pour des expèriences d'information quantique

Résumé Les atomes de Rydberg couplés à des cavités supraconductrices sont des outils remarquables pour l'exploration des phénomènes quantiques élémentaires et des protocoles d'information quantique. Ces atomes «géants» ont des propriétés uniques. Ils sont soumis à une forte interaction dipôle-dipôle, fonction de la distance interatomique, qui est responsable du mécanisme de blocage dipolaire : dans le régime de Van der Waals, l'énergie d'interaction croît comme n^{11}, où n est le nombre quantique principal. Si on illumine un nuage atomique avec un laser d'excitation à la fréquence de la transition de Rydberg pour un atome isolé, on s'attend à exciter au plus un atome dans un volume de blocage de $\sim 8(\mu m)^3$. Nous avons mis en place une expérience pour préparer un atome de Rydberg de façon déterministe. Elle utilise un petit nuage d'atomes de rubidium 87 dans l'état fondamental, piégés magnétiquement sur un puce à atomes supraconductrice à 4 K, et excités à l'aide de lasers vers les états de Rydberg. L'effet de blocage dipôlaire est sensible à l'élargissement spectral de la transition par des champs électriques parasites. Une fois un atome excité dans l'état cible $\left|60S_{1/2}\right\rangle$, nous explorons les transitions atomiques étroites, de longueur d'onde millimétrique, entre états de Rydberg pour étudier ces champs parasites. La surface de notre puce étant couverte d'une pellicule d'or, nous observons comme d'autres groupes de recherche de forts gradients de champs électriques, dus au dépôt progressif d'atomes de rubidium à la surface de la puce. Nous contournons le problème, en déposant une couche de rubidium métallique sur la puce. Les gradients sont alors réduits d'un ordre de grandeur. Cette amélioration nous permet d'observer des temps de cohérence très élevés, de l'ordre de la milliseconde, pour des atomes de Rydberg au voisinage d'une puce supraconductrice.
Sur le plan théorique, nous présentons un protocole simple pour la création rapide et efficace de superpositions quantiques de deux champs cohérents d'amplitudes classiques différentes dans une cavité. Il repose sur l'interaction de deux atomes à deux niveaux avec le champ dans la cavité. Leur détection avec une grande probabilité dans un état bien défini projette le champ dans une superposition mésoscopique d'états du champ. Nous montrons que ce protocole est nettement plus efficace que ceux utilisant un seul atome. Nous réalisons cette étude dans le contexte de l'électrodynamique en cavité (CQED), où les atomes à deux niveaux sont des atomes de Rydberg de grand temps de vie interagissant avec le champ d'une cavité micro-ondes supraconductrice. Mais ce travail peut également s'appliquer au domaine en plein essor de l'électrodynamique quantique des circuits. Dans ces deux contextes, il peut conduire à d'intéressantes études expérimentales de la décohérence à la frontière quantique-classique.

Mots-clés Atomes de Rydberg, Puce à atomes supraconductrice, Spectroscopie micro-ondes, CQED, Superpositions d'etats mésoscopiques.

Towards deterministic preparation of single Rydberg atoms and applications to quantum information processing.

Abstract Rydberg atoms and superconducting cavities are remarkable tools for the exploration of basic quantum phenomena and quantum information processing. These giant atoms are blessed with unique properties. They undergo a strong distance-dependent dipole-dipole interaction that gives rise to the dipole blockade mechanism: in the Van der Waals regime, this energy shift scales as n^{11}, where n is the principal quantum number. If we shine an excitation laser tuned at the frequency of the isolated atomic transition on an atomic cloud, we expect to excite at most one atom within a blockade volume of $\sim 8(\mu m)^3$. We have set up an experiment to prepare deterministically one Rydberg atom. It uses a small cloud of ground-state Rubidium 87 atoms, magnetically trapped on a superconducting atom chip at 4 K, and laser-excited to the Rydberg states. The dipole blockade effect is sensitive to the line broadening due to the stray electric fields. Once an atom has been excited to our target state $\left|60S_{1/2}\right\rangle$, we explore the narrow millimeter-wave transitions between Rydberg states in order to assess these stray fields . With a gold-coated front surface for the chip, we observe as other groups large field gradients due to slowly deposited Rubidium atoms. We circumvent this problem by coating the chip with a metallic Rubidium layer. This way the gradients are reduced by an order of magnitude. This improvement allows us to observe extremely high coherence times, in the millisecond range, for Rydberg atoms near a superconducting atom-chip.
Theoretically, we present a simple scheme for the fast and efficient generation of quantum superpositions of two coherent fields with different classical amplitudes in a cavity. It relies on the simultaneous interaction of two two-level atoms with the field. Their final detection with a high probability in the proper state projects the field onto the desired mesoscopic field state superposition (MFSS). We show that the scheme is notably more efficient than those using a single atom. This work is done in the context of cavity QED, where the two-level systems are circular Rydberg atoms whose lifetime may reach milliseconds, interacting with the field of a superconducting microwave cavity. But this scheme is also highly relevant for the thriving field of circuit-QED. In both contexts, it may lead to interesting experimental studies of decoherence at the quantum-classical boundary.

Keywords Rydberg atoms, Superconducting atom-chip, Microwave spectroscopy, CQED, Mesoscopic field state superpositions.

Hacía la preparación determinista de átomos de Rydberg únicos y sus aplicaciones a procesos de información cuántica.

Resumen Átomos de Rydberg y cavidades superconductoras son herramientas notables para la exploración tanto de fenómenos cuánticos básicos como de procesos de informa-

ción cuántica. Estos átomos gigantes están dotados de propiedades únicas. Se someten a interacciones fuertes del tipo dipolo-dipolo dependientes de la distancia que los separe: en el régimen de Van der Waals, el desplazamiento de energía debido a esta interacción escala con n^{11}, donde n es el número cuántico principal. Si hacemos incidir un láser de excitación a una nube atómica sintonizado a la frecuencia de transición de un solo átomo a un nivel de Rydberg dado, esperamos que este excite a lo más a un solo átomo dentro de un volumen de $\sin 8(\mu m)^3$. Hemos preparado un setup experimental para preparar de forma determinista un solo átomo de Rydberg. Se utiliza una nube pequeña de átomos neutros de rubidio 87, magnéticamente atrapados en un chip superconductor a 4 K, y excitados a estados de Rydberg con la ayuda de láseres. El efecto de bloqueo dipolar es sensible al ensanchamiento de línea debido al campos eléctricos parásitos. Una vez que un átomo ha sido excitado a nuestro estado objetivo $\left|60S_{1/2}\right\rangle$, exploramos las delgadas transiciones atómicas de longitud de onda milimétrica, entre estados de Rydberg con el fin de evaluar estos campos parásitos. Dado que la superficie del chip esta recubierta de oro, hemos observado como otros grupos grandes gradientes de campo debido al deposito lento de átomos de rubidio en ella. Solucionamos este problema mediante el recubrimiento de la superficie del chip con una capa metálica de rubidio. Así, los gradientes se redujeron por un orden de magnitud. Esta mejora nos permite ahora observar tiempos de coherencia extremadamente largos para nuestros átomos de Rydberg cerca de la superficie, en el rango de los milisegundos.

Teóricamente, presentamos un simple esquema para la generación rápida y eficiente de superposiciones cuánticas de dos componentes de campo con diferentes amplitudes coherentes clásicas dentro de una cavidad. Esta generación se basa en la interacción simultanea de dos átomos de dos niveles de energía con un campo coherente. La detección del estado final del sistema atómico proyecta al campo en la deseada superposición mesoscópicas. Demostramos que este esquema es notablemente más eficiente que su contraparte con un solo átomo. Este trabajo esta realizado en el contexto de CQED, donde los sistemas de dos niveles de energía son átomos de Rydberg circulares cuyos tiempos de vida alcanzan los milisegundos, interactuando con un campo atrapado en una cavidad superconductora. Pero este esquema también es bastaste relevante para el campo emergente de circuitos QED. En ambos contextos, el sistema propuesto puede conducir a estudios experimentales interesantes de decoherencia en el límite cuántico-clásico.

Palabras claves Átomos de Rydberg, Chip superconductores, Espectroscopía de microondas, CQED, superposiciones de campo mesoscópicos.